COLLECTED PAPERS

ON

NANO/ATOM PHOTONICS

Volume 11

August 1995—August 1996

Professor

Motoichi OHTSU

TOKYO INSTITUTE OF TECHNOLOGY

Interdisciplinary Graduate School of Science and Engineering

4259 Nagatsuta, Midori-ku, Yokohama, Kanagawa 226, JAPAN

TEL : +81—45—924—5455

FAX: +81—45—921—1204

E-mail : ohtsu@ae. titech. ac. jp

PREFACE

In order to realize the ultimate status of light and matter, M. Ohtsu tries to control the spatial properties of light. The approach he has used is through the research of near-field optics and its application to nano-fabrication and atom manipulation. This will open up a new era of nano/atom photonics. It should be pointed out that the nano/atom photonics is closely related to quantum optics, atom optics, high density optical storage, bio-technology, and so on (see the figure on the next page). And by means of this relationship of near-field optics with a variety of fields, nano/atom photonics exhibits rapid progress. Further research will be done to realize novel nanometric materials and devices.

A "PHOTON CONTROL" project, Kanagawa Academy of Science and Technology (KAST)(*), directed by Ohtsu is also engaged in the research subject described above. Twelve research staffs including three visiting scientists from industries and one visiting STA fellow from Canada have obtained several results on nano/atom photonics. Their details are reviewed in this issue of the COLLECTED PAPERS.

September 1996

Motoichi OHTSU
大津　元一

(*) Address: Photon Control Project,
Kanagawa Academy of Science and Technology
KSP East, Rm.408, 3-2-1 Sakado, Takatsu-ku,
Kawasaki-shi, Kanagawa 213, JAPAN
Phone: +81-44-819-2071
Fax: +81-44-819-2072
E-mail: ohtsu@net.ksp.or.jp
〒２１３　神奈川県川崎市高津区坂戸３－２－１
ＫＳＰ東棟４０８号室
（財）神奈川科学技術アカデミー
フォトン制御プロジェクト

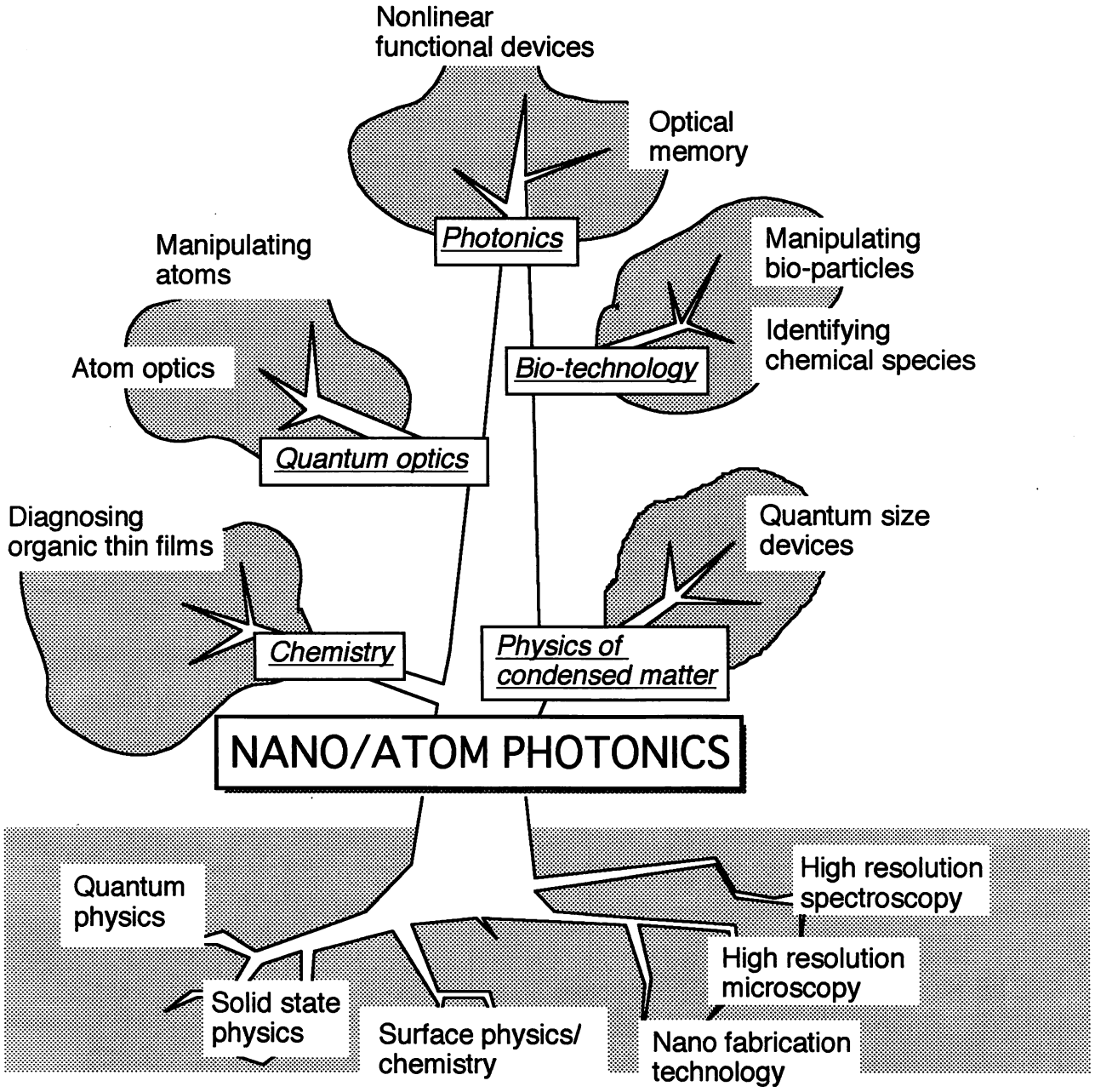

Nano/atom photonic tree with its roots and leaves covering a wide range of fields

MEMBERS

(From April 1, 1996)

[I] *TOKYO INSTITUTE OF TECHNOLOGY*

Professor

Motoichi OHTSU [a)]	(Dr. Eng.)

Research Associate

Motonobu KOUROGI [b)]	(Dr. Eng.)

Graduate Students (Doctor Candidates)

Mikio KOZUMA	(M. Eng.)
Shuji SAYAMA	(M. Eng.)
Andrei Vasilyevich ZVYAGIN	(M. Sci.)
Kazuhiro IMAI	(M. Eng.)
Takuya MATSUMOTO	(M. Eng.)
Keiji SAKAKI	(M. Eng.)
Vitali Vasilyevich POLONSKI	(M. Sci.)

Graduate Students (Master Course)

Shintaro TAKEHARA	(B. Eng.)
Takashi YATSUI	(B. Eng.)
Yoshitaka YOKOYAMA	(B. Sci.)
Yoh YAMAMOTO	(B. Eng.)
Kazumi WATANABE	(B. Sci.)

Undergraduate Students

Kouichi OTAKE
Tsuyosi NAKANO
Kouichi YAMAGUCHI

Visiting Scientists

Myung-Bok LEE [c)]	(Dr. Eng.)

Research Students

Bambang WIDIYATMOKO (M. Eng.)

Secretaries

Chikako ISHIDA
Kaoru OGURA

a) Also with Kanagawa Academy of Science and Technology
(Director, "Photon Control" Project)
b) Also with Kanagawa Academy of Science and Technology
(Research staff member, "Photon Control" Project)
c) Permanent affiliation: National Institute for Advanced Interdisciplinary Research, Ministry of International Trada and Industry

[II] *KANAGAWA ACADEMY OF SCIENCE AND TECHNOLOGY*

Full-Time Researchers

Toshiharo SAIKI	(Dr. Eng.)
Rajagopalan UMAMAHESWARI	(Dr. Eng.)
Shuji MONONOBE	(M. Eng.)
Haruihko ITO[d]	(Dr. Sci.)
Kazuyoshi KURIHARA	(Dr. Sci.)
Makoto ASHINO	(Dr. Eng.)

Part-Time Researchers

Motonobu KOUROGI[e]	(Dr. Eng.)
Hirofumi KADONO[f]	(Dr. Eng.)

Visiting Researchers

Hiroaki FUKUDA[g]	(M. Eng.)
Toshiyasu TADOKORO[h]	(B. Sci)
Yoshihito NARITA[h]	(M. Sci.)

STA Fellow

Johathon David WHITE (Ph.D.)

Secretary

Nobue Lucy WATANABE

d) Also with Precursory Research for Embryonic Science and Technology, Japan Science and Technology Corporation
e) Permanent affiliation: Tokyo Institute of Technology
f) Permanent affiliation: Saitama University
g) Permanent affiliation: RICOH Corporation
h) Permanent affiliation: JASCO Corporation

LIST OF PAPERS

[**(pp.XX-XX)** : pages in this issue of the COLLECTED PAPERS]

[I] PAPERS IN NANO/ATOM PHOTONICS

[I-1] ATOM PHOTONICS

(a) Journal Papers

(b) International Conferences

[I-2] NANO PHOTONICS

(a) Journal Papers

(b) International Conferences

(pp.66-67)

[5] H. Hori, K. Kitahara and M. Ohtsu, "Comment on the Possibility of Longitudinal Electromagnetic Waves on the Surface of Dielectrics", Abstracts, The First Asia-Pacific Workshop on Near Field Optics, August 1996, Seoul, Korea, p. 49

(p.68)

[6] R. Micheletto, S. Mononobe, M. Ohtsu, M. Yoshimoto, T. Maeda, T. Ohnishi and H. Koinuma, "Observation of an atomic sapphire step by a collection mode near-field optical microscope", Abstracts, The First Asia-Pacific Workshop on Near Field Optics, August 1996, Seoul, Korea, pp.54-55

(pp.69-70)

[7] T. Saiki, Y. Yokoyama, M. Ohtsu, N. Saito, J. Kusano, "Determination of slant angle of p-n interface by multi-wavelength near-field photocurrent measurement", Technical Digest, The XXth International Quantum Electronics Conference(IQEC'96), paper number WL1, July 1996, Sydney, Australia, p.135

(p.71)

[8] N. Saito, J. Kusano, H. Okumura, T. Aida, K. Takizawa, T. Saiki and M. Ohtsu, "Spatially resolved detection of photoluminescence and electroluminescence from lateral p-n junctions on GaAs(111)A patterned substrates uging a photon scanning tunneling microscope", Technical Digest, The XXth International Quantum Electronics Conference(IQEC'96), paper number FO2, July 1996, Sydney, Australia, pp.282-283

(pp.72-73)

[9] K. Kurihara, K. Watanabe and M. Ohtsu, "Photon scanning tunneling microscopy with light-emitting probes", Technical Digest, The 11th International Conference on Optical Fiber Sensors (OFS-11), paper number Fr2-3, May 1996, Sapporo, Japan, pp.694-697

(pp.74-77)

[10] M. Ohtsu, "Near Field Optics Toward Nano-scale Photonic Materials", Proceedings of the 1st International Symposium on Advanced Physical Fields", Application to Materials Science on the Nanometer Scales, March 1996, Tsukuba, Japan, pp.43-48 **[Invited]**

(pp.78-83)

[I-3] REVIEW PAPERS

[II] PAPERS IN OTHER FIELDS

(a) Journal Papers

[2] M. Kourogi, B. Widiyatmoko and M. Ohtsu, "3.17-THz Frequency-Difference Measurement Between Lasers Using Two Optical Frequency Combs", IEEE Photonics Technol. Lett., vol.8, no.4, April 1996, pp.560-562

(pp.118-120)

[3] M. Kozuma, K. Nakagawa, W. Jhe and M. Ohtsu, "Observation of Temporal Behavior of an Atomic Wave Packet Localized in an Optical Potential", Phys. Rev. Lett., vol.76, no.14, April 1996, pp.2428-2431

(pp.121-124)

[4] T. Saitoh, E. Durand, M. Kourogi and M. Ohtsu, "Proposal of a Multiplex Optical Frequency Comb Generation System", IEEE Photonics Technol. Lett., vol.8, no.2, February 1996, pp.287-289

(pp.125-127)

[5] E. Durand, T. Saitoh, M. Kourogi and M. Ohtsu, "0.4-THz Frequency Offset Locking Between Two Optical Frequency Combs", IEEE Photonics Technol. Lett., vol.8, no.1, January 1996, pp.163-165

(pp.128-130)

[6] M. Kourogi, B. Widiyatmoko, Y. Takeuchi and M. Ohtsu, "Limit of Optical-Frequency Comb Generation Due to Material Dispersion", IEEE J. Quantum Electron., vol.31, no.12, December 1995, pp.2120-2126

(pp.131-137)

[7] M. Kozuma, Y. Imai, K. Nakagawa and M. Ohtsu, "Observation of a transient response of recoil-induced resonance: A method for the measurement of atomic motion in an optical standing wave", Phys. Rev.A, vol.52, no.5, November 1995, pp.R3421-R3424

(pp.138-141)

[8] Y. Awaji, K. Nakagawa, M. de Labachelerie, M. Ohtsu and H. Sasada, "Optical frequency measurement of the $H^{12}C^{14}N$ Lamb-dip-stabilized 1.5-μm diode laser", Opt. Lett., vol.20, no.19, October 1995, pp.2024-2026

(pp.142-144)

(b) International Conferences

[1] M. Kourogi, T. Saito and M. Ohtsu, "High efficient electro-optic modulation of semiconductor lasers", Abstracts, The XXVth General Assembly of the International Union of Radio Science, paper number AD.3, August 1996, Lille, France, p.597 **[Invited]**

(p.145)

(c) Review Papers

[1] M. Ohtsu, "Optical Frequency Reference and Its Measurement", Optronics, vol. 15, no.5, May 1996, pp.153-156
【大津元一、「光周波数の基準と計測」、オプトロニクス、第15巻、第5号、1996年5月、pp.153-156】

(pp.146-149)

[III] PUBLISHED BOOKS

[1] M. Ohtsu(Editor), *Frequency Control of Semiconductor Lasers*, John Wiley & Sons, Inc., New York, 1996 (240 pages)

[2] M. Kougori and M. Ohtsu, " Phase Noise and its Control in Semiconductor Lasers", Chapter 3, *Semiconductor Lasers, Past, Present, and Future*, Ed. by G.P. Agrawal, AIP Press, New York, 1995, pp.71-109

[3] M. Ohtsu, "Generation of Ultra-wide Band Optical Frequency Grids", Section 2.4, *Ultrafast and Ultra-parallel Optoelectronics*, Ed. by T. Sueta and T. Okoshi, John Wiley & Sons, Inc., New York, 1995, pp.84-93

[4] M. Ohtsu, "Light control and noise in semiconductor lasers", Chapter 9, *Handbook of Semiconductor Lasers and Photonic Integrated Circuits*, Ed. by Y. Suematsu and A.R. Adams, Chapman & Hall, London, 1994, pp.292-316

[IV] PRESENTED PH.D. THESIS

[1] Y. Toda, "High resolution diagnostics of photonic devices by near-field optics", January 1996
【戸田泰則、「近接場光学手法による光デバイスの高分解能評価」、1996年1月】

[2] A. Awaji, "Study on highly accurate optical frequency references at 1.5-μm wavelength region", January 1996

【淡路祥成、「１．５μｍ帯高確度光周波数基準に関する研究」、1996年1月】

[3] K. Tanaka, "Study on Optical Detection by Patterned $YBa_2Cu_3O_{7-\delta}$ Thin Films", January 1996
【田中健一、"Study on Optical Detection by Patterned $YBa_2Cu_3O_{7-\delta}$ Thin Films"、1996年1月】

[I] PAPERS IN NANO/ATOM PHOTONICS

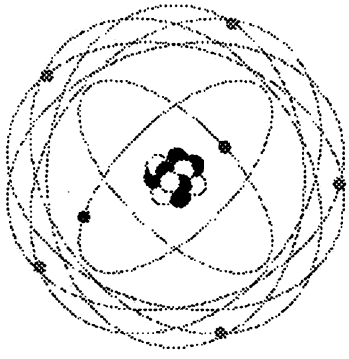

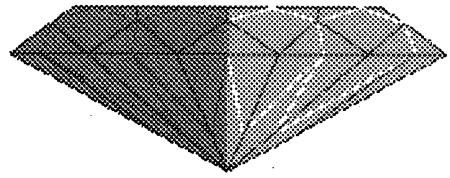

[I-1] ATOM PHOTONICS

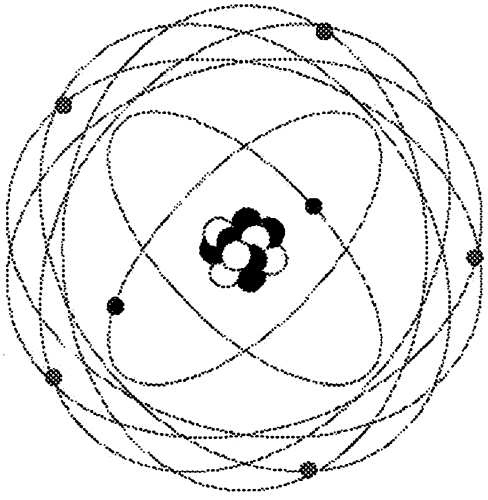

Laser Spectroscopy of Atoms Guided by Evanescent Waves in Micron-Sized Hollow Optical Fibers

H. Ito,[1] T. Nakata,[2] K. Sakaki,[2] and M. Ohtsu[1,2]
[1]*Kanagawa Academy of Science and Technology, KSP, Takatsu, Kawasaki 213, Japan*
[2]*Interdisciplinary Graduate School of Science and Engineering, Tokyo Institute of Technology, Yokohama 226, Japan*

K. I. Lee and W. Jhe
Department of Physics, Seoul National University, Seoul 151-742, Korea
(Received 26 January 1996; revised manuscript received 10 April 1996)

We report the first laser spectroscopic experiments on the Rb beam guided by blue-detuned evanescent waves in micron-sized hollow fibers. The two-step photoionization spectra show the long-range dispersive properties of dipole interaction between guided atoms and evanescent waves. A large enhancement factor of 20 in in the transmitted atomic flux is obtained at optimal conditions and the total guidance efficiency is estimated to be above 40%. The state- and species-selective guide with proper frequency detunings of the guide laser realizes in-line spatial separation of two stable Rb isotopes. [S0031-9007(96)00434-6]

PACS numbers: 32.80.Lg, 32.80.Pj, 39.10.+j, 39.30.+w

As a feasible method to realize a precise manipulation of neutral atoms, two kinds of atomic waveguides using optical fibers have been proposed [1–4]. The first is one using a red-detuned Gaussian laser beam propagating into a hollow-core fiber [1]. The dipole force from the intense Gaussian beam guides atoms by attracting them to the center of the hollow region where the laser intensity is maximum. However, it causes strong heating of the guided atoms due to the spontaneous emission. The other scheme is one using evanescent waves such that the spontaneous-emission effect is relatively negligible [2–4]. The evanescent wave produced near a glass-vacuum interface acts as a mirror for atoms under blue detuning [5], which leads from the walls within only a few hundred nanometers for visible light. Therefore, the guided atoms interact with the light field only when they approach the walls, but otherwise they are free. The atom guidance with the evanescent wave enables one to use a hollow fiber with a small hollow diameter of 1 μm. Such a micron-sized atom guide will not only enhance the precision of atom manipulation but will also be useful for interesting studies such as the cavity QED effects in a cylindrical dielectric, the gravitational cavity [6], the atomic quantum wire [7], and the atom lithography [8].

The experimental demonstration of the Rb atom guidance were performed in hollow-core glass capillaries with relatively large hollow diameters of more than 20 μm [9,10]. They employed the hot-wire technique and detected four kinds of Rb atomic states including two isotopes at the same time so that the dependence of the guidance on the frequency detuning is ambiguous. In this Letter, we report the first laser-spectroscopy experiments on the Rb atomic beam guided by the blue-detuned evanescent wave in the cylindrical-core hollow fibers with 7- and 2-μm hollow diameters. The hollow areas are 10 and 100 times smaller than that of the glass capillary used in Ref. [10]. The combination of the small hollow fibers and the collimated atomic beam realizes the high efficient guidance and the fine control of the lateral atomic motion, which allows one to detect the cavity QED effects.

First of all, we have performed two-step photoionization spectroscopies on the guided Rb atoms with micron-sized hollow fibers. The result clearly shows the long-range dispersive characteristics of the optical dipole interaction between the guided atoms and the evanescent field. Contrary to the glass capillary scheme, since the energy of the laser field is stored in the 4-μm thin cylindrical core, even a small coupled power from a guide laser beam can produce an optical potential barrier high enough to guide a thermal atomic beam. Consequently, a large enhancement factor of 20 in the flux of the transmitted ^{85}Rb atoms is obtained for a 3-cm-long hollow fiber with a 7-μm hollow diameter. We also estimate that more than 40% of the incident atoms are guided by the fiber with 280-mW coupled power at an optimal detuning. Finally, we have performed an in-line isotope-separation experiment for the two stable Rb isotopes by the state- and species-selective guidance of atoms through the fiber under proper frequency detunings of the guide laser.

Let us first consider that a laser beam with the frequency ω and the wave number k is coupled into the cylindrical core of a hollow fiber having a propagation constant β. For atoms with resonance frequency ω_0 and longitudinal velocity v_z along the waveguide, the evanescent wave leaked into the hollow region produces an optical potential $U_{\rm op}(r,\theta)$ at a distance r from the fiber center and an azimuthal angle θ given by [5]

$$U_{\rm op}(r,\theta) = \tfrac{1}{2}\hbar\Delta \ln\left\{1 + \frac{P(r,\theta)/P_0}{1 + 4\Delta^2/\Gamma^2}\right\}, \qquad (1)$$

where Γ, P_0, and $\Delta = \omega - \omega_0 - \beta v_z$ are the natural linewidth (= 6.1 MHz), the saturation intensity

 0031-9007/96/76(24)/4500(4)$10.00

(= 1.6 mW/cm^2), and the frequency detuning, respectively. As shown in previous works [4], the weakly guiding approximation can be applied to describe the hollow fiber having a small refractive-index difference between core and cladding. As a result, it greatly simplifies the description of the evanescent waves in terms of the linearly polarized (LP) modes. Under this approximation, the intensity $P(r,\theta)$ of the LP_{m1} evanescent wave can be written as [4]

$$P(r,\theta) = \frac{\beta}{2\omega\mu_0} C^2 I_m^2(\upsilon r)\cos^2(m\theta), \qquad (2)$$

where $\upsilon = \sqrt{\beta^2 - k^2}$, μ_0 is the magnetic permeability, and $I_m(\upsilon r)$ is the modified Bessel function of the first kind of order m, respectively. The constant C can be determined by the boundary conditions and the laser power. Note that the total atomic potential consists of the repulsive optical barrier $U_{op}(r,\theta)$ due to the evanescent wave in Eq. (1) and the attractive cavity potential $U_{cp}(r)$ due to the atomic interaction with the surrounding cylindrical surface of the core [4]. Provided that the evanescent wave is sufficiently intense, the total potential becomes positive so that atoms can be reflected and guided.

Figure 1 shows a schematic diagram of the experimental setup. A thermal atomic beam from a heated Rb oven, which was collimated within 1 mrad, was introduced into the hollow fiber having a hollow diameter of 7 μm (2 μm), core thickness of 3.8 μm (4 μm), and length of 3 cm. The atoms which do not enter the hollow region upstream were blocked by a large fiber holder so that they are not detected downstream. We aligned the straight hollow fiber with the atomic beam path using a He-Ne laser. A guiding laser beam from a Ti:sapphire laser was coupled at the core at the entrance by a mirror with a hole that allowed the atoms to pass. The coupling efficiency of the guide laser into the core was about 40%. At the wavelength of 780 nm for guiding the Rb atoms,

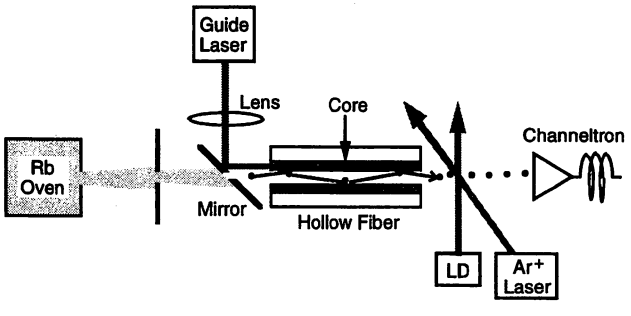

FIG. 1. Sketch of the experimental setup. A collimated atomic beam from a Rb oven impinges into a cylindrical-core hollow fiber with a hollow diameter of 7 or 2 μm and guided by the blue-detuned evanescent waves therein. A Ti:sapphire laser, focused on the core in the upstream, is used for atom guidance and isotope separation. A diode laser and an Ar-ion laser, overlapping downstream, are used for the two-step photoionization spectroscopy.

three propagation modes can be excited: LP_{01}, LP_{11}, and LP_{21} [4]. The mode patterns at the exit facet of the fiber were monitored by a charge coupled device camera from the outside of the ultrahigh vacuum chamber. In the 3-cm-long fiber, although the three modes were not clearly distinguished, an effectively round mode (i.e., $m = 0$) could be excited.

For the spectroscopy on the Rb atoms guided through the hollow fibers, we employed the two-step photoionization (PI) technique using two overlapping lasers near the exit of the fiber downstream. The ions, produced by the ionized atoms, were then detected by a channel electron multiplier (CEM) biased at a high voltage of -3 kV. A grating-feedback diode laser tuned to a wavelength of 780 nm saturates the $5S_{1/2} \rightarrow 5P_{3/2}$ transition. At the same time, an Ar-ion laser focused on the 100-μm beam waist ionizes the atoms in the $5P_{3/2}$ state (the ionization level is at 4.177 eV above the ground state). With the applied high bias, the photoionization at three wavelengths of 457.9, 476.5, and 488 nm from the Ar-ion laser was possible. The ionization efficiency of this scheme can be estimated by using the ionization cross section of the $5P_{3/2}$ state ($\sigma_i \approx 10^{-17}$ cm^2) [11] and the condition of efficient ionization [12]

$$P_i \approx P_0(\sigma_0/\sigma_i), \qquad (3)$$

where P_i and σ_0 are the optimum ionization-laser intensity and the resonant excitation cross section for the $5S_{1/2} \rightarrow 5P_{3/2}$ transition, respectively. Therefore, with an Ar-ion laser with 4 W focused on a spot of 100-μm diameter, we estimate the PI efficiency to be 32%. Assuming the quantum efficiency of the CEM to be 0.9, the total detection efficiency is then 29%.

An enhanced transmission of the guided atoms is expected at the blue detuning of the guide laser. Figure 2 shows a Doppler-free photoionization signal for the ^{85}Rb atoms in the $F = 3$ hyperfine level of the ground state passed through the 7-μm hollow fiber as a function of the frequency detuning of the guide laser with a coupled power of 130 mW. Note that the detuning is measured with respect to the transition frequency of the upper $F = 3$ level and does not include the Doppler shift βv_z. The oven temperature of 160 °C provides a most probable longitudinal velocity of 292 m/s and a most probable transverse velocity of 0.3 m/s for our collimation angle. The incident flux of the Rb atoms impinging on the hollow entrance of 7-μm diameter is estimated to be 10^6 s^{-1}[13] (note that the ^{85}Rb isotope occupies 73% of the incident atoms). The diode laser was tuned to the $5S_{1/2}, F = 3 \rightarrow 5P_{3/2}, F = 4$ transition and the Ar-ion laser was wavelength selected at 476.5 nm with a power of 4 W to ionize the guided atoms. In Fig. 2, we observe the expected dispersive spectrum with a peak at a blue detuning of 2.7 GHz. The foot level of the ion-counting signal extended over a 20-GHz detuning. The maximum atom flux at the transmission peak was 3×10^4 s^{-1} as

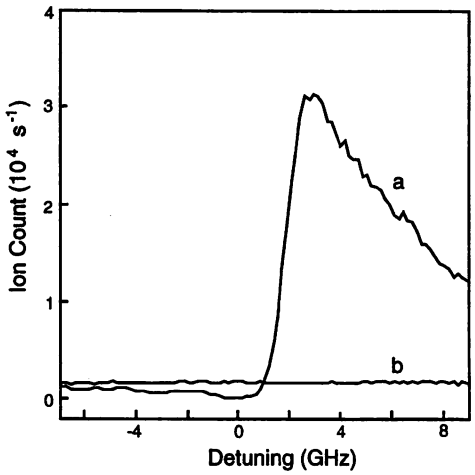

FIG. 2. Ion-counting rates for the transmitted atoms versus the frequency detunings of the guide laser in the 7-μm hollow fiber. The guide laser with 130 mW power is on in (a) and off in (b). The detuning is measured with respect to the resonance frequency of the $5S_{1/2}, F = 3 \rightarrow 5P_{3/2}, F = 4$ transition of ^{85}Rb. The grating-feedback diode laser is locked to this D_2 line and the Ar-ion laser is selected at a wavelength of 476.5 nm with 4 W power.

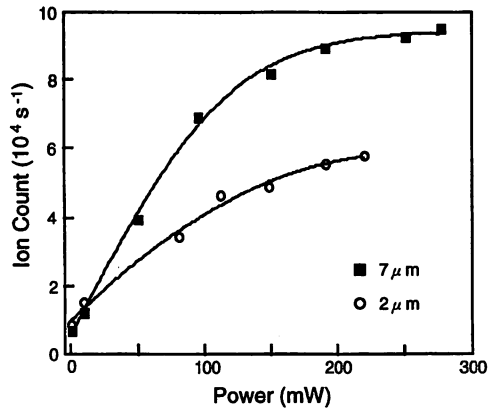

FIG. 3. Variation of the guided atomic flux versus the coupled power of the guide laser in the 7- and 2-μm hollow fibers. The background level in the absence of the guide laser is subtracted from the observed lux of ^{85}Rb in the $F = 3$ level. We estimate that the total guidance efficiency is more than 40% in the case of the 7-μm hollow fiber.

shown in Fig. 2(a). On the other hand, flux without the guide laser was 1.5×10^3 s^{-1} as shown in Fig. 2(b). Therefore, we estimate a very large enhancement factor of 20, which is possible due to the use of the well-collimated atomic beam and the micron-sized hollow fiber.

In the red-detuning region, however, the atomic flux was decreased below the background level without the guide laser probably due to adsorption on the inner wall by the attractive optical force. Moreover, in the vicinity of the $5S_{1/2}, F = 3 \rightarrow 5P_{3/2}, F = 4$ resonant transition, it seems that the ^{85}Rb atoms in the $F = 3$ ground-state hyperfine level are pumped into the lower $F = 2$ level due to the interaction with the resonant evanescent wave of the guide laser which is slightly leaked into the hollow region at the entrance. We have confirmed this effect by detecting the guided atoms in the lower hyperfine level by tuning the diode laser to the $5S_{1/2}, F = 2 \rightarrow 5P_{3/2}, F = 1$ transition. As a result, a small increase (about 30% of the background signal) of the ^{85}Rb atoms in the $F = 2$ level was observed near the resonant guidance frequency of the $5S_{1/2}, F = 3 \rightarrow 5P_{3/2}, F = 4$ transition.

Figure 3 shows the transmitted ^{85}Rb atom flux in the $F = 3$ level as a function of the coupled power of the guide laser at the optimal detuning of 2.7 GHz. The oven temperatures were 174 and 183 °C in the case of the 7- and 2-μm hollow fibers, respectively. The flux is plotted after the background signal without the guide laser is subtracted (1.6×10^4 s^{-1} for the 7-μm hollow fiber). Therefore, the data in Fig. 3 represent the net transmission flux only due to the optical guidance. As shown in the curve for the 7-μm hollow fiber, saturation behavior in the transmission can be observed as the coupled power is increased above 150 mW or so. Moreover, a maximum net flux of 9.5×10^4 s^{-1} could be obtained at the 280 mW power. Using the total detection efficiency of 29% and the incidence flux of 9×10^5 s^{-1} for the ^{85}Rb isotope, and also adding the background signal, we estimate that the total guidance efficiency of the atom waveguide is about 43% for the ^{85}Rb atom in the $F = 3$ level, whereas the pure optical guidance efficiency is 37%.

If we take into account the fact that the ^{87}Rb isotope [see Fig. 4(a)] as well as the ^{85}Rb atoms in the lower $F = 2$ level are also guided, we estimate the total efficiency exceeds 50%. The very high guidance efficiency is realized mainly because we have used a collimated atomic beam, which is discussed in the following. In the case of the excitation of the LP_{01} mode at a 300 mW power and a 3 GHz blue detuning in the 7-μm hollow fiber, from Eqs. (1) and (2), we obtain the optical potential of 120 mK in terms of the equivalent temperature of the atomic kinetic energy, which then corresponds to the maximum transverse velocity of 3.4 m/s that can be reflected. Therefore, since the most probable transverse velocity due to our beam collimation is 0.3 m/s, most of the atoms entering the hollow fiber are expected to be guided.

Now, let us consider the cavity potential $U_{cp}(r)$ which reduces the height of the optical potential barrier. By using the results of the two parallel-dielectric case [14,15], we can roughly estimate the effects of the cavity potential [5]. For the excitation of the LP_{01} mode at 280 mW in the 7-μm hollow fiber, a reduction of about 30% occurs in the potential barrier. On the other hand, with 1 mW power, the potential barrier almost disappears due to the attractive cavity potential. The ^{85}Rb atoms can be guided above the coupled power of 1 mW as shown in Fig. 3, but we observe a rapid decrease of the guided flux below 1 mW.

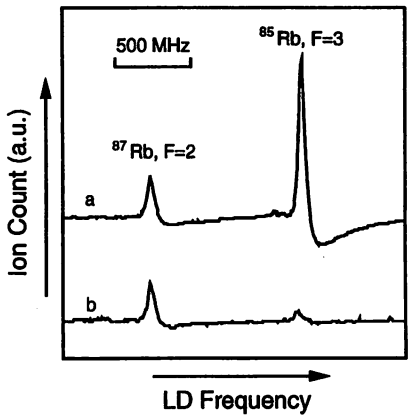

FIG. 4. In-line separation of the two stable Rb isotopes. Atomic transmission signals as a function of the diode-laser frequency are presented at a large blue detuning for both Rb isotopes in their upper hyperfine levels (a), and at a blue detuning for ^{87}Rb but near red detuning for ^{85}Rb (b).

Note that the maximum transverse velocity due to $U_{op}(r)$ for 1 mW power is about 0.3 m/s, which is equivalent to that determined by the beam collimation. Therefore, the observed threshold behavior near 1 mW power may be considered as an indirect indication of the cavity QED effects of the cylindrical dielectric. In order to study the cavity QED effects more quantitatively, we measured a guide-laser power that does not increase the transmission on ^{87}Rb atoms in the upper ground state with the 2 μm hollow fiber. The result shows a threshold power of 2 mW, which agrees well with the theoretical calculation. The detailed results will be published elsewhere.

Finally, we have performed an isotope-separation experiment for the two stable Rb isotopes in their upper hyperfine levels of the ground state, by the state-selective and species-selective guidance of atoms in the fiber which is done with proper frequency detunings of the guide laser. Based on the dispersive nature of the guidance shown in Fig. 2, we can select a specific isotope by adjusting the guide-laser frequency. Figure 4 shows a demonstration of the isotope separation by the 7-μm hollow fiber. The upper hyperfine levels of the ground states of the two isotopes ^{85}Rb and ^{87}Rb are separated by about 1 GHz. In Fig. 4(a), the laser frequency was set at a large blue detuning for both the $5S_{1/2}, F = 2$ level of ^{87}Rb and the $5S_{1/2}, F = 3$ level of ^{85}Rb. On the other hand, in Fig. 4(b), the laser was blue detuned for the ^{87}Rb atoms but nearly red detuned for the ^{85}Rb atoms. As is clear in the figure, the transmission flux of the ^{85}Rb isotope is greatly suppressed down to one-tenth of the background level. Therefore, our hollow fiber can be considered as an in-line isotope separator or an atomic-state filter.

In conclusion, the two-step photoionization spectroscopy has been performed so that the long-range dispersive character of the atom-field interaction has been clearly observed. The precise control of the atomic lateral motion has been realized within 2 μm through a long distance. We have shown that more than 40% of the incident atoms are guided, and obtained a large guiding enhancement factor of 20; they are 40 and 7 times improvement over the result in Ref. [10], respectively. Moreover, the state selectivity and species selectivity have been demonstrated through a separation between two Rb isotopes. Since the evanescent wave is localized within the size of an object [16], we may even manipulate atoms with a nanometric accuracy using a sharpened tip on an optical fiber [17]. The atom guidance in very small hollow fibers will open a new way to such a nanoscale atom manipulation as well as novel atomic physics experiments.

This work was supported by the MATSUO Foundation of Japan and the Korean Science and Engineering Foundation (KOSEF) of Korea.

[1] M. A. Ol'Shanii, Yu. B. Ovhinnikov, and V. S. Letokhov, Opt. Commun. **98**, 77 (1993).
[2] S. Marksteiner, C. M. Savage, P. Zoller, and S. L. Rolston, Phys. Rev. A **50**, 2680 (1994).
[3] W. Jhe, M. Ohtsu, H. Hori, and S. R. Friberg, Jpn. J. Appl. Phys. **33**, L1680 (1994).
[4] H. Ito, K. Sakaki, T. Nakata, W. Jhe, and M. Ohtsu, Opt. Commun. **115**, 57 (1995); Ultramicroscopy (to be published).
[5] V. I. Balykin, V. S. Letokhov, Yu. B. Ovchinnikov, and A. I. Sidorov, Phys. Rev. Lett. **60**, 2137 (1988).
[6] D. J. Harris and C. M. Savage, Phys. Rev. A **51**, 3967 (1995).
[7] J. P. Dowling and J. Gea-Banacloche, Phys. Rev. A **52**, 3997 (1995).
[8] R. W. McGowan, D. M. Giltner, and S. A. Lee, Opt. Lett. **20**, 2535 (1995).
[9] M. J. Renn, D. Montgomery, O. Vdovin, D. Z. Anderson, C. E. Wieman, and E. A. Cornell, Phys. Rev. Lett. **75**, 3253 (1995).
[10] M. J. Renn, E. A. Donley, E. A. Cornell, C. E. Wieman, and D. Z. Anderson, Phys. Rev. A **53**, R648 (1996).
[11] T. P. Dinneen, C. D. Wallace, Kit-Yan N. Tan, and P. L. Gould, Opt. Lett. **17**, 1706 (1992).
[12] V. S. Letokhov, *Laser Photoionization Spectroscopy* (Academic Press, New York, 1987).
[13] N. F. Ramsey, *Molecular Beams* (Oxford University Press, New York, 1956).
[14] W. Jhe, Phys. Rev. A **43**, 5795 (1991); H. Nha and W. Jhe (to be published).
[15] C. I. Sukenik, M. G. Boshier, D. Cho, V. Sandoghdar, and E. A. Hinds, Phys. Rev. Lett. **70**, 560 (1993).
[16] K. Jang and W. Jhe, Opt. Lett. **21**, 236 (1996).
[17] H. Hori, S. Jiang, M. Ohtsu, and H. Ohsawa, *International Quantum Electronics Conference, Technical Digest* (OSA, Washington, DC, 1992), Vol. 8 p. 48.

ELSEVIER

Ultramicroscopy 61 (1995) 91–97

ultramicroscopy

Optical guidance of neutral atoms using evanescent waves in a cylindrical-core hollow fiber: theoretical approach

Haruhiko Ito [a], Keiji Sakaki [b], Takeshi Nakata [b], Wonho Jhe [c], Motoichi Ohtsu [a,b]

[a] *Kanagawa Academy of Science and Technology, KSP East, 3-2-1 Sakado, Takatsu-ku, Kawasaki 213, Japan*

[b] *Interdisciplinary Graduate School of Science and Engineering, Tokyo Institute of Technology, 4259, Nagatsuta-cho, Midori-ku, Yokohama 226, Japan*

[c] *Department of Physics, Seoul National University, Seoul 151-742, South Korea*

Received 9 May 1995; accepted 30 May 1995

Abstract

An atomic waveguide made by a cylindrical-core hollow fiber is described using numerical analyses in the weakly guiding approximation. We describe a potential barrier made up of the optical potential due to evanescent waves and the attractive potential due to cavity QED effects. The feasibility of atomic guidance experiments with a Rb beam is discussed in terms of an evaluation of the potential barrier including interference effects.

1. Introduction

The development of atomic waveguides is an interesting subject involving atom optics and near-field optics. Atomic waveguides can be applied to research on quantum effects [1], cavity QED effects [2], topological phenomena [3] and so on. They may also be useful for semiconductor technology. The atom guidance by evanescent waves from optical fibers has been proposed [4–6]. By using a hollow fiber with a thin cylindrical core, we plan to make an atomic waveguide [6]. This type of atomic waveguide is simple and convenient for a first demonstration. The evanescent wave decaying into the hollow central region gives an intense repulsive force under appropriate blue-detuning, hence neutral atoms are guided along the hollow fiber while being repelled by the force as shown in Fig. 1a. The hollow fiber with its internal evanescent wave allows for one-dimensional manipulation of atoms. This technique may eventually allow for atomic-level crystal growth and single-atom manipulation [7].

Using exact solutions of the electromagnetic field [6], we have done an analysis of light propagation modes of a cylindrical-core hollow fiber and an evaluation of the optical potential that may be used to guide Rb atoms. In this paper, we present a new analysis of this atomic waveguide based on the weakly guiding approximation. This approximation gives convenient formulae for the evanescent field and the dispersion equation. As a result, it extremely simplifies the estimation of the potential barrier and easily yields its clear-cut image.

First we introduce the weakly guiding approximation and then derive expressions for the electric field and the dispersion equation to determine the light propagation modes in the cylindrical-core hollow fiber. Second, the potential barrier to guide Rb atoms is evaluated for the LP_{01} excitation, including cavity QED effects. Finally,

0304-3991/96/$15.00
SSDI 0304-3991(95)00129-8

we discuss the feasibility of an atomic beam experiment by considering tunneling through the potential barrier and spontaneous emission effects.

2. Analysis of cylindrical-core hollow fibers in the weakly guiding approximation

In our previous work, the exact solution of the electromagnetic field in the cylindrical-core hollow fiber was utilized for evaluating the evanescent field and the potential barrier to guide atoms [6]. However, it leads to rather complicated expressions of the dispersion equations determining the light propagation modes and the transverse electromagnetic field describing the evanescent field. For simplifying the procedure, we can use the weakly guiding approximation, which can be applied if the relative refractive index difference $\Delta n = (n_1^2 - n_2^2)/2n_1^2$ between the core n_1 and the cladding n_2 is far less than unity. We consider a specific step-index hollow fiber with a thin cylindrical core shown in Fig. 1b; the hollow diameter $2a$, the core thickness d and the relative refractive index difference Δn are 7 μm, 3.8 μm and 0.18%, respectively. In this case, from the experimental observation of mode patterns [6], the weakly guiding approximation is still valid in spite of the considerable refractive index difference between the core and the vacuum hollow region. Under this approximation, Maxwell's equations are reduced to their scalar forms, which leads to the LP modes [8]

It is convenient to divide the amplitude $\boldsymbol{E}_0$ of the electric field into two components in the cylindrical coordinate system (r, θ, z); the transverse one $\boldsymbol{E}_t$ and the longitudinal one $\boldsymbol{E}_z$;

$$\boldsymbol{E}_0(r,\theta) = \boldsymbol{E}_t(r,\theta) + \boldsymbol{E}_z(r,\theta). \tag{1}$$

Provided that the gradient of the refractive index is small enough, we can get a scalar equation for the transverse component $\boldsymbol{E}_t$ [8];

$$\nabla^2 E_i(r,\theta) + (k^2 n^2 - \beta^2) E_i(r,\theta) = 0 \quad (i = x \text{ or } y), \tag{2}$$

where k, n and β are the wave number, the refractive index and the propagation constant, respectively. It should be noted that we have either $(E_x, 0)$ or $(0, E_y)$ as the transverse component $\boldsymbol{E}_t$. The component E_i is written as the product of the radial part and the azimuthal one;

$$E_i(r,\theta) = E(r)\sin(m\theta + \varphi), \tag{3}$$

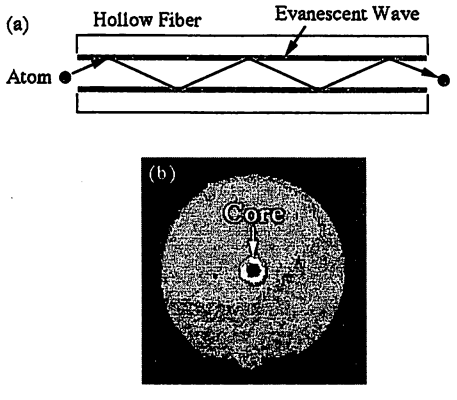

Fig. 1. (a) A hollow fiber atomic waveguide. Neutral atoms are guided in the hollow region by the repulsive force due to the evanescent wave. (b) The cross-section of a cylindrical-core hollow fiber. The diameter $2a$ of the hollow region and the thickness d of the cylindrical-core are 7 μm and 3.8 μm, respectively. The relative refractive index difference Δn is 0.18%, $(n_1 > n_2 > 1)$.

where φ is an initial phase constant. The radial part of an order m follows the equation [8]

$$\frac{d^2E(r)}{dr^2} + \frac{1}{r}\frac{dE(r)}{dr} + \left(k^2n^2 - \beta^2 - \frac{m^2}{r^2}\right)E(r) = 0. \tag{4}$$

The solutions satisfying Eq. (4) can be expressed by the Bessel functions $J_m(ur)$ and $N_m(ur)$, and the modified Bessel functions $I_m(vr)$ and $K_m(wr)$ as follows;

$$E(r) = \begin{cases} C_1 I_m(vr), & r < a, \\ C_2 J_m(ur) + C_3 N_m(ur), & a \le r \le b, \\ C_4 K_m(wr), & r > b, \end{cases} \tag{5}$$

where C_1, C_2, C_3 and C_4 are the constants to be determined by the continuity conditions on the two boundaries $r = a$ and $r = b = a + d$. The magnetic field is similarly obtained. Three characteristic constants u, v and w regulating the change of the electromagnetic field are written as

$$\begin{cases} u = \sqrt{k^2n_1^2 - \beta^2}, \\ v = \sqrt{\beta^2 - k^2}, \\ w = \sqrt{\beta^2 - k^2n_2^2} \end{cases} \tag{6}$$

Applying the continuity conditions to the electric field of Eq. (5) gives the dispersion equation

$$\left[\frac{J_m(ua)}{I_m(va)} - \frac{u}{v}\frac{J'_m(ua)}{I'_m(va)}\right]\left[\frac{N_m(ub)}{K_m(wb)} - \frac{u}{w}\frac{N'_m(ub)}{K'_m(wb)}\right] = \left[\frac{N_m(ua)}{I_m(va)} - \frac{u}{v}\frac{N'_m(ua)}{I'_m(va)}\right]\left[\frac{J_m(ub)}{K_m(wb)} - \frac{u}{w}\frac{J'_m(ub)}{K'_m(wb)}\right]. \tag{7}$$

From the numerical analysis of Eq. (7), we find that three LP modes (LP_{01}, LP_{11} and LP_{21}) can be excited for the wavelength 780 nm of the Rb D_2 line.

3. Potential barrier for guidance of Rb atoms

The evanescent wave decaying into the hollow region produces a deep optical potential due to the position-dependent Stark effect. We can apply the two-level scheme to alkali-metal atoms such as Rb; strictly speaking, they have multiple hyperfine levels. For the two-level atom with resonance frequency ω_0 and longitudinal velocity v_z, we get the optical potential [9]

$$U_{op}(r,\theta) = \frac{1}{2}\hbar\Delta \ln\left\{1 + \frac{I(r,\theta)/I_0}{1 + 4\Delta^2/\Gamma^2}\right\}, \tag{8}$$

where Γ, I_0 and $\Delta = \omega - \omega_0 - \beta v_z$ are the natural linewidth, the saturation intensity and the detuning from the laser frequency ω, respectively. When the detuning is positive (blue-detuning), the potential gives a repulsive force. The field intensity $I(r,\theta)$ derived from the z-component of the time-averaged Poynting vector can be written as

$$I(r,\theta) = \begin{cases} \alpha C_1^2 I_m^2(vr)\sin^2(m\theta + \varphi), & r < a, \\ \alpha\left(C_2 J_m(ur) + C_3 N_m(ur)\right)^2 \sin^2(m\theta + \varphi), & a \le r \le b, \\ \alpha C_4^2 K_m(wr)^2 \sin^2(m\theta + \varphi), & r > b, \end{cases} \tag{9}$$

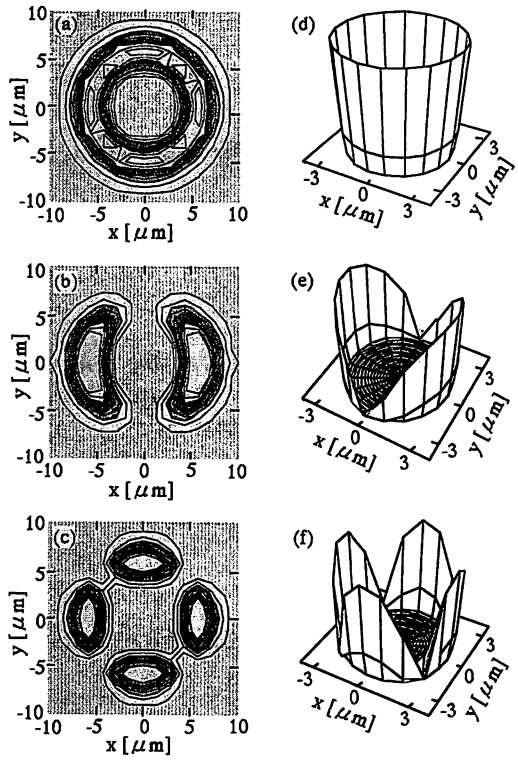

Fig. 2. The contours of the field intensity of the cross-section of the cylindrical-core hollow fiber and the corresponding potential barriers in the hollow region. For the wavelength of 780 nm, three LP modes can be excited; (a,d) for LP_{01}, (b,e) for LP_{11}, (c,f) for LP_{21}.

where $\alpha = \beta/2\omega\mu_0$. Fig. 2 shows the contours of the field intensity [(a)–(c)] and the potential barriers [(d)–(f)] of the three LP modes. The excitation of the LP_{01} mode is required for the stable guidance of atoms because there is no vanishing region of the evanescent field on the inner surface.

The height of the potential barrier to guide Rb atoms is calculated to be 1 mK for a few mW excitation [6]. The temperature of 1 mK corresponds to the transverse velocity of 30 cm/s for Rb atoms. This velocity can be achieved by a well collimated atomic beam or the laser cooling of atoms which can cool down alkali-metal atoms to a few μK [10]. It is not necessary to cool the waveguide. The atoms interact with the mechanical force from the evanescent wave, but they do not interact with the blackbody radiation from thermal objects. In order to estimate the maximum transverse velocity available for the experiments, we will examine several effects to lower the potential barrier or cause the loss of atoms in the hollow fiber.

4. Discussion

There are three leading factors to interfere with the optical guidance of atoms; cavity QED effects, tunneling of atoms through the potential barrier and spontaneous emission effects, which were first discussed in Ref. [4]. We treat these effects under the weakly guiding approximation for the present cylindrical-core hollow fiber.

The potential barrier of Eq. (8) is modified by the cavity QED effect. This attractive force somewhat reduces

the height of the potential barrier in the vicinity of the inner surface. In the case of the parallel mirrors, for a ground-state atom, the cavity potential can be expressed as [2,11]

$$U_{cp}(r) = -\frac{\pi p^2}{48\epsilon_0 a^3}\int_0^{\infty}\frac{\cosh(\pi\rho r/a)}{\sinh(\pi\rho)}\tan^{-1}(\rho\lambda/4a)\rho^2\,\mathrm{d}\rho, \tag{10}$$

where p and λ are the matrix element of the dipole moment and the wavelength of the transition, respectively. Unfortunately, the exact cavity potential near a dielectric cylindrical surface is not known yet while that near a dielectric sphere is recently calculated[12]. However, given the similar conditions, the cavity potential for the cylindrical surface is expected to be larger than that for the parallel surface but smaller than that for the sphere. In addition, the atomic energy shift in a dielectric is generally smaller than that for a metal. Therefore, resonance behaviours due to the cavity are neglected, and we treat the cavity potential near the cylindrical surface in an approximate way, by simply introducing two adjustable factors in Eq. (10): the dielectric factor $\xi \sim (n_1^2 - 1)/(n_1^2 + 1)$ [4] and the geometrical factor for the cylinder η ($1 < \eta < 10$; $\eta = 1$ corresponds to the parallel surface case). Fig. 3 shows the modified potential barrier in terms of temperature representing the transverse kinetic energy of ^{85}Rb under the LP_{01} excitation of 2 mW in the case of $\Delta = 100\Gamma$ and $\eta = 5$. In the region within 100 nm for the inner surface, the potential barrier is somewhat reduced by the cavity QED effect, which is the Casimir–Polder force rather than the van der Waals force because $a > \lambda$ [11].

Next we consider tunneling through the potential barrier. In order to estimate the tunneling rate γ_T of atoms with mass M and transverse kinetic energy E_t for the total potential $U(r,\theta) = U_{op}(r,\theta) + U_{cp}(r)$, the well known WKB formula can be applied [13];

$$\gamma_T = \exp\left[-\frac{2}{\hbar}\int_{r_{CT}}^{r_0}\sqrt{2M(U(r,\theta) - E_t)}\,\mathrm{d}r\right]\left[\frac{\mathrm{d}}{\mathrm{d}E_t}\int_{-r_{CT}}^{r_{CT}}\sqrt{2M(E_t - U(r,\theta)}\,\mathrm{d}r\right]^{-1}_{E_t = E_{CT}}, \tag{11}$$

where r_0 and r_{CT} are the position of the maximum potential and the classical turning point, respectively. The first factor of the tunneling rate γ_T is the tunneling probability per bounce and the second one expresses the number of bounces per second [4]. Taking the classical turning point to be 40 nm from the inner surface for the potential barrier shown in Fig. 3, the tunneling rate is plotted as a function of the transverse velocity v_t of ^{85}Rb in Fig. 4a. Provided that the longitudinal velocity v_z is 300 m/s and the fiber length L is 3 cm, the transmission loss $L\gamma_T/v_z$ of atoms is ten percent at about $v_t = 50$ cm/s.

The optimal detuning is basically determined by the height of the potential barrier, i.e. the coupling power of a laser beam to the hollow fiber. In general, the optimal detuning increases with excitation power. For small

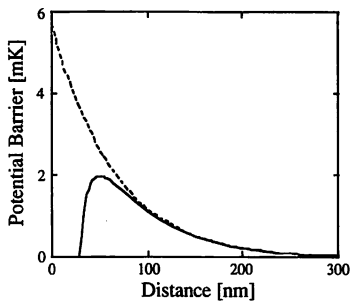

Fig. 3. The cross-sectional change of the potential barrier under the excitation of the LP_{01} mode ($m = 0$) with 2 mW and $\Delta = 100\Gamma$ as a function of the distance from the inner surface in terms of temperature corresponding to the transverse kinetic energy of ^{85}Rb. The saturation intensity I_0, the natural linewidth Γ and the dipole moment p are 1.6 mW/cm^2, 6.1 MHz and 7.6 D (2.5×10^{-29} C·m) for the ^{85}Rb D_2 line of the wavelength $\lambda = 780$ nm, respectively. The solid line shows the total potential made up of the optical potential and the cavity potential in the case of $n_1 = 1.45$ and $\eta = 5$. The broken line shows the optical potential.

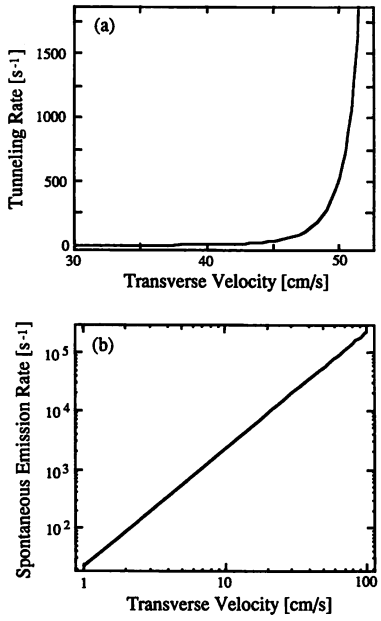

Fig. 4. (a) The tunneling rate of the potential barrier under the LP_{01} excitation of 2 mW. The right-hand edge corresponds to the classical turning velocity in the present case, in which the turning point is taken to be 40 nm away from the inner surface. (b) The spontaneous emission rate. Each rate is plotted as a function of the transverse velocity of ^{85}Rb in the case of $\Delta = 100\Gamma$.

power of several milliwatts, it becomes about 10Γ. In this case, however, spontaneous emission cannot be ignored. The rate γ_{sp} of the spontaneous emission is approximately estimated by the ratio of the transverse kinetic energy E_t to the detuning energy $\hbar\Delta$;

$$\gamma_{sp} \sim \frac{\Gamma}{va}\frac{E_t}{\hbar\Delta}, \tag{12}$$

where the factor va appears from the localizability of the evanescent wave. Fig. 4b is a plot of γ_{sp} as a function of the transverse velocity of ^{85}Rb under $\Delta = 100\Gamma$. About twenty percent of the atoms with the longitudinal velocity of 300 m/s and the transverse velocity of 10 cm/s suffer spontaneous emission through the 3 cm fiber. The spontaneous emission rate does not necessarily express the loss of atoms though some atoms may be sufficiently heated to cross the potential barrier and to be pumped to non-interactive hyperfine levels.

Since the atoms experiencing spontaneous emission loss their coherence, this may be important for some applications such as atomic interferometers [14]. In order to suppress spontaneous emission, low transverse velocity and large detuning are required. They may be satisfied by the transverse cooling and the increase of the excitation power so as not to lower the potential barrier. Note that a minimum longitudinal velocity exists because the far smaller longitudinal velocity results in the increase of the spontaneous emission rate.

5. Conclusions

The weakly guiding approximation is quite valid for the analysis of the atomic waveguide made by a cylindrical-core hollow fiber. Although the approximation gives a height of the potential barrier of about 3.5 times larger compared with the exact solution, it reproduces the same mode patterns as the experimental results. The evanescent field in the hollow region is simply expressed by the modified Bessel function of the second kind.

For the 2 mW excitation of the LP_{01} mode, the evanescent wave produces a sufficiently deep optical potential to guide atoms in spite of the reduction of the potential barrier by the cavity QED effect. From the estimation of the tunneling and spontaneous emission rates, we can use the Rb atoms with the transverse velocity of 10 cm/s out of an atomic beam for experiments, which are currently in progress. In the future, an exact solution of the cavity potential for the dielectric cylindrical surface will be derived to describe this type of atomic waveguide.

References

[1] D.J. Harris and C.M. Savage, Phys. Rev. A 51 (1995) 3967.
[2] W. Jhe, Phys. Rev. A 43 (1991) 5795.
[3] K. Sangster, E.A. Hinds, S.M. Barnett and E. Riis, Phys. Rev. Lett. 71 (1993) 3641.
[4] S. Marksteiner, C.M. Savage, P. Zoller and S.L. Rolston, Phys. Rev. A 50 (1994) 2680.
[5] W. Jhe, M. Ohtsu, H. Hori and S.R. Friberg, Jpn. J. Appl. Phys. 33 (1994) L1680.
[6] H. Ito, K. Sakaki, T. Nakata, W. Jhe and M. Ohtsu, Opt. Commun. 115 (1995) 57.
[7] H. Hori, S. Jiang, M. Ohtsu and H. Ohsawa, in: Proc. Int. Quantum Electronics Conf., Vol. 8, 1992, OSA Technical Digest Ser. (Optical Society of America, Washington, DC, 1992) p. 48.
[8] D. Marcuse, Theory of Dielectric Optical Waveguides, 2nd ed. (Academic Press, New York, 1991).
[9] M.A. Ol'Shanii, Yu.B. Ovchinnikov and V.S. Letokhov, Opt. Comm. 98 (1993) 77.
[10] For example, see the special issue in J. Opt. Soc. Am. B 6 (November 1989).
[11] C.I. Sukenik, M.G. Boshier, D. Cho, V. Sandoghdar and E.A. Hinds, Phys. Rev. Lett. 70 (1993) 560.
[12] W. Jhe and J.W. Kim, Phys. Rev. A 51 (1995) 1150.
[13] E. Merzbacher, Quantum Mechanics, 2nd ed. (Wiley, New York, 1970).
[14] For example, see the special issue in Appl. Phys. B 54 (May 1992).

MC5 **12.15 pm**

Experiments on atom guidance with evansecent waves

H Ito, *T Nakata, *K Sakaki, **W Jhe, **M Ohtsu,
Kanagawa Academy of Science and Technoloyg, KSP East, 3-2-1 Sakado, Takatsu-ku, Kawasaki 213, Japan

For further precise manipulation of atoms, the methods of atom guidance with optical fibers have been proposed. [1-5] The atomic waveguide realizes one-dimensional control of atomic motion. Re

cently, an experimental demonstration through a hollow-core capillary fiber with a hollow diameter of 40 mm was reported,[6] which was based on dipole force from an intense red-detuned Gaussian laser beam propagating into the hollow region.[1] The other way of atom guidance, as shown in Fig. 1, is to use blue-detuned evanescent waves in a hollow fiber.[3-5] In this work, we present the progress of the experiment of the atomic waveguide with evanescent waves. Since the evanscent wave is localized near the inner wall, atoms interact with the light only when approaching the inner wall; otherwise they are free. Therefore, compared to the Gaussian beam method, one with evansecent waves extremely reduces the influence of spontaneous emission on atomic motion.

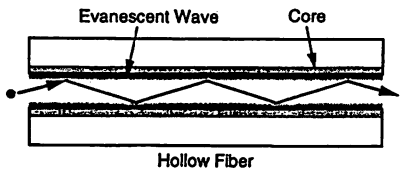

MC5 Fig 1. Atomic waveguide made by a cylindrical-core hollow fiber. The evanescent wave leaked to the hollow region acts as a mirror to reflect atoms.

The experiment with Rb atoms is under progress. Figure 2 illustrates the experimental setup. Rb atoms from a well-collimated atomic beam are introduced into the cylindrical-core hollow fiber with a length of 3 cm; the hollow diameter and the core thickness are 7 mm and 3.8 mm respectively. The laser beam with a blue-detuning to form the evanescent wave is coupled into the core through a mirror with a hole to pass the atoms. For the guidance of atoms, excitation of the LP_{01} mode is required.[4,5] We could excite it with the power coupling efficiency of more than 30%. It is convenient to introduce the guide laser beam directly from the side of the fiber. We present the way by fabricating the facet.

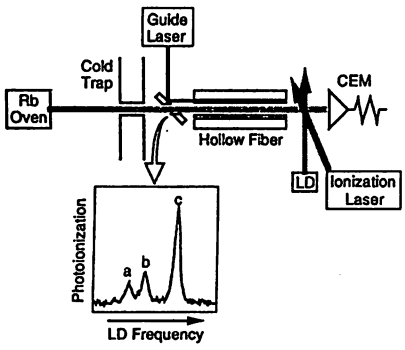

MC5 Fig 2. Sketch of the experimental setup with a Rb atomic beam. The Rb atoms are guided through the hollow fiber with the length of 3 cm and then detected by a channeltron electron multiplier (CEM) after photoionization with a diode laser and an Ar ion laser or a Q-switch YAG laser. The inserted graph shows a photoionization signal of an incident Rb beam as the function of the frequency of the diode laser; a, b and c correspond to the transitions of F=3→2, F=3→3 and F=3→4, respectively.

Guided atoms are ionized by two-step photoionization method and detected with a channeltron electron multiplier; a diode laser stimulates the $5S_{1/2}$Æ$5P_{3/2}$ transition of Rb atoms and an Ar ion laser (457.9 nm) or a Q-switch YAG laser (355 nm) ionizes them from the $5P_{3/2}$ state.The inserted graph in Fig. 2 shows a photoionization spectrum of an incident Rb beam. Figure 3 shows the ionization efficiency of ^{85}Rb experimentally measured with an Ar ion laser. We get the efficiency of 0.1% in the case of the power of 30 mW. The flux of guided atoms is expected to be more than $10^3 s^{-1}$ so that the iionization cross section of 10^{-17} cm^2, we use a high power Ar ion laser of 1.5W to achieve it. As an alternative method for the detection, hot wires are employed in the experiment.

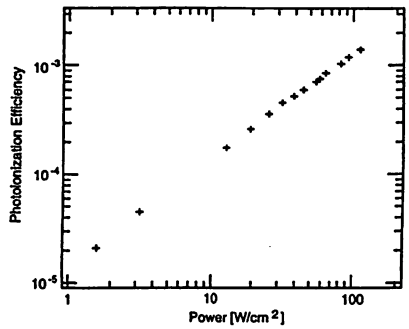

MC5 Fig 3. Photoionization efficiency of ^{85}Rb measured with an Ar ion laser.

We will also discuss the feasibility of the atomic funnel with evanescent waves to efficiently couple atoms into the atomic waveguide; in particular, the funnel is applied to manipulate cold atoms dropped from an MOT. To compensate for the acceleration due to gravitation, the cooling mechanism with an additional pumping beam is involved in the funnel.[7]

1. MA Ol'shanii, YB Ovchinnikov, VS Letokov, Opt. Commun. **98**, 77 (1993).
2. W Jhe, M Ohtsu, H Hori, SR Friberg, Jpn. J. Appl. Phys. **33**, L1690(1994).
3. S Marksteiner, CM Savage, P Zoller, SL Rolston, Phys. Rev. A **50**, 2680 (1994).
4. H Ito, K Sakaki, T Nakata, W Jhe, M Ohtsu, Opt. Commun. **115**, 57 (1995).
5. H Ito, K Sakaki, T Nakata, W Jhe, M Ohtsu, Ultramicroscopy (in press).
6. MJ Lenn et al, Phys. Rev. Lett. **75**, 3253 (1995).
7. J Soding, R Grimm, YB Ovchinnikov, Opt. Commun, **119**, 652 (1995).

**Interdisciplinary Graduate School of Science and Engineering, Tokyo Insitute of Technology, 4259, Nagatsuta, Midori-ku, Yokohama 226, Japan*
***Department of Physics, Seoul National University, Seoul 151-742, Korea*

MD 11.00 am
Meeting Room 4
Nonlinear processes and photonic materials

MD1 (Invited) **11.00 am**

Cascaded optical nonlinearities in organic structures

W E Torruellas, P Vidakovik, J Zyss, G J Krijnen, HJ Hoekstra, Z Wang, DY Kim, Y Baek, M Jaegger, DJ Hagan, E W VanStryland, G I Stegeman *CREOL, University of Central Florida Orlando FL 32826*

The inability of finding advanced highly nonlinear materials processible in low loss waveguide structures has lead to a radical new approach to the nonlinear optical switching problem: cascaded second-order parametric

Spectroscopy of Atoms Guided by Evanescent Waves in Cylindrical-Core Hollow Fibers

H. Ito[1], T. Nakata[2], K. Sakaki[2], W. Jhe[3], and M. Ohtsu[1,2]

[1] *Kanagawa Academy of Science and Technology, KSP East, 3-2-1 Sakado, Takatsu-ku, Kawasaki 213, Japan*

[2] *Interdisciplinary Graduate School of Science and Engineering, Tokyo Institute of Technology, 4259, Nagatsuta, Midori-ku, Yokohama 226, Japan*

[3] *Department of Physics, Seoul National University, Seoul 151-742, Korea*

Atom guidance by a Gaussian laser beam in a hollow fiber has been proposed [1] and demonstrated [2]. On the other hand, some methods to guide atoms using evanescent waves have been proposed [3-5]. The evanescent wave produced near a glass-vacuum interface acts as an atomic mirror under blue-detuning [6]. Since the evanescent field is localized within a wavelength from a surface, it well meets the fine control of atomic motion. In particular, the three-dimensional evanescent light has a size-dependent character [7,8] and it is expected to be used for the 3D trapping of atoms [9]. Here, we present the atom guidance experiments with the evanescent wave in small hollow optical fibers. Contrary to a light waveguide, the blue-detuned evanescent wave makes an optical tunnel to reflect atoms in the hollow region and successfully carry them along the fiber. In addition, because of the localizability of the evanescent wave, this kind of atomic waveguide works as a sort of dark trap.

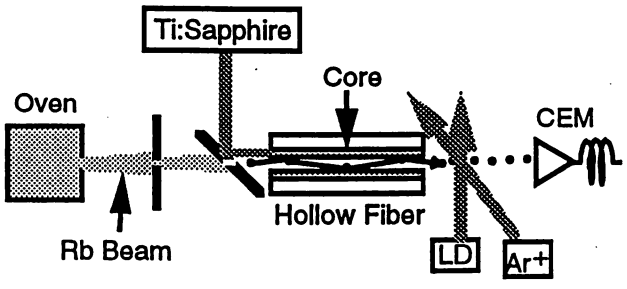

Fig. 1 Experimental setup

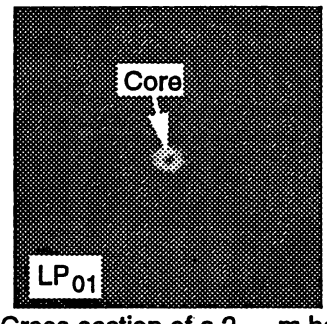

Fig. 2 Cross-section of a 2- μ m hollow fiber

Figure 1 shows a sketch of the experimental setup. A Rb atomic beam from a heat-up oven is introduced into a well-aligned hollow fiber with a small hollow diameter of 7 μm and a length of 3 cm. At an oven temperature of 180 C°, the average longitudinal atomic velocity along the fiber is 340 m/s and the average transverse one becomes 0.2 m/s in our collimation scheme. The incidence flux is approximately 10^6 atom/s. We also use a 2-μm hollow fiber as shown in Fig. 2 [10]. A guide beam from a Ti:Sapphire laser is coupled to a thin core of the fiber through a mirror with a hole to pass the atomic beam. The guided atoms through the hollow fiber are ionized by the two-step photoionization (PI) and detected by a channeltron electron multiplier (CEM). For the photoionization, two laser beams are overlapped just behind the exit of the fiber; a grating feedback diode laser is tuned to the Rb D_2 line, and then an Ar^+ laser with a wavelength of 476.5 nm and a power of 4 W ionizes the excited Rb atoms in the $5P_{3/2}$ state. By focusing the Ar^+ laser beam on a spot of 100 μm in the detection region, we get the PI efficiency of about 30 %.

Use of the Doppler-free PI detection including a resonant transition enables one to carry out a "spectroscopic "observation of the guided atoms in a state-selective manner. The curve A of Fig. 3 shows an ion-counting PI signal of ^{85}Rb in the upper ground state through the 7-μm hollow fiber as a function

of a frequency detuning of the guide light, where the diode laser is tuned to the $5S_{1/2}$, F=3 → $5P_{3/2}$, F=4 transition. The coupled power of the guide light is 250 mW and it provides an optical potential of about 100 mK assuming an excitation of the LP_{01} mode [5]. It should be noted that the detuning does not include Doppler shifts. In the blue-detuning region, a large enhancement of about 10 times on the transmission flux occurs at an optimal detuning of 2.7 GHz, compared with a background transmission level without the guide light (a broken line in Fig. 3). The observed dispersion-like PI signal has a long tail over 20 GHz. On the other hand, in the red-detuning region, the transmission decreases below the background level, which may indicate adsorption of atoms.

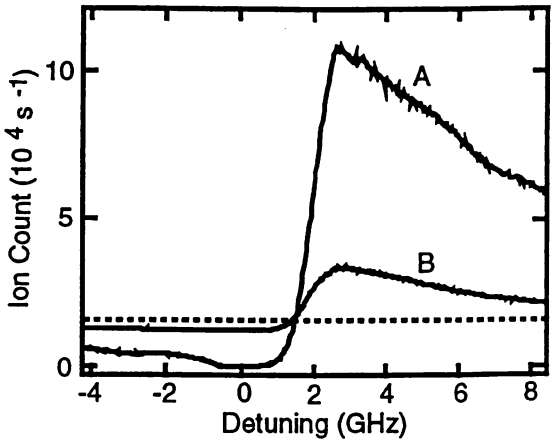

Fig. 3 Ion-counting PI signals

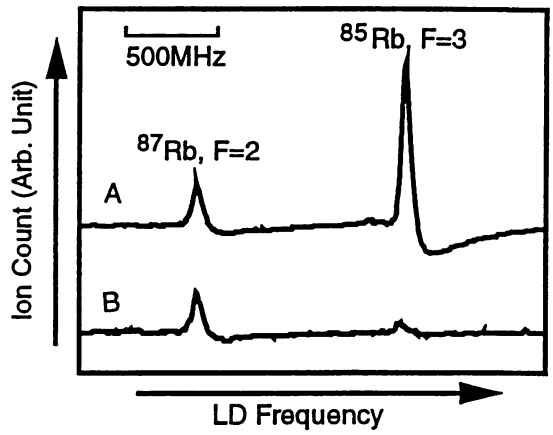

Fig. 4 In-line separation of two Rb isotopes

Based on the dispersion nature of the atom guidance, we also demonstrate a separation between two Rb isotopes by adjusting the frequency of the guide light. Figure 4 shows PI signals as a function of the frequency of the diode laser. In the curve A of Fig. 4, the frequency of the guide light is set at a large blue-detuning for both Rb isotopes in the upper ground states. On the other hand, in the curve B of Fig. 4, the guide light is blue-detuned for the ^{87}Rb atoms but nearly red-detuned for the ^{85}Rb atoms. As is clear in the figure, our hollow fiber can be considered as an atomic-state filter.

It is interesting to make the hollow diameter small. The curve B of Fig. 3 shows a PI signal on a similar experiment with a 2-μm hollow fiber. In order to compare with the 7-μm result, the background level is taken to be the same. Another experiment using a 1.4-μm hollow fiber is under progress. Atom guidance with these small fibers can be applied to studies of the cavity QED effects [11], the quantum motion under gravity [12], and the atomic quantum wire [13]. We also expect to use them for the atom lithography technique [14], and the single atom manipulation using a sharpened tip of a fiber probe [9].

In summary, we performed a laser-photoionization spectroscopy on the atoms guided by the evanescent wave in small hollow fibers. A precise control of the atomic lateral motion was realized within a few micrometers through a long distance. We acknowledge MATSUO FOUNDATION for financial support.

[1] M.A.Ol'Shanii, et al. Opt.Commun.**98**, 77 (1993). [2] M.J.Renn,e t al. Phys.Rev.Lett.**75**, 3253 (1995). [3] S.Marksteiner, et al. Phys.Rev.**A50**, 2680 (1994). [4] W.Jhe, et al. Jpn.J.Appl.Phys.**33**, L1680 (1994). [5] H.Ito, et al. Opt.Commun.**115**, 57 (1995): ibid, Ultramicroscopy (1996) (in press). [6] V.I.Balykin, et al. Phys.Rev.Lett.**60**, 2137 (1988). [7] T.Saiki, et al. Digest of QELS,**16**, 84 (1995). [8] W.Jhe, et al. Opt.Lett. (15 Feb.1996 issue in press). [9] H.Hori, et al. Digest of IQEC,**8**, 48 (1992). [10] S.Sudo,e t al. IEEE Photon.Technol.Lett.**2**, 128 (1990). [11] W.Jhe, Phys.Rev.**A43**, 5795 (1991). [12] D.J.Harris, C.M.Savage, Phys.Rev.**A51**, 3967 (1995). [13] J.P.Dowling, J.Gea-Banacloche, Phys.Rev.**A52**, 3997 (1995). [14] R.W.McGowan, et al. Opt.Lett.**20**, 2535 (1995).

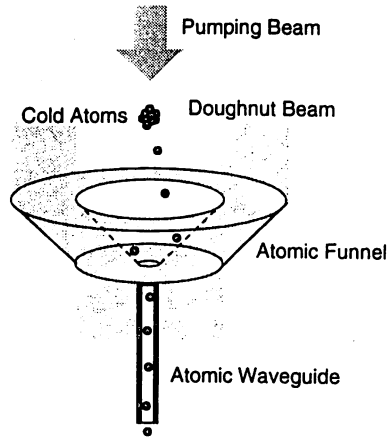

QTuE5 Fig. 1 Sketch of an atomic funnel made by a conical hollow prism to pour cold atoms dropped from a MOT into an atomic waveguide. A blue-detuned doughnut beam from below produces an evanescent wave on the inner wall of the prism by total reflection, while a weak pumping beam irradiated from above cools atoms accelerated by gravitation.

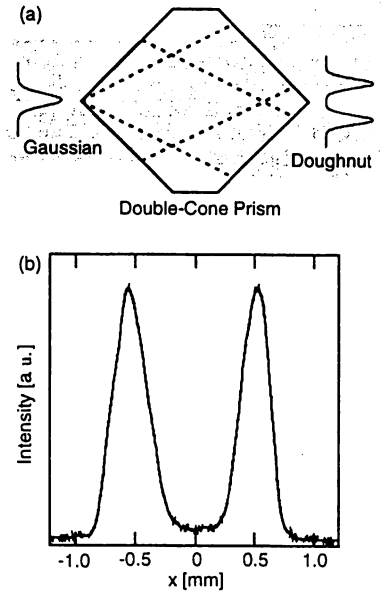

QTuE5 Fig. 2 (a) Conversion of a Gaussian beam into a doughnut-shaped beam through a double-cone prism. (b) Intensity profile of a doughnut beam experimentally produced. A Gaussian beam with a waist of 0.85 mm is converted by a double-cone prism with a length of 4.25 mm and a diameter of 2.5 mm.

QTuE5 **5:45 pm**

Atomic funnel with evanescent waves

Haruhiko Ito, Keiji Sakaki,* Takeshi Nakata,* Wonho Jhe,** Motoichi Ohtsu,
Kanagawa Academy of Science and Technology, KSP East, 3-2-1 Sakado, Takatsu-ku, Kawasaki 213, Japan

Cold atoms are expected to be applied to experiments on quantum motion, topological phenomena, cavity QED, and so on. Most of the interesting experiments require precise control on atomic motion. We have proposed the atomic waveguide by evanescent waves to enable the precise one-dimensional manipulation of atoms.[1,2] The atomic waveguide is composed of a cylindrical-core hollow fiber with a hollow diameter of a few microns. The attachment of a funnel for atoms should be effective in coupling atoms to the atomic waveguide. In this work we present a novel scheme of the atomic funnel based on the dipole force from evanescent waves. Compared to the 2D MOT funnel,[3] the evanescent-wave funnel has a further advantage of acting as a gravitational trap.

The funnel consists of a conical hollow prism illuminated by a intense doughnut-shaped laser beam from below, as shown in Fig. 1. The evanescent wave is formed on the inner wall of the prism by total reflection of the doughnut beam. Under blue-detuning condition the evanescent wave exerts repulsive force on atoms approaching the inner wall and results in reflection of them.

The conversion of a Gaussian beam into a doughnut beam has been performed by use of holographic techniques.[4,5] However, the conversion rate in the works is up to 50%. We introduce a simpler geometric method by a double-cone prism, shown in Fig. 2a, with an al-

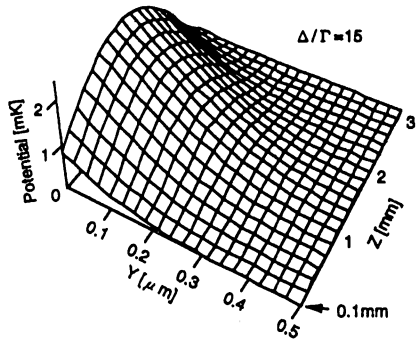

QTuE5 Fig. 3 Map of a potential barrier for metastable argon atoms produced by a doughnut beam of 500 mW. The blue-detuning Δ is taken to be 15 times the natural linewidth Γ. The slope angle and exit hole of the funnel prism are assumed to be 60° and 0.2 mm, respectively. The *Y* axis shows the distance from the inner wall, while the *Z* axis indicates the distance along the fall line from the center of the exit hole.

most 100% conversion rate. A Gaussian beam branches into two paths in the first refraction on the prism, and then a non-divergent doughnut beam appears after the second refraction. Figure 2b shows the intensity profile of the doughnut beam formed through the double-cone prism with a length of 4.25 mm and a diameter of 2.5 mm. The hollow diameter and ring thickness of the doughnut beams are determined by the prism length and the waist of the input Gaussian beam, respectively.

The funnel can be available for reflection of cold atoms fallen from a MOT. Figure 3 shows the potential barrier for metastable argon atoms expressed in terms of temperature, assuming the funnel prism with an exit hole of 0.2 mm and a slope of 60°. The doughnut beam converted from the Gausian beam with a waist of 1.6 mm and a power of 500 mW produces the potential barrier of more than 1 mK through a distance of 3 mm along the fall line. Unless the funnel includes some cooling mechanisms to compensate acceleration resulting from gravitation, the atoms with the velocity of more than 10 cm/s cannot escape from the exit hole. Recently the addition of a weak pumping beam to cool atoms down to the recoil limit has been reported.[6] The use of the additional beam propagating downward makes up for the lack of cooling mechanisms. Progress of the atom-guidance experiment will be also presented.

Interdisciplinary Graduate School of Science and Engineering, Tokyo Institute of Technology, 4259, Nagatsuta, Midori-ku, Yokohama 226, Japan
**Department of Physics, Seoul National University, Seoul 151-742, Korea*

1. H. Ito, K. Sakaki, T. Nakata, W. Jhe, M. Ohtsu, Opt. Commun. **115**, 57 (1995).
2. H. Ito, K. Sakaki, T. Nakata, W. Jhe, M. Ohtsu, Ultramicroscopy (in press).
3. J. Yu, J. Djemaa, P. Nosbaum, P. Pillet, Opt. Commun. **112**, 136 (1994).
4. H. S. Lee, B. W. Stewart, K. Choi, H. Fenichel, Phys. Rev. A **49**, 4922 (1994).
5. S. Friebel, R. Deutschmann, M. Schiffer, G. Wokurka, W. Ertmer, *QELS'95*, Vol. 16, 1995 OSA Technical Digest Series, p. 196.
6. J. Söding, R. Grimm, Yu. B. Ovchinnikov, Opt. Commun. **119**, 652 (1995).

NEAR FIELD OPTICS TOWARD NANO-PHOTONICS AND ATOM MANIPULATION

M. OHTSU[1,2)]

1) Graduate School, Tokyo Institute of Technology, 4259 Nagatsuta, Midori-ku, Yokohama 226, JAPAN
2) Kanagawa Academy of Science and Technology, KSP East, Rm 408, 3-2-1 Sakado, Takatsu-ku, Kawasaki 213, JAPAN

Present status of our study on near-field optical science and technology is reviewed. After pointing out that the near-field optics is based on a short-range electromagnetic interaction between two nanometric particles via a size-dependent evanescent field, emphasis is given to the importance of nano-fabrication of fiber probes. Following topics will be covered in the presentation:

(1) Selective chemical etching process and selective resin coating method are reviewed, and a probe with cone angle, tip diameter, and aperture diameter of 15 deg., < 3 nm, and < 30 nm, respectively, are presented. High throughput probe for photoluminescence(PL) detection and further, a light-emitting probe with dye molecules attached to the top of the probe-tip are also demonstrated.

(2) In order to demonstrate high normal resolution of the near-field optical microscope(NOM), an image of an ultra-flat sapphire plate with atomic layers step of 2 nm-height is presented. Further, spatial power spectral analysis is carried out for the image of 20 nm diameter gold particles, and transfer function of the NOM is estimated. From this analysis, the -3 dB cutoff spatial frequency is extrapolated, which gives a measure of resolution of 0.8 nm.

(3) As an application of the NOM, images of flagellar filaments (25 nm diameter) of salmonella in water as well as in air, microtubuline (25 nm diameter) in the branching axon of neuron, etc. are presented. PL/EL(electroluminescence) spectroscopy and photocurrent measurement of a GaAs lateral p-n junction are presented. PL spectroscopy of a GaAs quantum dot at liquid-helium temperature is also demonstrated.

(4) Photon-mode optical storage of the photochromic thin film is demonstrated.

(5) After pointing out the possibility of trapping a single atom by an evanescent field localized on the probe tip, the first successful result of atom guidance by the evanescent field present on the inner wall of a hollow fiber is presented. The dipole force induced by a cylindrical evanescent field generated from the lowest guided mode of the cylindrical core fiber (780 nm wavelength) can guide Rb atoms through the hollow fiber of 7 um inner diameter and 3 cm length. By the blue detuning, the number of guided atoms is increased by 20 times of that without the evanescent field. Selective guidance of a specific isotope of Rb is demonstrated. Estimation of cavity QED effect and contribution of spontaneous emission are discussed. Possible applications of such a novel atom manipulation are, studying Aharonov-Casher effect, Berry's phase, etc., isotope separation, and atomic-level crystal growth.

[I-2] NANO PHOTONICS

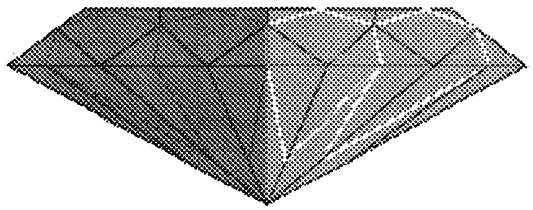

Spatially and spectrally resolved imaging of GaAs quantum-dot structures using near-field optical technique

Yasunori Toda,[a] Motonobu Kourogi,[b] and Motoichi Ohtsu[b]
Interdisciplinary Graduate School of Science and Engineering, Tokyo Institute of Technology, 4259 Nagatsuda, Midori-ku, Yokohama, Kanagawa 226, Japan

Yasushi Nagamune and Yasuhiko Arakawa
Institute of Industrial Science, University of Tokyo, 7-22-1 Roppongi, Minato-ku, Tokyo 106, Japan

(Received 15 December 1995; accepted for publication 29 May 1996)

We present experimental result on spatially and spectrally resolved imaging of GaAs quantum dot (QD) structures using a near-field optical microscope. Three photoluminescence (PL) peaks which originate from QD, quantum well (QW), and bulk regions were observed at liquid-He temperature. Carriers were observed to diffuse effectively from the AlGaAs barriers to the QD and QW regions. The region of the intension carrier capture manifests itself by emitting a sharp PL peak, and is estimated to be about 300 nm. © *1996 American Institute of Physics.* [S0003-6951(96)04232-5]

Development of the optical communication and the information processing systems require advanced semiconductor devices with high-dimension confinement of carriers, which can be realized in quantum wire and quantum dot (QD) structures.[1] Moreover, these quantum device structures enable us to investigate an attractive phenomenon of carriers in the sharp density of states. So far, various fabrication methods of the QD structures, e.g., dry-etching,[2] self-organization,[3,4] and selective epitaxial growth,[5] have been reported. Among these fabrication methods, the selective epitaxial growth is advantageous because of its damage-free formation and a high regularity of the dots position arrangement.

On the other hand, requirements of optical spectroscopy of these quantum device structures is generally met by statistical far-field technique. However, of technical and scientific importance are the optical study of such quantum device structures with subwavelength resolution, which is possible by using the near-field technique.[6] Recently, individual spectroscopy characteristics of localized electrons in low-dimensional quantum structures using the near-field technique have been reported.[7–9] In this letter, we present experimental results on spatially and spectrally resolved imaging of GaAs QD structures and investigation of their insignificant spectroscopic properties using a near-field optical microscope. To our knowledge, this is the first letter to study the near-field spectroscopic characteristics of the QD structures.

A schematic of the low-temperature experimental setup is shown in Fig. 1. This experiment was carried out by exciting carriers by a fiber tip. The inset of Fig. 1 shows the image of a sharpened nanometric fiber tip fabricated by the chemical etching method.[10] The chemical etching developed in our group was confirmed to be a reproducible method because it tailors the versatile tip conformations to optimize sensitivity and/or spatial resolution.[11] Since the quality of the near-field spectroscopic image depends not only on the spatial resolution but on the efficiency of illuminating the sample, it is not useful for the present study to fabricate the smallest aperture size. This tradeoff between spatial resolution and detection sensitivity was overcome by applying the selective resin coating method[12] which is one of the advantageous methods to optimize the size of the aperture. In order to increase the intensity as high as possible, the tips with the aperture size from 100 to 200 nm were chosen by considering the size of dot. The sample was held by the tube-type piezoelectric transducer and its three-dimensional scanning range at 10 K amounts to 12% of the value at room temperature ($80\times80\times5\mu$m). A whole scanning setup was installed in a He-flow-type optical cryostat. In order to control the tip-sample separation, a shear-force (Sh-F) technique was employed.[13] Besides, this enabled us to refer the PL image to the geometrical device structure. A multilines Ar^+ laser was employed for exciting carriers in the AlGaAs barriers. A 1.3 μm laser diode was used for Sh-F controlling. In order to obtain the PL spectrum, PL light was collected by a lens in the cryostat and focused onto a photon counting Si-avalanche photodiode in conjunction with a 200-mm-long grating monochromator.

The cross-sectional configuration of the GaAs QD structures is also shown in Fig. 1. They were fabricated by the selective epitaxial growth on SiO_2-patterned GaAs (100) substrates with metalorganic chemical vapor deposition.[5]

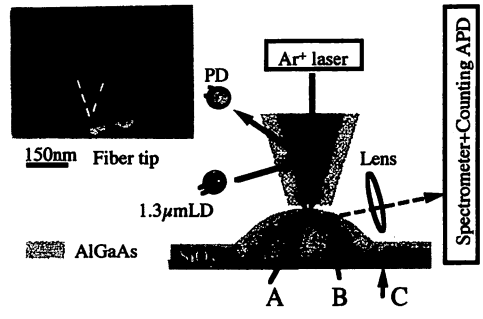

FIG. 1. Experimental setup of near-field optical microscope in the cryostat and cross section quantum dot structure. A: GaAs QD; B: GaAs QW; C: GaAs bulk. Inset: Scanning electron micrograph of the top of the fiber tip. The tip structure at the aperture is marked by a broken line.

[a]Electronic mail: toda@yari.iis.u-tokyo.ac.jp
[b]Also with Kanagawa Academy of Science and Technology, KSP East Rm 408, 3-2-1 Sakado, Takatsu-ku, Kawasaki 213, Japan.

 0003-6951/96/69(6)/827/3/$10.00

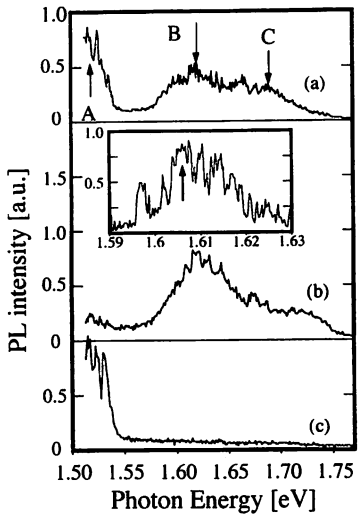

FIG. 2. Spatially resolved PL spectra at the temperature of 18 K, (a) maintaining the tip 200 nm above the QD, (b) less than 10 nm above the QD, (c) less than 10 nm above the SiO_2 mask. Inset: PL spectra at the tip position less than 10 nm above the QD with lower excitation power.

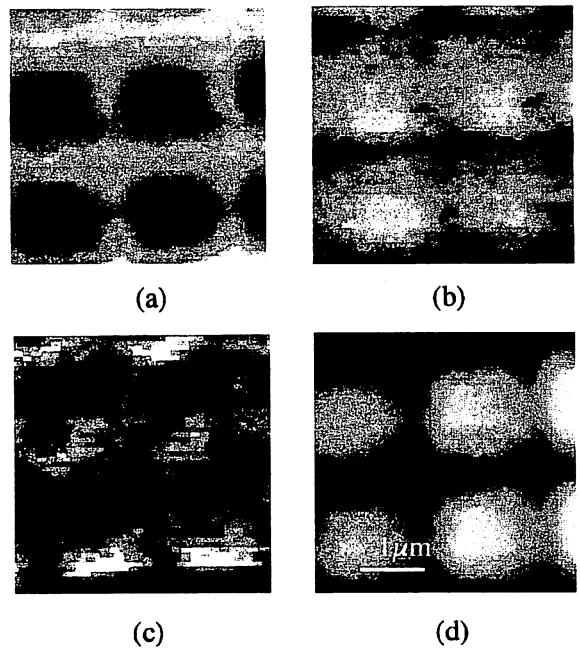

FIG. 3. Spatial profiles of spectrally resolved PL images at 18 K with the energy region (a) labeled A, (b) labeled B, and (c) labeled C in Fig. 2(a). The scanned area is 4 μm×4 μm with the pixel size of 100 nm×100 nm. (d) Simultaneously observed topographic image.

The difference of the growth rate of the crystal plane gives rise to three-dimensional confinement of the carriers. A scanning electron micrograph of the sample provides us with information on the size of the QD pattern (190 nm×160 nm×12 nm) and the separation between dots (2μm). The effective lateral size is estimated to be 70 nm by magneto-PL measurements. In the case of illumination mode, carriers are excited in the localized area, whereas the PL light comes from the extended region after the carrier diffusion into the AlGaAs barrier which covers the QD. In order to reduce this carrier diffusion in the barrier we grew the sample with the barrier thickness of 50 nm.

Figure 2 shows the spatially resolved PL spectra at a temperature of 18 K. For the purpose of investigating the PL spectra on various positions, the structures were monitored by Sh-F technique before detecting the spectrum. The PL spectrum shown in Fig. 2(a) was obtained by positioning the tip 200 nm above the top of a QD. This provided us with the PL spectrum from the carriers excited in the whole QD structure. Figures 2(b) and 2(c) show the PL spectra with the tip position less than 10 nm above the region of the QD and that of the SiO_2 mask, respectively. Figures 3(a), 3(b), and 3(c) show the spectrally resolved optical images corresponding to each energy region indicated by arrows labeled A, B, and C in Fig. 2(a). In order to map the luminescent region, simultaneously monitored Sh-F image was taken [Fig. 3(d)].

Judging from the photon energy at PL peaks, position dependence of the PL spectra and optical images, it was confirmed that energy region A, B, and C in Fig. 2(a) are originated from the GaAs bulk, the GaAs QD and the GaAs quantum well (QW), respectively. Since the QW is thinner than the QD in this sample, the energy shift in the QD is smaller than that of QW. The intensity distribution of PL from the QW was asymmetrical with respect to the dot structures as shown in Fig. 3(d). This asymmetry can be understood from the tapered sample structure and the lens position; the PL light originated from further QW was partially screened by the tapered sample.

It should be noted that no peaks exist corresponding to the bulk in Fig. 2(b) and the QD/QW in Fig. 2(c), respectively. Moreover, in Fig. 2, the PL peak intensity from the QD was large enough in comparison with that from the bulk. These results mean that the carriers excited in the barrier region diffuse and are captured effectively in the QD and the QW regions. Therefore, the sample was proved to be free from the bottleneck problem and the following three-dimensional confinement nature can be revealed; the carrier diffusion from the outer regions, or a giant oscillator strength owing to the confined structure.

The PL spectrum obtained by positioning the tip above the top of a single QD with lower power is shown in the inset of Fig. 2(b). There exists a number of sharp lines with a full width at half-maximum (FWHM) narrower than a few meV, which is determined by the resolution of the monochromator. These peaks were reproducible and therefore concluded to be originated from the QD. This broad band spectrum is due to the following two reasons. As can be estimated from the PL peak energy dependence on magnetic field, the interlevel spacing was 7.5 meV. Therefore, first of all there seem to be a number of transitions from the upper excited states which contribute to the spectrum. Second, the carriers confined within the valleys, which are induced by the vertical size fluctuation of the QD. It gives rise to nonuniform distribution of the carriers throughout a QD, and consequently can be a reason of multipeaks generation. The fact, that we could not find any significant difference between each PL peak from the images, it can be attributed to our resolution limit of 200 nm. It still seems to be reasonable to interpret this multipeak structure as a convolution of these two reasons.

Monitoring the carrier diffusion and obtaining the effec-

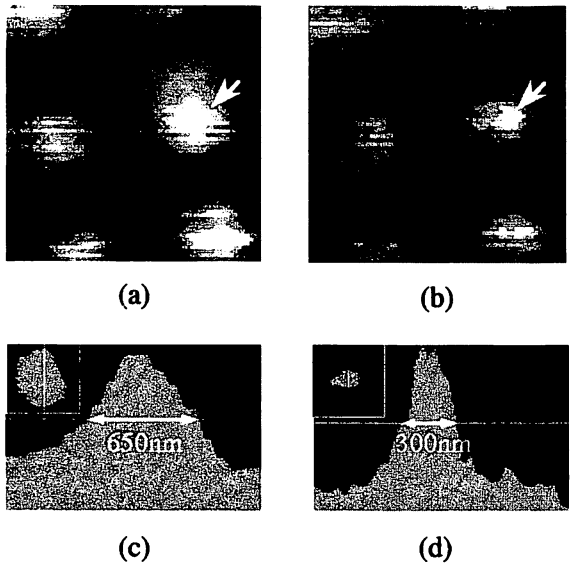

FIG. 4. PL images obtained at the excitation power of (a) ~50 nW and (b) ~5 nW. The scanned area is 3 μm×3 μm with the pixel size of 45 nm×45 nm. Cross-sectional distribution of the luminescent area corresponding to the QD indicated by an arrow in (a) and (b) are shown in (c) and (d), respectively. Inset: Two-dimensional profiles normalized on full width at half-maximum of the PL intensity corresponding to the QD. These images are 1 μm×1 μm in size.

tive excited region of the QD can be carried out by varying intensity of the excitation light. Figures 4(a) and 4(b) show PL images with excitation power of about 50 and 5 nW, respectively. Comparing these two images, one can see that the region, where the carriers can diffuse and be captured in the QD, expands with increasing the excitation power. This result indicates that the carriers excited with higher intensity posses larger momenta and longer diffusion lengths. One- and two-dimensionally resolved cross-sectional intensity profiles at the QD position indicated by the arrow in Figs. 4(a) and 4(b) are shown in Figs. 4(c) and 4(d). The FWHM of these luminescence intensity profiles are about 650 and 300 nm, respectively. With lower excitation power we observed a single PL peak indicated by an arrow in the inset of Fig. 1. Thus, we interpret that the FWHM of 300 nm obtained with lower excitation power indicates the effective region of the intensive carriers caption at the PL peak.

In conclusion, we carried out the near-field spectroscopy of the quantum dot structures fabricated by the selective epitaxial growth at low temperature, and resolved spatially and spectrally the PL regions of carriers which diffuse and are captured in the region of the GaAs QD, the GaAs QW, and the GaAs bulk. The spread of the carrier was observed by varying the excitation power. We estimated the effective region of the carriers captured at one of the confined states of the QD structure to be about 300 nm.

This work is partly supported by a Grant-in-Aid for Scientific Research on Priority Area, "Quantum Coherent Electronics" from the Ministry of Education and University-Industry Joint Project on "Quantum Nanoelectronics."

[1] Y. Arakawa and H. Sakaki, Appl. Phys. Lett. **40**, 929 (1982).
[2] K. Tsutsui, E. L. Hu, and C. W. Wilkinson, Jpn. J. Appl. Phys. **32**, 6233 (1993).
[3] L. Goldstein, F. Glas, J. Y. Marzin, M. N. Charasse, and G. LeRoux, Appl. Phys. Lett. **47**, 1099 (1985).
[4] J. Oshinowo, M. Nishioka, S. Ishida, and Y. Arakawa, Appl. Phys. Lett. **65**, 1421 (1994).
[5] Y. Nagamune, S. Tsukamoto, M. Nishioka, and Y. Arakawa, J. Cryst. Growth **126**, 707 (1993).
[6] M. Ohtsu, J. Lightwave Technol. **13**, 1200 (1995).
[7] R. D. Grober, T. D. Harris, J. K. Trautman, E. Betzig, W. Wegscheider, L. Pfeiffer, and K. West, Appl. Phys. Lett. **64**, 1421 (1994).
[8] H. F. Hess, E. Betzig, T. D. Harris, L. N. Pfeiffer, and K. W. West, Science **264**, 1740 (1990).
[9] U. Mohideen, M. J. Yoo, H. Hess, W. S. Hobson, F. Ren, R. Kopf, and R. E. Slusher, Tech. Dig. Quantum Electron. Laser Sci. **16**, 95 (1995).
[10] T. Pangaribuan, S. Jiang, and M. Ohtsu, Electron. Lett. **29**, 1978 (1993).
[11] T. Saiki, S. Mononobe, M. Ohtsu, N. Saito, and J. Kusano, Appl. Phys. Lett. **67**, 2191 (1995).
[12] S. Mononobe, T. Saiki, M. Naya, and M. Ohtsu, Appl. Opt. (unpublished).
[13] E. Betzig, P. L. Finn, and J. S. Weiner, Appl. Phys. Lett. **60**, 2484 (1992).

Determination of slant angle of $p-n$ interface by multiwavelength near-field photocurrent measurement

T. Saiki
Kanagawa Academy of Science and Technology, Takatsu-ku, Kawasaki, Kanagawa 213, Japan

N. Saito and J. Kusano
NHK Science and Technical Research Laboratories, Setagaya-ku, Tokyo 157, Japan

M. Ohtsu[a)]
Interdisciplinary Graduate School of Science and Engineering, Tokyo Institute of Technology, Midori-ku, Yokohama, Kanagawa 226, Japan

(Received 2 January 1996; accepted for publication 21 May 1996)

Near-field photocurrent measurements with multiwavelength excitation sources are applied to the investigation of a lateral $p-n$ junction grown on patterned GaAs (111)A substrate. In order to probe the internal properties of this device, propagation modes into the sample are utilized retaining high resolution with the contribution of a penetration depth smaller than the aperture diameter. By systematically varying the penetration depth over a wide range up to 900 nm, photocurrent signals due to internal optical response clearly appear. The capability of "tomographic" diagnostics is demonstrated and the slant angle of the $p-n$ interface is determined to be $30\pm8°$. © *1996 American Institute of Physics.* [S0003-6951(96)03531-0]

Photocurrent measurement with near-field excitation[1,2] is a novel technique for the diagnostics of semiconductor photonic devices including laser diode, photodetector, and light emitting diode. So far, a near-field optical microscope, which is called NSOM,[3] SNOM,[4] and so on, has been employed for the spatially resolved observation of small structures on the surface, such as single molecules[5–7] and quantum dots,[8] or optically thin materials, such as quantum wells[9] and wires.[10] In the study of bulk devices,[11] however, their internal optical and transport properties should also be precisely examined. For this purpose, propagating modes of the aperture is expected to make an important contribution. Though propagating modes into a crystal do not have any resolving power, "tomographic" information of the investigated material can be obtained by systematically varying the optical penetration depth over a wide range, i.e., from less than the aperture diameter to the order of wavelength. Here, it should be emphasized that in the case of the penetration depth being smaller than the aperture diameter, the resolution is determined only by the aperture diameter. This multiwavelength imaging corresponds to the energy-dependent source size in electron-beam induced current (EBIC) measurement.[12] In EBIC imaging, the resolution is restricted to ~1 μm and its accuracy in tuning excitation energy near the band edge is not so adaptable compared to the optical excitation.

In this letter, using multiwavelength excitation sources ($\lambda=488-830$ nm), near-field photocurrent imaging is applied to the lateral $p-n$ junction on a patterned GaAs substrate. With the smallest penetration depth of 80 nm, the response profile of the $p-n$ active region involving diffusion properties of photoexcited carriers is imaged with the spatial resolution determined by the aperture diameter of 200 nm. Varying the penetration depth up to 1.0 μm, the ability of investigating the internal structure of the sample is demonstrated. The slant angle of the $p-n$ interface is quantitatively determined for the first time.

A schematics of the sample structure is shown in Fig. 1.[13,14] After the etching of a semi-insulating GaAs (111)A substrate with photolithography technique, Si-doped GaAs layers with a thickness of 1 μm are grown by molecular beam epitaxy. The concentration of Si is about 1×10^{18} cm^{-3}. Due to the amphoteric nature of the Si dopant in GaAs,[15,16] the lateral $p-n$ junctions are achieved at the upper and the lower interfaces. The configuration of electrodes for the investigation of the lower junction is depicted in Fig. 1.[13] Injecting current through these electrodes, a strong electroluminescence from the active region has been collected by a fiber probe of the near-field optical microscope.[17]

A sharpened fiber probe is prepared with selective etching processes in buffered hydrofluoric acid.[18] After metallizing the exterior surface of the etched probe with 200-nm-thick gold, a 200 nm aperture is fabricated using a selective resin coating method. In order to obtain a high transmission

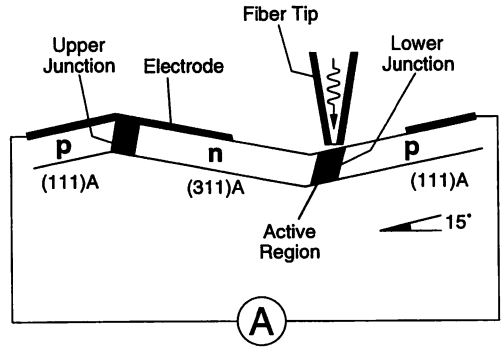

FIG. 1. Schematic structure of lateral $p-n$ junctions and diagram of experimental geometry. In this measurement, the lower junction is examined. The sample is tilted by 15° in order to avoid its contact with the cladding of the fiber probe.

[a)]Also with Kanagawa Academy of Science and Technology, Takatsu-ku, Kawasaki, Kanagawa 213, Japan.

 0003-6951/96/69(5)/644/3/$10.00

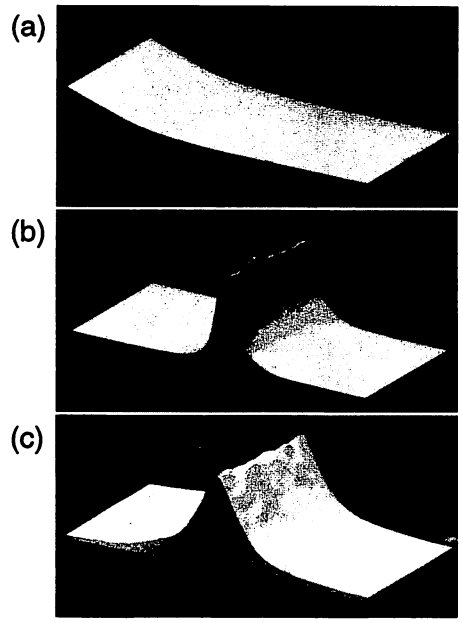

FIG. 2. Perspective views of the (a) topographic image in the vicinity of lower junction, (b) the near-field photocurrent image at the excitation wavelength λ=488 nm, and (c) λ=830 nm. The image size is 5×10 μm^2. The height of the slope in (a) is 1 μm.

efficiency, the shape of the tip is optimized by a multistep chemical etching technique.[19] The transmission coefficient is estimated as 1×10^{-3} by collecting the far-field throughput with a 0.4 numerical aperture objective lens. As multiwavelength light sources, Ar^+ laser (λ=488 nm), He–Ne laser (λ=633 nm), and Ti:sapphire laser (λ=780 and 830 nm) are coupled into the fiber probe. By using these lights, the optical penetration depths in GaAs can be tuned from 80 nm to 1.0 μm. In order to keep near-field excitation, the tip is controlled in close proximity to the sample (~10 nm) by applying the shear-force feedback technique.[20] The photocurrent induced by the light through the aperture is collected at electrodes and amplified with current injection preamplifier. The signal is synchronously detected with a lock-in amplifier.

The excitation light through the subwavelength aperture is composed of propagating modes and evanescent ones. The evanescent-mode distribution in the tangential wave vector $k_{\|}$ (component parallel to the surface) space is determined by the aperture radius a. Ünlü *et al.* concluded that the cutoff wave vector of the evanescent-mode distribution lies at $\pi/2a$.[2] In free space, if the aperture diameter $2a$ is less than half the wavelength $\lambda/2$, there is a dominant occupation of the evanescent modes in the region $k_{\|}>2\pi/\lambda$. When the aperture is positioned closely to the optically dense material, a part of the evanescent modes present in the region $k_{\|}<n(2\pi/\lambda)$, where n is the refractive index of the material, are coupled into propagation modes in the material. For the case of a 200 nm aperture and n=3.5 (refractive index of GaAs), almost all the evanescent modes are coupled into propagating ones for the entire wavelength range (λ=488–830 nm), where $\pi/2a<n(2\pi/\lambda)$. The beam spread angle of the light propagating into GaAs (shown as ϕ in Fig. 4) is finally determined by the aperture radius. In this experimental situation, the resolution is limited not only by the aperture size but also by the penetration depth. In the present work,

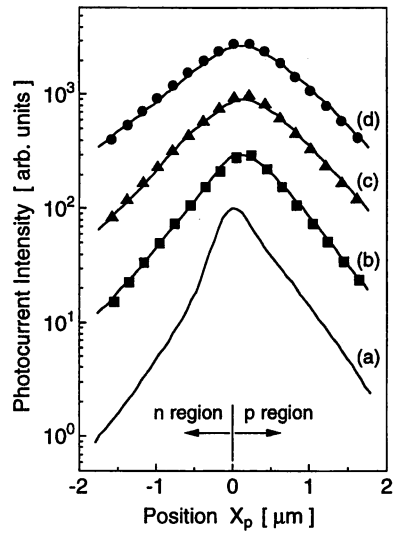

FIG. 3. Cross-sectional profiles of the near-field photocurrent signals at the excitation wavelength (a) λ=488 nm, (b) 633 nm, (c) 780 nm, and (d) 830 nm. Symbols correspond to the calculated results from Eq. (4) with fitting parameters being θ=15°, ϕ=40° (●), 37° (▲), and 27° (■).

however, it is demonstrated that the wavelength-dependent imaging with propagating light also makes a large contribution to the "tomographic" analysis of the internal structure of the $p-n$ interface.

Near-field photocurrent images at the excitation wavelengths of 488 and 830 nm are shown with a topographic image in Fig. 2. Uniformity of photocurrent intensity is seen along the $p-n$ active region. The full widths at half-maximum of photocurrent signal profile are 0.6 and 1.7 μm at λ=488 and 830 nm, respectively. The increase of penetration depth results in the decrease of the resolving power. Figure 3 shows the cross-sectional profiles of photocurrent intensities in logarithmic scale. At the excitation wavelength of 488 nm, due to the shallow penetration depth of 80 nm, the resolution is determined by the aperture size and the diffusion length of photoexcited carriers. The ratio of the diffusion length of electron to that of hole is estimated as ~5 (the diffusion coefficient for electron D_e~220 cm^2/s and for

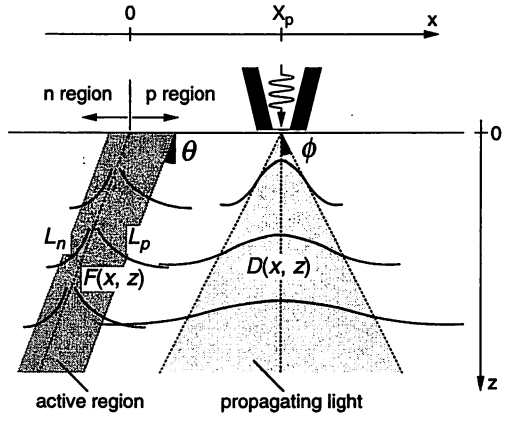

FIG. 4. Schematics of the slant $p-n$ interface and the propagating light into GaAs. The response profile of the $p-n$ region is assumed to be exponential with decay lengths L_n and L_p determined by the curve (a) in Fig. 3. The slant angle θ and the beam spread angle ϕ are the fitting parameters in the calculation of Eq. (4).

hole $D_h \sim 10$ cm^2/s). This large difference can be observed through the slower rise of photocurrent signal in the p region than in the n region, which results in the asymmetry of the signal profile.[1] Moreover, on increasing the penetration depth, the decay length becomes longer and the asymmetric behavior reverses. We believe that the longer decay length in the n region than in the p region at a larger penetration depth can be explained by the slant of the $p-n$ interface (shown as θ in Fig. 4).

Here, we make an analysis of the asymmetric signal behavior using a one-dimensional model as shown in Fig. 4. Here, the fitting parameters are the slant angle of the $p-n$ interface θ and the beam spread angle ϕ. The application of this model to the curve (b)–(d) in Fig. 3 is appropriate since, for the excitation with λ=633, 780, and 830 nm, their respective penetration depths are much larger than their wavelengths in GaAs. With regard to the signal profile of λ=488 nm, which is free from the long propagation into the sample, the characteristic decay lengths of the photocurrent signal due to the carrier diffusion effect are exactly imaged at least in the region $|x|>2a$ (=200 nm); curve (a) in Fig. 3 depicts the spatial response profile of the $p-n$ active region, which can be expressed as

$$F(x,z)=\exp(x/L_n), \quad x<-z\tan\theta,$$
$$=\exp(-x/L_p), \quad x>-z\tan\theta, \tag{1}$$

where L_n=400 nm and L_p=520 nm. For the angular distribution of propagating light into GaAs, we assume a Gaussian profile given by

$$D(x,z)=\exp[-(x-Xp)^2/(z\tan\phi)^2]/z, \tag{2}$$

where X_p indicates the position of the aperture and ϕ is a function of the wavelength. The effect of the wavelength-dependent penetration depth is

$$A(x,z)=\exp(-l/L_{\mathrm{pd}}), \tag{3}$$

where $l^2=x^2+z^2$ and L_{pd}=0.25, 0.65, and 1.0 μm are the penetration depth for the excitation wavelengths of 633, 780, and 830 nm, respectively. The intensity of the photocurrent signal is proportional to

$$I(X_p)=\int_0^d\int_{-\infty}^{+\infty} D(x,z)A(x,z)F(x,z)dxdz, \tag{4}$$

where d=1 μm is the depth of the $p-n$ interface. The experimental curves (b)–(d) in Fig. 3 are perfectly fitted by using Eq. (4). From this calculation, we obtain the slant angle of the $p-n$ interface $\theta=15\pm8°$ and the beam spread angle $\phi=40\pm8°$ for the wavelength of 830 nm. This angle ϕ determines the tangential wave vector of the propagating light to be $n(2\pi/\lambda)\sin\phi=0.017$ nm^{-1}, which is in good agreement with $\pi/2a=0.016$ nm^{-1}. This result implies that, as concluded by Ünlü *et al.*, the cutoff wave vector of the evanescent-mode distribution lies at $\pi/2a$.

A total slant of the $p-n$ interface of $30\pm8°$ to the p side, which is the sum of the observed slant angle θ of $15\pm8°$ and the intended tilt angle of 15° in the experimental setup, can be explained by the crystal orientation dependence of the growth nature.[21] The most significant origin is that the growth rate of GaAs on (311)A is faster than that of (111)A, which causes the shift of n-type region to p side on growth. Other factors are also examined taking into account the experimental results on photoluminescence and electroluminescence measurements.

In summary, we demonstrate that multiwavelength near-field photocurrent measurement applied to the lateral $p-n$ junction is a powerful technique to investigate not only the surface properties but internal structures of bulk devices with high spatial resolution. By using various laser sources, the optical penetration depth into GaAs are varied from 80 nm to 1.0 μm. The smallest penetration depth gives the spatial response profile of the active region including carrier transport properties with the resolution of the aperture diameter. In the imaging with larger penetration depth, the internal optical response of the $p-n$ interface appears and its slant structure is quantitatively determined. The "tomographic" diagnostics with the present method will provide a new insight in understanding the crystal growth mechanism.

The authors thank Y. Yokoyama for the fabrication of the fiber probe and other experimental contributions.

[1] S. K. Buratto, J. W. P. Hsu, E. Betzig, J. K. Trautman, R. B. Bylsma, C. C. Bahr, and M. J. Cardillo, Appl. Phys. Lett. **65**, 2654 (1994).
[2] M. S. Ünlü, B. B. Goldberg, W. D. Herzog, D. Sun, and E. Towe, Appl. Phys. Lett. **67**, 1862 (1995).
[3] E. Betzig, J. K. Trautman, T. D. Harris, J. S. Weiner, and R. L. Kostelak, Science **251**, 1468 (1991).
[4] U. Dürig, D. W. Pohl, and F. Rohner, J. Appl. Phys. **59**, 3318 (1986).
[5] E. Betzig and R. J. Chichester, Science **262**, 1422 (1993); J. K. Trautman, J. J. Macklin, L. E. Brus, and E. Betzig, Nature **369**, 40 (1994).
[6] W. P. Ambrose, P. M. Goodwin, J. C. Martin, and R. A. Keller, Phys. Rev. Lett. **72**, 160 (1994).
[7] X. S. Xie and R. C. Dunn, Science **265**, 361 (1994).
[8] H. F. Ghaemi, B. B. Goldberg, C. Cates, P. D. Wang, C. M. Sotomayor Torres, M. Fritze, and A. Nurmikko, Superlattices Microstruct. **17**, 15 (1995).
[9] H. F. Hess, E. Betzig, T. D. Harris, L. N. Pfeiffer, and K. W. West, Science **264**, 1740 (1994).
[10] R. D. Grober, T. D. Harris, J. K. Trautman, E. Betzig, W. Wegscheider, L. Pfeiffer, and K. West, Appl. Phys. Lett. **64**, 1421 (1994).
[11] T. Saiki, S. Mononobe, M. Ohtsu, N. Saito, and J. Kusano, Appl. Phys. Lett. **67**, 2191 (1995).
[12] H. J. Leamy, J. Appl. Phys. **53**, R51 (1982).
[13] N. Saito, M. Yamaga, F. Sato, I. Fujimoto, M. Inai, T. Yamamoto, and T. Watanabe, Proceedings of the 1993 International Symposium on GaAs and Related Compounds, Freiburg [Inst. Phys. Conf. Ser. **136**, 601 (1994)].
[14] M. Fujii, T. Yamamoto, M. Shigeta, T. Takebe, K. Kobayashi, S. Hiyamizu, and I. Fujimoto, Surf. Sci. **267**, 26 (1992); M. Fujii, T. Takebe, T. Yamamoto, M. Inai, and K. Kobayashi, Superlattices Microstruct. **12**, 167 (1992).
[15] J. M. Ballingall and C. E. C. Wood, Appl. Phys. Lett. **41**, 947 (1982).
[16] W. I. Wang, E. E. Mendez, T. S. Kuan, and L. Esaki, Appl. Phys. Lett. **47**, 826 (1985).
[17] S. K. Buratto, J. W. P. Hsu, J. K. Trautman, E. Betzig, R. B. Bylsma, C. C. Bahr, and M. J. Cardillo, J. Appl. Phys. **76**, 7720 (1994).
[18] T. Pangaribuan, K. Yamada, S. Jiang, H. Ohsawa, and M. Ohtsu, Jpn. J. Appl. Phys. **31**, L1302 (1992); T. Pangaribuan, S. Jiang, and M. Ohtsu, Electron. Lett. **29**, 1978 (1993).
[19] T. Saiki, S. Mononobe, M. Ohtsu, N. Saito, and J. Kusano, Appl. Phys. Lett. **68**, 2612 (1996).
[20] E. Betzig, P. L. Finn, and J. S. Weiner, Appl. Phys. Lett. **60**, 2484 (1992).
[21] T. Nishinaga, K. Mochizuki, H. Yoshinaga, C. Sasaoka, and M. Washiyama, J. Cryst. Growth **98**, 98 (1989).

Tailoring a high-transmission fiber probe for photon scanning tunneling microscope

T. Saiki, S. Mononobe, and M. Ohtsu[a)]
Kanagawa Academy of Science and Technology, Takatsu-ku, Kawasaki, Kanagawa 213, Japan

N. Saito and J. Kusano
NHK Science and Technical Research Laboratories, Setagaya-ku, Tokyo 157, Japan

(Received 7 September 1995; accepted for publication 29 February 1996)

Transmission efficiency of a fiber probe used in photon scanning tunneling microscope is evaluated as a function of aperture diameter. The apertured probe has been fabricated by chemical etching technique and metal coating. By comparing two types of probes with different cone angles, we determine the most influential factor in the transmission property of the metal-cladding tapered waveguide. A long tip with high efficiency is developed by a multistep etching method so as to be suitable during actual scanning operation. Photoluminescence imaging of lateral p-n junctions on the GaAs substrate is demonstrated in the illumination-collection hybrid mode operation of photon scanning tunneling microscope. © *1996 American Institute of Physics.* [S0003-6951(96)01819-0]

In the optical investigation of semiconductor devices, a photon scanning tunneling microscope (PSTM)[1] has made a remarkable contribution to the subwavelength-resolution imaging and spectroscopy. Recently, several variations of PSTM combined with the conventional spectroscopic techniques have been successfully implemented in the study of luminescence spectroscopy of quantum structures at low temperature,[2,3] pump-probe measurement of semiconductor microdisk,[4] and photocurrent detection of quantum well structure[5,6] with the resolution of 100–250 nm. In the imaging studies of local optical properties of semiconductor devices, an illumination-collection hybrid (reflection) mode should be used. This is because the light traverses the aperture twice which essentially avoids the deterioration of the resolution, limited by the carrier diffusion effect. For such advanced experiments, the most serious problem is the small detected signal due to the low excitation or collection efficiency by the tiny aperture. To overcome this difficulty, it is necessary to improve the efficiency of transmission to the aperture by tailoring the shape of fiber tip.

For the preparation of sharpened fiber probe, we reported a chemical etching technique with high reproducibility.[7] Recently, fabrication of a small aperture with high controllability of its diameter has also succeeded. In Fig. 1, a schematic of chemically etched fiber probe with metal coating is shown introducing our terminology. The metal-coated fiber probe, which is regarded as a metal-cladding tapered waveguide, has complex loss mechanisms. The existence of cutoff diameter even in the lowest mode is the most specific feature of the metallic waveguide.[8] Beyond the cutoff diameter, the intensity of the light exponentially decreases. With respect to the transmission efficiency, the distance between the aperture and the cutoff diameter is expected to be one of the significant aspects. It has been pointed out that the efficiency of delivering the light into the lowest mode is also an important factor.[9] Here, it should be emphasized that the shape of the fiber probe fabricated by chemical etching technique is perfectly reproducible and finely controllable. These are the most desirable features when precisely investigating the function of each part of the tip.

In this letter, we determine the tip parameters which are required to obtain the high transmission efficiency. By preparing probes with different cone angles and hence the resultant tip lengths, the transmission coefficients are evaluated for a wide range of aperture diameters (80–900 nm). On the basis of these results, we optimize the shape of the tip taking into account the experimental utilities; for example, by lengthening the tip part, we can avoid contact between the cladding and bumpy surface structure of the sample. The capability of this optimized tip is demonstrated by examining lateral p-n junctions grown on a patterned GaAs substrate.

Since the fabrication technique of fiber tip with selective etching process is described in detail in Ref. 7, we report it briefly here. The cone angle θ can be controlled by buffering condition of etching solution, which is adjusted by the volume ratio X of NH_4F maintaining that of HF to H_2O at 1:1. Here, the composition of the solution is expressed as X:1:1. In order to observe the dependence of transmission efficiency on cone angle, two types of fiber tips are prepared using a one-step etching technique with a solution of $X=10$ (tip A) and $X=2.7$ (tip B). The cone angle θ and the tip length l of the tip A are 20° and 6 μm, respectively, and those of the tip B are 50° and 2.5 μm.

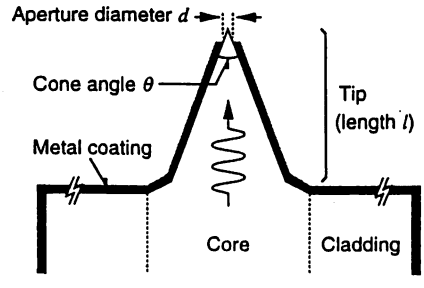

FIG. 1. A schematic of chemical-etched fiber probe with metal coating.

[a)]Also with Interdisciplinary Graduate School of Science and Engineering, Tokyo Institute of Technology, Midori-ku, Yokohama, Kanagawa 226, Japan.

 0003-6951/96/68(19)/2612/3/$10.00

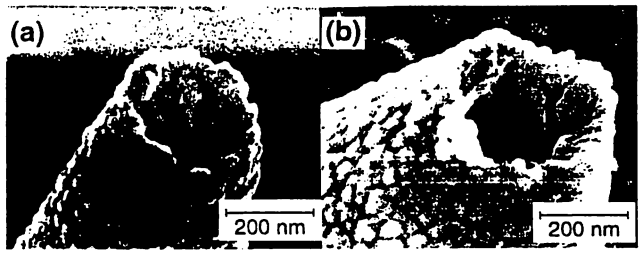

FIG. 2. Apertured tip with two different cone angles: (a) tip A (θ=20°), (b) tip B (θ=50°). Aperture diameters of (a) and (b) are 80 and 200 nm, respectively.

Using a sputter coating method, the exterior surface of the etched probe is metallized with gold of 200-nm thickness, which is 7 times the skin depth at 633 nm. For the fabrication of small aperture, selective resin coating method is employed. Acrylic resin solved in organic solution is coated as a guard layer on the sides of tapered part leaving the top of the tip free of acrylic resin. Here, surface tension of the resin is utilized. On removing the gold coating from the top of the tip with the commonly used $KI-I_2$ etching solution, a small aperture is fabricated. The aperture diameter can be varied by controlling the etching time in the $KI-I_2$ solution and the coating condition which can be adjusted by changing the cladding diameter and the viscosity of the resin solution. Scanning electron microscope (SEM) images of apertures of the tip A (the diameter $d\sim$80 nm) and the tip B ($d\sim$200 nm) are shown in Fig. 2.

For the estimation of transmission coefficient, light from a He–Ne laser (632.8 nm) of 130 μW is coupled into the fiber probe with a coupling efficiency of 60%. The far-field light ejected from the aperture is collected with a 0.4 NA objective lens. The output power is measured with an optical power meter. The transmission coefficient is defined as the ratio of the collected output power to the input power. The geometrical size of the aperture is estimated with SEM after the throughput measurement.

In Fig. 3, transmission coefficients are plotted as a function of the aperture diameter d for the tip A (closed circles) and the tip B (closed triangles). For the diameter d that is larger than the wavelength of He–Ne laser light in glass d_c

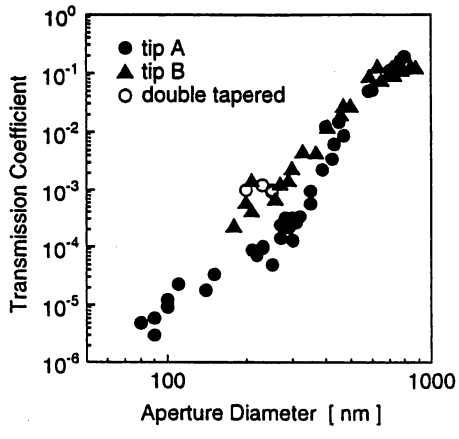

FIG. 3. Transmission coefficients as a function of the aperture diameter: tip A (closed circle), tip B (closed triangle), and double tapered tip (open circle).

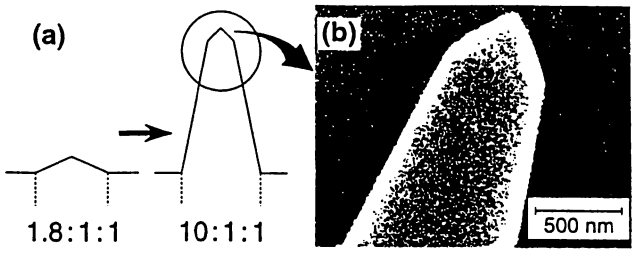

FIG. 4. (a) Fabrication process of a double tapered tip, (b) scanning electron microscope image of the double tapered apex region of the tip.

(~400 nm), the transmission coefficients of the tip A and the tip B take almost the same values when the aperture diameter is the same. This result shows that the efficiency for delivering light into the region $d>d_c$ is not so strongly dependent on the length and the cone angle of the metallic tapered waveguide, which is 5 μm long at most. On the other hand, in the region $d<d_c$, the differences between the two types of probes are remarkable under the influence of metal coating. For the case of aperture diameter being 200 nm, transmission efficiency of the tip A is lowered by 10 times to that of the tip B. The dependence of transmission power on the cone angle is thought to be coming from the evanescent propagation of light into the metallic cladding waveguide with the diameter less than the cutoff. In order to increase the transmission efficiency, it is reasonable to shorten the distance between the aperture and the cutoff diameter by increasing the cone angle.[9] In theoretical consideration, assuming perfect conductivity of the cladding, the cutoff diameter of the lowest bound mode in a metallic cylindrical waveguide is 250 nm for 633-nm light.[8] The discrepancy between d_c and the theoretical cutoff may be explained by considering the tapered structure and a complex dielectric permeability of metal cladding.

Although highly efficient, a short tip with large cone angle leads to contact between its cladding and the bumpy surface of the sample during actual scanning operation. To avoid this inconvenience, it is necessary to lengthen the tip still maintaining the large transmission coefficient. For this purpose, we have successfully developed a fabrication technique of a double tapered tip with high reproducibility. Two-step etching process is employed as shown in Fig. 4(a). In the first step, using a solution with a composition of X=1.8, a short tip with a large cone angle of 150° is fabricated. Second, a long tapered region, which delivers light to the cutoff diameter, is obtained with a solution having X=10. As shown in the SEM image of Fig. 4(b), the resultant top cone angle is about 90°. The fabrication technique of small aperture is the same as that mentioned earlier. To demonstrate the high efficiency of this tip, we again measure the transmission coefficients of some tips with diameters of around 200 nm. The results are plotted in Fig. 3 (open circles). Higher transmission efficiency by an order of the tip A (closed circles) is achieved. This comparison confirms that the most important factor in determining the transmission efficiency is the length of the cutoff region of metallic waveguide.

In order to demonstrate the utility of the optimized probe, luminescence imaging of novel-structured semiconductor optical device is performed with the illumination-

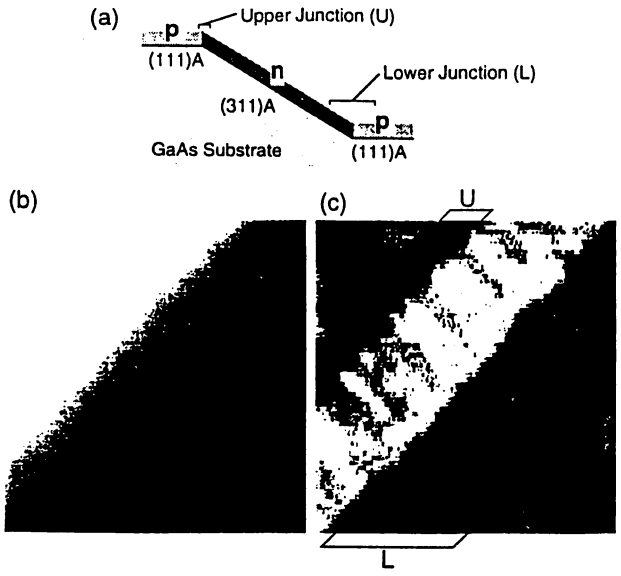

FIG. 5. (a) A schematic showing the cross-sectional profile of lateral p-n junctions grown on a patterned GaAs (111)A substrate. The width and the height of the slope are 10 and 6 μm, respectively. (b) Shear force image and (c) photoluminescence image in the vicinity of the slope. The scanning area is 15.2×15.2 μm^2. U and L indicate the transition regions of the upper and lower junctions, respectively.

collection hybrid mode photon STM, where the photon counting technique is employed for the detection of a small signal. A strict correspondence between the local emission properties and surface structures of lateral p-n junctions grown on a patterned GaAs (111)A substrate is investigated.[10] A schematic showing the cross-sectional profile of the sample structure is shown in Fig. 5(a). Si-doped GaAs layers with the thickness of 1 μm is grown by molecular beam epitaxy.[11,12] By utilizing the amphoteric nature of the Si dopant in GaAs, lateral p-n junctions are achieved at the upper and the lower interfaces. The width and the height of the slope are 10 and 6 μm, respectively. Due to this bumpy structure, we could not use a short tip, such as tip B, without making contact between the cladding and the slope. By employing the optimized probe with the aperture diameter of 200 nm and a transmission coefficient of 1.0×10^{-3}, the illumination-collection hybrid mode is successfully employed to map the two-dimensional emission intensity near the p-n junctions. Since the tip locally collects the luminescence in addition to being a local excitation source, the resolution is not affected by the carrier diffusion effect but is determined solely by the aperture diameter. The resulting image of the emitted intensity map is shown in Fig. 5(c) with the corresponding shear force image shown in Fig. 5(b). The signal intensity in the transition region is much lower than that in the other regions due to the separation of photoexcited electrons and holes by the internal electric field. In the lower junction, a local increase of the emission intensity is observed. The size of the smallest optical structure is 300 nm, which is much smaller than diffusion length of ~1 μm. A nonuniform distribution of Si dopants and of the resultant internal electric field may affect the local optical responses.

In summary, for a wide range of aperture diameter, the transmission efficiency is evaluated for two types of tips with different cone angles. The important factor determining the efficiency is the distance between the aperture and the cutoff diameter, which is the most significant feature of the metal-cladding waveguide. Taking into account the utility in scanning over the bumpy sample, we develop the double tapered probe with the long tip and large cone angle at the apex. For the aperture diameter of 200 nm, the transmission coefficient of 1.0×10^{-3} (evaluation with 0.4 NA objective lens) is realized. Using this optimized probe, the illumination-collection hybrid mode operation is demonstrated for the novel-structure p-n junctions. Highly sensitive detection of the emission is achieved with the resolution free from the carrier diffusion effect.

[1] *Near Field Optics,* edited by D. W. Pohl and D. Courjon (Kluwer, Dordrecht, 1993).
[2] R. D. Grober, T. D. Harris, J. K. Trautman, E. Betzig, W. Wegscheider, L. Pfeiffer, and K. West, Appl. Phys. Lett. **64**, 1421 (1994).
[3] H. F. Hess, E. Betzig, T. D. Harris, L. N. Pfeiffer, and K. W. West, Science **264**, 1740 (1994).
[4] J. B. Stark, U. Mohideen, and R. E. Slusher, in *Quantum Electronics and Laser Science Conference OSA Technical Digest Series* (Optical Society of America, Washington, DC, 1995), Vol. 16, paper QTuJ1.
[5] S. K. Buratto, J. W. P. Hsu, E. Betzig, J. K. Trautman, R. B. Bylsma, C. C. Bahr, and M. J. Cardillo, Appl. Phys. Lett. **65**, 2654 (1994).
[6] M. S. Ünlü, B. B. Goldberg, W. D. Herzog, D. Sun, and E. Towe, Appl. Phys. Lett. **67**, 1862 (1995).
[7] T. Pangaribuan, K. Yamada, S. Jiang, H. Ohsawa, and M. Ohtsu, Jpn. J. Appl. Phys. **31**, L1302 (1992); T. Pangaribuan, S. Jiang, and M. Ohtsu, Electron. Lett. **29**, 1978 (1993).
[8] E. L. Buckland, P. J. Moyer, and M. A. Paesler, J. Appl. Phys. **73**, 1018 (1993).
[9] G. A. Valaskovic, M. Holton, and G. H. Morrison, Appl. Opt. **34**, 1215 (1995).
[10] T. Saiki, S. Mononobe, M. Ohtsu, N. Saito, and J. Kusano, Appl. Phys. Lett. **67**, 2191 (1995).
[11] N. Saito, M. Yamaga, F. Sato, I. Fujimoto, M. Inai, T. Yamamoto, and T. Watanabe, Inst. Phys. Conf. Ser. **136**, 601 (1994).
[12] M. Fujii, T. Yamamoto, M. Shigeta, T. Takebe, K. Kobayashi, S. Hiyamizu, and I. Fujimoto, Surf. Sci. **267**, 26 (1992); M. Fujii, T. Takebe, T. Yamamoto, M. Inai, and K. Kobayashi, Superlatt. Microstruct. **12**, 167 (1992).

Direct observation of size-dependent features of the optical near field on a subwavelength spherical surface

T. Saiki and M. Ohtsu

Kanagawa Academy of Science and Technology, 3-2-1 Sakado, Takatsu-ku, Kawasaki, Kanagawa 213, Japan

K. Jang and W. Jhe

Department of Physics, Seoul National University, Seoul 151-742, Korea

Received October 23, 1995

We investigate the characteristics of the optical near field of a subwavelength dielectric sphere by using a nanometric fiber tip and a sensitive technique of wavelength conversion. The decay length of the near field induced around the single sphere is directly measured to be 0.3 of its radius, obtained by precise positioning of the probe tip. A numerical calculation of the optical near field based on the Mie scattering theory is in good agreement with the experimental results. The enhancement of fluorescence collection efficiency in the near-field region is also observed. © 1996 Optical Society of America

The optical near field of a subwavelength dielectric object is of current interest because of its remarkably different characteristics from those of the corresponding far field. The following general properties of the near-field pattern can be deduced from a simple example based on Rayleigh scattering[1]: (i) the range of the near field is a fraction of the size of a particle and is independent of the wavelength of the irradiation light and (ii) the intensity of the near field is comparable with that of irradiation field. These specific features of the optical near field have been successfully used in the development of superresolution imaging with a photon-scanning tunneling microscope[2,3] (PSTM): when a sharpened fiber tip approaches the near field of a small object, the field is frustrated and the scattered light is coupled into the optical fiber. It has been reported that a PSTM has attained a resolution of $\lambda/100$,[4,5] assisted by techniques such as the fabrication of a sharpened fiber probe, the detection of a small signal in the presence of large background, and the regulation of tip–sample separation by an all-optical method. With regard to this superresolution of the PSTM, the confinement feature of the optical near field of a subwavelength object depends strongly on the object's size and conformation. However, so far, direct characterization of the near field of a three-dimensional object by a simple experimental configuration has not been fully accomplished. The approach of a sharpened tip to a single object with precise positioning enables us to obtain direct information on the near-field distribution with tip–sample separation as a parameter.

We report, for the first time to our knowledge, measurement of the characteristic decay length of the optical near field of a subwavelength sphere. The experimental result is compared with the numerical calculation based on Mie scattering,[6] which is more appropriate than Rayleigh scattering for the subwavelength sphere.

Figure 1 shows schematics of measurement of the near field with a sharpened fiber probe. The decay length of the near field can be measured by observation of the tip–sample-distance dependence of the signal intensity. When we observe the scattered field of a subwavelength object irradiated by excitation light as shown in Fig. 1(a), an intense background of the planar evanescent field from the substrate that is due to the incident light is also detected. Moreover, the exponential behavior of the evanescent field is superimposed upon the decay curve of the near-field signal. This complexity of the signal structure makes it difficult to determine clearly the decay length of the near field. To overcome this difficulty we apply the wavelength conversion technique by using fluorescent light from dye molecules doped in a sphere as a light source [Fig. 1(b)]. In this method the background signal is rejected by optical filters, and the near-field signal on the sphere can be selectively detected.

Local detection of fluorescence with the small tip is also an attractive subject from the aspect of quantum optics. With regard to the sensitivity of the PSTM, the enhancement of the collection efficiency as the result of the short-range electromagnetic interaction between tip and sample is expected. The approach of the tip to a fluorescent material in the near-field region will

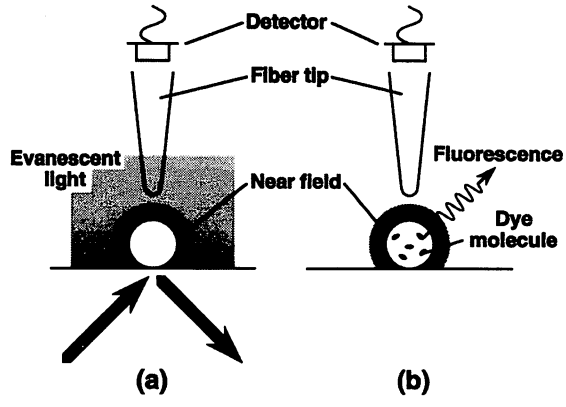

Fig. 1. Experimental configuration for measurement of the decay length of the optical near field. (a) Conventional collection-mode PSTM. (b) Fluorescence PSTM. Excitation light is omitted in (b) for clarity.

0146-9592/96/090674-03$10.00/0

modify its radiation mode. This modification leads to a change in its radiation pattern and in its lifetime, which offers the possibility of highly effective collection of fluorescence.

An experimental schematic of fluorescence detection is shown in Fig. 2. As a sample, Rhodamine-doped polystyrene spheres are dispersed upon a silica substrate by an atomizer. The density of the spheres is <0.2 particles/μm^2 to suppress the background fluorescence. The dye molecules in the spheres are excited by a p-polarized Ar^+ laser (488.0 nm), which is incident under conditions of total internal reflection. The sharpened fiber probe with a 20-nm-diameter tip is fabricated by a highly reproducible chemical etching technique.[7] Here, a shear-force feedback technique[8] is employed to control the tip in the vicinity of the sphere. The fluorescence (wavelength, $\lambda \approx 600$ nm) from a single sphere is picked up by the tip and is coupled to the waveguide mode of the fiber. The excitation light is rejected with optical filters. The fluorescence signal is measured by photon counting. Note that a sphere of $a = 50$ nm (a is the sphere radius) is used as a sample in our study for the following technical reasons: (i) measurement of spheres of $a < 50$ nm is rather difficult because of the low collection efficiency of our collection-mode PSTM shown in Fig. 1 (note that direct detection of the decay length is not possible with the commonly used illumination-mode PSTM despite its higher collection efficiency) and (ii) the decay length of the plane evanescent wave intensity at our incident angle of 50° is ~70 nm, within which the sample is more easily embedded (therefore a larger sample may not be desirable for our setup).

For a precise evaluation of the decay length of the near field we measure the dependence of the pickup fluorescence intensity on tip–sample separation by positioning the tip just above the sphere. A rapid change of signal intensity near the sphere is observed as shown in Fig. 3 (curve a). The decay length of the near-field intensity is ~15 nm, which is much smaller than the illumination wavelength. The same measurement is performed at a lateral position of 500 nm outside the sphere (curve b in Fig. 3). Its intensity is constant in the region $z < 80$ nm, as expected. We also have observed that the baseline of the signal from the single sphere lies between the horizontal axis and curve b. From these results the enhancement factor γ, which is defined as the ratio of the signal intensity at $z = 0$ to that at $z > a$, is estimated to be $3 < \gamma < 4$.

Now let us compare the experimental results with the theoretical calculation based on the Mie scattering theory.[6] The conventional Mie theory concerns the far field that is produced as the result of the scattering of an incident homogeneous plane wave by a dielectric sphere. However, considering the general incident plane wave (inhomogeneous and homogeneous)[9] and focusing on the scattering region just near the sphere, one can obtain the intensity distribution of the near field produced by the scattering of a plane evanescent wave, which can be s or p polarized. Inasmuch as the fluorescent dye molecules are uniformly distributed inside the sphere, one can approximate the object as a macroscopic fluorescent dielectric sphere. By averaging the near-field intensity distribution over the possible polarization directions of the induced dipoles, one can obtain the theoretical curve shown in Fig. 4. Here the size parameter ka of 0.5, which corresponds to the experimental condition ($a \approx 50$ nm and $\lambda \approx 600$ nm), is assumed. Note that any coherent or interfering effect arising from the radiated fluorescence from many dipo-

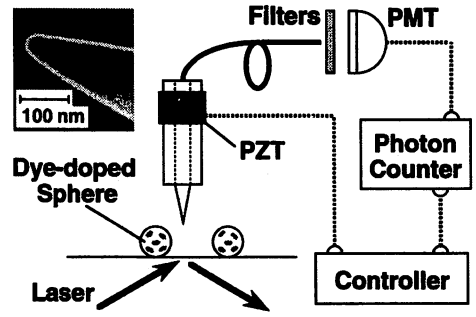

Fig. 2. Experimental schematic of fluorescence detection with the collection-mode PSTM system: PZT, piezoelectric transducer; PMT, photomultiplier tube. The inset shows a scanning electron microscope image of the fiber tip.

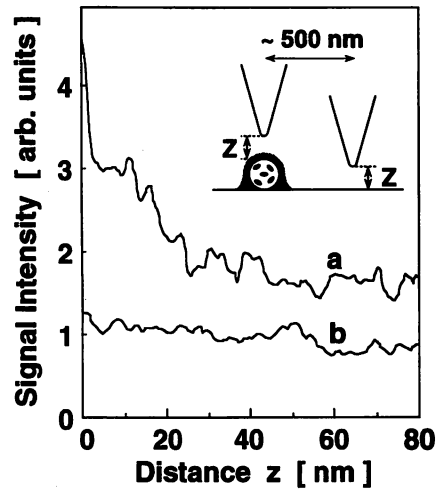

Fig. 3. Dependence of the fluorescence-detection intensity on the tip–sample separation. Curve a, just above the sphere; curve b, ≈500 nm from the sphere.

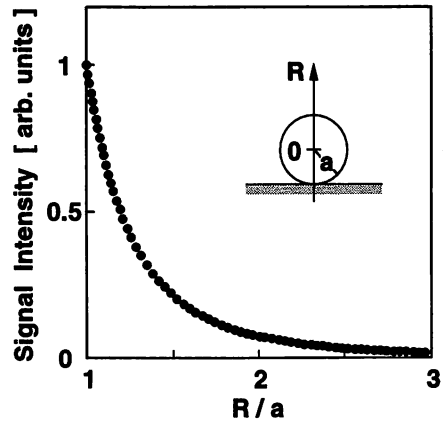

Fig. 4. Numerical plot of the scattered-field intensity of a subwavelength sphere averaged over polarizations with a size parameter ka of 0.5 and evanescent-wave excitation assumed.

lar molecules is neglected because of the random orientations of the molecules inside the dielectric sphere. The expected decay length of $0.3a$ ($\approx$15 nm) shown in Fig. 4 is in good agreement with the experimental result in Fig. 3. By theoretical calculation of other values of ka the general property of the optical near field is also expected: the near field is strongly confined around the sphere within a fraction of its diameter, independently of the wavelength of the excitation light. This size-dependent confinement certainly contributes to the superresolution imaging of the PSTM.

The emission properties of a fluorescent material in near-field optics are interesting and important, but sometimes different results are obtained by some researchers.[10,11] For better understanding it is necessary to accumulate more independent experimental results. The scattering of the near field of a fluorescent material by a subwavelength tip can result in a modification of radiation properties because of the short-range electromagnetic interaction of the material with the tip. For example, Xie *et al.* observed the change in radiative lifetime of single molecules owing to the presence of a PSTM tip in the near-field region.[10] They reported that, compared with the lifetime for far-field detection, the one studied here is shortened from 2.7 to 1.6 ns by the approach of the glass part of the tip to the sample within 5-nm gap distance. However, the shortened lifetime is closely related to the enhanced radiation rate, which then results in increased radiation power and therefore can be associated with our complementary enhancement factor γ ($3 < \gamma < 4$). Moreover, we believe that our bigger value of γ can be attributed to another cavity effect: the change in the emission property of each dye molecule doped in the spherical dielectric cavity.[12] For example, for a radiating dipole near a surface, its emission rate is enhanced by several times, independently of its polarization.[12,13] One can obtain a quantitative estimate of γ by a theoretical consideration that takes into account cavity QED effects, for example.

Finally, and in conclusion, we have performed what we believe is the first experiment that gives insight into and direct evidence for the origin of the intrinsic superresolution feature of the PSTM. By observing the fluorescence from a dye-doped subwavelength sphere, we have shown that the optical near field around the sphere is localized within a fraction of its size ($0.3a$), which is determined only by the sphere size and is much shorter than the wavelength. This decay length is in good agreement with the result of a numerical calculation based on Mie scattering theory.[6] We also demonstrated that the approach of the tip to the sample in near-field region contributes to the enhancement of the collection efficiency by a factor of $3 < \gamma < 4$ in fluorescence detection. A more extensive theoretical as well as experimental study of cavity QED effects in the near-field region is in progress. The experimental results clearly indicate that the application of a PSTM will provide valuable and novel insight into near-field optics, quantum optics, and nanofabrication.

M. Ohtsu is also with the Interdisciplinary Graduate School of Science and Engineering, Tokyo Institute of Technology, 4259 Nagatsuta-cho, Midori-ku, Yokohama, Kanagawa 226, Japan.

References

1. J. D. Jackson, *Classical Electrodynamics* (Wiley, New York, 1975).
2. H. Heinzelmann and D. W. Pohl, Appl. Phys. A. **59,** 89 (1994).
3. D. W. Pohl and D. Courjon, eds., *Near Field Optics* (Kluwer, Dordrecht, The Netherlands, 1993).
4. F. Zenhausern, M. P. O'Boyle, and H. K. Wickramasinghe, Appl. Phys. Lett. **65,** 1623 (1994); F. Zenhausern, Y. Martin, and H. K. Wickramasinghe, Science **269,** 1083 (1995).
5. M. Naya, S. Monomobe, R. Uma Maheswari, T. Saiki, and M. Ohtsu, Opt. Commun. **124,** 9 (1996).
6. K. Jang and W. Jhe, Opt. Lett. **21,** 236 (1996).
7. T. Pangaribuan, K. Yamada, S. Jiang, H. Ohsawa, and M. Ohtsu, Jpn. J. Appl. Phys. **31,** L1302 (1992); T. Pangaribuan, S. Jiang, and M. Ohtsu, Electron. Lett. **29,** 1978 (1993).
8. E. Betzig, P. L. Finn, and J. S. Weiner, Appl. Phys. Lett. **60,** 2484 (1992).
9. H. Chew, D. S. Wang, and M. Kerker, Appl. Opt. **18,** 2679 (1979).
10. X. S. Xie, and R. C. Dunn, Science **265,** 361 (1994); R. C. Dunn, R. X. Bian, R. C. Dunn, X. S. Xie, and P. T. Leung, Phys. Rev. Lett. **75,** 4772 (1995).
11. J. K. Trautman, J. J. Macklin, L. E. Brus, and E. Betzig, Nature (London) **369,** 40 (1994).
12. W. Jhe and K. Jang, Phys. Rev. A **53,** 1126 (1996).
13. J. M. Wylie and J. E. Sipe, Phys. Rev. A **30,** 1185 (1984); D. Meschede, W. Jhe, and E. A. Hinds, Phys. Rev. A **41,** 1587 (1990).

ELSEVIER

15 February 1996

Optics Communications 124 (1996) 9–15

OPTICS COMMUNICATIONS

Imaging of biological samples by a collection-mode photon scanning tunneling microscope with an apertured probe

Masayuki Naya [a,b], Shuji Mononobe [a], R. Uma Maheswari [a], Tosiharu Saiki [a], Motoichi Ohtsu [a,c]

[a] *Kanagawa Academy of Science and Technology, KSP East Rm408,3-2-1, Sakado, Takatsu-ku, Kawasaki-shi, Kanagawa-ken, 213, Japan*

[b] *Fuji Photo Film Co., Ltd. Miyanodai Technology Development Center, 798, Miyanodai, Kaisei-machi, Ashigarakami-gun, Kanagawa, 258, Japan*

[c] *Interdisciplinary Graduate School of Science and Engineering, Tokyo, Institute of Technology, 4259 Nagatsuta, Midori-ku, Yokohama 226, Japan*

Received 2 May 1995; revised version received 3 October 1995

Abstract

We report on high resolution imaging by a collection-mode photon scanning tunneling microscope (c-mode PSTM). In our PSTM system, we have used a novel probe with a nanometric protrusion formed from a metal coated sharpened fiber. By using this probe, flagellar filaments of salmonella of diameter 25 nm could be imaged to have a full width at half maximum of 50 nm. Obtained images strongly depended on the separation of the sample to the probe, the diameter of the aperture, and polarization of the irradiated light. Comments on the origins of these dependencies are given.

1. Introduction

A photon scanning tunneling microscope (PSTM), (alternatively called scanning tunneling optical microscope (STOM), near-field scanning optical microscope (NSOM) or scanning near-field optical microscope (SNOM)), based on the short-range electromagnetic interaction between a small dielectric tip and a sample via an induced evanescent field has been recently developed. Because of the possibility of realizing nanometric resolution without any special sample processing, many applications have been proposed [1,2].

The PSTM technique is commonly implemented in two modes. One is illumination mode (i-mode) which uses an evanescent field generated on a nano-aperture to illuminate the sample [3]. By this mode super resolution beyond the diffraction limit is realized due to the sub-wavelength diameter of the aperture. High contrast can be obtained in this mode which paves a way to perform a variety of experiments [4–6]. However additional auxiliary servo-control technique using, e.g., shearing force, has to be used for maintaining the sample-probe separation constant, which makes the instrument complicated and sometimes damages the sample surface. Furthermore, the polarization-state of the emitted evanescent field depends on the shape of the apertured probe in a complex manner. The other scheme is the collection-mode (c-mode) using a nanometric dielectric tip as a scatterer [1] of the non-radiative evanescent field. Usually the evanescent field can be easily generated on the sample surface by irradiating it with the propagating light under the condition of total reflection [7–9]. Since the scattered light intensity decreases rapidly with increasing sample-probe separation, the

SSDI 0030-4018(95)00644-3

separation can be maintained constant by a simple servo-control loop using only conventional collection optics. This is an outstanding instrumental advantage of this mode. Furthermore, the capability of controlling the polarization state of the incident light makes the analysis and evaluation of the observed images simpler. However, in spite of these advantages experimental results with high resolution c-mode PSTM have not yet been fully documented and we believe this can be mainly due to un-matured fabrication technique of a nanometric probe tip.

In this paper, we demonstrate high resolution imaging experiments by the c-mode PSTM with a novel type of nano-apertured probe. To evaluate the performance of the microscope, we used straight-type flagellar filaments of salmonella (FFS) with diameter of 25 nm, as a reference sample. Dependence of the image characteristics on operation parameters such as sample-probe separation, tip size, and polarization state of the incident light have been investigated.

In section 2 we describe the probe, experimental system and the sample, section 3 gives a discussion of the experimental results and finally section 4 gives a summary.

2. Experiments

For detecting only the high spatial-Fourier frequency components of the evanescent field to realize high resolution, a probe with a small dielectric tip is indispensable. To realize such a tip, we have developed a highly reproducible technique. By means of this technique, a probe whose nanometer sized fiber tip protruding out from a gold film (see Fig. 1a) [10] could be fabricated. The fabrication processes can be summarized as: (i) An optical fiber was sharpened to have a tip with a curvature diameter smaller than 10 nm by using the selective chemical etching technique [11–13]. (ii) The sharpened fiber was coated with a gold film of about 150 nm thickness. Because the optical skin depth of gold is about 30 nm, this thickness was sufficient to block the unwanted propagating light. (iii) The gold coated sharpened fiber was dipped into a resin solution (METAL PRIMER, Gunze Sangyo Inc.) and immediately taken out. Due to the surface tension of the resin solution, only the top of the sharpened fiber protrudes out from the resin film. (iv) Next, by dipping it in a KI

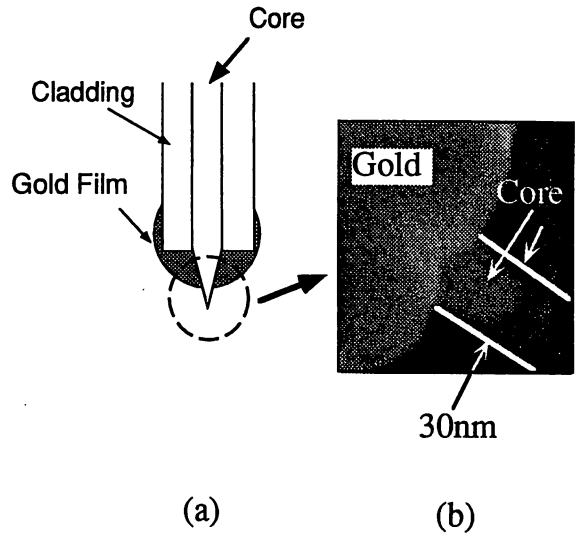

Fig. 1. (a) Schematic of apertured fiber probe. (b) SEM image of probe tip. The diameter at the foot of the protruded fiber is found to be 30 nm.

solution ($KI:I_2:H_2O = 20:1:24000$) to remove the gold film, only gold film protruding out from the resin was removed, because resin film acts as a guard layer for the gold film. Fig. 1b shows a SEM image of the apertured probe. Although the diameter at the foot of the protruded fiber is found to be 30 nm from this figure, its real value should be even smaller because the protruded fiber can be buried in the contamination at the stage of SEM observation. (For this contamination, see Fig. 1 of Ref. [12]). Furthermore, the effective aperture diameter governing the resolution of the PSTM can be even smaller because the high spatial-Fourier frequency components of the evanescent field are preferably scattered at the protruded fiber tip.

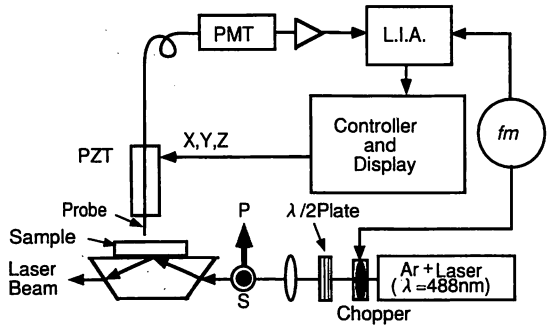

Fig. 2. Experimental system of the c-mode PSTM. A half wavelength plate is used to control the polarization state of the incident light.

Fig. 2 shows the experimental system of the c-mode PSTM. An Ar^+ laser with a wavelength of 488 nm was used as a light source, and a half wavelength plate was installed for adjusting the polarization state of the incident light. A thin glass plate was used as a substrate for the sample and was fixed on a glass prism with index matching oil. The laser beam was made incident into the prism under the condition of total reflection. The evanescent field generated on the sample surface was scattered and picked up by the optical fiber probe. The probe is set on a PZT tube to scan in the *XYZ* direction. A photomultiplier and a lock-in amplifier were used for the phase sensitive detection. A commercial AFM controller (Seiko Instruments Inc.; SPA3700) was used for scanning and image processing.

The probe was scanned under constant-height mode. Rapidly decreasing optical power from the substrate was used to set the initial height of the probe. In order to compensate for the effects of the tilts substrate, we have carefully adjusted the time constant of the servo control loop. The response time of the controller was shorter than 0.1 s, and scanning frequency was 2 Hz for a scanning length of 5 μm. Therefore this feed back control loop does not respond to sample features of size smaller than 1 μm.

Straight-type flagellar filaments of salmonella (FFS) were used as the reference sample for evaluating the performance of the c-mode PSTM. The FFS has been popularly known as a molecular motor [14], and thus, its size and structure have been well calibrated. The FFSs were fixed on a hydrophilized glass plate. Fig. 3 shows an image of FFSs observed by a transmission electron microscope (TEM), from which the diameter of the FFS was measured to be 25 nm.

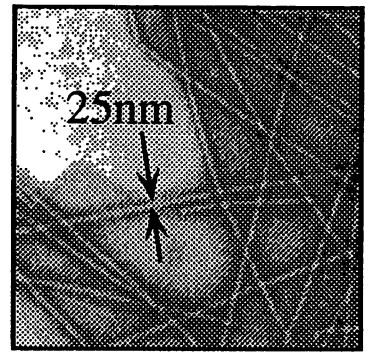

Fig. 3. TEM image of the straight-type flagellar filaments of salmonella (FFS) provided by S.-I. Aizawa. The diameter of each filament was 25 nm, which was confirmed by images taken by a transmission electron microscope.

3. Results and discussion

Fig. 4a is a PSTM image of the FFSs when the incident light was s-polarized, i.e., the electric field vector lies in the substrate surface plane. The fiber probe shown by Fig. 1b was used for this imaging. Scanning area is 5 μm × 5 μm with the corresponding number of pixels being 256 × 256. Therefore the size of one pixel is about 20 nm × 20 nm. For this scan, the sample-probe separation was estimated to be less than 15 nm, and this was estimated in the following way: After finishing this scan, the probe was approached towards the sample by applying a voltage corresponding to a distance of 15 nm to the PZT. At this position, when the scanning process was repeated, we observed streaks in the image due to the probe scratching the sample surface.

Fig. 4a shows that FFSs fixed perpendicular to the direction of the incident beam (see the arrow in the figure) were clearly imaged with high contrast. Fig. 4b shows a cross-sectional profile of the detected signal intensity for the part identified by a white bar in Fig. 4a. This profile was obtained by performing averaging 100 lines along the orientation shown by white line. The bright region corresponds to filament of FFS while the dark region on either sides of the bright region corresponds to "shadow" formed by the short range electromagnetic interaction between the probe tip, the filament and the substrate. The full width at half maximum (FWHM) of the bright region is 50 nm which corresponds to the diameter of FFS. Such a smaller value, suggests for a high resolution capability of the present system. This was used by the fact that the high-spatial Fourier frequency components are selectively picked up by the fiber tip protruding out of the gold film [15]. However, for accurate estimation of resolution, the definition of resolution is required. Furthermore it should be noted that this experimental result is still preliminary because the pixel size is larger than the size of probe tip and is as large as the FFS diameter. Smaller FWHM, i.e., higher resolution, is expected by reducing the pixel size.

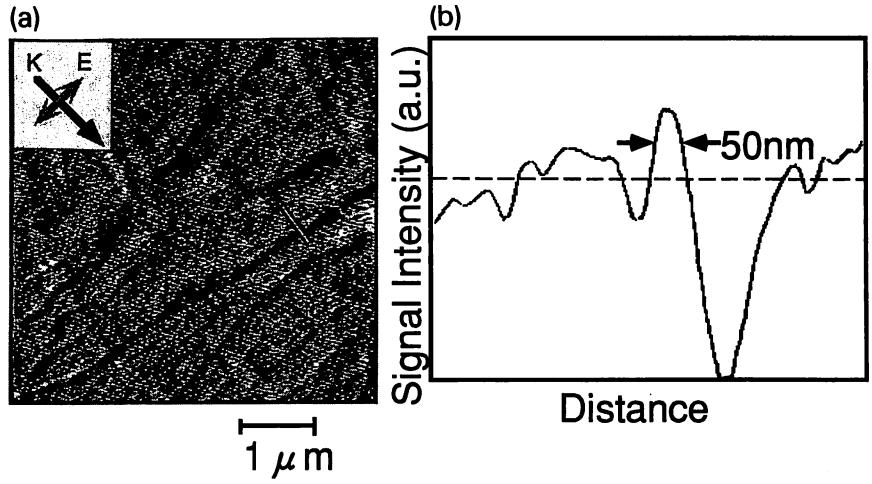

Fig. 4. (a) A PSTM image of the FFSs for the s-polarized incident light. The sample-probe separation was about 15 nm. Black and gray arrows represent the direction of the wave vector k of the incident light and gray arrow indicates the electrical field E respectively. (b) A cross-sectional profile of the detected signal intensity for the part identified by a white bar in (a). This profile was obtained by performing averaging 100 lines, along the orientation shown by the white line. The full width at half maximum (FWHM) of the bright region is 50 nm which corresponds to the diameter of FFS.

Fig. 5 shows an image taken under the same condition as Fig. 4a, except for the sample-probe separation being increased to 65 nm. Almost the same image was obtained, except that the FWHM of the cross-sectional profile of he detected signal intensity of image was increased to about 150 nm. This dependency of the size of the images on the sample-probe separation can be resulting from the confinement characteristics of the evanescent field, i.e., the penetration depth of the evanescent field is of the order of the sample size. In other words, the decay length of higher spatial frequency component of the evanescent field is shorter [15]. Therefore, for efficient pick up, the probe must be brought closer to the sample.

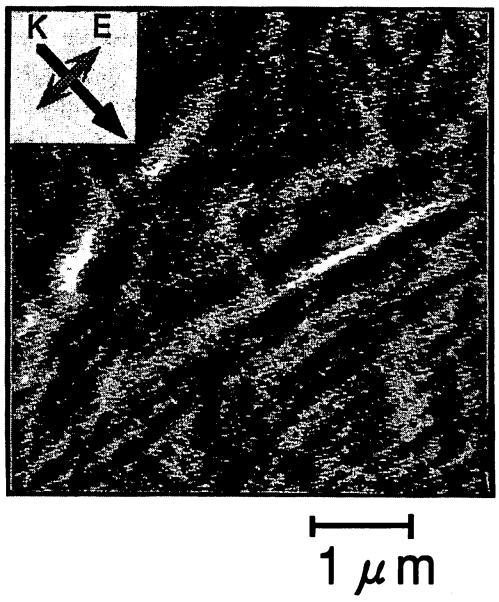

Fig. 5. A PSTM image taken under the same conditions as of Fig. 4a, except for the sample-probe separation being increased to 65 nm.

In order to study the dependence of the pick up efficiency on sample-probe separation more quantitatively, the spatial Fourier spectrum of the images obtained under a separation of 15 nm and 65 nm shown respectively in Figs. 4a and 5 were calculated. For an exact estimation, the whole data, containing many FFSs, were used for the calculation. Results are shown in Fig. 6, and comparing the two curves in this figure, it can be seen that the strength of the high spatial frequency component decreases with increasing sample-probe separation. This supports the theory of confinement of high frequency components in the previous paragraph.

Fig. 7 shows the PSTM image of the same sample obtained by using a probe tip with an aperture diameter as large as 100 nm. The sample-probe separation was fixed to be less than 15 nm. Comparison with Fig. 4a confirms that the image suffers also a kind of defocusing. The origin of this defocusing is straight forward,

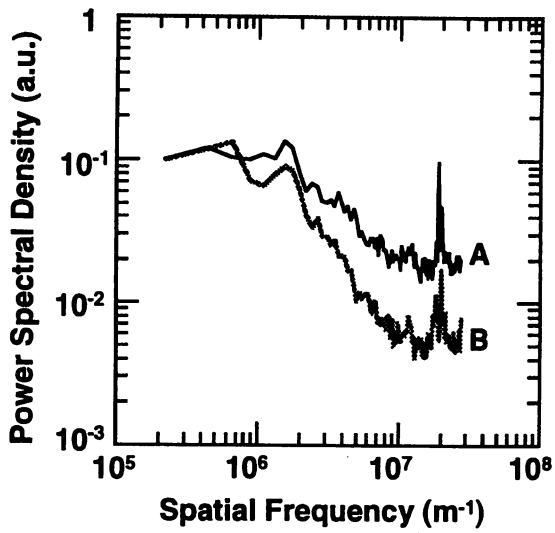

Fig. 6. The spatial Fourier spectrums of PSTM images for sample-probe separations of (A) 15 nm (corresponding to Fig. 4a) and (B) 65 nm (corresponding to Fig. 5).

i.e., the lower spatial frequency components were effectively picked up by the larger aperture [15].

As a next step for evaluating the performances of the c-mode PSTM, the dependency of the image on the vectorial property of the light field was studied. Fig. 4a is taken when the incident light was s-polarized. Fig. 8a shows the PSTM image for exactly the same scanned area as that of Fig. 4a taken when the incident light was p-polarized, i.e., the electric field vector is normal to the substrate surface. This image was apparently different from the image of Fig. 4a. Fig. 8b shows a cross-sectional profile of the detected signal intensity for the part identified by a white bar in Fig. 8a. This profile was obtained by performing averaging 100 lines along the orientation shown by white line. Here, in contrast to that of Fig. 4b the bright areas can be seen on both sides of the sample. This difference can be explained by considering the distributions and directions of the optically induced dipoles on the sample surface and the probe tip, where the evanescent field mediates the short-range electromagnetic interaction between the sample and the probe tip [16]. Figs. 9a and 9b explain the origin of this difference depicting the schematic view of the induced dipoles on the sample surface and probe tip, and the electric lines of force of the evanescent field. In the case of s-polarization, as shown in Fig. 9a, the direction of the dipole, induced on the sample surface are in parallel to the substrate surface plane. Thus, the lobes of electric lines of force of the evanescent field is generated above the sample. Since the dipole induced on the probe tip by this evanescent field lies along the lines of electric force of this lobe, it is in parallel to the substrate surface plane when the probe tip is just above the sample. The wave vector of the scattered propagating light, generated by this dipole, is thus, inparallel to the probe axis, which is most efficiently coupled to the guided mode of the fiber. This coupling efficiency is always lower when the probe tip is deviated from this position. This is the reason for the single intensity peak detected seen in the cross sectional profile as Fig. 4a.

On the other hand, since the direction of the dipole on the sample, induced by the p-polarized light, is perpendicular to the substrate surface, the lobes of the generated evanescent-field are on both sides of the sample. Thus, when the probe tip is just above the sample, the direction of the induced dipole is also perpendicular to the substrate. The wave-vector of the scattered light is, then, perpendicular to the probe axis, which gives the lowest coupling efficiency to the guided mode of the fiber. Therefore, the cross sectional light intensity shows two peaks.

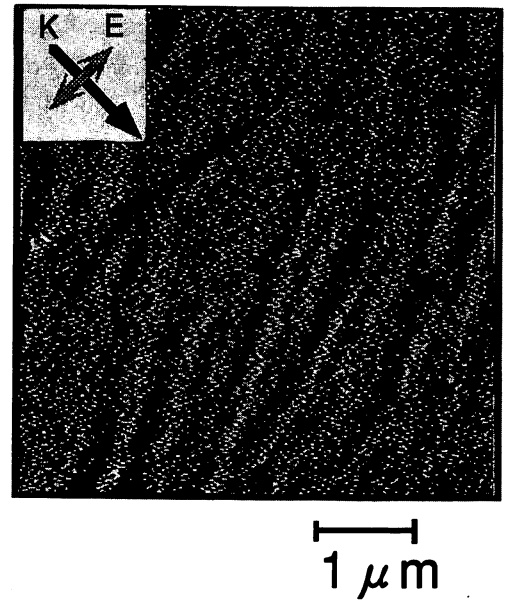

Fig. 7. A PSTM image of the FFS obtained by using a probe tip with an aperture diameter as large as 100 nm. Sample-probe separation is about 15 nm.

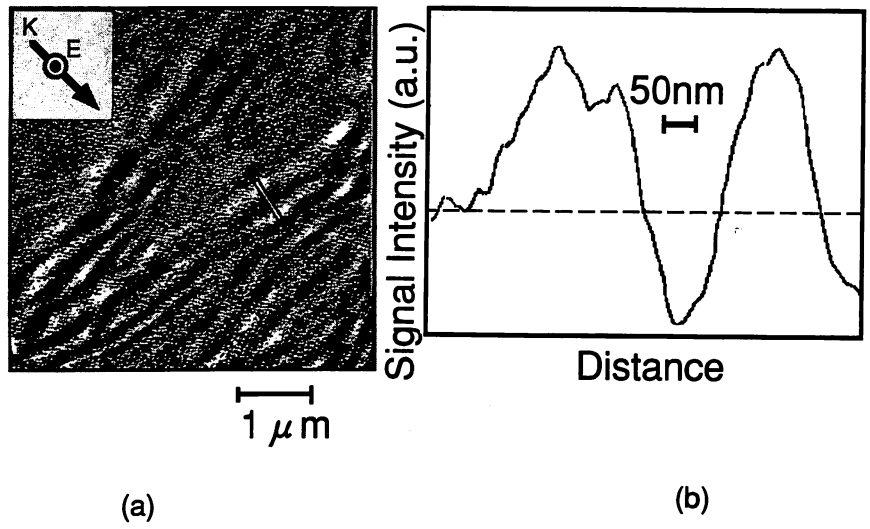

Fig. 8. (a) A PSTM image for exactly the same scan area and the same conditions as that of (a), when the incident light was p-polarized. (b) A cross-sectional profile of the detected signal intensity for the part identified by a white bar in (a). This profile was obtained by performing averaging 100 lines along the orientation shown by white line.

4. Summary

This paper demonstrated the capability of high resolution imaging by a c-mode PSTM with a nano-apertured probe. The system could be operated under all optical mode without any auxiliary control by taking advantage of the exponential dependence of the evanescent field intensity. High resolution imaging of flagellar filament of salmonella of nominal diameter of 25 nm was carried out and the observed image had the FWHM of 50 nm. The dependencies of the image on the sample-probe separation, and diameter of the aperture were studied. It has been confirmed that the probe tip picks up the evanescent field that is confined to the nanometric sample with penetration depth corresponding to the sample size. We also observed the dependency of the image on the polarization state of incident light, and this result was explained in terms of the lirection of the induced dipole in the near-field region.

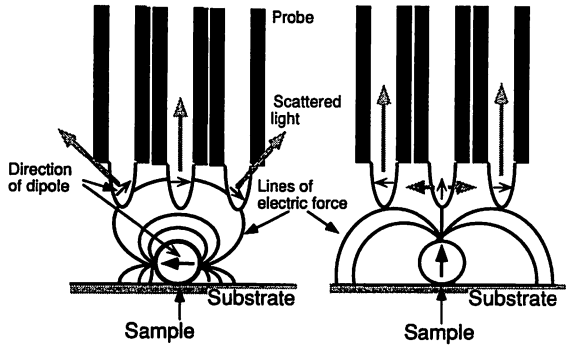

Fig. 9. Illustrations of the directions of the lines of electric force of the evanescent field and the direction of scattered light by dipole of the optical fiber probe. (a) For the s-polarized incident light. (b) For the p-polarized incident light.

Acknowledgements

The authors wish to thank Prof. S. Aizawa at Teikyo Univ. for providing the flagellar filaments of salmonella, and Dr. M. Sano of T.I.T. for providing software to perform the spatial Fourier spectral analysis of the PSTM images.

References

[1] D.W. Pohl and D. Courjon, eds., Near field optics, NATO ASI series E, Vol. 242 (Kluwer, Dordrecht, 1993).
[2] M. Ohtsu, J. Lightwave Tech. 13 (1995) 1200.
[3] D.W. Pohl, W. Denk and M. Lantz, Appl. Phys. Lett. 44 (1984) 651.

[4] E. Betzig and J.K. Trautman, Science 10 (1992) 189.
[5] E. Betzig, J.K. Trautman, J.S. Weiner, T.D. Harris and R. Wolfe, Appl. Optics 22 (1992) 4563.
[6] J.K. Trautman, E. Betzig, J.S. Weiner, D.J. DiGiovanni, T.D. Harris, F. Hellman and E.M. Gyorgy, J. Appl. Phys. 15 (1992) 4659.
[7] D. Courjon, K. Sarayaddine and M. Spajer, Optics Comm. 71 (1989) 23.
[8] S. Jiang, N. Tomita, H. Ohsawa and M. Ohtsu, Jpn. J. Appl. Phys. 30 (1991) 2107.
[9] S. Jiang, H. Ohsawa, K. Yamada, T. Pangari-Buan, M. Ohtsu and K. Imai, Jpn. J. Appl. Phys. 7 (1992) 241.
[10] S. Mononobe, M. Naya, R. Uma Maheswari, T. Saiki, M. Ohtsu, NFO-3, EOS-Topical Meeting, 8 (1995) 105.
[11] T. Pangaribuan, K. Yamada, S. Jiang, H. Ohsawa and M. Ohtsu, Jpn. J. Appl. Phys. 9A (1992) L1302.
[12] T. Pangaribuan, S. Jiang and M. Ohtsu, Electron. Lett. 22 (1993) 1978.
[13] T. Pangaribuan, S. Jiang and M. Ohtsu, Scanning 16 (1994) 362.
[14] S. Kato, H. Okino, S.-I. Aizawa and S. Yamaguchi, J. Mol. Biol. 219 (1991) 471.
[15] H. Hori, Near Field Optics, NATO ASI series E, Vol. 242 (Kluwer, Dordrecht, 1993) p. 105.
[16] B. Labani and C. Girard, J. Opt. Soc. Am. B 6 (1990) 936.

Control of Apex Shape of the Fiber Probe Employed in Photon Scanning Tunneling Microscope by a Multistep Etching Method

R. Uma Maheswari, Shuji Mononobe, and Motoichi Ohtsu, *Senior Member, IEEE*

Abstract— **In this paper, we discuss about the control of the shape of the very apex of a sharpened fiber probe used in photon scanning tunneling microscope (PSTM) by means of a method based on selective chemical etching. Under ambient conditions, through a multistep etching method proposed here, fiber probes with a flattened apex having a diameter of around 15–20 nm could be produced with high reproducibility. It has also been discovered that, during the etching process, the shape of the apex of the probe takes a rounded or a flattened shape with respect to the etching time in an almost cyclic fashion and such a phenomenon could help in understanding the mechanism of the etching process. These kind of probes with flat apex after metal coating are suitable for the fabrication of apertured probes used in PSTM and also for super tips which have a promising future as nanosensors in the fields of biology and biochemistry.**

I. Introduction

PHOTON scanning tunnelling microscope (PSTM) and its different variations generally known as near-field scanning optical microscope (NSOM or SNOM, for e.g., see review by Pohl [1]) are rapidly gaining attention for their unique ability in the study of optical properties of different materials beyond the diffraction limit introduced by the wave length of the light used, for example, in field of spectroscopy and in the study of biological specimens. Further, these kind of microscopes have also been successively employed for investigating optical wave guides used in the field of integrated optics [2]. Such a wide variety of applications is not possible with a more popular and versatile AFM or STM. The heart of such a microscope (for that case any scanning probe microscope) is the nanometric probe which is used either in a collection or illumination mode geometry of PSTM. In the collection mode geometry, the nanometric sample of interest is illuminated under total internal reflection and the evanescent field generated over the sample is collected with a metal coated probe having a nanometric dielectric protrusion with a radius of curvature of around few nanometers [3]–[5]. In the illumination mode geometry, the sample is illuminated by light from a metal coated nanoapertured fiber probe and the scattered field from the sample is collected by an objective lens having a high numerical aperture [5], [6].

In this communication, we discuss about a method of fabricating such fiber probes employed in PSTM studies. By this method, we could fabricate fiber probes with flattened apex. These kind of probes with flattened apex could be used for aperture fabrication and also for fabricating a super tip. Actually, some preliminary results have been obtained on the fabrication of super tips with these fibers [7]. Super tips are gaining importance for their application as a nanosensor in the field of biochemistry and biology [8]. Though there are other methods such as pulling of a fiber by a commercial micro pipette puller [9] while heating it with a CO_2 laser exist for the fabrication of fiber probes with a flattened apex, it is difficult to produce apex with dimensions less than 50 nm reproducibly. The advantage of the present method lies on its reproducibility and also the possibility of controlling the shapes and the cone angle.

The proposed method involves a multistep etching process and is based on the selective chemical etching technique proposed and investigated in detail by Pangaribuan *et al.* [10], [11]. In this method, first, the sharpened fiber probes having a rounded apex were fabricated by means of a two-step etching method [12]. Next, by etching these fibers in an etching solution having a very slow etching speed, it is possible to fabricate a fiber probe with a flattened apex. The diameter of the flattened apex is around 15–20 nm.

Further, we discovered that, during the flattening process, some pseudo-cyclic changes in the morphology of the apex occur out of a complex process which involve etching of a few tens to a few hundreds of atoms at the apex region of the probe.

In Section II, we discuss about the etching method and Section III discusses about the limit cycle characteristics of the etching process and finally, Section IV gives a summary.

II. Fabrication Method of a Probe with Flattened Apex

Here, in order to fabricate sharpened fiber probes, special fibers with pure silica cladding and 27 mol% GeO_2 doped silica core are used. Sharpening of these fiber probes is done through etching in an etching solution containing hydrofluoric acid (50% weight) [HF], ammonium fluoride (40% weight) [NH_4F] and deionized water [H_2O]. Here ammonium fluoride acts as a buffer in controlling the etching rate. For convenience,

Manuscript received March 1, 1995; revised September 15, 1995.

R. U. Maheswari and S. Mononobe are with the Kanagawa Academy of Science and Technology, Kanagawa 213, Japan.

M. Ohtsu is with the Kanagawa Academy of Science and Technology, Kanagawa 213, Japan. He is also with the Interdisciplinary Graduate School of Science and Engineering, Tokyo Institute of Technology, Yokohama 226, Japan.

IEEE Log Number 9415873.

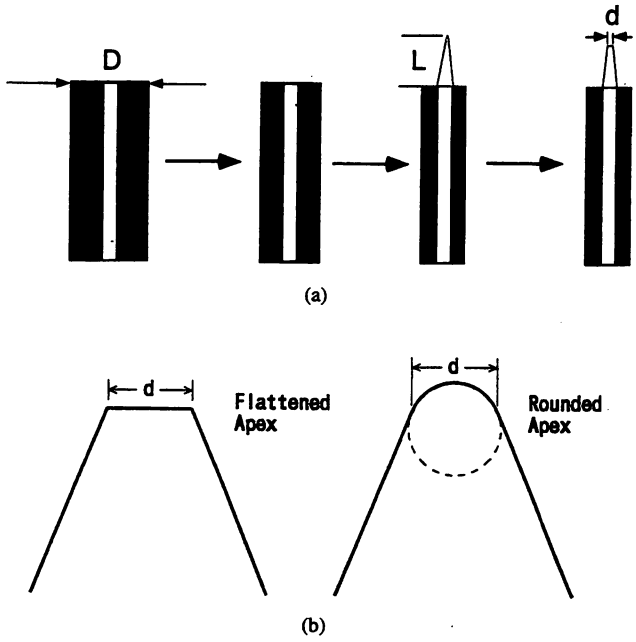

Fig. 1. (a) A schematic illustration of the etching procedure consisting of three steps. In step (A) fiber is etched in a solution of composition ratio 1.7:1:1 for 90 min to reduce the diameter of the cladding. In next step (B) the core is sharpened to form a tip with rounded apex by etching in a solution of composition 10:1:1 for 120 min. Finally in step (C) the sharpened fiber is etched in a solution of composition 10:1:120 for 120 s to obtain a flattened apex tip. (b) A schematic illustrating the terms apex shape and apex diameter (d) of the sharpened fiber probe. Here the left side shows a flattened shape apex and right side shows a rounded apex. For the case of rounded apex, the apex diameter is defined as the distance between the intersection points of the tangents drawn along the slope of the sharpened core to the completed circle (indicated by dotted line) of the rounded apex.

from now onwards, we denote the volume ratio of etching solution as $X : 1 : 1$ which corresponds to the order of NH_4F, HF, and H_2O, respectively.

A schematic of the multistep etching process for fabricating a fiber probe with flattened apex is shown in Fig. 1(a). Here, steps (A) and (B) correspond to the fabrication of a sharpened fiber with rounded apex by means of a two-step etching method proposed by Pangaribuan [12]. By this two step etching method it is possible, not only to control the sharpening of the core but also the dimensions of the cladding. For a detailed discussion, refer to [12]. We define the terms flattened and rounded apex shapes and apex diameter (d) in Fig. 1(b) to get a better understanding of the following discussion.

As shown in Fig. 1(a), in the first step (A), the fiber is etched in an etching solution of composition ratio 1.7:1:1 for a duration of around 90 min. to reduce the cladding diameter (D) finally to approximately 20 μm. The tip length corresponding to the sharpened core (L) has got a length of 10 μm. So, by reducing the cladding radius ($D/2$) to be less than or equal to L, it is possible, to some extent to coat metal in a vacuum evaporation unit only the on sides and on the clad face leaving an aperture at the top. This is due to the fact that no shadow of the cladding is formed on the sharpened core part while performing metal coating at an inclination of around 25 or 30° with respect to the evaporation source in a vacuum evaporation unit. In the next step, these fibers are etched in a solution of composition ratio 10:1:1 for around 120 min to get a sharpened

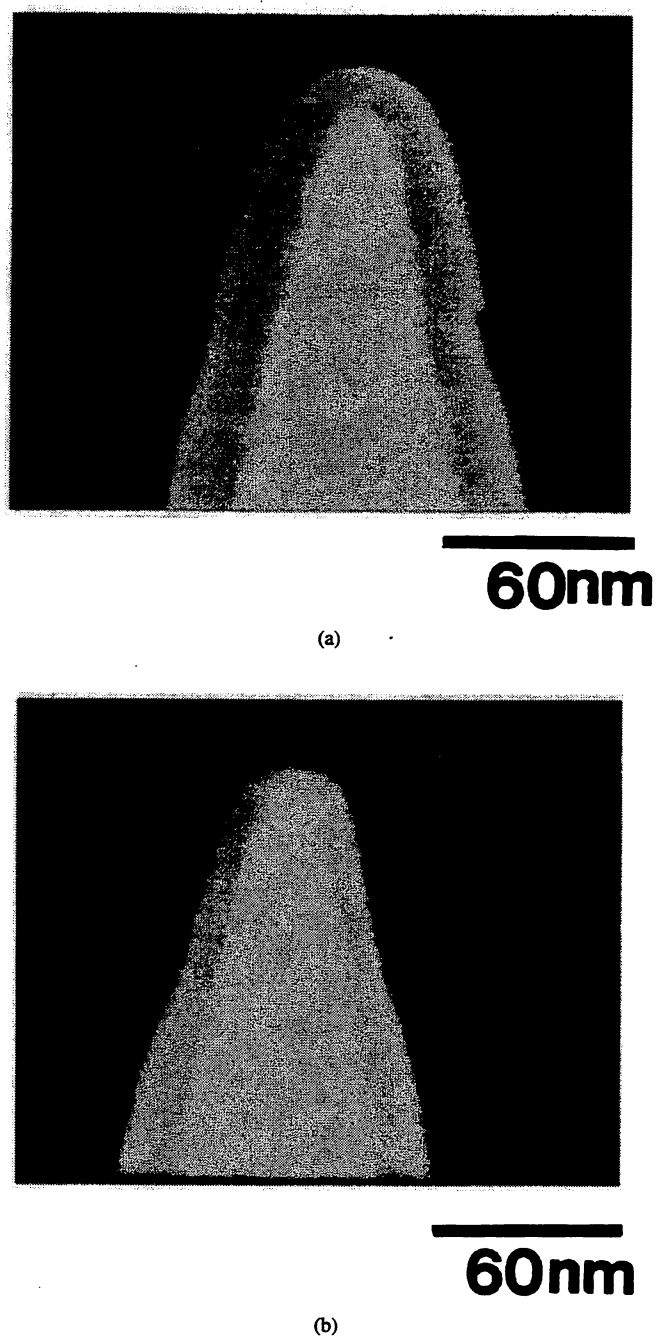

Fig. 2. Etching results due to (a) step B and (b) step C. The rounded apex is flattened due to etching in a solution of composition 10:1:120 for 120 s at 22.5°C. The aura or envelope covering the probe is due to the effect of contamination while conducting SEM observations. In all observations, the sharpened glass fiber probes had been initially coated with a Platinum/Palladium film of thickness 10 nm.

core with rounded apex as shown in Fig. 2(a). For this case, the apex diameter d is less than 10 nm and the cone angle is around 20°. The cone angle can be controlled by a proper choice of the concentration of the ammonium fluoride.

Now, in order to make a fiber probe with a flattened apex, this fiber is further etched in an etching solution of composition of 10:1:120 corresponding to step (C) of Fig. 1. The result of the final step is shown in Fig. 2(b). From the figure, it can be seen that the shape of the apex of the fiber probe is

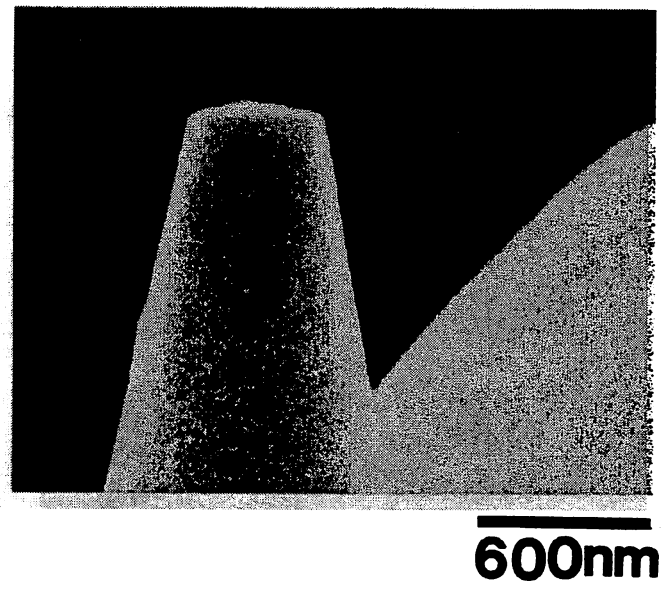

(a)

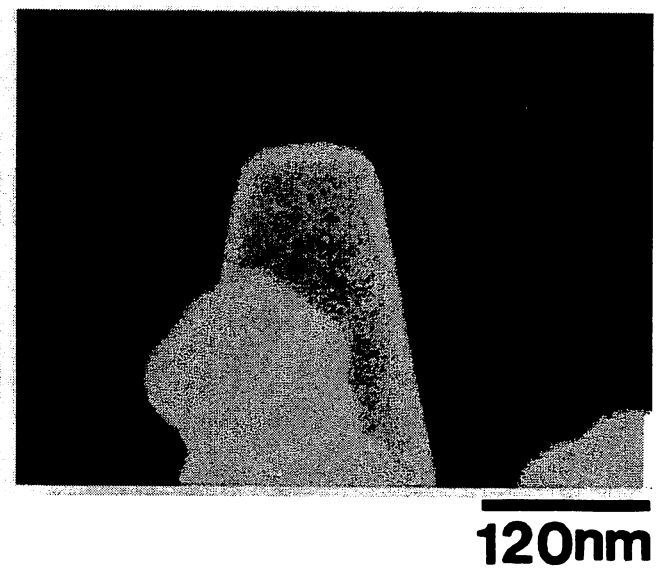

(b)

Fig. 3. Results of flattened apex due to step B for an etching duration of (a) 60 min and (b) 90 min.

changed from a rounded form to a flattened shape. The apex diameter d is approximately around 20 nm. Hence, by accurate control of the etching time and other environment such as temperature, the flat shape of the apex of the sharpened core could be obtained with quite high reproducibility. It should be mentioned here that in the process of this multistep etching, it is of course possible in some extent to fabricate an apex with flattened shape as shown in Fig. 3 during the second step by controlling the etching time. However, the diameter of the flattened apex d is around 100 nm and it becomes very difficult, almost impossible to fabricate apex with diameters of around 50 nm or less than that. All the etchings were performed at a temperature of 22.5 ± 0.5°C.

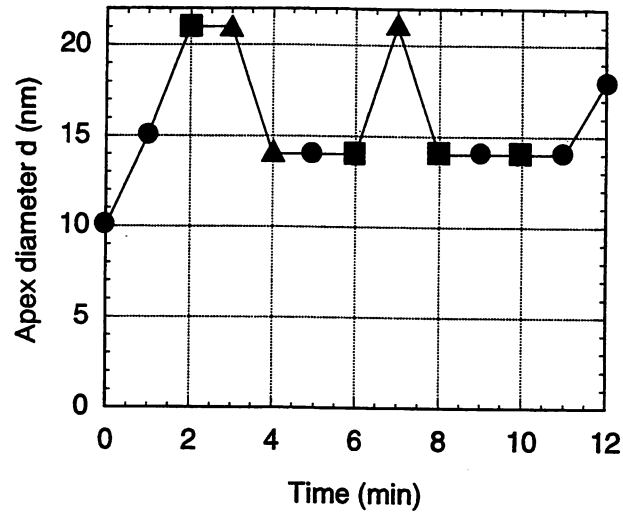

Fig. 4. Variation of the apex shape and the apex diameter d of the sharpened core as a function of the etching duration of the third step. Here, the dark circle indicates a rounded apex, dark square corresponds to a flattened apex and a dark triangle indicates an intermediary shape.

We discovered accidentally that these changes of the shape of the apex of the fiber probe from a rounded to a flattened form during the third stage of the etching process rather repeats itself in an almost cyclic fashion with respect to etching time. In the next section we discuss about this phenomenon.

III. Limit Cycle Morphological Variation of Apex of Probe

Fig. 4 shows the variation in the shapes of the apex as a function of etching duration with the vertical axis being the apex diameter d (nm) of the final step (C) discussed in Section II. Here, the dark circle corresponds to an apex with a rounded shape and the dark square corresponds to that of a flattened shape. Further, in this figure the dark triangle mark corresponds to an intermediary shape where it is difficult to discriminate the rounded and flattened shapes of the apex. The shape corresponding to each data point in this figure is actually the average shape obtained from at least three measurements or in other words result of at least three etching results. It should be reminded that all these evaluations were done with scanning electron microscope (SEM) and prolonged observations with SEM will certainly damage the shapes heavily. So, in order to avoid that, these observations were done as fast as possible before the effects due to the electron beam bombardment and heat effects start up. As can be seen from the figure, the rounded apex at the zeroth time of the etching changes to a flattened apex at every two minutes approximately. Though, there are a little variations in the period of the limit cycle of repeatable shapes, there is almost a certain periodicity occurring almost at every two minutes. This kind of pseudo periodic changes in the shape with respect to etching time is fairly reproducible and we believe this kind of cyclic variation in the morphology of the apex will throw some light in understanding the mechanism of the etching process.

As in Fig. 4, the diameter of the flattened apex is always greater than that of the rounded apex at the zeroth time of

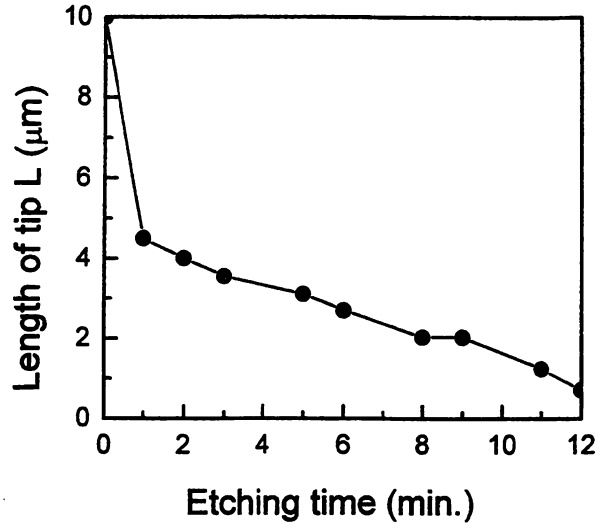

Fig. 5. Variation of the length of the sharpened core L as a function of the etching time in the third step C.

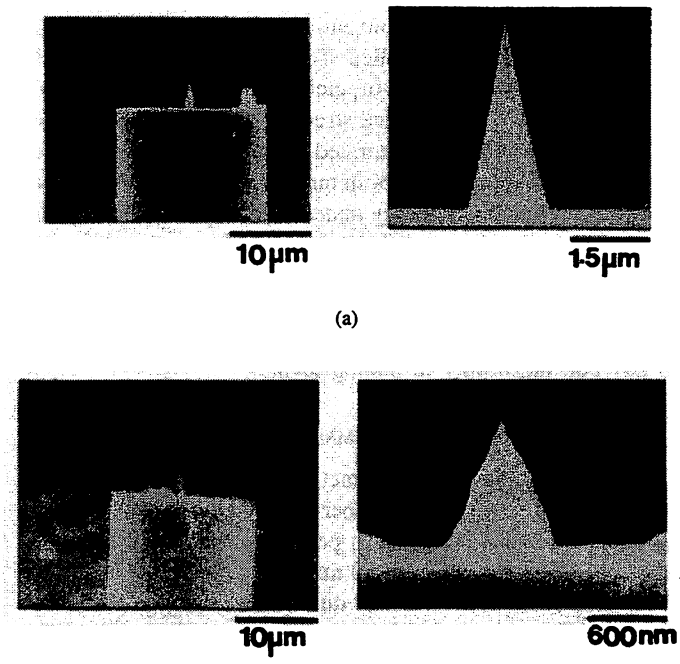

Fig. 6. Changes in the structure of the sharpened fiber probe for a third step etching time of (a) 1 min and (b) 11 min. Here, the micrographs on the right side show magnified views of the sharpened core region of the corresponding ones shown on the left side.

etching. This can be expected as the etching process involves only the dissolution of the core with negligible changes in the cladding. Moreover, the average diameter of the flattened apex is around 15–20 nm and the largest diameter obtained is around 30 nm when the etching time is as long as around 10 min.

In general, when the fiber is introduced into an etching solution [13], a meniscus is formed at the interface and the height of the meniscus from the interface is influenced by the radius of the fiber, wettability of the glass and the viscosity of the etching solution. The etching proceeds along the meniscus isotropically. In other words, etching process takes place at the same rate in all the directions around the axis of the cylindrical fiber. In Fig. 5, the effect of deshortening of the sharpened core due to this isotropic etching is shown. Here, the variation of the length of the sharpened core (L) is plotted as a function of the third-step etching time. As seen from the figure, the length of the sharpened core L becomes small drastically with respect to the initial etching and decreases slowly as the process of etching proceeds. After a period of around 20 min, there is absolutely no evidence remaining to account for the previous existence of such a sharpened core. This corresponds to an average etching rate of 8.3 nm/s.

Actually, from the studies based on etching of oxide doped silica by A. S. Tenney *et al.* [14], in the etching process of the core containing GeO_2 doped SiO_2, Si-O-Ge and Ge-O-Ge bonds are formed and they have to be broken in order to dissolve the material. For the case of etching of such doped silica in buffered HF solution, the etching process can be simply seen as a combination of breaking of Si-O-Si and Ge-O-Si bonds by F^- and HF_2^- species of buffered HF and that of Ge-O-Ge by water. When the doping ratio of GeO_2 is high as in our case, the Ge-O-Ge bonds become abundant and they are easily attacked by water. Therefore, when the etching solution is dilute with high values of pH, the etching rate of the core becomes higher with gradual decrease in length of the sharpened core as in Fig. 5.

Even though the length of the sharpened core decreases monotonously as expected, the structure of the sharpened core shows some strange behavior discussed earlier. Fig. 6(a) and (b) show the sharpened cores when the third step etching durations were 1 min and 11 min, respectively. As seen from Fig. 6(b), the sharpened core has got two structures in contrast to the sharpened core shown in Fig. 6(a). The upper part of the sharpened core is an acute angled cone while the bottom part or the lower part is oblique shaped. The presence of the two different structures in the third-step etched sharpened core part of the fiber probe puts some doubts about the existing explanation for the etching process. If the etching proceeds only in an isotropic fashion with the rate being same in all the directions [15]–[17], then, the presence of this double structure could not be explained. In the actual case, this shows some evidence for the existence of anisotropic dissolution proceeding in the vertical direction as well during the etching process.

Now, in order to explain the changes in the morphology at the apex, the etching process has to be considered as a discrete process with the dissolution taking place in the form of dissolution of particulates or clusters. One possible explanation for the existence of such discrete nature is that, some structural changes are necessary in order to remain in an equilibrium state with minimum free energy. However, more detailed investigations are required to understand why this kind of changes in the shape of the apex should follow some regularity or in other words happen in a pseudocyclic fashion.

Further, at the apex part of the sharpened core, the dimensions involved are a few to a few tens of nanometers and this means it involves a few tens to a few hundreds of atoms. Under the case of such nano scale structures of mesoscopic

nature, it seems that the conventional etching theories [17], [18] could no longer be applied. The existing etching theories to explain the mechanism of etching of SiO_2 by buffered HF are meant for planar silica structures usually employed in fabrication of large scale integrated devices and they are suited for dimensions much larger or in macroscopic scales. This kind of changes in the morphology under nanoscopic scale suggests for the presence of some order existing in the macroscopically amorphous glass material [19]. As this kind of phenomenon is reproducible for a slightly different doping level of 25 mol% of GeO_2 in the core, the limit cycle characteristics is not due to any non uniformity in doping levels.

IV. Summary

In this study, we proposed a method based on chemical etching technique for fabricating fiber probes with flattened apex. By means of this method, it is possible to fabricate flattened apex of diameter around 15–20 nm with good reproducibility. It has also been discovered that during the etching process, the shapes of the apex change from a rounded to a flattened one in a pseudocyclic fashion with respect to the duration of etching. Though the reasons for the existence of such phenomenon is not known, we believe this kind of phenomenon is very special to the case of etching involving a few tens to hundreds of atoms or molecules at the apex region of the sharpened fiber. Presence of this kind of phenomenon suggests for the existence of some order in the material which is of amorphous nature in the macroscopic scale.

Finally, it is worth to mention that with the fiber probes fabricated by the proposed technique to have a flattened apex were coated with metal film in order to fabricate nanoapertured probes. The fabricated apertures have got a diameter of less than 30 nm. With these apertures, high contrast and high resolution images of subcellular structures such as microtubulins present inside the axon of neurons from the brain of a Wistar rat could be obtained by the illumination mode PSTM. The observed microtubulins had an average diameter of 26 nm which agrees well with the value estimated by an electron microscope and this kind of very high resolution is believed to be due to the presence of edges at the boundary of the glass and the metal coating of the fiber probe. The details of these results are reported elsewhere [20].

References

[1] D. W. Pohl, *Nano-Optics and Scanning Near-Field Optical Microscopy*, R. Wiesendanger and H. J. Guntherodt, Eds. Berlin, Germany: Springer-Verlag, 1992, vol. II, pp. 233–271.

[2] N. Toda and M. Ohtsu, "High spatial resolution diagnostics of optical wave guide using a Photon Scanning Tunneling Microscope," *Photon. Technol. Lett.*, Jan. 1995.

[3] S. Jiang, H. Ohsawa, K. Yamada, T. Pangaribuan, M. Ohtsu, K. Imai, and K. Ikai, "Nanometric scale bio-sample observation using a Photon Scanning Tunneling Microscope," *Japan. J. Appl. Phys.*, vol. 31, pp. 241–246, 1992.

[4] S. Jiang, N. Tomita, H. Ohsawa, and M. Ohtsu, "A Photon Scanning Tunneling Microscope using an AlGaAs laser," *Japan. J. Appl. Phys.*, vol. 30, pp. 2107–2111, 1991.

[5] R. Uma Maheswari, S. Mononobe, M. Naya, T. Saiki, and M. Ohtsu, "Fabrication of a fiber probe with nano aperture for Photon Scanning Tunneling Microscope," in *OSA Annu. Meeting Digest*, 1994, p. 179.

[6] E. Betzig and J. K. Trautman, "Near-field optics: Microscopy, spectroscopy and surface modification beyond the diffraction limit," *Science*, vol. 257, pp. 189–195, 1992.

[7] K. Kurihara, Private communication.

[8] W. Tan, Z. Shi, and R. Kopelman, "Development of submicron chemical fiber optic sensors," *Anal. Chem.*, vol. 64, pp. 2985–2990, 1992.

[9] E. Betzig, A. Lewis, A. Harootunian, M. Issacson, and E. Kratschmer, "Near-field scanning optical microscopy," *Biophys. J.*, vol. 47, pp. 269–279, 1986.

[10] T. Pangaribuan, K. Yamada, S. Jiang, H. Ohsawa, and M. Ohtsu, "Reproducible fabrication technique of nanometric tip diameter fiber probe for Photon Scanning Tunneling Microscope," *Japan. J. Appl. Phys.*, vol. 31, pp. L 1302–1304, 1992.

[11] T. Pangaribuan, S. Jiang, and M. Ohtsu, "High controllable fabrication of fiber probe for photon scanning tunneling microscope," *Scanning*, vol. 16, pp. 362–367, 1994.

[12] T. Pangaribuan and M. Ohtsu, "Two-step etching method for fabrication of fiber probe for Photon Scanning Tunneling Microscope," *Electron Lett.*, vol. 29, pp. 1978–1979, 1993.

[13] K. M. Takahashi, "Meniscus shapes on small diameter fibers," *J. Colloid and Interface Sci.*, vol. 134, pp. 181–187, 1990.

[14] A. S. Tenney and M. Ghezzo, "Etch rates of doped oxides in solutions of buffered HF," *J. Electrochem. Soc.*, vol. 120, pp. 1091–1095, 1973.

[15] J. S. Judge, "A study of the dissolution of SiO_2 in acidic fluoride solutions," *J. Electrochem. Soc.*, vol. 118, pp. 1172–1775, 1971.

[16] G. A. C. M. Spiering, "Wet chemical etching of silicate glasses in hydrofluoric acid based solutions," *J. Mat. Sci.*, vol. 28, pp. 6261–6273, 1993.

[17] H. Kikuyama, M. Waki, M. Miyashita, T. Yabune, N. Miki, J. Takano, and T. Ohmi, "A study of the dissociation state and the SiO_2 etching reaction for HF solutions of extremely low concentration," *J. Electrochem. Soc.*, vol. 141, pp. 366–374, 1994.

[18] S. Verhaverbeke, I. Teerlinck, C. Vinckier, G. Steven, R. Cartuyvels, and H. M. Heyns, "The etching mechanisms of SiO_2 in hydrofluoric acid," *J. Electrochem. Soc.*, vol. 141, pp. 2852–2857, 1994.

[19] S. Iijima and T. Ichihashi, "Structural instability of ultrafine particles of metals," *Phys. Rev. Lett.*, vol. 56, pp. 616–619, 1986.

[20] R. Uma Maheswari, H. Tatsumi, Y. Katayama, and M. Ohtsu, "Observation of subcellular nanostructure of single neurons with an illumination mode photon scanning tunneling microscope," *Opt. Commun.*, vol. 20, pp. 325–334, 1995.

R. Uma Maheswari was born in Tamil Nadu, India, on April 30, 1963. She received the M.S. degree in physics from the American College, Madurai, India, and the M.Tech. degree in applied optics from the Indian Institute of Technology, Delhi, India, and the Ph.D. degree from Hokkaido University, Japan in 1985, 1987, and 1991, respectively.

From 1987 to 1988, she was a visiting research student at Hokkaido University. From 1992 to 1993, she worked as a visiting researcher at Joensuu University, Finland. Since April 1993, she has been working as a researcher at Kanagawa Academy of Science and Technology, Kawasaki, Japan. Her current research interests are photon scanning tunnelling microscopy and its applications to the biological field.

Dr. R. Uma Maheswari is a member of the Japan Society of Applied Physics, the Optical Society of India, and the Optical Society of America.

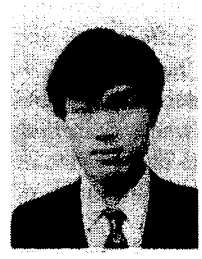

Shuji Mononobe was born in Osaka, Japan, in 1967. He received the B.S., M.S. degrees from the University of Osaka Perfecture, Sakai, Japan, in 1991 and 1993, respectively.

Since April 1993, he has been with Kanagawa Academy of Science and Technology, Kawasaki, Japan, as a researcher. His current research interests are fiber probes for photon scanning tunnelling microscopy.

Mr. Mononobe is a member of the Japan Society of Applied Physics.

Motoichi Ohtsu (M'88–SM'90) was born in Kanagawa, Japan, on October 5, 1950. He received the B.E., M.E. and D.E. degrees in electronics engineering from the Tokyo Institute of Technology, Tokyo, Japan, in 1973, 1975, and 1978, respectively.

In 1978, he was appointed as a research associate and in 1982, he became associate professor at the Tokyo Institute of Technology. From 1986 to 1987, while on leave from Tokyo Institute of Technology, he joined AT&T Bell Laboratories, Holmdel, NJ. In 1991, he became a professor at the Tokyo Institute of Technology. Since April 1993, he has been the leader of the "PHOTON CONTROL" project at the Kanagawa Academy of Science and Technology, Kanagawa, Japan. His main fields of interest are photon scanning tunnelling microscopy and its applications to nanoscale photonics and quantum optics, and laser frequency control. He has written over 130 papers and has received a number of patents. He is the author and co-author of 13 books including "Highly Coherent Semiconductor Lasers" (Artech House, Boston, MA: 1992), and "Coherent Quantum Optics and Technology" (Dordrecht, The Netherlands: Kulwer–Academic, 1993). He has been a tutorial lecturer of the SPIE and the OSA.

Dr. Ohtsu is a member of the Institute of Electronics, Information and Communications Engineering of Japan, the Institute of Electrical Engineering of Japan, the Japan Society of Applied Physics, and the Optical Society of America. He has been awarded eight prizes from academic institutions including Issac Koga Gold medal of URSI in 1984, Japan IBM Science Award in 1988, and two awards of the Japan Society of Applied Physics in 1982 and 1990.

Reprinted from LANGMUIR, 1995, 11.

A Simple Method for the Production of a Two-Dimensional, Ordered Array of Small Latex Particles

R. Micheletto,* H. Fukuda, and M. Ohtsu†

Ohtsu "photon control" project, Kanagawa Academy of Science and Technology, KSP East Room 408, 3-2-1 Sakado, Takatsu, Kawasaki City, Kanagawa 213, Japan

Received November 18, 1994. In Final Form: May 25, 1995®

We present here a simple technique for depositing wide monolayers of submicron-sized latex particles. The method is straightforward and does not require any special apparatus. We also studied the quality of the arrays formed, giving information on either the large scale structure or the small scale one. With this technique we succeeded to deposit arrays of 42 nm sized latex spheres, as far as we know, the smallest regular monolayer array ever deposited.

Introduction

In order to perform some experiments to study high-density optical storage media, beyond the optical diffraction limit, by a near field optical method,[1,2] we needed a regular two-dimensional array of submicron-sized latex spheres on which a photochromic Langmuir–Blodgett film could be deposited for use as the optical storage medium. This array works to concentrate the evanescent light from the subwavelength aperture within the area equivalent to the sphere diameter. The deposition of such an array became increasingly difficult as the diameter of the particle decreased. Strong Brownian motion and capillary forces create a state of disorder in the system that is difficult to control.[3] Several authors have developed techniques to create such colloidal crystals, but, as far as we know, they did not involve particles smaller than 55 nm and they used special devices to deposit the film.[3–9]

We consider our method a simple and efficient derivation from the various techniques described in refs 3–9. The main differences with respect to other proposed techniques are due to the fact that with our method it is possible to use simple commercial untreated spheres; we do not need salt or surfactant in solution, nor do we need to electrically charge the particles, also, there is no confinement between any boundaries nor surface pressure controls. The introduction of a fine thermal control together with execution of the evaporation in a small volume and under a determined water to particle concentration allow the formation of our monolayers. We obtained rather large crystalline arrays even of very small particles, down to 42 nm diameter, as far as we know the smallest to be deposited in a regular monolayer array.

With the optical technique introduced above, the size of the data bit coincide with the area occupied by one particle. With a 42 nm size, it would be possible to reach the extremely high data density of approximately 200 Gbit per square inch, which is 2 orders of magnitude greater than magneto-optical compact disk medium.

We will give a detailed explanation of the method used and we will show the results and a preliminary analysis of the structure of the films, made by SEM and AFM. We will evaluate quantitatively the quality of the array formed by means of Fourier analysis.

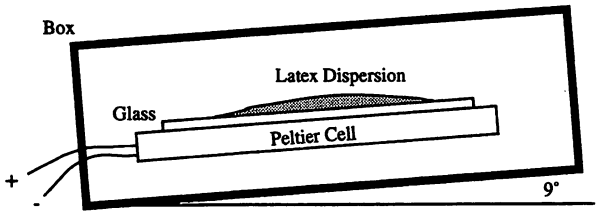

Figure 1. Schematic drawing of the evaporation system.

Experimental Procedure

As is well-known, the production of a latex particle monolayer film is usually realized by the evaporation of a solution on a substrate.[3,4,7,8] We believe that the quality of the results depends strongly on the properties of the substrate as well as on how homogeneous the process of evaporation is. Thus we focused our efforts on obtaining an efficient treatment to clean the substrate and, at the same time, we controlled the temperature and the humidity of the system by means of common tools. We use slide glasses (Matsunami, 18 × 18, thickness 0.15 mm) as substrates. We treated the glasses with pure sulfuric acid for 24 h, to obtain a clean and hydrophilic surface. The glasses were then preserved in ethanol until used.

Polystyrene latex beads (JSR, Stadex/Dynospheres, catalog SC-004-R), with a diameter of 42 nm were used. These particles did not have any surface treatment, were monodisperse (CV = 12.8%), and were originally dispersed in pure water at 1.0 wt %. A droplet of this mixture, with an opportune ratio of water/particles, was deposited on a glass surface. The proper water/particles ratio was calculated depending on the deposition area and on the size of the spheres (refer to the Appendix for details of the easy calculations). We found that the quality of deposition did not depend strongly on the concentration. As the matter of fact, we noticed that if the concentration is 1 or even 2 orders of magnitude higher than the theoretical value, the results were still sufficiently good.

The thin glasses used as substrate were fixed on a Peltier cell (Netsu Denshi, PW-124) for a good thermal stability (0.1 °C). We noticed that the value of the temperature is not as important for the quality of the film as its precise stability. For all the samples presented here, the temperature control of the Peltier cell was set to room temperature (22 °C, known with ±1 °C precision). The whole system was enclosed in a small plastic box (around 300 cm³). We believe that the small volume helps to slow down the evaporation process, which takes approximately 2 h to take

† Also with Tokyo Institute of Technology, 4259, Nagatsuta-cho, Midori-ku, Yokohama 227, Japan.

® Abstract published in *Advance ACS Abstracts,* August 15, 1995.

(1) Betzig, E.; Trautman, J. K.; Wolfe, R.; Gyorgy, E. M.; Finn, P. L.; Kryder, M. H.; Chang, C. H. *Appl. Phys. Lett.* **1992**, *61* (2), 142.

(2) Jiang, S.; Ichihashi, J.; Monobe, H.; Fujihira, M.; Ohtsu, M. *Optics Commun.* **1994**, *106*, 173.

(3) Denkov, N. D.; Velev, O. D.; Kralchevsky, P. A.; Ivanov, I. B.; Yoshimura, H.; Nagayama, K. *Langmuir* **1992**, *8*, 3183.

(4) Kralchevsky, P. A.; Nagayama, K. *Langmuir* **1994**, *10*, 23.

(5) Pieranski, P.; Strzelecki, L.; Pansu, B. *Phys. Rev. Lett.* **1983**, *50*, 900.

(6) Murray, C. A.; Van Winkle, D. H. *Phys. Rev. Lett.* **1987**, *58*, 1200.

(7) Dimitrov, A. S.; Dushkin, C. D.; Yoshimura, H.; Nagayama, K. *Langmuir* **1994**, *10*, 432.

(8) Van Winkle, D. H.; Murray, C. A. *Phys. Rev. A* **1987**, *34*, 562.

(9) Dushkin, C. D.; Nagayama, K.; Miwa, T.; Kralchevsky, P. A. *Langmuir* **1993**, *9*, 3695.

0743-7463/95/2411-3333$09.00/0

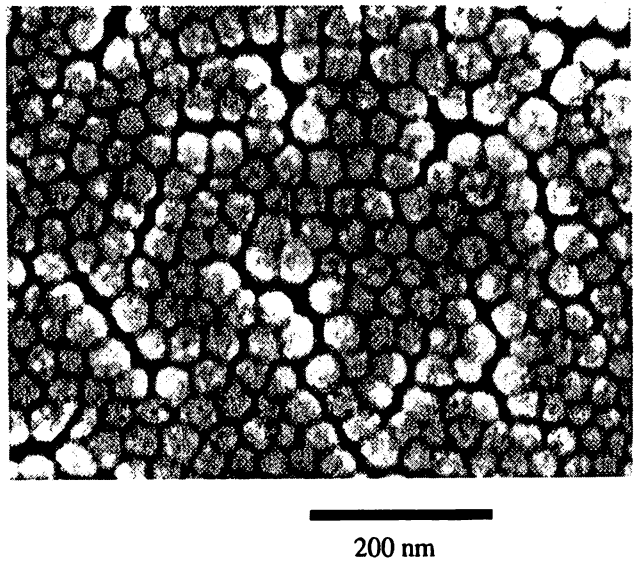

Figure 2. A sequence of SEM images of a latex particle array monolayer deposited with the method described. The picture is taken in the same position at different magnification scales. The particles are JSR Stadex/Dynospheres, catalog SC-004-R, 42 nm in diameter.

place completely. The box also protects the surface from the external air flow, which can disturb it. The whole system was tilted about 9°. In this way the evaporation starts from the top

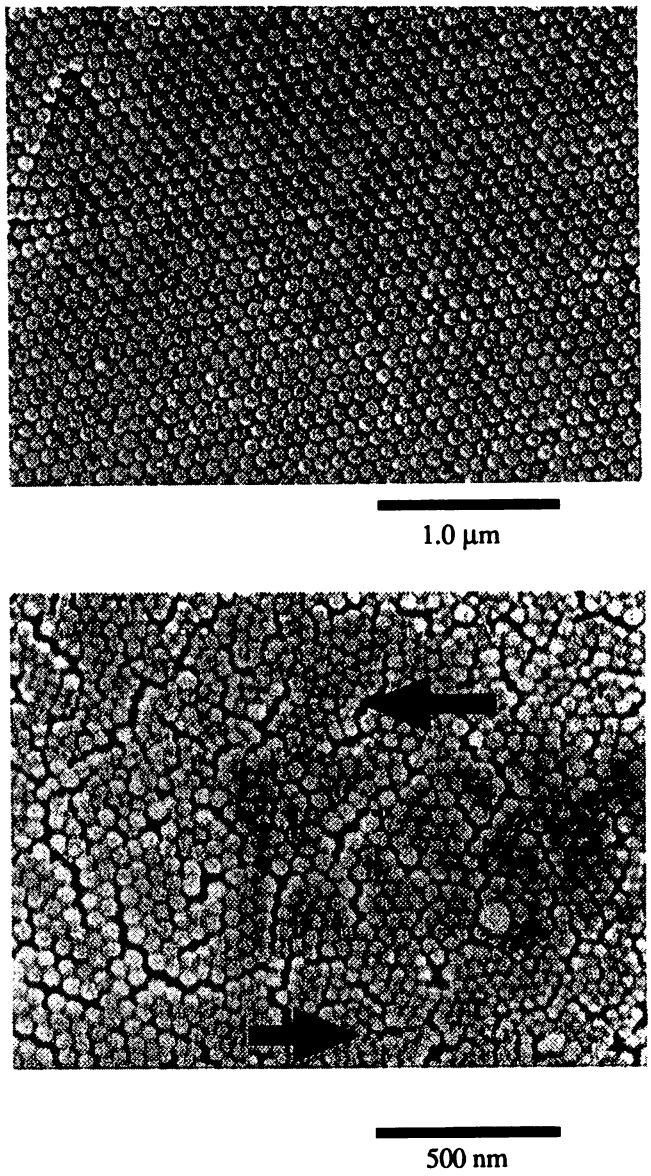

Figure 3. A regular structure of 100 nm CV = 2.6% latex spheres (a, top) compared with CV = 13% spheres (b, bottom). We can see rather irregular regions where not all the spheres have the same radius (top left and bottom right of b).

of the sample on a horizontal border where evaporation takes place. This border moves then to the bottom of the sample until it is completely dry. The speed of evaporation and the quality of the resulting sample depends on this angle; 9° was used on all samples presented here. Refer to Figure 1 for a schematic view of the setup.

Our depositions covered an area of about 1 cm^2, but in any sample only around half of the area was covered by monolayers. The other half is the one where the evaporation take place at last, at the bottom of the sample. We believe that in such regions the remaining of water concentrates impurities and the excess particles, creating multilayers and clusters.

To analyze the resulted deposition we used an atomic force microscope (SII, SPI-3700) and a scanning electron microscope (Hitachi, S-4500). All the samples were sputtered with a thin layer of gold (around 10 nm thickness) with a Hitachi E-1030 ion sputter machine.

Results and Evaluations

We show in Figure 2a–c a sequence of SEM images taken in the same location but at different magnification scales. The array looks sufficiently regular, for our purposes, in the first image at low scale.

The irregular features in these films are essentially due to the size dispersion. Comparing, for example, parts a and b of Figure 3 provides clues. The first represents

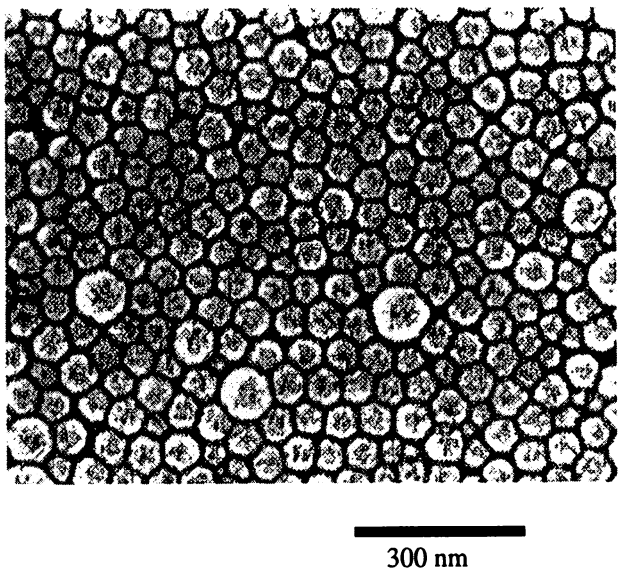

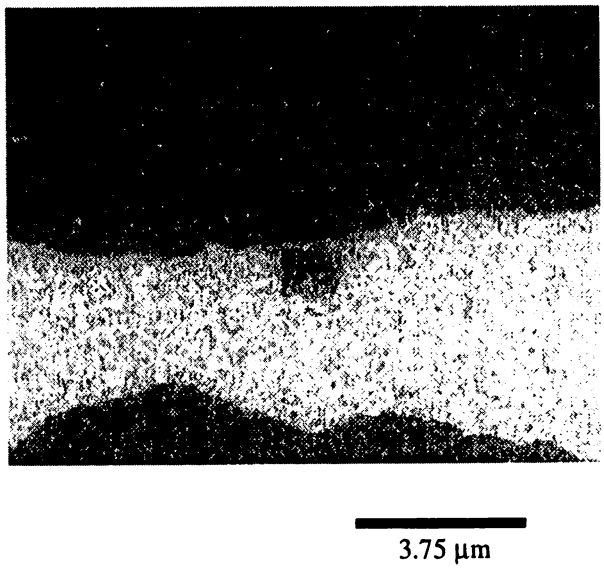

Figure 4. Two SEM image of a monolayer of 56 nm Polyscience carboxylate latex spheres, catalog 16661. In the short scale (a, top) we do not observe shrinkage-associated empty spaces (see the text).

a highly regular structure; in this case the particles are 100 nm in diameter with a rather low size dispersion (2.6%). The second shows 42 nm particles with 13% dispersion. This time we can spot regions where the particles have the same size (central part of the picture), and the array is regular; elsewhere we can notice zones of disorder where the particles present great differences in size (top left and bottom right).

The regular spaces in the two-dimensional array that we noticed on low-scale images has been observed also by other authors and are known to be due to the shrinking of the particles.[7] In spite of this, we propose that this irregularity is due solely to the particle–water–particle forces that acts in the evaporation process. To confirm this, we have chosen some polystyrene surface-treated particles. We deposited, with the same procedure described above, a film of surface-treated 59 nm particles (Polyscience Inc., Polybead, Fluoresbrite Carboxilated Microspheres, monodispersity CV < 5%, originally in pure water at 2.5%). As shown in Figure 4a,b, the large scale behavior is similar, but the small-scale, shrinkage-associated empty spaces do not appear. Since the inner material (polystyrene) and the deposition procedure used are the same, we can claim that the phenomena is due to the collective interactions between the water and the surface of the spheres, not a physical shrinking of the particles.

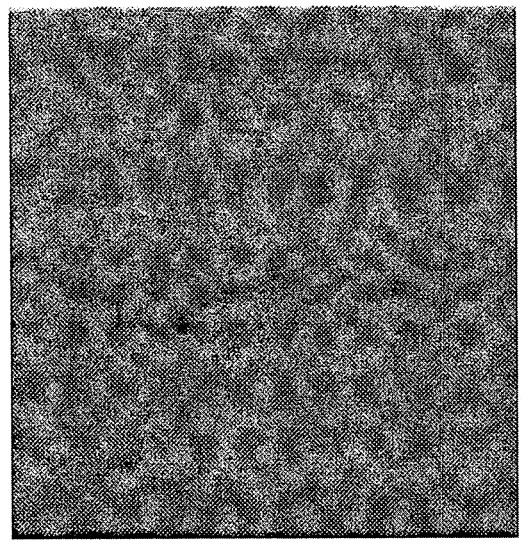

Figure 5. AFM image of an array of 42 nm Stadex latex particles. The image has been filtered for measurements.

At large scales the structure appear to be a grid of long stripes (Figure 2c). These stripes are 10–20 μm wide and several millimeters long. We tried to understand their nature and to avoid the formation of them. Our strategy was mainly to reduce the temperature because in some of our preliminary experiments we noticed that the macroscopic stripes got wider at lower temperatures; however, the nature of these macrostripes is not clear and is under investigation.

To evaluate the quality of the produced two-dimensional array, we used Fourier analysis. In Figure 5 is shown the original AFM scan of 42 nm particles on a 780 × 780 nm area. Notice that the image has been band-pass filtered to emphasize the center of the spheres.

In Figure 6a we show its one-dimensional spatial Fourier spectrum, averaged on about 10 rows of particles, as shown by the rectangular area in Figure 6b. Figure 6c is the space-amplitude representation of the same Fourier spectrum; the 42 nm period can be clearly seen.

The regularity of the array is given by the sharpness of the peak indicated in Figure 6a; we claim, for our sample, $\Delta f_x = 14\ \mu m^{-1}$ (width at half-maximum of the spectral shape). To present this value in space unities we simply consider that the center of the peak is located at $f_{x0} = 24\ \mu m^{-1}$ ($x_0 = 1/24 = 41.7$ nm), then we can conclude that $x_0 \cong 42 \pm 22$ nm (Δx has been estimated as $\Delta x = x_0/f_{x0}\Delta f_x$).

In Figure 7 is shown the two-dimensional Fourier power spectrum calculated on the same pattern shown in Figure 5. The hexagonal structure of the two-dimensional crystal can be easily recognized with the six peaks indicating the three main directions of the array.

Discussion and Conclusions

We succeeded in depositing a highly regular two-dimensional array of small polystyrene latex spheres. The monolayer lay on the glass substrate in the form of long stripes (see Figure 2c or 4b). These stripes are several micrometers large and millimeters long. The area covered by the monolayer is approximately 50% of the total deposition area. We have still not performed a complete optical storage experiment, but we claim that the samples realized can be used to investigate our optical medium systems[2,10] and it is possible to obtain a very high data

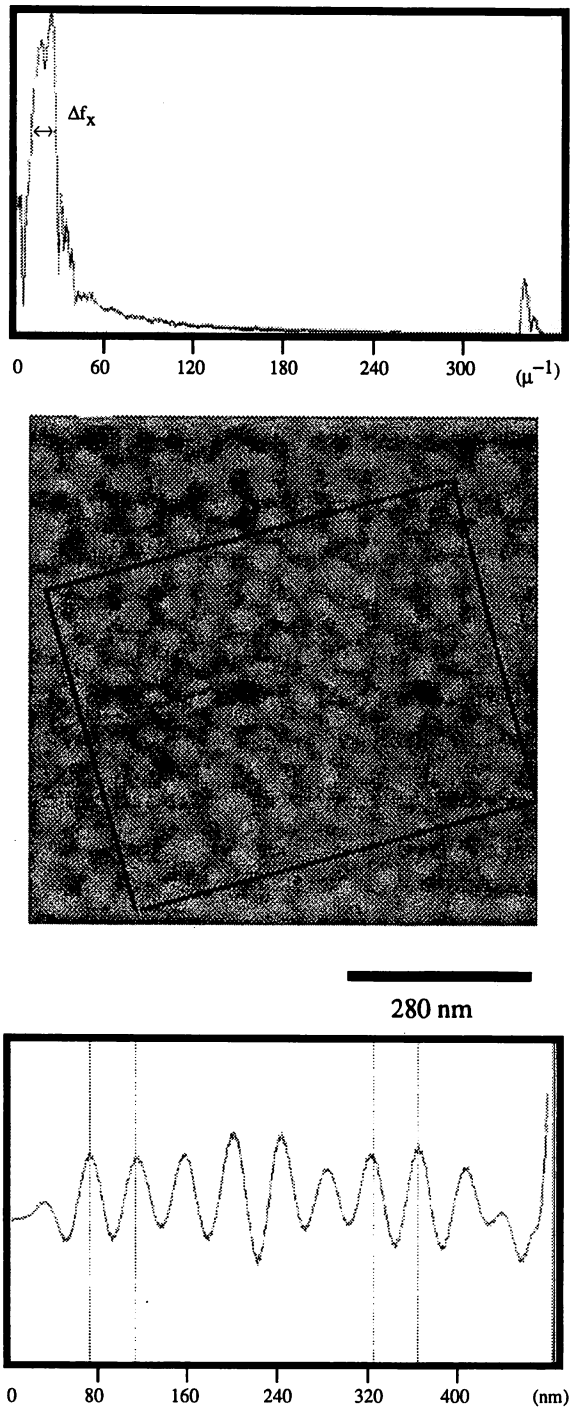

Figure 6. (a, top) Fourier one-dimensional spectrum, averaged on the region showed in part b. (b, middle) The region in which measurement has been calculated. (c, bottom) Space-amplitude representation of the Fourier spectrum in b. The 42 nm period can be clearly seen.

density. In fact, the dimension of the bit, for 42 nm particles, would be $2.8e^{-12}$ in.^{2}, which, considering that the covering of the monolayer is 50%, yields around 200 Gbit per inch. This figure is 2 orders of magnitude greater than the most advanced optical storage devices.

The samples obtained are easy to reproduce and require no particular skill or precise instruments. The quality of the formed arrays has been quantitatively evaluated through Fourier analysis.

On the basis of what we have experienced, we think that improvement in the thermal and humidity control

(10) Fukuda, H.; Micheletto, R.; Ohtsu, M. Proceeding of the Near Field Optics 3, EOS Topical Meeting, Brno, Czech Republic, May 1995, p 183.

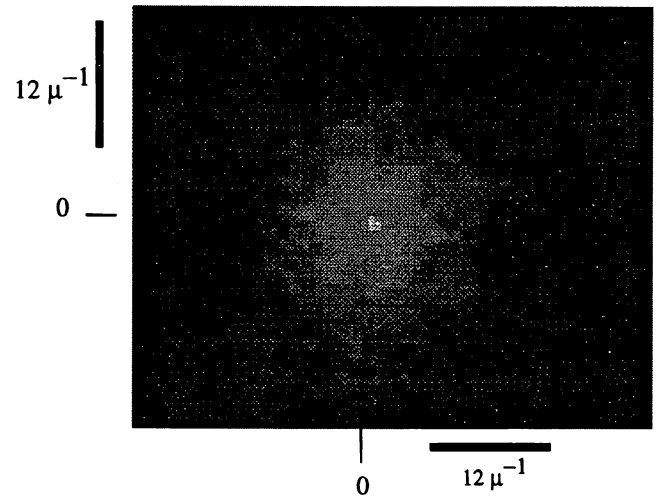

Figure 7. Two-dimensional spectrum of the array in Figure 5. The hexagonal structure of the crystal is visible.

can increase the quality of the samples. The deposition process can be carried out at lower temperatures, such as 4 °C, for example, to obtain better results. We have found problems in doing so, due to water condensation on the sample at such temperatures. We believe that improving humidity control can overcome this and lead to more regular depositions and higher coverage with the monolayer. Many other different applications may be found.

Appendix

We calculated the latex/water proportion simply by imposing that a monolayer of spheres should cover evenly the area of deposition. We choose, for example, an area $A = 1$ cm^2; we suppose that a droplet of $C = 10$ μL of water will dry in such area. Usually the company which produces the particles will give the original concentration of the particles as

$$\eta = 6\omega/(\pi\varrho\phi^3) \times 10^{12} \text{ particles mL}$$

where ω is the percentage of solid latex, ϱ is the density of polymer, and ϕ is the diameter of the spheres in microns. For 42 nm Dinosphere, we apply that formula using $\omega = 0.01$ (1 wt %), $\varrho = 1.05$ (polystyrene), and $\phi = 0.042$, which yields

$$\eta = 2.45 \times 10^{14} \text{ particles/mL}$$

This is the original concentration we start with. Now we determine what concentration we should have to obtain one monolayer over the area A. Firstly we calculate the number of particles that will cover evenly such an area (N_p). Since a particle of 42 nm diameter will occupy an area $A_p = \pi/(\phi/2)^2$, we have

$$N_p = A/A_p = 7.2 \times 10^{10} \text{ particles}$$

then we divide this by the amount of water we need, 10 μL, and we have the concentration:

$$\eta^* = N_p/C = 7.2 \times 10^{12} \text{ particles/mL}$$

Acknowledgment. We wish to thank Antony S. Dimitrov of Nagayama Proj. (ERATO, Tsukuba, Japan), Prof. Vladimir I. Troitsky of Technobiochip (Marciana, Italy), and Prof. Atsushi Ikai of T.I.T. (Tokyo, Japan) for their keen support and suggestions. This work has been partially supported by S.T.A. Fellowship of Japan.

LA940921L

Spatially resolved photoluminescence spectroscopy of lateral *p-n* junctions prepared by Si-doped GaAs using a photon scanning tunneling microscope

T. Saiki and S. Mononobe
Kanagawa Academy of Science and Technology, Takatsu-ku, Kawasaki, Kanagawa 213, Japan

M. Ohtsu[a)]
Interdisciplinary Graduate School of Science and Engineering, Tokyo Institute of Technology, Midori-ku, Yokohama, Kanagawa 226, Japan

N. Saito and J. Kusano
NHK Science and Technical Research Laboratories, Setagaya-ku, Tokyo 157, Japan

(Received 24 April 1995; accepted for publication 3 August 1995)

An accurate correspondence between the local optical responses and the structures of semiconductor light-emitting devices is demonstrated by using an illumination-mode photon scanning tunneling microscope with noncontact atomic force microscope technique. We study the novel-structured lateral *p-n* junctions grown on patterned GaAs(111)A substrate. Measuring the spatially resolved photoluminescence spectra with a 200 nm apertured probe, we precisely determine the position and the width of the transition region of *p-n* junctions. The illumination-collection hybrid mode is also employed to map the two-dimensional emission efficiency with higher resolution, which is not affected by carrier diffusion. © *1995 American Institute of Physics.*

In the investigation of semiconductor optical devices with novel structures, such as quantum dots and quantum wires, a spatially resolved spectroscopy technique in strict correspondence with their sizes, shapes, and structures has been strongly required. So far, cathodoluminescence (CL) technique, whose resolution is limited to the order of 1 μm, has been frequently used for this purpose.[1] Recently, a photon scanning tunneling microscope (PSTM) has been progressed in the observation of nanometric structures,[2,3] and also successfully employed in the spectroscopy of single molecules[4–6] and quantum devices[7,8] with the resolution of 100–250 nm. Furthermore, using the noncontact atomic force (shear-force) microscope technique,[9] a high-resolution optical imaging can be achieved tracing surface structures of the samples.

In this letter, we demonstrate the spatially resolved spectroscopy of lateral *p-n* junctions on a patterned GaAs substrate. The advantages of PSTM—its higher resolution than CL and the capability of measuring the surface structures and the optical properties simultaneously makes it a powerful tool for the characterization of these types of devices. We clarify the profile of the conduction type in the junction relating it to the surface structures. The illumination-collection hybrid mode, whose resolution is not limited by the carrier diffusion, is also employed to obtain the higher-resolution two-dimensional imaging of emission efficiency in the vicinity of the *p-n* junction.

The lateral *p-n* junction is expected to be applied to the lateral carrier confinement structures, such as surface-emitting laser diode. The conduction type of GaAs layers with Si dopant depends on growth conditions and the orientation of the substrate.[10,11] By using this amphoteric nature of Si, both *n*- and *p*-type regions can be grown simultaneously on a patterned substrate, and lateral *p-n* junctions are formed at the boundary of the two regions.[12,13] The luminescence peak wavelength strongly depends on the conduction type and the carrier concentration of GaAs layers.[14] By measuring the photoluminescence spectra with high spatial resolution, we can precisely examine the carrier distribution in the transition region of the *p-n* junction.

Since the fabrication procedure of the sample is described in detail elsewhere,[12,13] we show it briefly here. A semi-insulating GaAs (111)A substrate was etched with photolithography technique to obtain a triangular (111)A surface surrounded by three slopes. For the present work, two different slopes were prepared; one was (311)A slope (sample No. 1) and the other was (210) slope (sample No. 2). After thermal cleaning, a Si-doped GaAs layer with the thickness of 1 μm was grown on the patterned substrate at 600 °C. The Si concentration was estimated as 1×10^{18} cm^{-3}.

A schematic of the experimental setup is shown in Fig. 1. A gold-coated fiber probe with a 200 nm aperture at its apex was employed as a tip[15] (shown in the inset of Fig. 1).

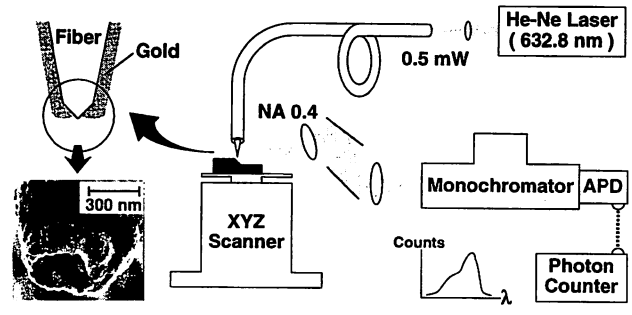

FIG. 1. Schematics of experimental setup for spatially resolved photoluminescence spectroscopy.

[a)]Also with Kanagawa Academy of Science and Technology, Takatsu-ku, Kawasaki, Kanagawa 213, Japan.

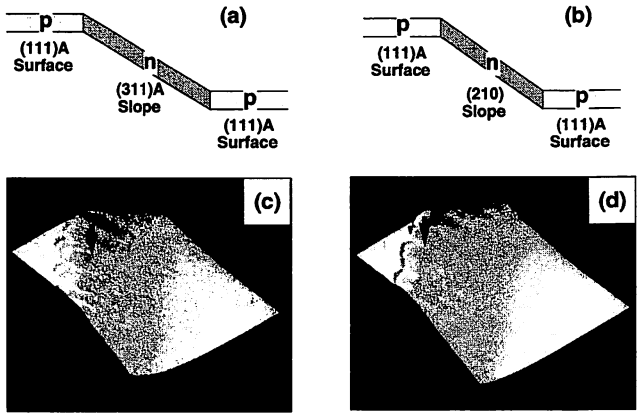

FIG. 2. Schematic structures of the lateral *p-n* junctions of (a) sample No. 1 and (b) sample No. 2. Perspective views of shear-force images are shown in (c) and (d), respectively. The image size is 15.2×15.2 μm^2.

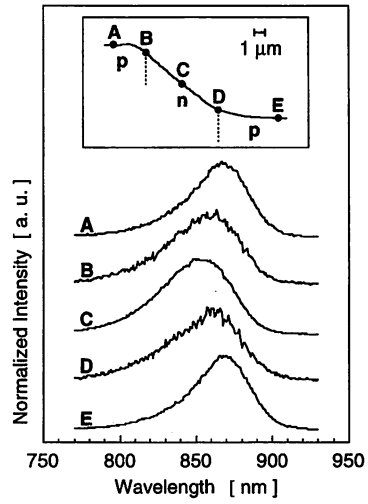

FIG. 3. Normalized photoluminescence spectra at some points in the vicinity of the slope of sample No. 1. The inset shows the cross-sectional view of the *p-n* junctions indicating the measuring points (A–E).

Taking into account both the experimental utility and the transmission efficiency, the shape of the probe was optimized by multistep chemical etching technique to realize a stepped cone angle (see the cross-sectional profile of the probe in Fig. 1).[16] As an excitation light source, 0.5 mW of He–Ne laser (632.8 nm) was coupled into the fiber probe. The transmission coefficient was estimated as 1.0×10^{-3} by collecting the far-field throughput from the aperture with a 0.4 NA objective lens. By positioning the tip <20 nm above the sample, the excitation region was restricted to $\sim(100\ nm)^2$ in lateral area and 200 nm in depth, which were determined by the aperture radius and the absorption coefficient of GaAs. In order to keep the same excitation efficiency on the (111)A surface as that on (311)A or (210) surfaces, the sample was tilted by 15° with respect to the plane of the aperture. The luminescence from the sample was collected on the same side of the sample with a 0.4 NA objective lens, and transported to a 20 cm monochromator with an avalanche photodiode for photon-counting detection. For the shear-force feedback, we used a 1.3 μm laser diode, whose photon energy is far below the absorption edge of GaAs.

Figure 2 shows shear-force images of two samples in the vicinity of the slopes. The width and height of the slope of sample No. 1 are approximately 10 and 6 μm, respectively, and those of sample No. 2 are 8 and 5.5 μm. From the top surface to the slope, some bumps, which may be produced in the etching process of the substrates, appears [indicated by arrows in Figs. 2(c) and 2(d)]. Compared with sample No. 1, relatively larger bumps are observed in sample No. 2, which can be attributed to the difference of etching behavior on the (311)A slope and the (210) slope.

Normalized photoluminescence spectra at some characteristic points on the slope of sample No. 1 are shown in Fig. 3. The peak wavelength at the top surface (position A in the inset of Fig. 3) and at the bottom surface (E) shows the same value of 870 nm. This peak wavelength corresponds to that of flat (111)A surface with the same Si concentration. Its conduction type (*p* type) is confirmed by the measurement of capacitance–voltage characteristics.[12] On the (311)A slope (C), the emission peak shifts to the higher-energy side. Its value of 855 nm is also in agreement with that of *n*-type flat (100)A surface investigated previously.[12] In the transition region (B and D), where the conduction type and carrier concentration gradually change, the emission peaks show the intermediate values. To examine the transition region more precisely with relating to the sample structure, we plot the emission peak, emission linewidth, and total intensity along the slopes (Fig. 4).

A variety of features are observed in the transition region of *p-n* junctions. At the lower junction, the emission peak shows graded changes with a transition width of 5 μm in the both samples. Since the conduction type and carrier concentration vary with tilt angle of the substrate from (111)A

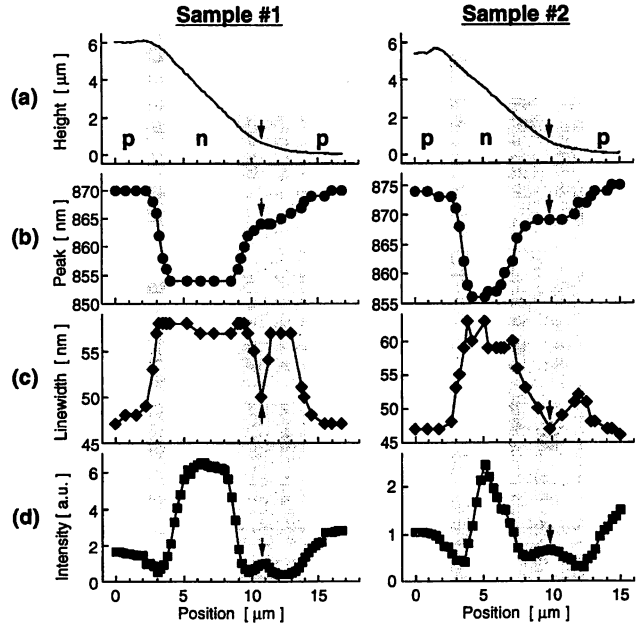

FIG. 4. (a) Cross-sectional views of the slopes. (b)–(d) Plots of emission peak, emission linewidth, and total emission intensity, respectively, at the slopes of sample No. 1 and of sample No. 2. The shaded areas indicate the transition regions of upper and lower junctions.

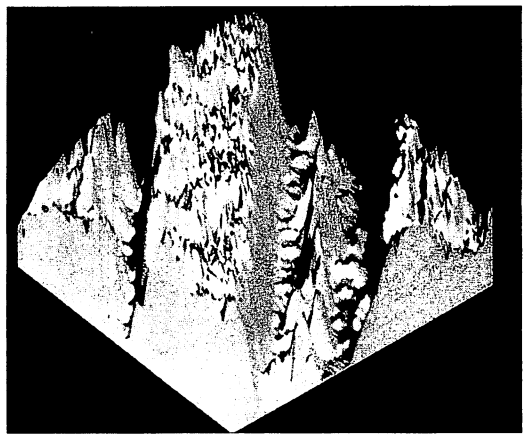

FIG. 5. Perspective view of the emission-intensity image measured with the illumination-collection hybrid mode. The scanned area is the same as that of image (c) in Fig. 2.

surface,[14] the transition width is closely relevant to the structure of the junction. The gradual change of tilt angle at lower junction, as shown in Fig. 4(a), causes the wide transition width of the carrier concentration. At the upper junction, on the other hand, the top surface and the slope make a clear ridge. This abrupt change results in the narrower transition width of 1 μm. From the fast rise of the emission peak in the upper junction, it is confirmed that we attain the spatial resolution of <400 nm. By comparing the spectral change with the shear-force image carefully, it can be found that the transition region is formed on the slope, not at the ridge. So far, to explain the results of capacitance–voltage measurements, it has been inferred that the modulation of carrier concentration occurs on the slope side of intersection.[17] This has been supported by the CL measurement with the resolution of ~1 μm.[12] We have determined the position of the boundary with a higher resolution through the accurate correspondence between the surface structure and the optical response.

The total emission intensity in the transition region is much lower than the other regions. This is mainly due to the separation and the drift of photoexcited electrons and holes by the internal electric field in the transition regions. From the slow rises of emission intensity in p and n side, the width of depletion layers can be estimated quantitatively. In the lower junction, some anomalous optical structures, plateau in the change of the emission peak, decrease of emission linewidth and increase of emission intensity, are observed as indicated by arrows in Fig. 4. It is important to investigate these local optical properties in the vicinity of the junctions in detail since the distribution of defects and strains, and nonuniformity of dopants in this active region will affect the emission efficiency as a light-emitting device.

To measure the two-dimensional distribution of the emission intensity, a bandpass filter was set in place of the monochromator and the illumination-collection hybrid (reflection) mode for detection was employed. In this mode, as the probe tip locally collects the emission in addition to being a local excitation source, we can achieve higher resolution (<200 nm), which does not depend on the diffusion length but is limited only by the aperture diameter. The emission-intensity image of sample No. 1 is shown in Fig. 5. In this image, the maximum and the minimum counting rates are 2×10^4 counts/s and 1×10^4 counts/s, respectively. In the transition region, as shown previously, the emission intensity decreases much, compared to the other regions. Some bright areas, where the emission intensity locally increases, appears in the lower junction. These signals indicate essentially optical properties since no corresponding structure is found in the shear-force image [Fig. 2(c)]. A nonuniform distribution of Si dopants and of the resultant internal electric field, or that of defects and strains will affect the local optical responses. Although, in this examination, we cannot specify the origin of these signal behaviors, further experiments, such as local electroluminescence and photocurrent measurements,[18] will provide valuable insights into the dynamics of induced carriers.

In conclusion, by employing the fiber tip with the aperture diameter of 200 nm, spectral properties of lateral p-n junction are investigated in strict correspondence with the surface structures. The conduction type profile in transition regions of p-n junctions is precisely determined by observing local photoluminescence spectra in two different samples. In the illumination-collection mode, a higher-resolution image of emission intensity can be obtained and the result yields information on the local emission efficiency affected by the distribution of dopants, defects, strains, and so on.

[1] D. Bimberg, J. Christen, A. Steckenbom, G. Weimann, and W. Schlapp, J. Lumin. **30**, 562 (1985).

[2] *Near Field Optics,* edited by D. W. Pohl and D. Courjon (Kluwer Academic, Dordrecht, 1993).

[3] S. Jiang, N. Tomita, H. Ohsawa, and M. Ohtsu, Jpn. J. Appl. Phys. **30**, 2107 (1991); S. Jiang, H. Ohsawa, K. Yamada, T. Pangaribuan, M. Ohtsu, K. Imai, and A. Ikai, Jpn. J. Appl. Phys. **31**, 2282 (1992).

[4] E. Betzig and R. J. Chichester, Science **262**, 1422 (1993); J. K. Trautman, J. J. Macklin, L. E. Brus, and E. Betzig, Nature **369**, 40 (1994).

[5] W. P. Ambrose, P. M. Goodwin, J. C. Martin, and R. A. Keller, Phys. Rev. Lett. **72**, 160 (1994); W. P. Ambrose, P. M. Goodwin, J. C. Martin, and R. A. Keller, Science **265**, 364 (1994).

[6] X. S. Xie and R. C. Dunn, Science **265**, 361 (1994); R. C. Dunn, G. R. Holtom, L. Mets, and X. S. Xie, J. Phys. Chem. **98**, 3094 (1994).

[7] R. D. Grober, T. D. Harris, J. K. Trautman, E. Betzig, W. Wegscheider, L. Pfeiffer, and K. West, Appl. Phys. Lett. **64**, 1421 (1994).

[8] H. F. Hess, E. Betzig, T. D. Harris, L. N. Pfeiffer, and K. W. West, Science **264**, 1740 (1994).

[9] E. Betzig, P. L. Finn, and J. S. Weiner, Appl. Phys. Lett. **60**, 2484 (1992).

[10] J. M. Ballingall and C. E. C. Wood, Appl. Phys. Lett. **41**, 947 (1982).

[11] W. I. Wang, E. E. Mendez, T. S. Kuan, and L. Esaki, Appl. Phys. Lett. **47**, 826 (1985).

[12] N. Saito, M. Yamaga, F. Sato, I. Fujimoto, M. Inai, T. Yamamoto, and T. Watanabe, Inst. Phys. Conf. Ser. **136**, 601 (1994).

[13] M. Fujii, T. Yamamoto, M. Shigeta, T. Takebe, K. Kobayashi, S. Hiyamizu, and I. Fujimoto, Surf. Sci. **267**, 26 (1992); M. Fujii, T. Takebe, T. Yamamoto, M. Inai, and K. Kobayashi, Superlattices and Microstruct. **12**, 167 (1992).

[14] Y. Okano, M. Shigeta, H. Seto, H. Katahama, S. Nishine, and I. Fujimoto, Jpn. J. Appl. Phys. **29**, L1357 (1990); M. Shigeta, Y. Okano, H. Seto, H. Katahama, S. Nishine, and K. Kobayashi, J. Cryst. Growth **111**, 284 (1991).

[15] T. Pangaribuan, K. Yamada, S. Jiang, H. Ohsawa, and M. Ohtsu, Jpn. J. Appl. Phys. **31** L1302 (1992); T. Pangaribuan, S. Jiang, and M. Ohtsu, Electron. Lett. **29**, 1978 (1993).

[16] A more detailed fabrication technique of fiber probe will be published in another paper.

[17] M. Inai, T. Yamamoto, M. Fujii, T. Takebe, and K. Kobayashi, Jpn. J. Appl. Phys. **32**, 523 (1993).

[18] S. K. Buratto, J. W. P. Hsu, E. Betzig, J. K. Trautman, R. B. Bylsma, C. C. Bahr, and M. J. Cardillo, Appl. Phys. Lett. **65**, 2654 (1994).

ELSEVIER

1 November 1995

Optics Communications 120 (1995) 325–334

OPTICS COMMUNICATIONS

Full length article

Observation of subcellular nanostructure of single neurons with an illumination mode photon scanning tunneling microscope

R. Uma Maheswari [a], H. Tatsumi [b,c], Y. Katayama [b], M. Ohtsu [a,d]

[a] *Kanagawa Academy of Science and Technology, KSP East 408, 3-2-1 Sakado, Takatsu-Ku, Kawasaki-Shi, Kanagawa 213, Japan*

[b] *Department of Autonomic Physiology, Medical Research Institute, Tokyo Medical and Dental University, Chiyoda-Ku, Tokyo 101, Japan*

[c] *PRESTO, Research Development Corporation of Japan, City, Japan*

[d] *Interdisciplinary Graduate School of Science and Engineering, Tokyo Institute of Technology, 4259 Nagatsuda, Midori-Ku, Yokohama Kanagawa 226, Japan*

Received 24 April 1995; revised version received 10 July 1995

Abstract

We report about the observation of microtubules lying underneath the cell membrane of neural process in neurons with a resolution as high as that of an electron microscope by an illumination mode photon scanning tunneling microscope. Nano-apertures used in our observations were fabricated by means of selective chemical etching and metal coating of an optical fiber. The narrowest observed tube has got an average diameter of 26 nm. Comparing this with its nominal value of 25 nm, the difference which is considered as a measure of resolution (δ) is 1 nm implying a resolution comparable to that of an electron microscope in imaging dielectric specimens. This was possible due to the presence of a boundary between the glass and the metal coating and also due to the use of an aperture of almost the same size as that of the microtubule that enhances the detection.

1. Introduction

Conventional optical microscopes are widely used in imaging biological specimens because of their cheap availability, non-invasiveness, flexibility of operation in liquid or air and possibility of spectroscopic labelling. However, their resolution is diffraction limited to the order of wavelength. To surpass this diffraction limit, recently the technique of near-field microscopy is getting popular and it is called by different names such as photon scanning tunneling microscopy (PSTM), scanning tunneling optical microscope (STOM), near-field scanning optical microscopy (NSOM) and scanning near-field optical microscope (SNOM) with the principle of operation being the same [1,2]. In our paper we use the acronym PSTM for it gives an image of the physical phenomenon behind the operation principle of the near-field microscope.

In PSTM, the sample is illuminated under total internal reflection and the localized three-dimensional evanescent field generated over the sample is scattered by a sharpened probe tip having a high radius of curvature at its top. As the volume of localization of the evanescent field is proportional to the spatial features (size and shape) of the sample, it is possible to detect features of higher spatial frequencies present in the sample with the sharpened probe tip. This process can be thought of as tunneling of evanescent photons from the sample to probe and it obeys the principle of reciprocity, i.e., the process is the same even when the positions of the sample and the probe are interchanged. In other words, the sample scatters the evanescent field generated by the sharpened probe tip. In our discussion, we call the

SSDI 0030-4018(95)00462-9

former one with sample to probe tunneling as *collection mode PSTM* [3–6] and the latter one involving probe to sample tunneling as *illumination mode PSTM* [7].

In this study, subcellular structures of neurons have been observed with PSTM operated in illumination mode. Nano-apertures used in our experiment were fabricated by chemical etching [8,9] and metal coating by vacuum evaporation. Neurons are studied largely by electron microscope and other varieties of optical microscope such as differential interference contrast microscope (DIC) and confocal microscope. While resolution of optical microscopes is limited to the order of wavelength, electron microscopes offer high resolution. However, with electron microscopes there are three main disadvantages:

1. all surface information is lost due to the use of special sample preparation techniques such as ultra thin sectioning employed in the case of transmission electron microscope and surface coating used in the case of scanning electron microscope (SEM);
2. the observation is destructive;
3. the requirement of high vacuum.

Actually, from the side of neurobiologists, surface information about the neural ends called as growth cones which stretch to develop neural interconnections such as synaptic contact is important to understand the mechanism about the formation of neural interconnections. Although with an optical microscope (DIC or confocal microscopes), it is possible to perform such studies on growth cone [10], resolution is limited to the order of wavelength. With atomic force microscope (contact mode) also, due to the presence of strong forces, it is difficult to investigate the soft surface membrane.

In contrast, PSTM has the following special features:

1. optical surface variation could be obtained with high resolution;
2. non-destructive observation;
3. there is no need for high vacuum;
4. spectroscopic labelling could also be done;

In this study, by making use of the above mentioned features of PSTM, we will demonstrate that neurons could be imaged with a resolution as comparable to that of an electron microscope non-destructively in air. We have employed illumination mode PSTM instead of collection mode PSTM for the following two reasons.

1. Neuron samples are relatively thick and difficult to be imaged by collection mode PSTM.
2. When the specimens are stained with absorption dyes, large absorption will lead to very weak signals in the case of collection mode.

In section 2, fabrication technique of the apertured probe and the experimental system are briefly described. Section 3 discusses results obtained for neurons labelled with and without an absorbing dye and gives a quantitative evaluation of the obtained images. Finally, section 4 gives a summary.

2. Experiments

In this section, we describe briefly about the technique of fabricating apertured fiber probes with diameters as small as a few tens of nanometers, sample preparation and experimental system.

2.1. Apertured probe fabrication

The fabrication of an apertured probe whose presence is inevitable for PSTM, involves two techniques.

2.1.1. Fabrication of sharpened fiber probe with flat top

Fiber probes with flat topped tips are suitable for fabricating aperture as the tip region could be controlled to be in the shadow region while performing metal coating. Such fiber probes are usually fabricated by a micropipette puller [11]. However, with a micropipette puller it is difficult to fabricate flat tops with sizes less than 50 nm reproducibly and also there is a lack of flexibility in controlling the shapes of the apex of the pulled fiber and the cone angle of the tapered probe. In our system, sharpened fiber probes with flat tops have been fabricated by a muti-step chemical etching technique. Here we give only a brief description of the technique. Details will be published elsewhere [12].

The fibers used were single-mode fibers with core having a high level of GeO_2 doping of 27% that corresponds to a difference of 2.7% in refractive indices between the cladding and the core. Sharpening of these fibers is done through etching in an etching solution containing hydrofluoric acid (50% weight) [HF], ammonium fluoride (40% weight) [NH_4F] and deion-

ized water [H_2O]. We denote the volume ratio of etching solution as X:1:1 which corresponds to the order of NH_4F, HF and H_2O, respectively.

The etching involves three steps: In the first step, the fiber is etched in an etching solution of composition ratio 1.7:1:1 for a duration of around 90 min to reduce the cladding diameter to approximately 20 μm from 125 μm. In the second step, these fibers are etched in a solution of composition ratio 10:1:1 for around 120 min to get a sharpened core with rounded apex. Fig. 1a shows SEM micrograph of the sharpened fiber probe with a magnified view of the rounded apex region shown in Fig. 1b. The radius of curvature is less than 5 nm and the cone angle is around 20°. Finally, in the third step, this fiber probe with a rounded apex is etched in an etching solution having a composition of 10:1:120 for 120 s to make a probe with a flattened apex as shown in Fig. 1c. The tip diameter is approximately 20 nm. This way of controlling the shape of the apex of the sharpened core could be performed with quite high reproducibility of around 90%. All the etchings were performed at a temperature of 22.5 ± 0.5°C.

2.1.2. Fabrication of nano-aperture

The sharpened fiber probes with flattened top were next coated with metal in a vacuum evaporation unit. The fibers were mounted at an inclination of 25° with respect to the evaporation source so as to coat the cladding face and the sides of the sharpened core and rotated at speeds of around 15 rpm. Gold was used as the coating metal for its simplicity in coating. To have a better bonding with the glass fiber, a thin coating of chromium of thickness around 10 nm was first done. The thickness of the coated gold film was around 150 nm. The skin depth of gold at 488 nm is around 40 nm and the thickness of gold film of 150 nm is sufficient to block the far-field from the face of the cladding and the sides of the sharpened core. Fig. 2a shows a SEM micrograph of the coated fiber with the encircled tip region magnified in Fig. 2b. During this observation by SEM, the electron beam was incident normal to the fiber. Fig. 2c shows a schematic view of the aperture. Here, the central circle corresponds to the flat apex of the fiber probe and the hatched region corresponds to metal film. The dark region corresponds to the rim of the sharpened probe. In spite of the difficulties existing in controlling the direction of the metal vapour to have a symmetric coating, the background far-field compo-

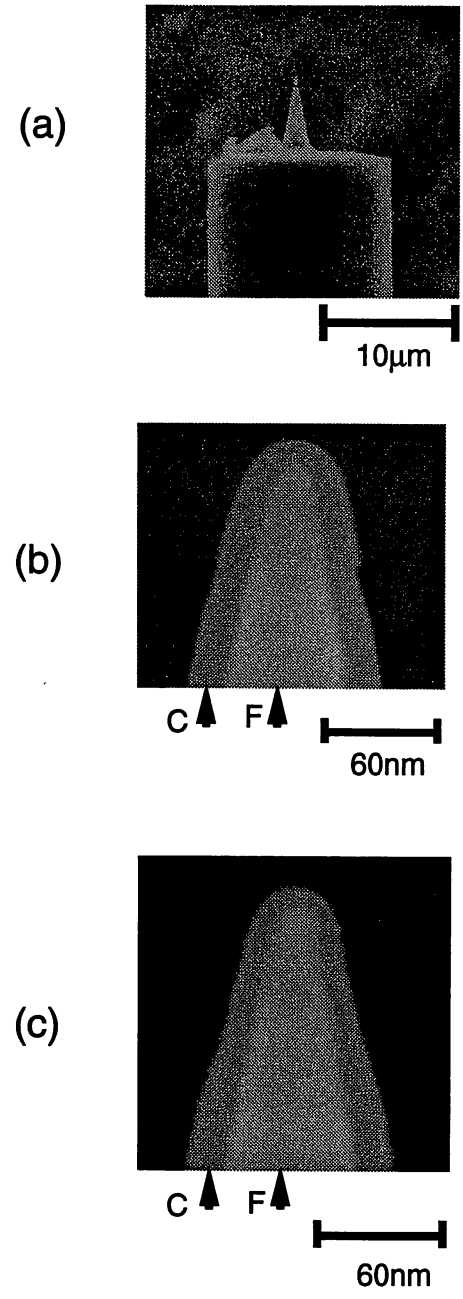

Fig. 1. SEM micrographs of a sharpened fiber probe (a) under low magnification with encirlcled region magnified in (b) rounded tip resulting from sharpening of the core by step 2 and (c) flattened tip resulting from etching in dilute solution in step 3. Here, C in figures (b) and (c) corresponds to contamination while making observation in SEM and F corresponds to the fiber. The fibers were sputtered with a Pt/Pd layer of thickness 10 nm prior to making observations in SEM.

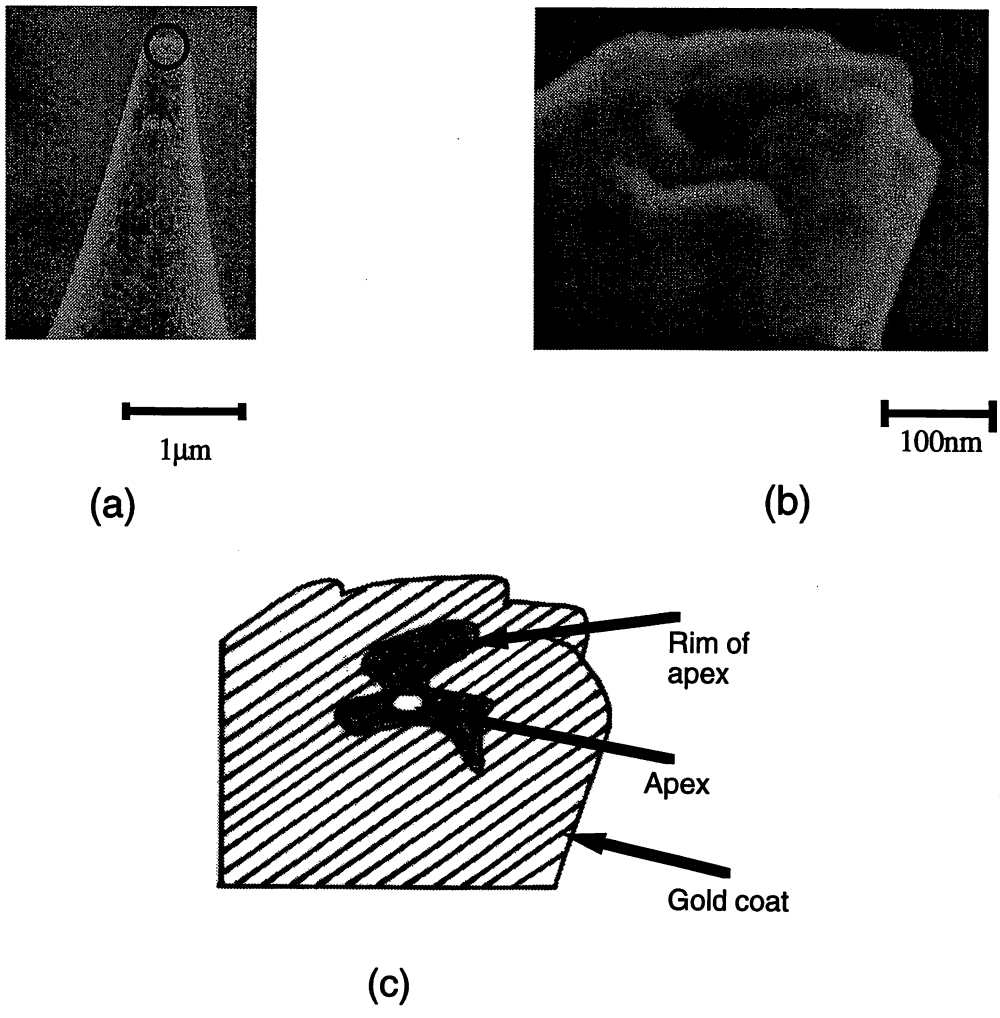

Fig. 2. A SEM micrograph of a fiber probe coated with gold film of 150 nm (a) under low magnification with encircled tip region magnified in (b). A schematic view of the aperture shown in (c) with the hatched region corresponding to the metal coating covering the sides of the sharpened probe and central circle corresponding to the flat apex. The dark region around the flat apex corresponds to the rim of the apex.

nents are largely reduced which lead to high resolution as will be demonstrated in our imaging results in section 3. The aperture diameter is approximately less than 30 nm.

2.2. *Experimental system*

Fig. 3 shows a simple schematic view of the experimental arrangement of an illumination mode PSTM. Light from an Ar ion laser of wave length (λ) 488 nm was coupled to the fiber probe having the sub-wave length aperture to illuminate the neuron sample. An objective lens with high numerical aperture of 0.8 was employed to collect the evanescent field scattered by the sample efficiently. Next, this collected light is imaged onto a photomultiplier tube and sent to a PSTM controller. In order to have a better signal to noise ratio (S/N), phase sensitive detection was applied and this was done through amplitude modulation of laser light by a chopper.

The sample was mounted on a *xyz* piezo scanner with in-built sensors compensating for hysterisis to perform two-dimensional (2D) raster scanning of the sample at constant sample–probe separations. For maintaining

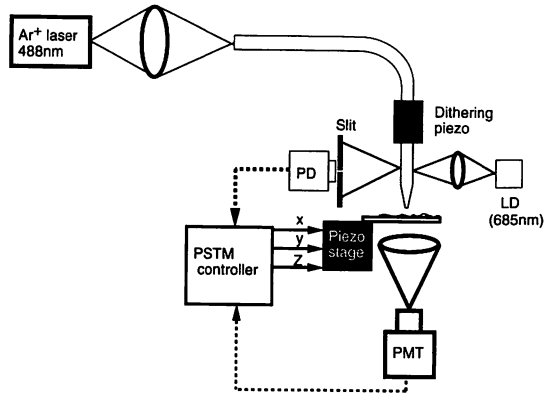

Fig. 3. A schematic view of the experimental arrangement of an illumination mode PSTM with simultaneous shear force control.

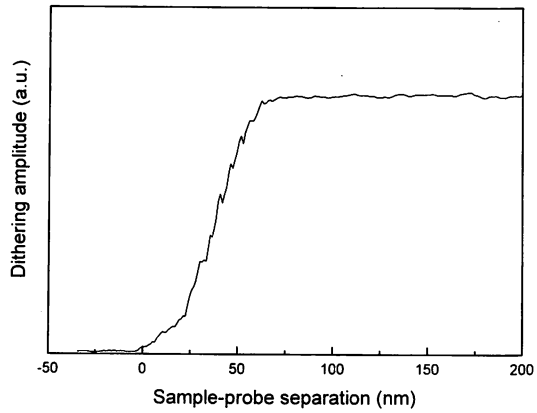

Fig. 4. Variation of dithering amplitude as a function of sample–probe separation.

constant sample–probe separations, the fiber probe has been employed as a cantilever of a non-contact force microscope. The fiber probe was mounted on a dithering piezo device and dithered at its resonance frequency [13,14]. Our probes fabricated by a method based on a two-step etching technique [8] have quite high resonance frequencies between 20 to 100 kHz. The dither vibrations were detected by illuminating the fiber with an auxiliary laser diode and detecting the scattered light with a photodetector and a slit. The linear variation of the detected signal amplitude with respect to sample probe separation as shown in Fig. 4 was used as a control signal in performing 2D scanning.

2.3. *Preparation of sample*

The neurons were taken from the tissues of hippocampal region of the brain of a Wistar rat. The functions of this region are related to learning and memory of the brain [15]. The neuron tissues were cultured for 30 days. Then they were fixed with para-pharmaldehyde (4%) and glutal aldehyde phosphate (2%) buffered saline solution and rinsed with distilled water. Finally they were dried on a microscopic cover glass substrate. We prepared two kinds of neuron samples one having a labelling with a dye called toluidine blue having the absorption band centered around the wavelength of 600 nm and the other one without any dye. We expect the dye to enhance the contrast of the overall image.

As mentioned earlier, with an electron microscope though it is possible to attain subnanometer resolutions, all surface information is lost and the observation is destructive requiring high vacuum while conventional optical microscopes are diffraction limited. In that sense, our study on observation of neurons by PSTM is important as it provides resolution as high as that of the electron microscope non-destructively in air.

For later discussion on imaging results, we show a rough sketch of the structure of neuron. Fig. 5 shows a schematic drawing of neuron. Neuron consists of a cell body and neural processes. Inside this branching neural process, there are many microtubules made up of a protein called tubulin [15]. They are responsible for the transport of proteins and intracellular vesicles (packets of protein substances) generated in the cell body to other parts. As mentioned earlier, the end of the neural process is called as growth cone and it has a palm like flat structure known as lamellipodium. Inside this growth cone as indicated by crosses there are many tubulin and actin filaments[1] forming a network like structure. This growth cone is thought to be stretching itself to make connections with other cells. Hence understanding its structure is very important in disclosing how the neural interconnections are formed.

3. Results and discussion

3.1. *Imaging of neurons without dye labelling*

Fig. 6a and 6b show respectively the variations of the optical intensity and the topography over a scan area of 100×100 μm^2 of the neuron obtained simul-

[1] Actin is the basic protein element involved in conducting the functions of neurons and it is responsible for muscular contraction.

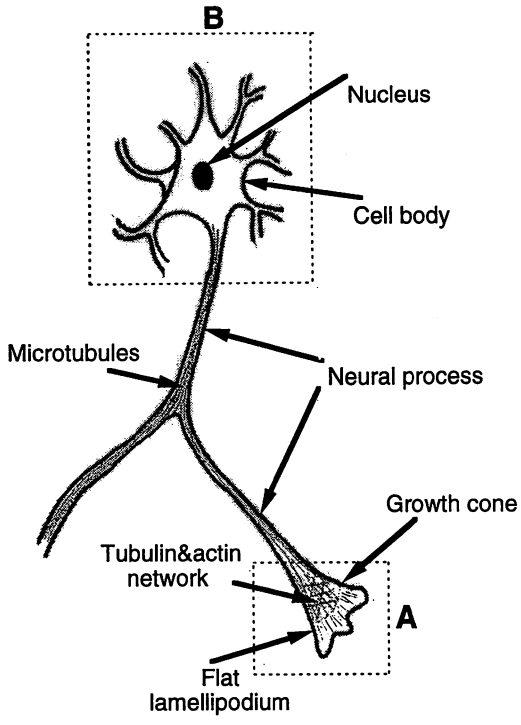

Fig. 5. A schematic view of neuron with its cell body and neural processes. The end of a neural process has a finger like structure called growth cone. In the growth cone, over the flat lamellipodium, there are many actin and tubulin filaments forming a network. Inside the neural process, there are many tubes called microtubules taking part in chemical transport. Areas A and B were imaged and shown in Figs. 6 and 7, respectively.

taneously under a constant sample–probe separation of less than 40 nm which is calibrated based on force curve measurement. In both the optical and the shear force images, arrow heads indicate the neural processes and arrow indicates the growth cone (refer to the area A of sketch in Fig. 5). This growth cone structure actually stretches to communicate with other cells [10] and understanding of its structure is important in understanding cell–cell communication. As seen, in the optical image, the edges of the neural processes are seen with better contrast.

Fig. 6c and 6d show, respectively, the magnified view of the variations of the optical intensity and the topography over a scan area of 5×5 μm^2 over the region indicated by a square in 6a and 6b in the flat lamellipodium (refer to Fig. 5) obtained simultaneously under a constant sample–probe separation of less than 20 nm. The honeycomb like network structure seen in either of these figures is believed to be the network of cytoskeleton consisting probably of actin and tubulin filaments. The network like structure is believed to have been formed during the drying of the sample. As seen from Fig. 6c, the bright filaments are seen with better contrast compared to shear force image.

3.2. *Imaging of neurons labelled with toluidine blue*

Fig. 7a and 7b show respectively the variations of the optical intensity and the topography over a scan area of 50×50 μm^2 of the neuron sample (area B of Fig. 5) labelled with toluidine blue obtained simultaneously under a constant sample–probe separation of less than 50 nm. In both the optical and the shear force images, the arrow heads indicate neural processes and arrows indicate cell bodies. In this case, in spite of the large thickness of the sample and large sample–probe separation, the optical image could be obtained with enhanced contrast compared to the shear force image. This is due to the presence of strong absorption variations.

Fig. 7c and 7d show respectively the magnified views of the variations of the optical intensity and of the topography over a scan area of 1×1 μm^2 over the neural process (shown by square in Fig. 7a and 7b at a constant sample–probe separation of less than 10 nm. In the optical image, fringe like structure could be seen in contrast to the force image where one sees only a constant variation. This is due to the fact that there is cell membrane present on the surface and because force is sensed by variations on the surface, no such structure could be seen in the shear force image. Hence, PSTM excludes the necessity of removing the cell membrane with detergent which damages ultra-cellular structures present underneath the membrane when making observations by electron microscopy and atomic force microscopy. In other words, light could resolve structures which lie below the cell membrane.

It is known from earlier research reports that microtubules are the main constituent cytoskeletal element of neural process [16] and these fringe-like structures seen in Fig. 7c, in actual, could be most likely microtubules. Further, presence of microtubules has been

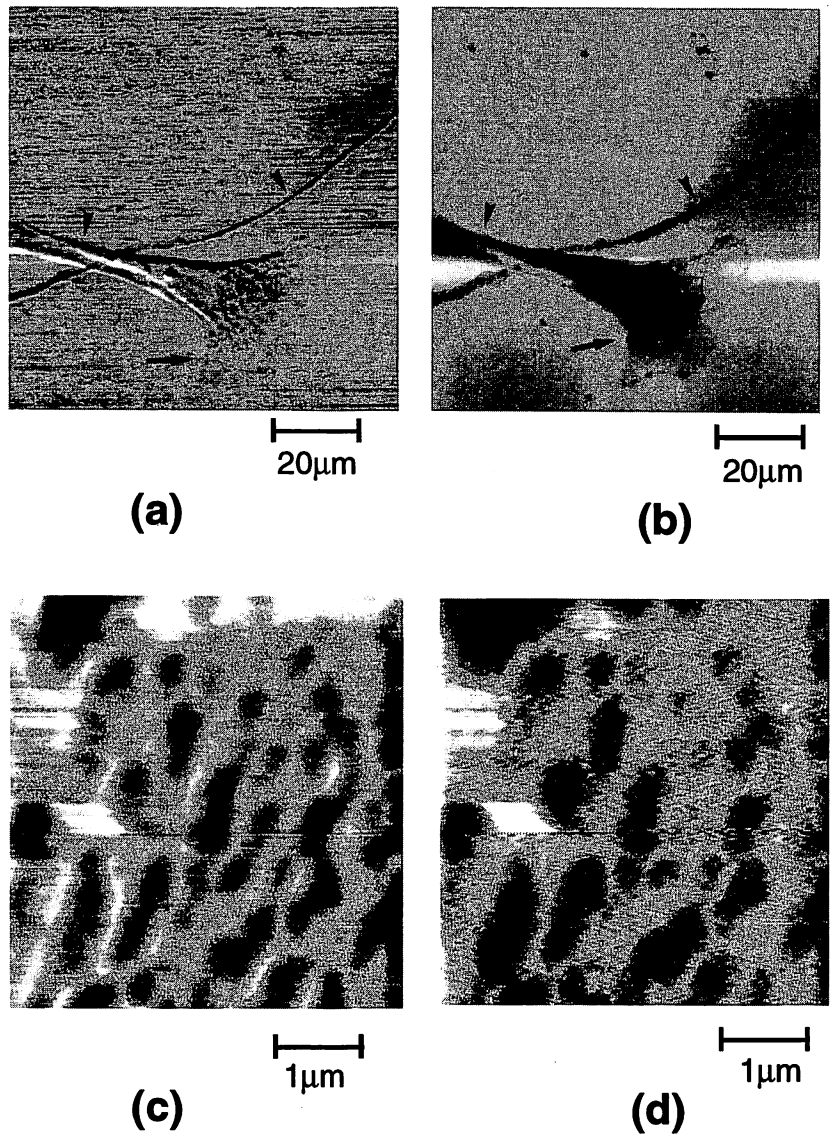

Fig. 6. Gray scale images (a,c) optical and (b,d) topographical variations obtained simultaneously by scanning a neuron sample (corresponding to region A in Fig. 5). In either figures (a) and (b), arrow indicates growth cone and arrow heads indicate neural processes. Here, the scan area for the case of (a) and (b) is 100×100 μm^2 while for (c) and (d) which show a magnified scan over the flat lamellipodium indicated by square in (a) and (b) is 5×5 μm^2. The network like structure consisting of tubulin and actin filaments is believed to have been formed during the drying of the sample. In the shear force image bright regions correspond to valley and dark region corresponds to hill.

confirmed by immuno-histochemical staining[2] of tubulin with a confocal microscope [17]. The bright regions of different width could correspond to microtubules observed either in the form of bundles or as a single tube. The dark regions having a still smaller width seen on either side of the bright regions are believed to be empty space between the microtubules. A cross sectional view of the intensity variation across the narrowest bright region indicated by a line in Fig. 7c

[2] Neurons were stained by monoclonal antibodies of mouse to tubulin and then labelled with rhodamine conjugated anti-mouse immunoglobulin.

is shown in Fig. 7e. The full width at half maximum (fwhm) of this narrowest tube is estimated to be 26 nm. Based on the observations of microtubules by electron microscope[18], the nominal diameter of a single microtubule is 25 nm.

In order to determine the actual resolution, resolution has to be defined in terms of the high frequency cut-off of the transfer function defined in the Fourier spatial frequency region. However, to get an easy estimate of the resolution capabilities of our system in observation of biological specimens, we introduce a parameter δ which is defined as the difference between the nominal value obtained by SEM and the value estimated by PSTM. This is possible because in case of biological

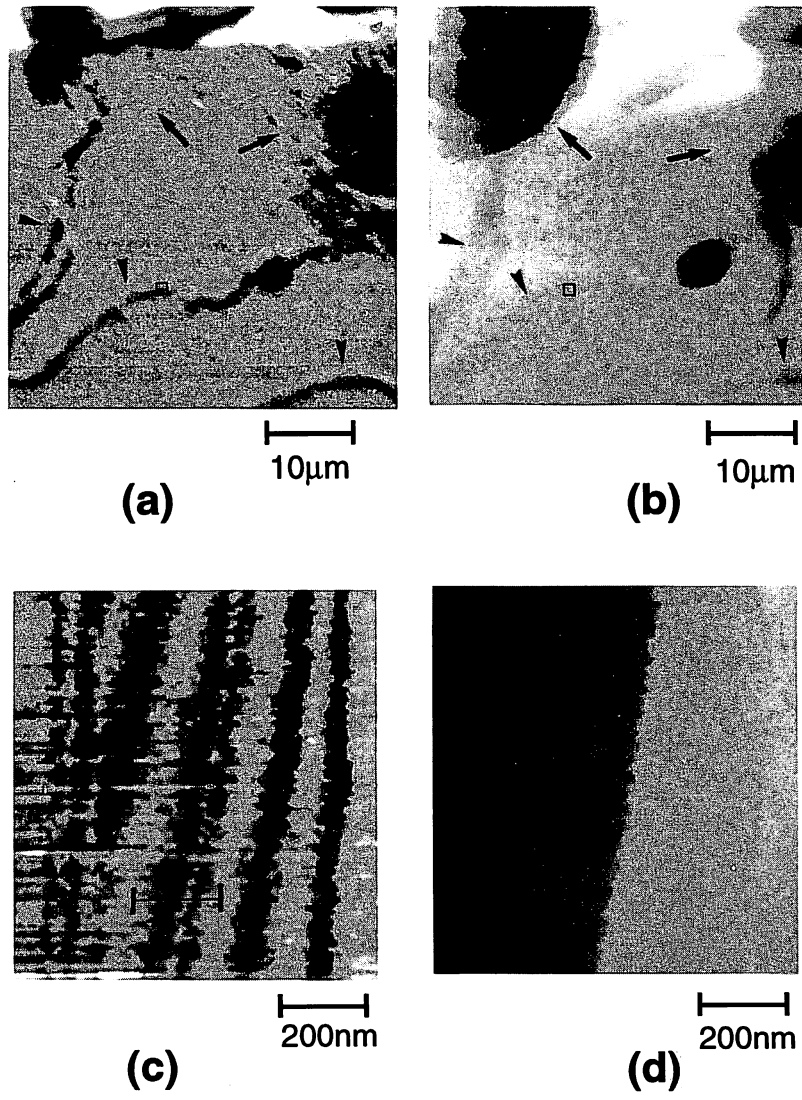

Fig. 7. Gray scale images (a,c) optical and (b,d) topographical variations obtained simultaneously by scanning a neuron sample (corresponding to region B in Fig. 5) labelled with toluidine blue. In either figures (a) and (b), arrows indicate cell bodies and arrow heads indicate neural processes. Here, the scan area for the case of (a) and (b) is 50×50 μm^2 while for (c) and (d) which show magnified scans over the neural process indicated by a square in (a) and (b) is 1×1 μm^2. The fringe like structures seen in (c) is believed to be microtubules and (e) shows a cross-sectional view of the intensity variation across the narrowest tube indicated by a line in (c). In the shear force image bright region corresponds to valley and dark region corresponds to hill.

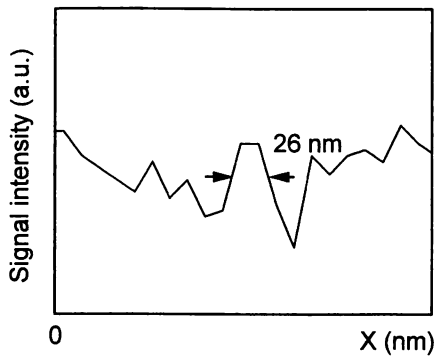

(e)

Fig. 7. Continued.

specimens such as neuron, its subcellular structures and their corresponding dimensions are well documented using an electron microscope. Therefore with the difference parameter δ, it is possible to get an immediate estimate of resolution, i.e., how well the present system could resolve. Therefore, comparing the observed value of 26 nm with the known value of 25 nm, the measure of resolution or δ could be estimated to be 1 nm which is quite small. This small value for δ suggests that the resolution of this observation results is very high and hence comparable to that of the electron microscope. To our knowledge, observations at such level take a leading edge of the results reported till now in imaging biological specimens. The reasons for this high resolution can be considered to be the result of the following factors.

1. Aperture diameter being almost the same as the sample size.
2. The observations were conducted very close to the aperture, i.e., in the proximity region or in other words the sample–probe separation being less than the radius of the aperture.
3. Field enhancement effects at the boundary existing between the glass fiber and the metal coating [19].

3.3. A quantitative comparison of labelled and unlabelled neuron samples

In our observations of neurons labelled with and without toluidine blue, we could clearly see some remarkable difference in the contrast of the overall image. In order to investigate these differences quantitatively, we define a following evaluating parameter contrast C and this is defined as follows.

Let the 2D image data array obtained from raster scanning of the sample be denoted by I. Let I_{max} and I_{min} be respectively the maximum and the minimum values of intensity in this 2D array of image data I. Then contrast C following the conventional definition is given as $C=(I_{max}-I_{min})/(I_{max}+I_{min})$.

The contrast values were calculated for different scanned images containing 256×256 pixels obtained for dyed and undyed neuron samples. It has been found that the average value of image contrast C for undyed samples is 0.17 while for dyed samples it is 0.35. This corresponds to an increase in the contrast of the overall image by nearly two times due to absorption labelling with dye.

4. Summary

In this paper, we reported about the high resolution imaging of microtubules present inside the neural process of neurons by PSTM operated under the illumination mode with shear force feedback. It has been demonstrated that with PSTM, it is possible to observe internal ultra structures such as microtubules lying underneath the cell membrane. Hence our results show that PSTM excludes the necessity of removing the cell membrane which is done to make observations by AFM and electron microscope and therefore demonstrate the immense potential of PSTM in conducting observations on biological specimens. The fwhm of the narrowest tube was found to be 26 nm. Comparing this with the diameter of a single microtubule of 25 nm determined using the electron microscope, the difference δ is as small as 1 nm which implies that the resolution of this observation is as high as that of the electron microscope. Such a level of observation takes a leading edge over the results reported so far. This high resolution is believed to be due to the existence of the boundary between the glass fiber and the metal coating of the apertured probe.

Acknowledgements

The authors would like to thank Dr. Hirofumi Kadono of Saitama University for his great assistance

in the development of scanning software for conducting PSTM experiments.

References

[1] D.W. Pohl and D. Courjon, eds., Near-field optics, NATO ASI series E, Vol. 242 (Kluwer, Dordrecht, 1993).
[2] M. Ohtsu, J. Opt. Dev. Techn. 10 (1995) to appear.
[3] S. Jiang, N. Tomita, H. Ohsawa and M. Ohtsu, Jpn. J. Appl. Phys. 30 (1991) 2107.
[4] S. Jiang, H. Ohsawa, K. Yamada, T. Pangaribuan, M. Ohtsu, K. Imai and K. Ikai, Jpn. J. Appl. Phys. 31 (1992) 241.
[5] N. Toda and M. Ohtsu, IEEE Photonics Technol. Lett. 7 (1995) 84
[6] M. Naya, T. Saiki, S. Mononobe, R. Uma Maheswari and M. Ohtsu, SPIE Proc. Scanning Probe Microscopes III, 2384 (1995).
[7] E. Betzig and J.K. Trautman, Science 297 (1992) 189.
[8] T. Pangaribuan and M. Ohtsu, Electron. Lett. 29 (1993) 1978.
[9] T. Pangaribuan, S. Jiang and M. Ohtsu, Scanning 16 (1994) 362.
[10] H. Tatsumi, H. Sasaki and Y. Katayama, Jpn. J. Physiology 43 (1993) S221.
[11] E. Betzig, A. Lewis, A. Harootunian M. Isaacson and E. Kratschmer, Biophys. J. 49 (1986) 269.
[12] R. Uma Maheswari, S. Mononobe and M. Ohtsu, IEEE J. Lightwave Technol., to be published.
[13] E. Betzig, P.L Finn and J.S. Weiner, Appl. Phys. Lett. 60 (1992) 2484
[14] M. Vaez-Iravani, R. Toledo-Crow and Y. Chen, J. Vac. Sci. Technol. A 11 (1993) 742.
[15] J.G. Nicholls, A.R. Martin, B.G. Wallace, From Neuron to Brain (Sinauer Assoc., Massachusetts, 1992).
[16] B. Alberts, D.Bray, J. Lewis, M. Raff, K. Roberts and J.D. Watson, Molecular Biology of the cell (Garland Publishing, New York, 1983).
[17] Our unpublished observations.
[18] H. Hartwig, J. Cell Biology 118 (1992) 1421.
[19] M. Specht, J.D. Pedaring, W.M. Heckl and T.W. Hansch, Phys. Rev. Lett. 68 (1992) 476.

Power spectral analysis for evaluating optical near-field images of 20 nm gold particles

R. Uma Maheswari[a], *H. Kadono*[a,b], *M. Ohtsu*[a,c]

[a] *Kanagawa Academy of Science and Technology,*
KSP East 408, 3-2-1 Sakado, Takatsu-Ku, Kawasaki-Shi, Kanagawa 213, Japan
Tel: +81-44-819-2071; Fax:+81-44-819-2072

[b]*Department of Environmental Science and Human Engineering*
Saitama University, 255 Shimookubo, Urawa, Saitama 338, Japan
Tel: +81-48-858-3460; Fax: +81-48-856-2577

[c]*Interdisciplinary Graduate School of Science and Engineering, Tokyo Institute of Technology, 4259 Nagatsuta, Midori -Ku, Yokohama Kanagawa 226, Japan,*
Tel: +81-45-924-5455;Fax: +81-45-924-1204

In spite of the very wide applications of a near-field optical microscope (NOM) in various fields such as observation of biological specimens, optical storage etc. [1,2], a systematic analysis of the images with respect to resolution and contrast is lacking. In this work using 20 nm gold particles (calibrated by electron microscope) fixed on a glass plate as the observation object, we have evaluated the transfer function of NOM.

Figure 1 shows a schematic of the experimental system of NOM operated along with shear force (SF) for sample-probe separation control. The inset shows the electron micrograph of apertured probe. Figure 2(a) shows the near-field image of gold particles obtained under a sample-probe separation of less than 5 nm with the inset showing a magnified view of the region indicated by arrow. Here the dark region corresponds to gold either observed as single or clustered. Figure 2(b) shows its Fourier power spectral density (PSD) . We have modelled the gold particles as a random array of circular dots and calculated the theoretical PSD [3]. Under large spatial fluctuations of the dots, the theoretical PSD could be approximated to that due to a single dot. Theoretical PSD of a circular dot is the Bessel function of first order with its first minimum occurring at the frequency (α_0) given by $\alpha_0=1.22/\rho_0$ where ρ_0 is the size of the dot. From Fig.2(b), the size of the gold particle could be determined using the minimum frequency f_0 as 22 nm. Further, by considering the imaging process as linear and approximating the spectrum in the region $f > 5\times10^6$ of Fig.2(b) as that due to a single particle, the transfer function could be estimated as $H(f/f_0) = 0.81(f/f_0)^{-0.16}$. The -3dB cutoff frequency, giving a measure of resolution is determined to be 1.2×10^9 which corresponds to a size of 0.8 nm. In other words, the system is capable of acheiving sub-nanometer resolution. This is much higher than the cut-off frequency determined by the size of the aperture ($\approx3.3\times10^8$). Such a high resolving ability of our NOM system could be attributed to the boundary effect which has been observed earlier by us [4]. Very high frequency evanescent fields would be generated at the metal-glass boundary present at the edges of the apex of the apertured probe. We believe this evanescent field was detected on being converted into propagation field by the sample.

REFERENCES

1. D. W. Pohl and D. Courjon, eds., *Near-field optics*, NATO ASI series E, Vol. 242 (Dordrecht, The Netherlands, 1993).
2. M. Ohtsu, J. Lightwave Tech., 13 (1995) 1200.
3. R. Uma Maheswari, N. Takai and T. Asakura, J. Opt. Soc. Am. A, 8 (1992) 1391.
4. R. Uma Maheswari, H.Tatsumi, Y. Katayama,M. Ohtsu, Opt. Comm.,120 (1995) 325.

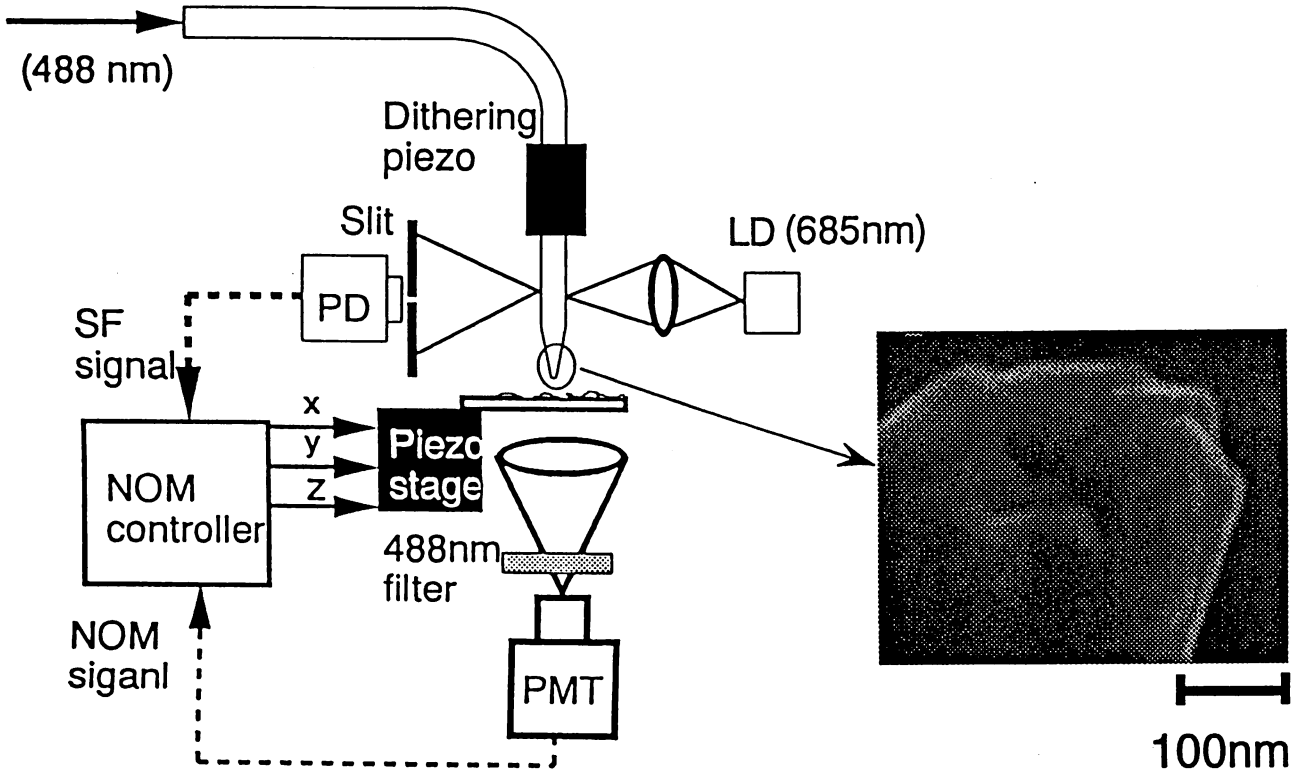

Fig.1 A schematic view of NOM with the inset showing electron micrograph of apertured probe

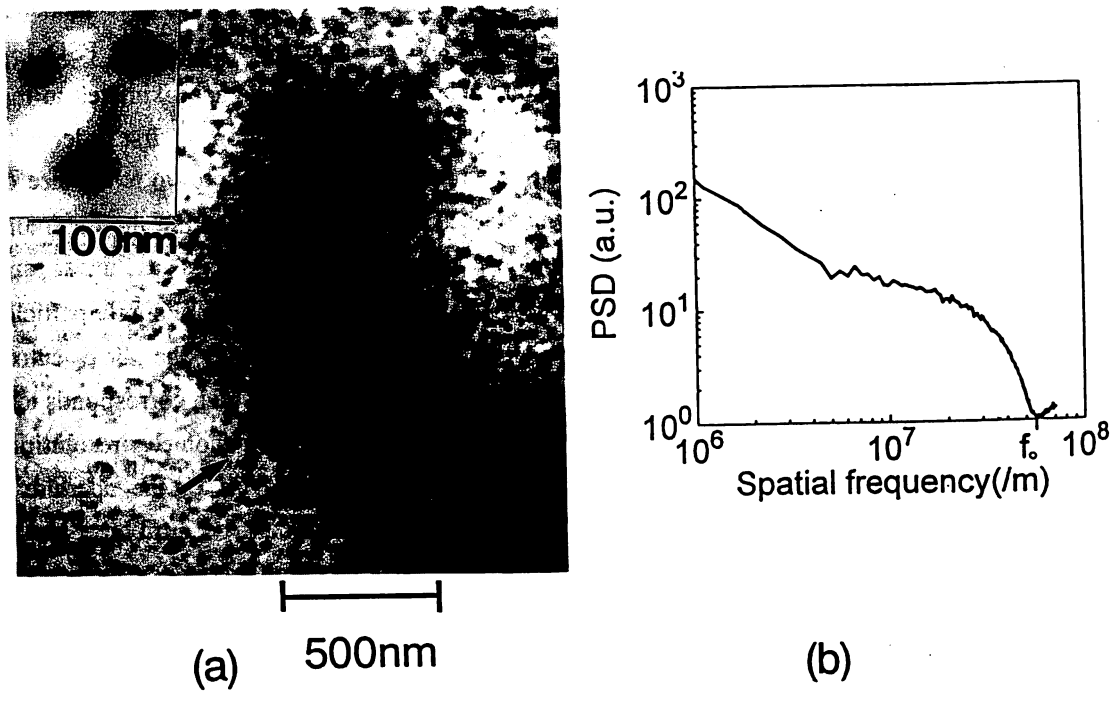

Fig.2 (a) Near-field image of 20 nm gold particles and (b) its PSD

Observation of subcellular structures of neurons by an illumination mode near-field optical microscope under an optical feedback control

R. Uma Maheswari*, S. Mononobe*, H.Tatsumi**,***, Y. Katayama** and M. Ohtsu*,****

* *Kanagawa Academy of Science and Technology, KSP East 408, 3-2-1 Sakado, Takatsu, Kawasaki, Kanagawa, Japan*

** *Medical Research Center, T,okyo Medical and Dental University, Chiyoda Ku, Tokyo, Japan*

*** *PRESTO JRDC, Japan*

**** *Tokyo Institute of Technology, 4259 Nagatsuta, Midori Ku, Yokohama, Japan*

Dynamic in-vivo observations of biological specimens are usually conducted by conventional optical microscope which provide only a diffraction limited resolution to the order of the wavelength of light. For conducting observations of smaller structures, an electron microscope is usually used and it could see only dried specially prepared samples. We reported earlier about the observation of microtubules present in the neural process of neurons with an illumination mode NOM operated along with shear-force sample-probe separation control with a resolution equivalent to that of the electron microscope [1]. However, the use of shear force technique has got problems such as (1) chance of damaging sample during dithering of the probe, (2) cross-talk problems between the shear force topographic image and the near-field optical image, (3) difficulty in interpretation of the image due to the mapping of equiforce contour and (4) difficulties in extending the operation in liquid.

In this study, we propose an illumination mode NOM that uses the rapid decay of the evanescent signal for controlling the sample-probe separation. The proposed method of optically controlling the sample-probe separation maps equipower contour of the evanescent field and hence the interpretation of the illumination mode image is made easier. Further, it is made easier to implement the system for conducting observation in liquid which is very essential for bio-specimens.

The experimental system of an illumination mode operated under optical feedback is shown in Fig.1. Light from Ar^+ laser is coupled into the probe having a nanometric protruded tip as shown in Fig.2 with foot and apex diameters of the protruded region being less than 30 nm and 10nm, respectively, to illuminate the sample. In order to generate the rapidly decaying evanescent light for feedback control, a small right angled prism was optically bonded to a parallel plate and light from an LD was made to incident at the angle of total reflection. The sample substrate with neurons fixed on the surface was mounted on the parallel plate with a sandwitch of index matching oil. The evanescent field generated on the sample surface is picked up by the same probe and detected through a photomultiplier tube. To have a better S/N ratio, phase-sensitive detection has been employed in both the detection of the evanescent field and the scattered Ar^+ light. To make a qualitative comparison of the images obtained under evanescent feedback, a shear force detection scheme has also been included in the system. It has been found that the rise of the evanescent intensity is as steep as the of decrease of dithering amplitude and hence the evanescent signal can be profitably used for sample-probe separation feedback control with high sensitivity.

Figures 3 (a) and 3(b) show a magnified view of the region of a branching neural process obtained under shear force and evanescent feedback, respectively. Our results show that under evanescent feedback control, it is possible to obtain

the topographical variations almost the same as that under shear force. However, apart from the existence of similar features in Figs. 3(a) and 3(b), apparently there exist also some differences. At the meeting, we will present results on our comparative study and on observations conducted in liquid.

1. R. Uma Maheswari, et.al., Opt. Commun., **120** (1995) 325.

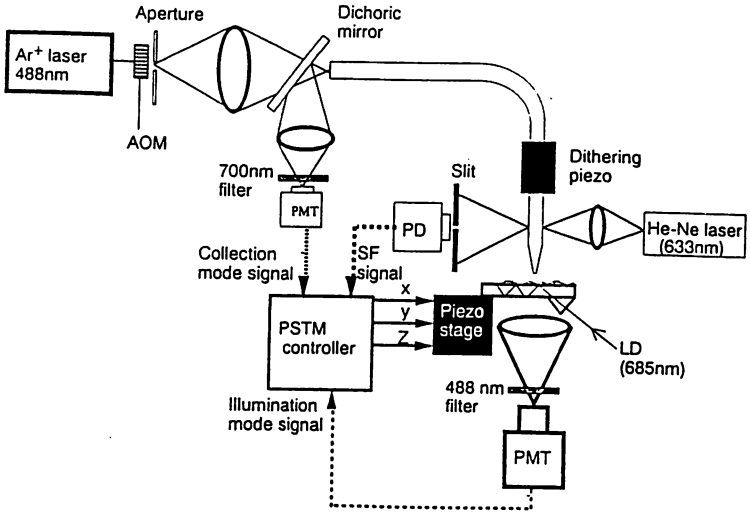

Fig. 1 Experimental system

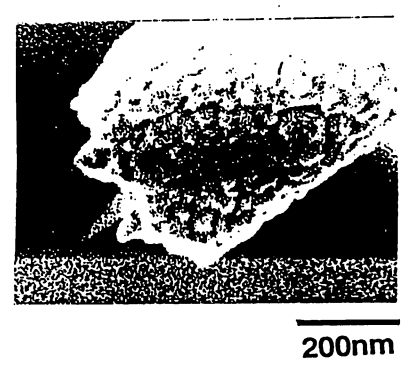

Fig.2 A SEM view of probe

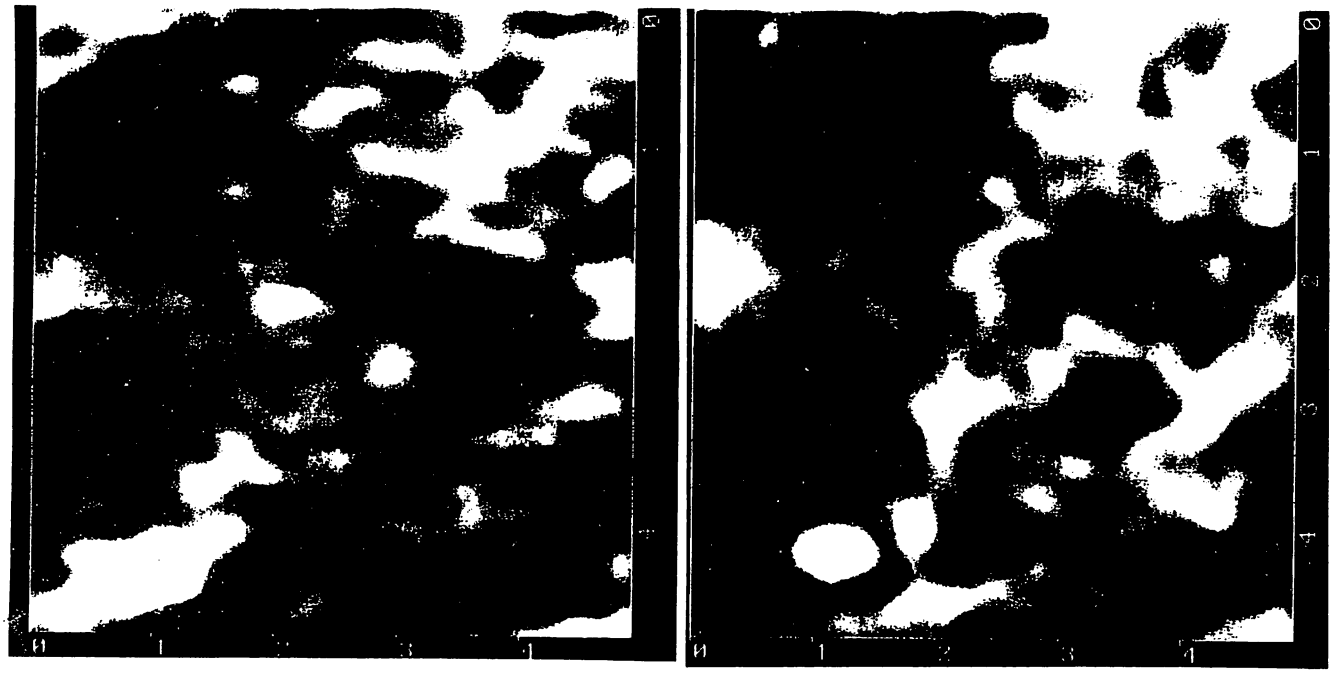

Fig.3 i-mode NOM image of neural process under different feedback control (a) shear force (b) evanascent

Study of Quantum Optical Effects with Scanning Near-Field Optical Microscopy

Sang-Kee Eah, Wonho Jhe

Physics Department, Seoul National University, 151-742 Seoul, South Korea

T. Saiki, and M. Ohtsu

Kanagawa Academy of Science and Technology, Ohtsu Photon Control Project, KSP

East Room 408, 3-2-1, Sakato, Takatsu-ku, Kawasaki 213, Japan

We did front surface photoluminescence measurement of Si-doped bulk GaAs using scanning near-field optical microscope. We used the fiber probe tip simultaneously as the excitation laser source and the collector of luminescence from GaAs. Due to Fabry-Perot etalon effect, the excitation laser is reflected or transmitted with oscillations of $\lambda_{He\text{-}Ne}/2$ period as the gap between the probe and the GaAs surface varies. The luminescence from GaAs is also transmitted with oscillations of $\lambda_{GaAs}/2$ period due to the same Fabry-Perot etalon effect. Therefore the luminescence light intensity collected through the fiber probe tip, shows beating oscillations due to two oscillations of different periods. When the probe is near to the GaAs surface, the collected luminescence light intensity increases due to tunneling of evanescent waves, which is not detected and thus lowers external quantum efficiency of conventional light emitting diode. When we collected the luminescence using lens with the probe near to GaAs surface, the intensity increases due to coupling of evanescent waves into propagating waves even though there is shadowing effect of the relatively large metal coating.

Theoretical Comparison of Collection-mode NOM Configurations

A. Zvyagin* and M. Ohtsu*,**
* Tokyo Institute of Technology, ** Kanagawa Academy of Science and Technology

The objective of our study of a near-field optical microscope (NOM) is to find such NOM configuration which will provide one with *true surface topography*. For this purpose we have theoretically modelled a *collection-mode* NOM in the following way: 1. A sample on the flat surface illuminated under TIR condition generates an optical field which can be represented as a spectrum of plane mostly evanescent waves. 2. This near-field can be probed by a protruded probe tip closely brought to the surface by means of scattering these plane evanescent waves, provided: a) the probe can be modelled by a small sphere; b) the small sphere scatters these evanescent waves as an electric point-like dipole; c) the system "probe-sample" is *almost uncoupled*. Then, intensity detection in the far-field zone versus lateral position of the probe enables one to obtain *true electric near-field* intensity surface mapping [1]. The question how the latter relates to the *true surface topography* can be approached in the result of analytical and numerical study of the near-field over a small sample via the perturbation theory based on the nonglobal macroscopic theory. The latter is stated as a homogeneous boundary-valued problem (Helmholtz equation) subject to nonlocal boundary conditions which are known as the optical extinction theorem written for the case of two dielectric media. Here we consider a plane wave incident from a dielectric (glass) upon another dielectric (air), as it is shown in Figure 1 (a).

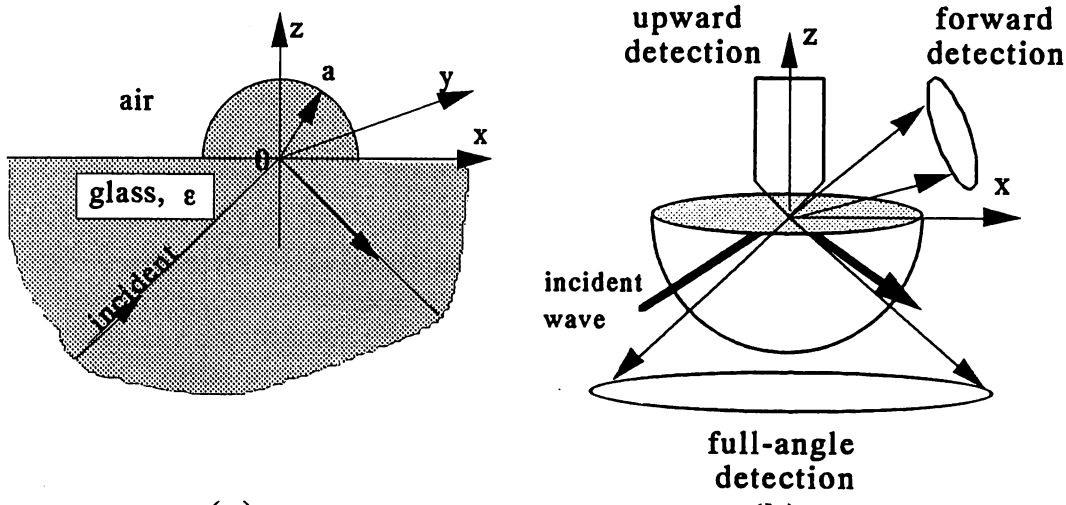

Fig. 1

The interface between two media consists of the planar surface and a small sample on it. The perturbation approach is applied to treat a small sample with its height as a perturbation parameter [2]. Analytically, the

near-field over the sample comes out in the following structural form:

$$\begin{bmatrix} measured \\ electric \\ near-field \end{bmatrix} = \begin{bmatrix} coupling \\ factor \end{bmatrix} \left\{ background + \begin{bmatrix} structure \\ function \end{bmatrix} \times filter \begin{pmatrix} propagation \\ translation \\ diffraction \end{pmatrix} \right\}.$$

The total near-field intensity over a semi-spherical sample is calculated to model the constant height scan (Fig. 2). It exhibits strong near-field localization around the sample, particularly, if it is illuminated by the p-polarized plane wave, as shown in Fig. 2 (c). On the other hand, if the s-wave is incident on it: the image is inverted and anisotropic (see Fig. 2 (a)).

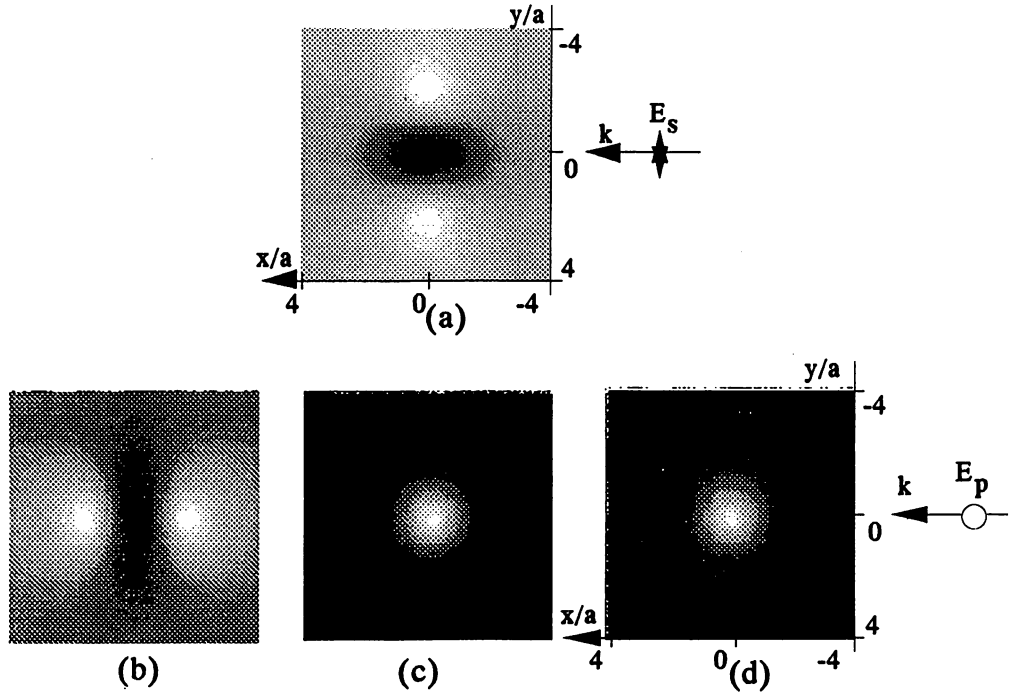

Fig. 2

The following collection-mode NOM configurations can be analysed: 1) upward detection; 2) full-angle detection; 3) forward (backward) detection, as they are shown in Figure 1(b). Corresponding for each configuration calculated grey-scale image is depicted in Figure 5 (b), (c), and (d), respectively - for the p-polarized incident light, and in Figure 5(a) - for the s-polarized incident light. On the basis of our results, we propose the 'full-angle detection' or the 'forward detection' configurations of collection-mode NOM in conjunction with the illumination by the p-polarized incident light which is advantageous for reproduction of the true surface topography, provided: (i) the sample is the same dielectric as the substrate and is small in all three dimensions; (ii) the probe is an ideal point-like weak-interacting electric dipole.

References

[1] - D. van Labeke and D. Barchiesi, J. Opt. Soc. Am. A **10**, 10 (1993) 2193.

[2] - G. S. Agarwal, Phys. Rev. B **15**, 4 (1977) 2371.

Comment on the Possibility of Longitudinal Electromagnetic Waves on the Surface of Dielectrics

H. Hori[a], K. Kitahara[b] and M. Ohtsu[c]
Dept. Elec. Info. Eng., Yamanashi Univ.[a]
Dpt. Appl. Phys., Tokyo Inst. Tech.[b]
Dpt. Elecron. System, Tokyo Inst. Tech.[c]

It is possible to produce longitudinal electromagnetic waves on dielectrics surface by combining two evanescent waves, which are transmitted from the dielectrics surface from the incident s-polarized waves. Suppose we have an incident s-polarized wave,

$$\boldsymbol{E}_i = E_s e^{ik(x\sin\theta_1 + z\cos\theta_1) - i\omega t}\boldsymbol{e}_y,$$

where $k = n\omega/c$ is the incident wave number and n is the refractive index of the dielectrics. The transmitted wave is

$$\boldsymbol{E}_t = E_t e^{i(xk_t\cosh\beta - \omega t) - zk_t\sinh\beta}\boldsymbol{e}_y,$$

with

$$E_t = \frac{2n\cos\theta_1 E_s}{n\cos\theta_1 + i\sinh\beta}$$

and $\theta_2 = i\beta + \pi/2$ is the transmission angle. In particular, at the critical angle, we have $\beta = 0$. Therefore $\boldsymbol{E}_t = E_t e^{i(xk_t - \omega t)}\boldsymbol{e}_y$,. We may send another incident wave in the y direction. Thus we may construct the following electric field on the surface,

$$\boldsymbol{E}_t = E_t^{(1)} e^{i(xk_t\cosh\beta - \omega t) - zk_t\sinh\beta}\boldsymbol{e}_y + E_t^{(2)} e^{i(yk_t\cosh\beta - \omega t) - zk_t\sinh\beta}\boldsymbol{e}_x.$$

If we choose $E_t^{(1)} = E_t^{(2)}$, then we have $\mathrm{rot}\boldsymbol{E}_t = 0$ along the line $x = y$.
The physical implication of this property will be discussed.

Observation of an atomic sapphire step by a collection mode near-field optical microscope

R. Micheletto*, S. Mononobe*, M. Ohtsu*,**, M. Yoshimoto*, T. Maeda*, T. Ohnishi* and H. Koinuma*

* Kanagawa Academy of Science and Technology, KSP East 408, 3-2-1 Sakado, Takatsu, Kawasaki 213, Japan.

** Tokyo Institute of Technology, 4259 Nagatsuta, Midori Ku, Yokohama-227, Japan.

We reported earlier about the successful observation of flagellar filaments of Salmonella of 25 nm [1]. Here, we present the improvement of the system, its optimization and calibration. In order to achieve higher resolution, it is necessary to examine a nanometric and calibrated sample as a reference. In our experiments, we have used an ultraflat sapphire plate consisting of 2.5 nm atomic steps distributed uniformly all along its surface as a reference sample. The sample was prepared by us using an innovative crystal growth technique [2]. The measurement was performed advantageously using the rapid variation of the evanescent intensity with respect to the sample-probe separation by a collection mode near-field optical microscope (c-mode NOM) without the use of the shear force technique which can injure the sample and create cross-talk problems between the optical image mapped and the shear force image. Moreover, a shear force system maps the equi-force contour lines which are not equivalent to the equi-power lines of the evanescent field. In Fig. 1 is shown a schematic diagram of the c-mode NOM used in our experiments. For comparison and calibration, we have examined the sapphire sample first by a commercial AFM system. The step resulted to be of 2.5 nm high and the step profile has got a horizontal spread of around 150 nm and hence is not perfectly sharp. To observe such a small feature by means of c-mode NOM, it is necessary to work under the condition of extremely small sample probe separation and with a protruded tip of the fiber probe as small as possible. To prepare our system to work at small distance (under 10 nm), we performed several modifications to improve vibration control and to optimize the performance of every device in the system of the feedback loop. The resulting NOM image of the detected 2.5 nm step is shown in Fig.2. Our measurement shows that the same morphology as the original sample with a lateral spread of around 150 nm is clearly visible and also the local roughness is reproduced. The image was taken at constant signal mode, i.e., the sample-probe separation is varied to have a constant evanescent intensity.

The image of Fig.2 has been obtained in S-polarization (electric field parallel to the sample surface) with light coming from left to right normal to the step line. The sample probe separation was around 5 nm evaluated approximately by making total contact between the sample and the probe at the end of the scan. We performed several experiment varying the sample probe separation from 5 to 100 nm distances. However, only at the smallest distance, the step could be observed. We tried also to measure at different polarization and direction of the wavevector, but the step was not visible in that conditions. This behaviour is in good agreement with the results of our earlier investigation on the dependence of the quality of the mapped image as a function of several optical parameters such as polarization, sample-probe separation, direction of light with flagellar filaments [1]. We believe that this work demonstrated the possibility to go toward sub-nanometric resolution with an all optical c-mode NOM system. We plan to apply power spectral analysis for more quantitative evaluation and we think that a more compact and miniaturized improved system is possible for even more high detection sensitivity.

1. M. Naya, S. Mononobe, R. Uma Maheswari, T. Saiki and M. Ohtsu, Opt. Commun., **124** (1996) 9.
2. M. Yoshimoto, T. Maeda, T. Ohnishi, H. Koinuma, O. Ishiyama, M. Shinohara, M. Kubo, R. Miura and A. Miyamoto, Appl. Phys. Lett., **67** (1995) 2615.

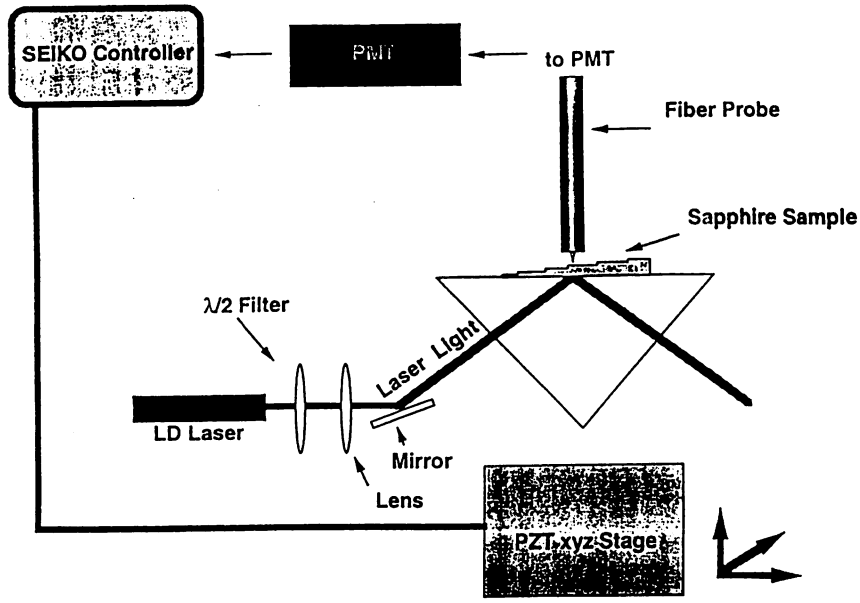

Fig.1 Experimental system

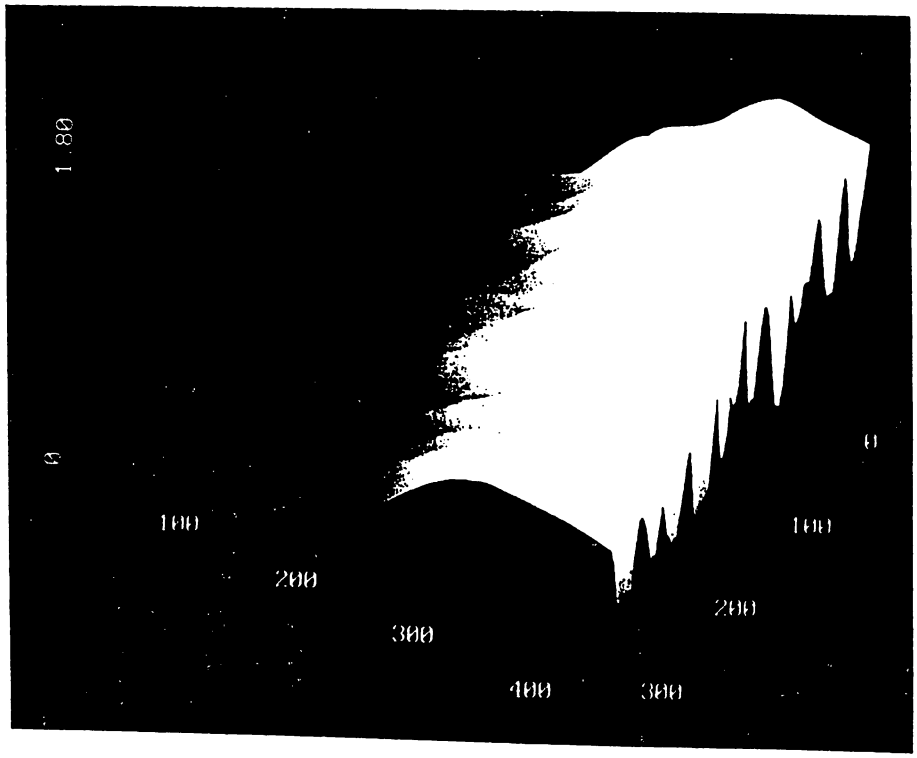

Fig. 2 c-mode NOM image of atomic step of sapphire of 2.5 nm height

WL1

Determination of slant angle of p-n interface by multi-wavelength near-field photocurrent measurement

GT Saiki, Y Yokoyama , M Ohtsu, *N Saito, *J Kusano,*Kanagawa Academy of Science and Technology, 3-2-1 Sakado, Takatsu-ku, Kawasaki, Kanagawa 213, Japan*

Photocurrent measurement with near-field excitation is a novel technique for the diagnostics of semiconductor photonic devices.[1,2] So far, near-field scanning optical microscope has been employed for the spatially-resolved observation of small structures on the surface or optically thin materials. In the study of bulk devices, however, their internal optical and transport properties should also be precisely examined. As a new technique, we propose a multi-wavelength near-field photocurrent measurement, applying to a lateral p-n junction. By systematically varying to the optical penetration depth from smaller than aperture diameter to the order of wavelength, we obtain "tomographic" information of the investigated material. Using this method, the orientation of p-n slanted interface is quantitatively determined for the first time.

A schematics of the sample structure is shown in Fig.1 (a).[3] Si-doped GasAs layers are grown on the patterned (111) A substrates by molecular beam epitaxy. Due to the amphoteric nature of Si dopant in GasAs, the lateral p-n junctions are achieved at the upper and the lower interfaces. 200 nm aperture is controlled in close proximity to the sample (z~10 nm). In the case of the 200 nm aperture, both propagating and evanescent modes of the aperture are coupled to propagating modes in GaAs (n=3.5) with cone angle ϕ as shown in Fig. 1 (b). By using various laser sources, optical penetration depth in GaAs is tuned from 80 nm to 900 nm.

WL1 Fig 1.(a) Schematic structure of lateral p-n junctions. The sample is tilted by 15° in order to avoid its contact with the cladding of the fiber tip.(b) Schematic of experimental geometry.

The cross-sectional profiles of photocurrent signal are shown in Fig.2. At the excitation wavelength of 488 nm, due to small penetration depth of 80 nm, the resolution is determined by the aperture size and the carrier diffusion length. With increasing the excitation wavelength, the decay length becomes longer and the symmetric nature reverses. We believe that the longer decay length in n-region than in p-region at deeper penetration depth can be explained by the slant of the p-n interface (shown as θ in Fig. 1 (b)). Here, we make an analysis of the asymmetric signal behavior using a one-dimensional model. Based on the signal profile of λ=488 nm excitation, we estimate the effective optical decay length in n-(L_n) and p-region (L_p). The geometrical meaning of L_n and L_p, relating to the penetration depth L_{pd}, is shown in Fig. 1 (b) and is also written as $L_i = (\sin\phi \pm \tan\theta\cos\phi)\, L_{pd}$ (+; i=n, -; i=p). Figure 3 shows plots of L_n and L_p as a function of penetration depth. From the gradients of the fitted lines, we find ϕ=25±5° and θ=9±5°, respectively. This cone angle ϕ corresponds to the cutoff wavevector of evanescent modes of the aperture $k_{//}$=0.011 nm^{-1}, which is in agreement with the value of 1/a (a the radius of the aperture). A total incline of the p-n interface of 24° to the p side, which is the sum of the observed slant angle θ and the intended tilt angle in the experimental setup, can be explained by the difference in the growth rates of GaAs on (311)A slope and (111)A surface.

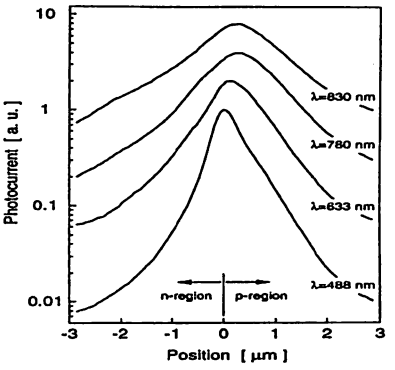

WL1 Fig 2. Cross-section al profiles of near-field photocurrent signal as a function of excitation wavelength.

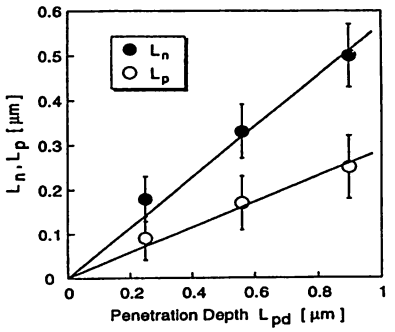

WL1 Fig 3. Plots of L_n and L_p as a function of penetration depth L_{pd} at wavelengths 633, 780 and 830 nm.

In summary, we demonstrate the ability of multi-wavelength near-field photocurrent measurement in the investigation of internal properties of bulk devices. The "tomographic" diagnostics with this method will provide a new insight into understanding the crystal growth mechanism.

1. SK Buratto et al, Appl Phys. Lett 65, 2654 (1994).
2. MS Unlu, BB Goldberg, D Herzog, D Sun and E Towe, Appl. Phys. Lett. 67, 1862 (1995).
3. T Saiki, S Mononobe, M Ohtsu, N Saito and J Kusano, Appl. Phys. Lett. 67, 2191 (1995).

NHK Science and Technical Research Laboratories, 1-10-11 Kinuta, Setagaya-ku, Tokyo 157, Japan.

FO2 **1.45 p m**

Spatially resolved detection of photoluminescence and electroluminescence from lateral p-n junctions on GaAs(111)A patterned substrates using a photon scanning tunneling microscope

N Saito, J Kusano, H Okumura, T Aida, K Takizawa, T Saiki*, M Ohtsu** *NHK Science and Technical Research Laboratories, Setagaya-ku, Tokyo, Japan*

Formation of lateral p-n junctions by the expitaxial growth on patterned substrates is proposed and intensively investigated for the advanced surface light emitting devices, which will be useful in parallel optical information processing system in future. It is important to make p-n junctions with abrupt interfaces for the fabrication of high-quality devices. For this purpose, it is necessary to clarify the interface structure of the p-n junctions with a high spatial resolution. Since photon scanning tunneling microscope (P-STM) has not only the spatial resolution of the order of 10nm, but also ability of simultaneously measuring the optical spectra and the sample structure through the shear-force measurements, it is suitable for the optical characterization of lateral p-n junctions, in which electronic state is determined by the structure. In this paper, we have studied the interface structure of the lateral p-n junctions through the spatially-resolved detection of electroluminescence (EL) using a collection-mode P-STM in combination with spatially-resolved photoluminescence (PL) measurement which uses an illumination-mode P-STM.

Silicon-doped GaAs layer was grown by molecular beam epitaxy on a GaAs (111)A substrate which has a (311)A slope (Fig. 1). Since Si acts as an acceptor on the (111)A substrate and as a donor on the (311)A slope, lateral p-n junctions are formed at the lower and the upper ends of the slope. The light emitted from the two junctions was independently collected by a fiber probe and directed to an avalanche photo diode. We have newly fabricated a special fiber probe whose tip has a stepped cone angle, so that the tip is long enough to avoid the crash of the probe shoulder to the sample, and thick enough not to suffer from the optical loss in the tip.

Spatial change of the PL peak wavelength is shown in Fig. 2(a) with the sample structure (Fig. 2(b)). The transition regions in which the PL peak wavelength shifted from the value of p-type (870nm) to that of n-type (855nm) were clearly observed. The width is determined to be 1.8 μm in the upper junction and 5.5 μm in the lower one. The intensity of EL for the two junctions is shown as functions of the position (Figs. 2(c) and (d)). Full width at half maximum is found to be 1.1 μm which is the same for the two junctions.

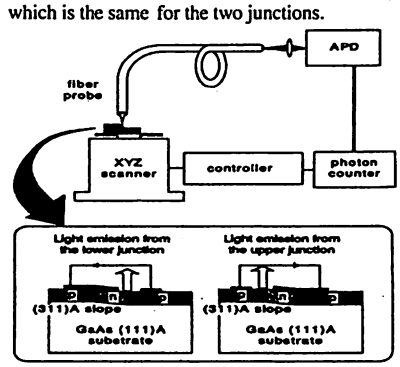

FO2 Fig 1. Schematic diagram of the sample structure and the experimental setup for a collection-mode photon scanning tunneling microscope.

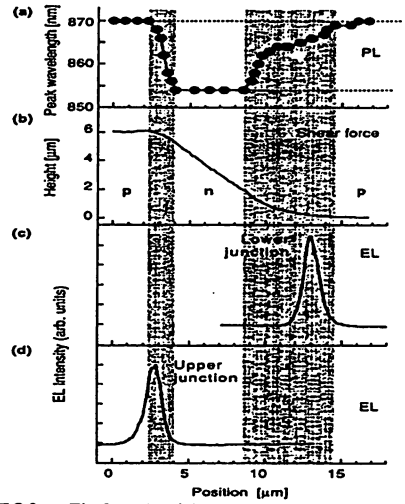

FO2 Fig 2. Spatial change of (a) the photoluminescence peak wavelength, (b) the sample structure, and the intensity of electroluminescense as a function of the position (c) for the lower junction and (d) for the upper junction.

Carrier distribution is determined from the PL measurement that the degree of mixing of n-type carriers and p-type ones changes gradually in the transition regions. The EL results show that the junctions exist at the point where PL peak wavelength has the same value in the transition regions.

In summary, we have demonstrated the direct determination of the position of light emission in lateral p-n junctions through the

spatially-resolved detection of photoluminescence and electroluminescence. Local characterization with a photon scanning microscope is shown to be useful in the analysis of optical devices.

**Kanagawa Academy of Science and Technology, Takatsu-ku, Kawasaki, Japan*
***Tokyo Institute of Technology, Midori-ku, Yokohama, Japan.*

Photon scanning tunneling microscopy with light-emitting probes

† K. Kurihara, ‡K. Watanabe and †‡ M. Ohstu

†Kanagawa Academy of Science and Technology
KSP East 408, 3-2-1 Sakado, Takatsu-Ku, Kawasaki-Shi, Kanagawa 213, Japan
Tel:+81-044-819-2071, Fax:+81-044-819-2072
E-mail:LDF03543@niftyserve.or.jp

‡Interdisciplinary Graduate School of Science and Engineering, Tokyo Institute of Technology
4259 Ngatsuta, Midori-Ku,Yokohama-Shi, Knagawa 226, Japan
Tel:+81-045-924-5455, Fax:+81-045-921-1204

Abstract

Photon scanning tunneling microscope is developed with a light-emitting probe which has laser dye on the top of a sharpened fibers. Images are obtained by detecting fluorescence from the dye excited by evanescent light.

1 Introduction

Recently, much attention has been focused on photon scanning tunneling microscope (PSTM) for its high spatial resolution [1, 2]. In conventional optical microscope, since objects are observed with propagating electromagnetic waves, spatial resolution is limited to diffraction-limit. However, in PSTM, as light to be observed with is not propagating waves but evanescent field which is confined to sub-wavelength distance from the object, spatial resolution is limited by the size of the probes used in PSTM.

PSTM is a part of scanning probe microscope (SPM) family, in which a sharp tip is used as a probe and is scanned on the sample surface at sub-wavelength distance. In PSTM, an optical fiber is usually used as the probe.

In this paper, we report PSTM with light-emitting probes which has laser dye molecules on the flattened top of the sharpened core of optical fibers. The light-emitting probes for PSTM are developed, then with the probes, for the first time to our knowledge, imaging results of PSTM are obtained. The light-emitting probes interest us in the following ways: a PSTM probe to improve the optical coupling efficiency between a probe and the sample surface, and a point light source to demonstrate optical quantum effects.

Further, the light-emitting probes we developed can work as a kind of submicrometer optical fiber sensors. Recently, submicrometer oxygen sensors have been reported [3]. Combining these submicrometer sensors with PSTM enables us to obtain images of chemical and biological materials. Developing PSTM with such functional probes is expected in chemistry and molecular biology.

2 Fabrication of light-emitting probes

Optical fiber probes with 0.3 μm diameter flattened top core are fabricated to attach light-emitting materials to the flattened top area. Attachment is performed mechanically with micromanipulater system.

As preliminary experiments, laser dye molecules of Rodamine 6G have been used as the light-emitting materials.

2.1 Fabrication of flattened top fiber probes

Flattened top fiber probes are fabricated by a chemical etching method. The fibers used here were single-mode fibers of a 125 μm cladding diameter and 3.5 μm core diameter. These fibers have a core with a high level of GeO_2 doping (doping ratio 27 mol %). Difference in etching rate between core and cladding is exploited to sharpen the core of fibers with buffered hydrofluoric acid solution. Here, fabrication of the flattened top fiber probes due to a two-step etching method [4]is described. First, fibers are etched at a temperature of 25°C for a duration of 75 *minutes* in an etching solution of composition ratio1.6:1:1, which corresponds to the order of NH_4F, HF and H_2O, respectively. Second, these fibers are etched at the same temperature for 60 *minutes* in an etching solution of composition ratio 10:1:1. Under these conditions, highly reproducible probes are obtained, with a cladding diameter of 30 μm diameter and flattened top core diameter of 0.3 μm.

2.2 Attachment of light-emitting dye to fiber probes

To attach light-emitting dye molecules to the flattened top fiber probes, micromanipulater system is used consisting of an optical microscope and mechanical micromanipulaters. The micromanipulater system has two jigs, one of which holds the flattened top fiber probe. The other jig holds a capillary containing solution of the light-emitting dye dissolved in ethanol. The capillary is made by pulling a Pyrex glass tube of 1 *mm* outer diameter and 0.6 *mm* inner diameter. The glass tube contains a 0.1 *mm* diameter glass rod, which makes the capillary easily filled with the dye solution owing to capillary attraction. The pulled capillary has a outer diameter of 1 μm and an inner diameter of 0.6 μm. The light-emitting dye solution is injected into the capillary. Rhodamine 6G is used as the light-emitting dye because it has a high optical damage threshold and high emission efficiency. We used several concentrations of the solution, starting from $0.063 mol/l$ up to $0.2 mol/l$. The procedure of attaching the dye on the top of probes is shown in Fig.1. It is done while observing with the optical microscope. First, the flattened top fiber probes and the capillary containing solution of the dye in ethanol are set

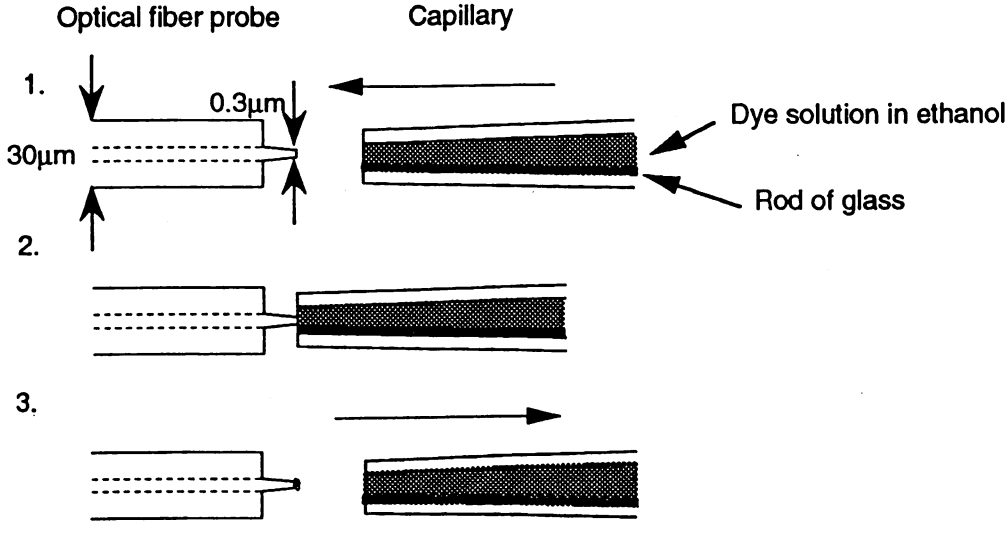

Fig. 1. A schematic of attaching the dye solution to the top of a fiber probe.

on the jigs of micromanipulater system. Then, the tip of the capillary is approached toward the top of the flattened top fiber probes and touched to it. Finally, they are separated. Figure 2 shows scanning electron micrographs of the light-emitting probe. The volume of the dye deposited on the probes as estimated from the SEM photograph is around $28 \times 10^{-18} l$ with radius being 150 nm diameter and thickness being 50 nm. Using this volume and the lowest concentration of the dye solution, the number of dye molecules at the top of the probes is estimated to be 1×10^6. However, due to the fast evaporation of alcohol at the top of the capillary, actual number of molecules is expected to be higher by a factor of 10 to 100.

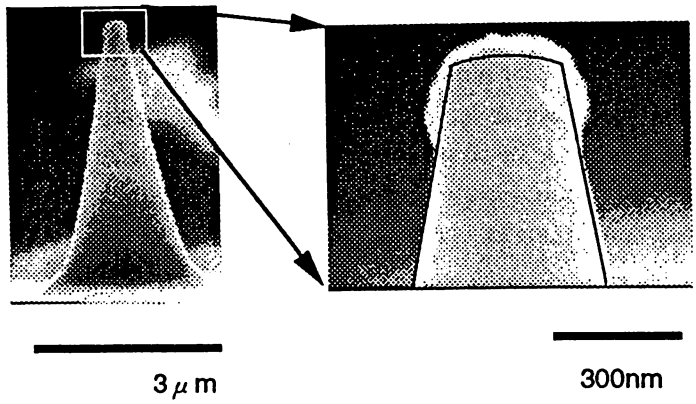

Fig. 2. SEM micrographs of flatten-top fiber probes with dye on the top of a core.

3 PSTM with light-emitting probes

Using these probes, PSTM is performed. A schematic of the setup is shown in Fig.3. The sample is a compact disc, which has a grating structure of period, 2 μm, and a Moth's eye pattern on the grating structure. Each eye has a diameter of 0.3 μm and a height of 0.1 μm. The interval between each eye is 0.1 μm. The sample is illuminated under total reflection by cw Ar^+ laser of 488 nm wavelength. The light-emitting probe is scanned on the sample surface by controlling separation between the sample and

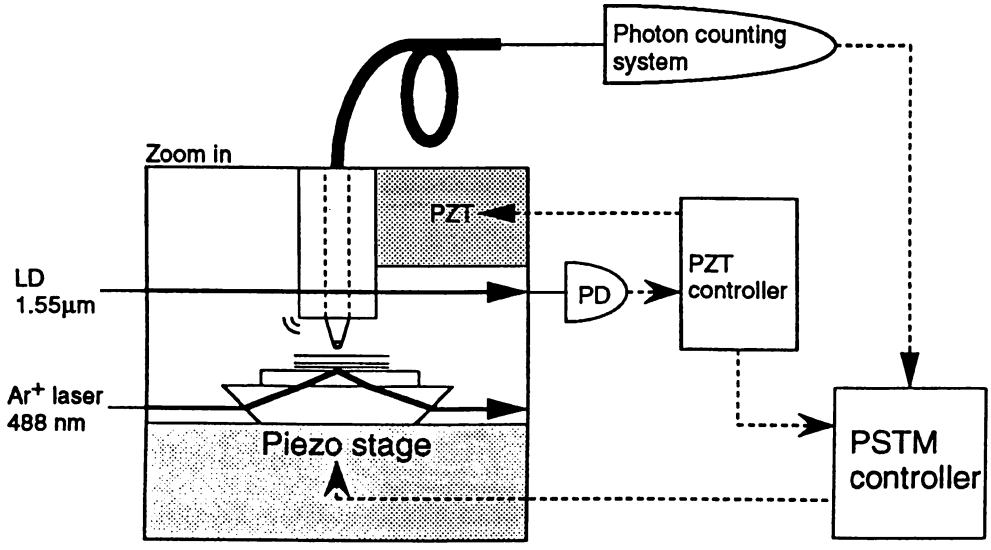

Fig. 3. A schematic of the experimental arrangement of PSTM with the light-emitting probe under shear force control.

the probe with shear force feedback. The Rhodamine 6G on the top of probes is excited by evanescent light generated on the sample surface and emits fluorescence centered around 600 nm wavelength. The fluorescence is coupled with the optical fiber, passed through a holographic notch filter (488nm cut filter by a factor of 10^6), a 30cm monochromator and finally detected with a photomutiplier tube by the photon counting method. Figure 4 shows (a) a shear force image and (b) a PSTM image. Compared with the share force image in Fig. 4 (a) which gives information on topography, the PSTM image in Fig. 4 (b) has low contrast of the grating structure of 2 μm period, but high contrast of the Moth's eye pattern. Further, spatial power spectrum analysis is applied to images of Fig. 4 (a) and (b). The obtained profiles reflect smallest structure of the interval of 0.1 μm between each eye. The results show an good agreement with CD structure.

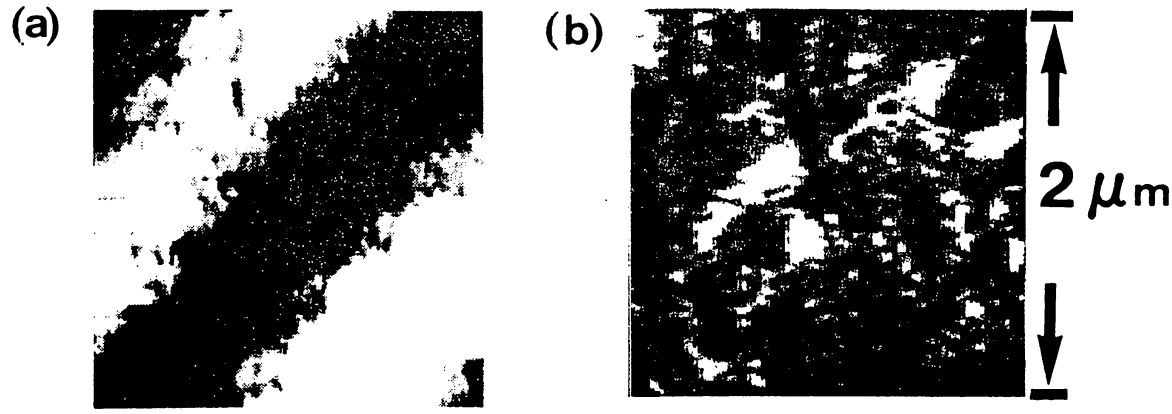

Fig. 4. CD images (a) due to shear force (b) due to PSTM with the light-emitting probe.

4 Conclusions

The light-emitting probes for PSTM are developed. The PSTM image with the probes shows high contrast of sub-wavelength structure but low contrast of wavelength structure. Fabricating light-emitting probes coated with metal is in progress. These probes are expected to give higher contrast images of PSTM.

References

[1] Near Field Optics, edited by D.W.Phol and D.Courjon, Kluwer Academic Publishers, Dordrecht, 1993.

[2] Motoichi Ohtsu, "Progress of High-Resolution Photon Scanning Tunneling Microscopy Due to a Nanometric Fiber Probe", Journal of Lightwave Technology, Vol.13, No.7, pp.1200-1221,1995.

[3] Zeev Rosenzweig and Raoul Kopelman, "Development of a Submicrometer Optical Fiber Oxygen Sensor", Analytical Chemistry, Vol.67, No.15, pp.2650-2654, 1995.

[4] Togar Pangaribuan, Shudong Jiang and Motoichi Ohtsu, "High Controllable Fabrication of Fiber Probe for Photon Scanning Tunneling Microscope", Scanning, Vol.16, pp362-367, 1994.

NEAR FIELD OPTICS TOWARD NANO-SCALE PHOTONIC MATERIALS

M. OHTSU[1,2)]

1) Graduate School, Tokyo Institute of Technology, 4259 Nagatsuta, Midori-ku, Yokohama 226, JAPAN
2) Kanagawa Academy of Science and Technology, KSP East, Rm 408, 3-2-1 Sakado, Takatsu-ku, Kawasaki 213, JAPAN

This presentation reviews the present status of our study on near-field optical science and technology toward fabrication of nanometric photonic materials[1]. After pointing out that the near-field optics is based on a short-range electromagnetic interaction between two nanometric particles via a size-dependent evanescent field[2], emphasis is given to the importance of nano-fabrication of fiber probes. Following topics will be covered in the presentation:

(1) Selective chemical etching process and selective resin coating method are reviewed, and a probe with cone angle, tip diameter, and aperture diameter of 15 deg., < 3 nm, and < 30 nm, respectively, are presented. High throughput probe for photoluminescence(PL) detection and further, a light-emitting probe with dye molecules attached to the top of the probe-tip are also demonstrated.

(2) In order to demonstrate high normal resolution of the near-field optical microscope(NOM), an image of an ultra-flat sapphire plate with atomic layers step of 2 nm-height is presented. Further, spatial power spectral analysis is carried out for the image of 20 nm diameter gold particles, and transfer function of

the NOM is estimated. From this analysis, the -3 dB cutoff spatial frequency is extrapolated, which gives a measure of resolution of 0.8 nm.

(3) As an application of the NOM, images of flagellar filaments (25 nm diameter) of salmonella in water as well as in air, microtubuline (25 nm diameter) in the branching axon of neuron, etc. are presented. PL/EL(electroluminescence) spectroscopy and photocurrent measurement of a GaAs lateral p-n junction are presented. PL spectroscopy of a GaAs quantum dot at liquid-helium temperature is also demonstrated.

(4) Photon-mode optical storage of the photochromic thin film is demonstrated.

(5) After pointing out the possibility of trapping a single atom by an evanescent field localized on the probe tip[3], the first successful result of atom guidance by the evanescent field present on the inner wall of a hollow fiber is presented. Possibility of this guiding has been proposed and theoretical analysis has been given by the authors[4,5].

The blue-detuned evanescent field on the inner wall of a hollow fiber forms an optical tunnel to reflect atoms in the hollow region and successfully carry them along the fiber. In addition, because of the localizability of the evanescent field, this kind of atom guidance works as a sort of dark trap.

Figure 1 shows a sketch of the experimental setup. A Rb atomic beam from a heat-up oven is introduced into a well-aligned hollow fiber with a small hollow diameter of 7-micron and a length of 3-cm. At an oven temperature of 180 C, the average

longitudinal atomic velocity along the fiber is 340 m/s and the average transverse one becomes 0.2 m/s in our collimation scheme. The incidence flux is approximately 10^6 atom/s. We also use a 2-micron hollow fiber as is shown by Fig.2[6]. A guide beam from a

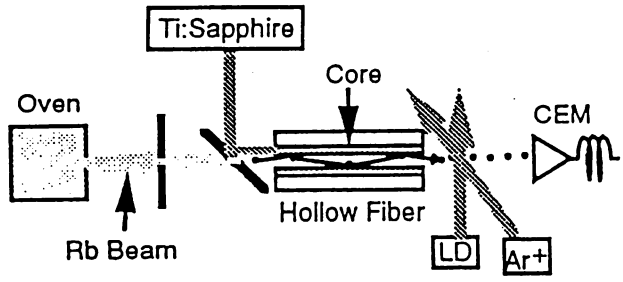

Fig. 1 Experimental setup

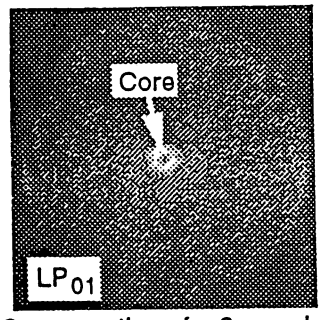

Fig. 2 Cross-section of a 2- μm hollow fiber

Ti:Sapphire laser is coupled to a thin core of the fiber through a mirror with a hole to pass the atomic beam. The guided atoms through the hollow fiber are ionized by the two-step photoionization (PI) and detected by a channeltron electron multiplier (CEM). For the photoionization, two laser beams are overlapped just behind the exit of the fiber; a grating feedback diode laser is tuned to the Rb-D_2 line, and then an Ar^+ laser (476.5 nm wavelength and 4 W power)ionizes the excited Rb atoms in the $5P_{3/2}$ state. By focusing the Ar^+ laser beam on a spot of 100-micron in the detection region, we get the PI efficiency of about 30 %.

Use of the Doppler-free PI detection including a resonant transition enables one to carry out a "spectroscopic" observation of the guided atoms in a state-selective manner. The curve A of Fig.3 shows an ion-counting PI signal of ^{85}Rb in the upper ground state through the 7-micron hollow fiber as a function of a frequency detuning of the guide light, where the diode laser is tuned to the $5S_{1/2}$, F = 3 $\rightarrow$ $5P_{3/2}$, F = 4 transition. The coupled

power of the guide light is 250 mW and it provides an optical potential of about 100 mK assuming an excitation of the LP_{01} mode[5]. It should be noted that the detuning does not include Doppler shifts. In the blue-detuning region, a large enhancement of about 10 times on the transmission flux occurs at an optimal detuning of 2.7 GHz, compared with a background transmission level without the guide light (a broken line in Fig.3). The observed dispersion-like PI signal has a long background level, which may indicate adsorption of atoms.

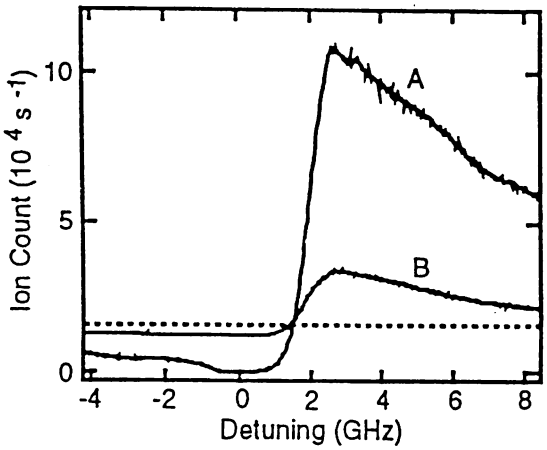

Fig. 3 Ion-counting PI signals

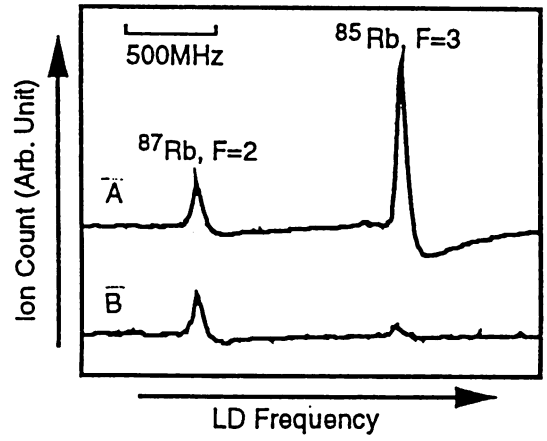

Fig. 4 In-line separation of two Rb isotopes

Based on the dispersion nature of the atom guidance, we also demonstrate a separation between two Rb isotopes by adjusting the frequency of the guide light. Figure 4 shows PI signals as a function of the frequency of the diode laser. For the curve A of Fig.4, the frequency of the guide light is set at a large blue-detuning for both Rb isotopes in the upper ground states. On the other hand, for the curve B, the guide light is blue-detuned for the ^{87}Rb atoms but nearly red-detuned for the ^{85}Rb atoms. As is clear in the figure, our hollow fiber can be considered as an atomic-state filter.

It is interesting to make the hollow diameter small. The curve B of Fig. 3 shows a PI signal on a similar experiment with

a 2-micron hollow fiber. In order to compare with the 7-micron result, the background level is taken to be the same. Another experiment using a 1.4-micron hollow fiber is under progress. Atom guidance with this small fiber can be applied to studies of the cavity QED effects[7], the quantum motion under gravity[8], and the atomic quantum wire[9]. We also expect to use them for the atom lithography technique[10], and the single atom manipulation using a sharpened tip of a fiber probe[3].

REFERENCES

[1] M. Ohtsu, J. Lightwave Technol., vol.13, p.1200 (1995)

[2] T. Saiki, M. Ohtsu, K. Jang and W. Jhe, Opt. Lett., to be published

[3] H. Hori, S. Jiang, M. Ohtsu and H. Ohsawa, Tech. Digest of IQEC, vol.8, p.48 (1992)

[4] W. Jhe, M. Ohtsu, H. Hori and S.R. Freiberg, Jpn. J. Appl. Phys., vol.33, p.L1680 (1994)

[5] H. Ito, K. Sakaki, T. Nakata, W. Jhe and M. Ohtsu, Opt. Commun., vol.115, p.57 (1995)

[6] S. Sudo, I. Yokohama, H. Yasaka, Y. Sakai and T. Ikegami, Photonics Technol. Lett., vol.2, p.128 (1990)

[7] W. Jhe, Phys. Rev., vol.A43, p.5795 (1991)

[8] D.J. Harris and C.M. Savage, Phys. Rev. vol.A51, p.3967 (1995)

[9] J.P. Dowling and J. Gea-Banacloche, Phys. Rev. vol.A52, p.3997 (1995)

[10] R.W. McGowan, D.M. Giltner and S.A. Lee, Opt. Lett., vol.20, p.2535 (1995)

Photon STM –Its application to Nano-Scale Photonic Materials
Motoichi Ohtsu
Questions and Answers

Questioner 1: You just mentioned that you can use this technique to spatially resolve photoluminescence spectra. Could you show us an example of this?

Ohtsu: Okay. For example, I have carried out some experiments on the photoluminescence spectroscopy of the gallium arsenide content of two-dimensional array. For example, here we have the cross-sectional view of a quantum dot on the pyramidal top. In order to get this kind of result, we have used ion illumination mode configuration in the liquid helium temperature. This is our commercial photo, at liquid helium temperature; it works very nicely. For example, photoluminescence spectrum. And because we can shine only one quantum dot by the property, we can remove the spatial inhomogenous broadening so that we get this kind of hyperfine structure by changing the excitation power intensity. We have estimated the diffusion lengths of the carrier, and also the saturation behavior of the carrier excitation.

Questioner 2: I'll ask one question. You mentioned that you may trap even one atom using luminescent waves, but due to some difficulties in the experiment you have not succeeded. What is the main difficulty?

Ohtsu: I think the main difficulty could be how to inject the atoms into a very small volume on the luminescent field. It depends on the atomic energy, or I mean, in the spread of the wave function of the atoms, and the property and the volume of the property. So, we have to control the temperature, or the thermal energy of the injected atoms. This could be something that will take some time, or maybe some years.

Questioner 2: So, in that sense it's more difficult to input atoms into gallery mode; circular shape. It's harder than to just put...

Ohtsu: I cannot say which is hard and more difficult or not, because nobody has ever tried it, but I think in principle it's possible to realize both of the schemes if I spend time and energy very carefully. So, in principle, I always encourage my students and collaborators to do that. I believe it could be successful in the near future; before my retirement, or when I'm fired.

Questioner 3: Very nice result. I'm an electron microscopist. Just very much conflict in spatial resolution. I have one question. You use a 3-nanometer probe, but finally your videograph is 0.8-nanometer spatial resolution. Can you explain the secret of that?

Ohtsu: Yes, and it's not a secret. Here we have this picture showing that the tip diameter is around 3 nanometers, but this is confirmed only by the scanning electron microscope by the effective tip diameter; the effectiveness for the near-field optical phenomenon may be different. For example, a very basic element of the tip is of course the atoms, so there can be several very small-diameter confirmations if you could magnify this center picture. So, I think my resolution observed by 8 microns was due to a very short sample tip separation so that even a very small-diameter part of the apex could get caught in the luminescence field. So, the success of high resolution depends not only on the very small tip, but also on the very short sample tip separation, as has been confirmed by the STM.

[I-3] REVIEW PAPERS

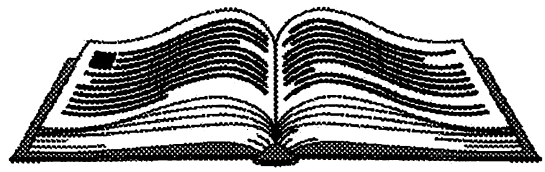

フォトン走査トンネル顕微鏡技術

大津元一*,**

エバネッセント場を利用した応用装置であるフォトン走査トンネル顕微鏡の原理，プローブ作製技術，各種試料の計測結果の現状を概説する．特に，微小加工，光機能素子開発，原子の操作への可能性を示す．関連する理論の現状についても触れる．

Keywords：evanescent field, microscope, fiber, probe, memory, manipulation

1. まえがき

光通信，光情報処理システムの高速化，高容量化のための基本技術の一つは光素子を小型化することである．しかし，光には回折の性質があるために，光素子の寸法は光波長以上必要であり，これが寸法の下限を与える．一方，上記システムや光素子の評価のためには光計測装置の高性能化も必要であるが，この場合にも光の回折が性能を制限している．たとえば光学顕微鏡の分解能も回折により制限され，光波長程度以下の寸法の試料の像は得られない．

以上のように光の回折限界が従来の光素子，光応用システムの性能を決めていたが，これは絶対的な制限ではない．すなわち，従来は光を電磁場の波としてとらえ，利用していたのでこの制限が課されていたが，形態の異なる光を使えばこの制限はなくなる．その一例として光波長以下の寸法の空間での制御された電磁相互作用を媒介する場として光をとらえ，利用することが可能で，そのような光の場はエバネッセント場（Evanescent field）と呼ばれる．これは物質表面にごく近い領域（近接場領域：表面から光波長以下の距離）に存在する光のうち非伝搬成分である．歴史的な発展としてはこの光を用いてまず顕微鏡が実現した．

しかし，エバネッセント場は物質表面近傍に存在し，この強度分布は物質の構造に強く依存するので，その分布を利用して物質を人口的に制御することが可能であり，したがって物質の極微加工などに使うことができる．すなわち計測器としての顕微鏡とともにナノメータ寸法の光加工や微小光素子の駆動などにも適している．このような研究分野は，近接場光学（Near-field Optics）と呼ばれている．

ところで，光波長以上の寸法の空間中での電磁現象では光を波として扱うことができ，光の局在[1]，共振器内量子電気力学[2]などはこの範ちゅうに入る．これに対し，近接場光学では対象とする物質の寸法のみならず光の場を考える空間の寸法も光波長以下である．したがって，実験結果の解釈や理論的記述が従来の光学の手法と異なる．本稿では顕微鏡への応用から始め，光加工，光機能への応用へと向かう研究開発の流れについて概説したい．なお，関連する分野の歴史的背景の解説として文献3，著者自身による最近の研究動向紹介として文献4がある．

2. フォトン走査トンネル顕微鏡の原理

近接場光学の応用システムとして代表的なものに，走査形近接場光学顕微鏡などと呼ばれ，光の回折限界を越える分解能を有する光学顕微鏡や開発されている．その提案は60年以上前にさかのぼるが[5]，その実現は1980年代に入ってからである[3]．

なお，6章で示すようにエバネッセント場を介した近距離電磁相互作用はエバネッセント光子のトンネル現象と捉えられるので，本稿ではこの顕微鏡をSTMの原理に対応させてフォトン走査トンネル顕微鏡（PSTM）と呼ぶ．

その原理について説明するために，ここで注目するエバネッセント場の性質の一つは次のとおりである．

（1） 光波長以下の半径をもつ誘電体球を平面基板上に置き，基板の裏面から全反射条件を満たす入射角で伝搬光を照射する．このとき発生する平面状のエバネッセント波*により誘電体球内に分極が誘起され，球表面に非伝搬光としてのエバネッセント場が発生する．その光強度は表面か

* 従来の波動光学によると基板表面にはエバネッセント波とよばれる平面波が発生し，その「しみだしの厚み」は光波長程度である．これは図1で扱うような3次元的形状をもつ微小物体表面上のエバネッセント場を平面波展開した場合の，$k > \omega/c$ なる波数 k をもつ平面波成分に相当する．ただし ω, c はそれぞれ光の角周波数，速度である．

* 東京工業大学大学院総合理工学研究科　〒226　横浜市緑区長津田4259.
** 神奈川科学技術アカデミー・フォトン制御プロジェクト　〒213　川崎市高津区坂戸3-2-1，KSP東棟408号.

分類番号　11.6，7.1

Photon scanning tunneling microscopes and related technologies. Motoichi OHTSU*,**.
* Interdisciplinary Graduate School of Science and Engineering, Tokyo Institute of Technology (4259 Nagatsuta, Midori-ku, Yokohama 226)
** "Photon Control" Project, Kanagawa Academy of Science and Technology (KSP East Rm. 408, 3-2-1 Sakado, Takatsu-ku, Kawasaki 213)

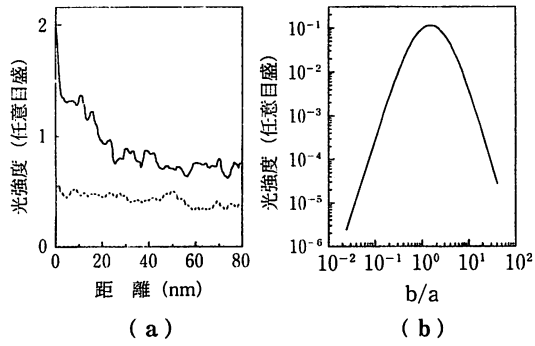

図1　エバネッセント場の二つの性質を表す実験結果(a)と計算結果(b)．(a)色素分子をドープした直径100nmのポリスチレン球にアルゴンレーザーを照射した場合の蛍光の近接場領域における光強度の測定結果(実線)(4.1節参照)．横軸は球表面からのプローブ距離．破線は雑音レベル．(b)半径aの誘電体微小球の表面のエバネッセント場を半径bの平面の円形開口で回折した場合に開口を透過する全光強度の計算値．球表面と開口との距離は光波長の1/250．bの値は光波長の1/125．

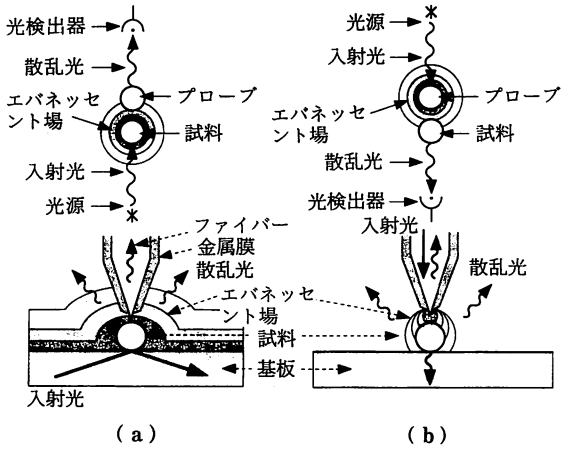

図2　PSTMの原理的構成（図の上部）とファイバーを用いた実際の構成（図の下部）．(a)Cモード．(b)Iモード．

ら遠ざかるにつれ減少する．ミー散乱理論によるとその減少の度合を表す「しみだしの厚み」は球の寸法と同程度であり，光波長には依存しない[6]．**図1(a)**にはこの性質を表す測定結果を示す（詳細は**4.1**節）．

(1)の性質により回折限界を越える分解能を有するPSTMが実現する．その原理的な構成を**図2(a)**，(b)の上部に示す．まず同図(a)の上部の図のように光波長以下の寸法をもつ球状の試料に光を照射して寸法依存のしみ出し厚みを有するエバネッセント場を発生する．これは非放射場であるので，遠方では測定不可能である．そこでプローブ用の微小球をエバネッセント場の中に置いてこの場を散乱させ，散乱光強度を測定する．プローブを走査しながら，その位置の関数として測定された光強度を図示すれば，これはエバネッセント場の分布を与え，したがって試料球の形状や構造についての情報を得ることができる．この図示が顕微鏡としての像を与える．この顕微鏡の分解能はプローブにより散乱される体積に依存するから，小さなプローブ球を試料近傍に置けば高い分解能が実現する．この分解能は従来の光の回折限界を越える値になり得る．

なお，図2(a)の上部の図において，光源と光検出器の位置を交換しても現象は変わらない．この場合の配置を同図(b)の上部の図に示すが，この場合にはプローブ用微小球表面に発生したエバネッセント場を試料球が散乱する．(a)ではプローブ球がエバネッセント場を散乱し，その光を光検出器に集めるのでCollection mode (Cモード)と呼ぶ．一方，(b)では試料球をエバネッセント場で照明するのでIllumination mode (Iモード)と呼ぶ．なお実際にはプローブは球ではなく，図2(a)，(b)の下部に示すようにガラスファイバーを先鋭化し，その根元に金属膜を蒸着して用いる．

次にエバネッセント場のもつ第二の性質を指摘する．

(2)　図2(a)の場合を考える際，解析を簡単にするために平面の円形開口のプローブを仮定する．すなわち微小球の寸法に依存する「しみだしの厚み」をもつエバネッセント場がこの円形開口により回折され，透過した後の全光強度を計算する．この場合，従来の回折理論を遠視野の近似なしに使う．その結果が図1(**b**)に示されている[6]．ただし，ここでは多重散乱は無視している．

図1(b)は試料の微小球の半径とプローブの円形開口半径とが等しいとき，開口裏面で検出される全光強度が最高になることを示している．一方，微小球半径が開口径よりも小さいときエバネッセント場のしみ出し厚みも小さく開口に到達しないので，効率よく回折・透過しない．他方，微小球半径が大きいときはエバネッセント場の等強度面は平面に近くなり，やはり効率よく回折・透過しない．すなわち，試料とプローブとの寸法に関して共鳴効果が存在する．

上記(2)の近似的な計算結果からもPSTMの動作原理について次のことがいえる．すなわち，微小球試料表面のエバネッセント場を散乱させ，その光強度を最高感度で測定するには，試料と同じ寸法のプローブを使うことである．したがって高い分解能を得るための技術的方策は小さなプローブを実現することである．この意味でPSTMおよびそれを扱う近接場光学は微小加工技術に立脚した科学技術といえる．

なお，従来の光学で扱うように二つの微小球が光波長にくらべ遠距離にある場合は光照射の有無にかかわらず両者は互いに分離独立している．他方，両者の距離がずっと近い場合は，光照射の有無にかかわらずファンデルワールス

力などにより結合している．これに対し，図2(a)，(b)の上部の図では二つの微小球が光波長にくらべて近距離にあるので，光照射時は両者の間で光の多重散乱が起こり，互いに光を介して結合した状態になっている．一方，光が照射されていない場合は両者は互いに独立である．すなわち，PSTMではエバネッセント場を介した近距離電磁相互作用によりプローブが試料と結合しており，この意味でPSTMは接触形の顕微鏡といえる．このことはまた，PSTMを微小試料の加工，操作に使うことが妥当であることを意味している．

3. プローブとその製作技術

プローブの寸法や材質がPSTMの性能を決めるのでプローブ製作のためのナノメータ加工技術が重要である．この技術の未成熟のためにPSTMの原理の提案から実験の成功まで約60年を必要としたが，最近ではガラスファイバーやガラス毛細管を加熱して引っ張り，次に金属膜を蒸着して先端部に微小開口を形成し，これをプローブとして使う技術が開発されている[7]．しかしこの場合は約20nm以下の先端寸法を再現性よく得ることが困難である．

それを解決する方法として緩衝フッ酸溶液による選択化学エッチングによりガラスファイバーを先鋭化し[8,9]，その後金属膜を蒸着し，先端部のみから蒸着膜を除去して先鋭化ファイバーの先端部を露出させる方法が開発された．この方法により小さなプローブを高い再現性で実現できるが，この露出先端部が図2の微小球プローブに対応する．

まず，体積比がNH_4F: HF: H_2O=X: 1: 1なる溶液中にガラスファイバーを約1時間浸すとコアが選択的に先鋭化され，クラッドの端面は除去される．ここでX>5ではコアの先鋭角はXの値によらずコア中のGeO_2濃度によって決まる．このことは先鋭角がエッチング溶液の組成のばらつきによらず，高い再現性で作製できることを示している．また，同一の溶液に20本程度の同一の構造のファイバーを同時に浸して先鋭化した結果，先鋭角のばらつきは0.5度以内であり，このことからも再現性の高さが確認できる．先鋭角の最小値は14度であり，これはコア中のGeO_2濃度が23モル%のとき得られた[9]．

なお，先鋭化の素過程として，コア，クラッドの組成の違いにより，発生する反応生成物(それぞれ$(NH_4)_2GeF_6$，$(NH_4)_2SiF_6$)が溶液へ溶け出す溶解速度の差に起因するといわれているが，詳細はいまだ不明である．

上記の基本的なエッチング過程を修正すると，図3および次に示すように多様な先端形状のファイバーが得られる．

(A) 小クラッド径型[9]：クラッド直径を8 μm程度まで小さくしたもの（当初の値は125 μm)．その先端の電子

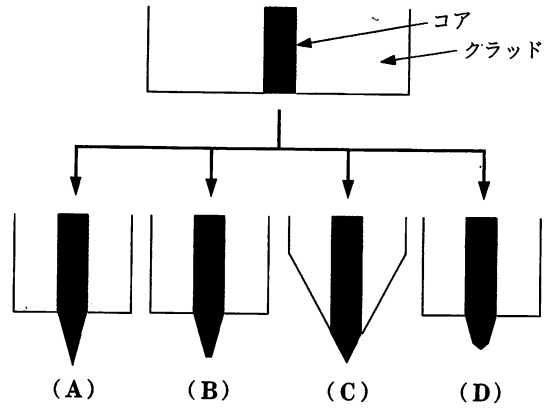

図3 選択化学エッチングにより先鋭化されたコアを持つファイバーの断面形状．(A)小クラッド径型．(B)先端平坦型．(C)ペンシル型．(D)二重先鋭型．

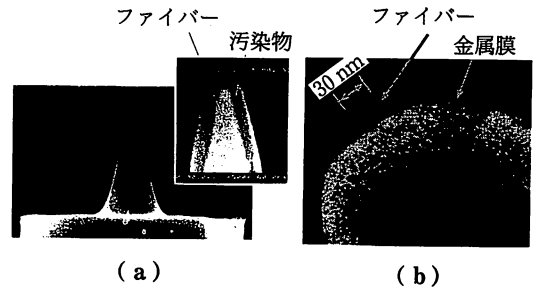

図4 (a)クラッド直径を8 μmまで減少させた先鋭化ファイバーの電子顕微鏡写真．右上図は先端の拡大写真（写真の横幅は1.6 μm．ファイバーには厚さ7nmの金属膜が蒸着されており，その表面には電子顕微鏡観察のための電子ビーム照射時に付着した汚染物層がある．(b)先鋭化コア先端部の金属膜を除去した後の電子顕微鏡写真．

顕微鏡写真を図4(a)に示す．先端曲率直径は3nmと推定されているが，この値は市販の原子間力顕微鏡のプローブし先端よりも小さい．この先鋭化ファイバーは次のような利点を有する；(1)クラッド端面の最外周の角部が試料表面に接することを防げる．(2)開口作製のためのフォト・リソグラフィにおいて塗布するフォトレジストの厚み制御に適する．(3)機械的振動の共振周波数が増大し，後述するせん断応力の高感度検出に適する．

(B) 先端平坦型[10]：生体のように柔らかい試料を扱う場合，コア先端が鋭すぎると試料を傷つける場合がある．これを避けるため，(A)においてコア先端に平坦部を残す．これにより先鋭角は(A)の場合と同様であるが，先端の平坦部の円形断面の直径を約20nmまで小さくできる．

(C) ペンシル型[11]：クラッド端面の最外周が角部を持たず，コア，クラッド併せてペンシル状の形をしたもの．先端曲率直径は(A)の場合とほぼ同等である．このフ

ファイバーの特長は(A)の(1)，およびこのエッチング過程を細部修正すると多様な形状の先鋭化ファイバーが実現すること，である．

（D） 二重先鋭型[12]：発光素子からの微弱な蛍光を検出する際には高い分解能は不要であるが，むしろプローブ先端に発生する励起用エバネッセント場の強度を増加させたり，プローブ先端での蛍光の集光効率を高める必要がある場合が多い．そのために，(A)をもとに図3(D)に示すように先端部の先鋭角を大きくし，根元では小さくする．この後，後記の方法により大きな先鋭角をもつ先端部を残して金属膜を蒸着するので，上記の蛍光測定の目的にかなう．ただしコア全体は鋭く，細長い形状を保っているので，試料表面近傍までプローブを近づけ，掃引することができる．

以上のように選択化学エッチングでは目的に応じて多様な形状の先鋭化ファイバーを再現性よく作製することができる．また，従来はコア中のGeO_2濃度が高いものを用いていたが，この方法ではその濃度が低い（すなわち通常の光伝送用の安価な）単一モードファイバー，または多モードファイバーも使用できる点が優れている．

次に，先鋭化したファイバーのコア先端部を除いて根元を金属膜を蒸着することにより，エバネッセント場の低空間フーリエ周波数成分の散乱（Cモードの場合），発生（Iモードの場合）を防ぎ，高い分解能を得る．その際，可視光に対して表皮厚の大きいアルミニウム，金などを100nm以上の厚みで蒸着する．蒸着後はKI溶液を用いたエッチングにより金属膜表面を除去し，コア先端のみを突出させる．その結果の電子顕微鏡写真を図4(**b**)に示す．突出したコアの根元が開口直径に相当するが，この図ではその値は約30nmである．

なお，このような金属開口を作る方法として，金属膜蒸着後に樹脂を先端部に塗布した後にエッチングする方法[11]，金属膜蒸着後にフォトレジストを塗布し，エバネッセント光で露光する立体ナノフォトリソグラフィの方法[13]，などが考案されている．

なお，図4(b)のように金属膜が開口を有し，そこからコア先端が突出している先鋭化ファイバーをプローブとして用いる場合，開口直径とコア先端曲率直径とによって決まる範囲内の寸法を持つエバネッセント場が散乱または発生する．すなわちエバネッセント場の検出効率は空間フーリエ周波数軸上では帯域通過特性を示し，その高域遮断周波数はコア先端曲率直径によって決まる．これが分解能の目安を与える．

図3で示したプローブの他に特記すべきは信号変換形のプローブである．すなわち光信号を他の信号に変換したり，またはその逆の機能を有する．前者の例としてGaAsのへき開端を利用してショットキー・コンタクトを形成し，発光形プローブとするもの[14]，周囲の媒質の酸性度に敏感な色素をファイバープローブ先端に付着させpHセンサーとして使うもの[15]，などが提案されている．後者の例として図3(B)のファイバーコア先端の平坦部に約1×10^6個の色素分子を塗布したものが製作されている[16]．試料表面のエバネッセント場により色素を励起して蛍光を発生させ，これを波長選択検出すれば，先鋭化ファイバーの先端のみが感度を有するプローブとして機能し，上記の帯域通過特性の低域遮断周波数を増大させることができる．このプローブを用いてPSTMの画像計測が実現している[16]．以上の信号変換形プローブは多様な物理量のセンサーとしての応用が可能で，今後の発展が期待される．

4. 画 像 計 測

4.1 エバネッセント場の基本的特性

PSTMの分解能の高さを裏付ける実験として，図1(a)に示す結果が報告されている[17]．すなわち蛍光色素分子を含む直径100nmのポリスチレン球をガラス基板に固定し，基板裏面から全反射角でアルゴンレーザー光を入射して色素を励起し，蛍光を発生させる．この球にCモードのPSTM用のファイバー・プローブを近づけ，球表面からの距離の関数として近接場領域における蛍光強度を測定する．球とプローブの距離が数10nm以内の領域ではエバネッセント場の強度が伝搬光のそれにくらべ非常に大きい．球内部の蛍光源の分極は任意の方向を向いているが，ミー散乱理論を使った計算結果でも強い偏光依存性がないので，理論とよく一致している．すなわち，球およびそれと相互作用しているプローブ先端の寸法程度の「しみだしの厚み」をもつエバネッセント場が測定されている．この測定では基板上に固定される球の数を少なくし，他の球からの蛍光の混入を避け，さらに蛍光を選択的に検出することによりアルゴンレーザー光の基板表面での散乱の影響を除去するなど，たくみな実験技術を駆使することによって，理論とよく合う結果を得た．

さらに，この測定の際，プローブによる蛍光の散乱および集光の効率の値は球から発生する蛍光の強度分布が全立体角にわたり均一であるとした場合の10倍以上であることが確認された[12]．これはプローブと色素分子との間の近距離電磁相互作用に起因する．すなわち，プローブが近接するので蛍光を発するための色素周囲の輻射場モードが自由空間の輻射場モードとはもはや異なり，蛍光強度が指向性を示している．いわば共振器内量子電気力学の現象が現れている．このような現象は蛍光寿命がプローブ位置によって異なるという報告によっても裏付けられている[18]．

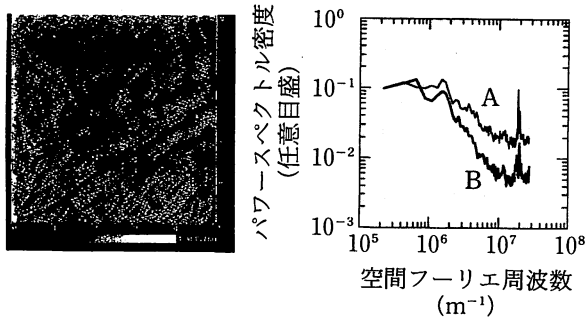

(a) (b)

図5 (a)ガラス基板に固定された複数のサルモネラ菌の鞭毛(帝京大学相沢慎一教授の提供)を空気中にてCモードで観察した結果．光源は波長488nmのアルゴンレーザー．入射光はs偏光(光の電界ベクトルは紙面内にある)．波数ベクトルは図の左上から右下に向い，図に対して45度の方向．図の一辺は5 μm．プローブと試料の間の距離は15nm．(b)複数のサルモネラ菌の鞭毛像の各画素の光強度から空間パワースペクトル密度を計算した結果．曲線A，Bは試料とプローブとの距離がおのおの15nm(図(a)を使い計算した結果)，65nmの場合．

4.2 生体試料の計測

光学顕微鏡の主要な適用分野は生体試料観測である．そのためにはPSTMに期待される性能は高い分解能を保ちながら水中で観測できること，蛍光を測定できること，などである[19]．ここでは二つの測定法による結果を示す．

(a) Cモードの測定

PSTMの性能評価も兼ねて，サルモネラ菌の直線状の鞭毛[20]をガラス基板に固定したものが試料として使われている．実験装置の基本的部分は図2(a)に示すとおりである．プローブの走査に用いるピエゾアクチュエータ，制御用および画像処理用コンピュータなどは従来のSTM，AFMなどのものが流用できる．

光源にはアルゴンレーザーを用い，その偏光を波長板によって調節する．基板状に固定された複数の鞭毛の電子顕微鏡像によると鞭毛直径は25nmであることがわかっている．

Cモードにより空気中で得た複数の鞭毛の像を**図5(a)**に示す．これは入射光をs偏光にして測定した結果であり，その電界ベクトルの方向は基板表面内にある．入射光の波数ベクトルは図の左上から右下に向いている．ここでは図4(b)と同形のプローブを用いた．この図はプローブ先端と試料の距離を15nmに固定しながら走査した結果である．そのためにはプローブ用ファイバーの末端での検出光強度が一定になるようにプローブ位置を制御している．この図では入射光の波数ベクトルと直角方向に固定された鞭毛の像の方が，平行に固定されたものよりも明瞭に，かつその幅が細く見えている．

さらに，プローブ先端と試料の距離を65nmに増加して

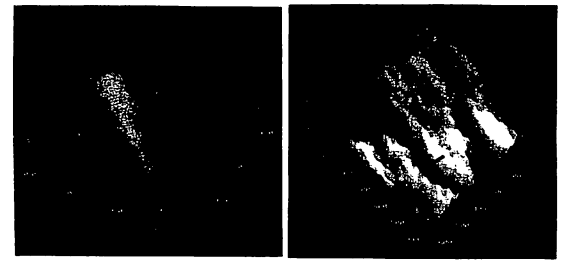

(a) (b)

図6 (a)図5(a)と同一の条件のもとに一本の鞭毛の端部を観測した結果．矢印で示された部分の鞭毛直径は30nmに相当．(b)水中での像．ここには5本の鞭毛がある．矢印で示された部分の鞭毛直径は50nm．

この図と同じ像を観察すると各鞭毛の像が明瞭でなくなり，分解能が低く感じられることが確認されている．これを評価するために距離15nm，65nmの場合について図の各画素ごとの光強度をパワースペクトル解析した結果を図5(**b**)に示す．これによると距離の増加とともに高い空間フーリエ周波数成分の強度が減少しており，分解能が低く感じられるのはこの減少に起因する．なお，これは2章の(1)に示したようにエバネッセントの場の「しみだしの厚み」が試料の寸法に依存していることによる．すなわち，高い空間フーリエ周波数成分のエバネッセント場の「しみだしの厚み」は小さいので，プローブ距離が増加するとこのような成分の散乱，検出効率は低下する．

一方，エバネッセント場のベクトル的な特徴を調べるために入射光をp偏光にした場合，同一の鞭毛が2本隣り合って並んだ像が観察されている．これはエバネッセント場によってプローブ先端に誘起される分極の方向の違いによって説明されている[21]．以上のように，PSTMの動作原理に基づき，像の主要な特徴が解釈できる．

図5(a)と同じ測定条件において鞭毛端部の像を拡大して観測した結果を**図6(a)**に示す．この図の鞭毛直径は約30nmである．これは電子顕微鏡による直径と大差ない値であり，従来の光学顕微鏡に比べ高い分解能が実現したことを意味している．

水中での試料観測では水の粘性のためにプローブの走査速度は減少するが，Cモードではせん断応力などの補助的手段をプローブ位置制御のために利用しなくてもよいので，空気中と同様の測定が可能である．たとえば図6(**b**)には複数の鞭毛の末端部の像を示すが，その直径は50nmであり，同図(a)に示す空気中の像の直径と大きな差がなく，水中でも高い分解能が維持されることが確認できた．

(b) Iモードの測定

この方式の利点はプローブからのエバネッセント場で試料のみを選択的に照射できることである．ただし，プロー

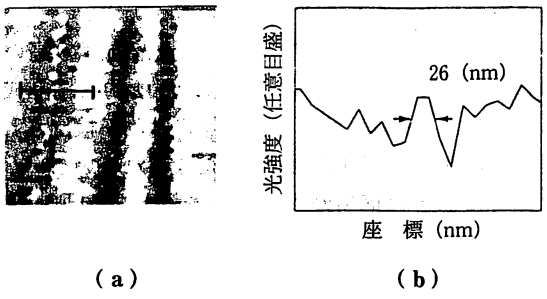

図7　（a）ニューロン軸窄（東京医科歯科大学辰巳仁史博士の提供）中の毛細管の束をIモードで観察した結果．（b）図（a）中の実線で示した部分の光強度断面分布．

ブと試料との間の間隔を制御するためには，せん断応力を測定する[27]などの補助的手段が必要である．せん断応力による生体試料の損傷を避けるために，3章（B）のプローブを用いて下記の測定が行われている[22]．

PSTMが他のプローブ顕微鏡と大きく異なる点の一つは試料内部の表面近傍の内部構造が見えることである．たとえばニューロンの軸窄内部には毛細管の束があるが，軸窄表面に沿ってプローブを走査することにより，軸窄表面付近にある毛細管の像が得られる．これを**図7（a）**に示す[23]．この図中の実線で示した箇所での軸窄の断面上の光強度分布を同図（b）に示すが，これより毛細管の直径を測ると26nmである．一方電子顕微鏡ではこれらの毛細管を軸窄から取り出して親察し，直径25nmの像を得ている．このことはPSTMでは軸窄から取り出さずに，電子顕微鏡と同等の寸法の毛細管像が得られることを意味している．先端が平坦なプローブを用いてもこのような高い分解能が得られた理由は物体寸法に依存する「しみ出しの厚み」をもつエバネッセント場による．すなわちファイバー先端と金属膜との境界の形状の曲率半径が小さいため，そこに高い空間フーリエ周波数をもつエバネッセント場が存在したためと推定されている．なお，水中での観測も試みられている[24]．この場合はせん断応力を測定するためにプローブを横方向に振動させる際の共振のQ値は水中では下がることが問題である．

さらに，色素分子をドープした生体試料からの蛍光も測定されており，水中での観測とも合わせてPSTMの生体観測への利用価値が高まってきている．

4.3　光エレクトロニクス用材料，素子の評価

従来の光エレクトロニクス素子は光波長以上の寸法を有するので，PSTMにとっては大きな試料である．しかしその表面の微小な構造変化などの計測や評価にはPSTMは有効である．受動素子の例としてはY分岐の$LiTaO_3$導波路の導波モードの観測，光波長以下の寸法の微小散乱光源の同定，さらには導波損失の測定などが行われている[25]．

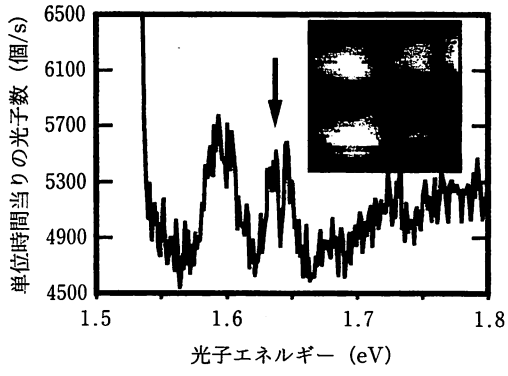

図8　基板上に間隔1 μmで二次元アレイ状に成長された直径200nm，厚さ20nmのGaAs量子ドット（東京大学荒川泰彦教授の提供）からのフォトルミネッセンスのスペクトルを，Iモードにより温度18Kで測定した結果．内挿図はスペクトル曲線中の矢印を示した位置でのフォトルミネッセンス光強度の空間分布を示す．この図の一辺は2 μmであり，4つの量子ドットが観察されている．

一方，単一分子またはそれらがいくつか集まった凝集体は，自分自身の周囲環境の違いを敏感に光学スペクトルに反映させる．したがってレーザー・ビームで多数の分子を同時に励起して光学スペクトルを測定するような従来方法では中心波長と形状の異なるスペクトルが重ね合わさり，不均一ひろがりをもつスペクトルを観測してしまい，個々の分子の性質を見いだすことが困難となる．特に半導体量子構造などの固体におけるスペクトルの不均一性に対しては光による励起，観測領域を決めることが必須で，そのためにはPSTMが有効である．以下では関連する半導体材料，素子についての計測評価例を示す．

（a）　半導体量子サイズ素子

たとえば半導体の量子ドットが基板上に二次元アレイ上に成長されている場合，従来の方法では空間的分解能が不十分なので個々のドットからの発光を分離測定することができないが，PSTMではそれが可能になる．なお，熱によるスペクトルの広がりや量子効率の低下を避けるために極低温で動作するPSTM装置が必要となる．すなわちプローブを走査するためのピエゾ・アクチュエータの熱膨張係数などに注意し，熱ドリフトの少ないIモードの装置を組み立てて使う．その他の装置構成は**4.2**節（b）の場合と同様である．光源はアルゴンレーザーであり，発光スペクトルは回折格子分光器と光子計数器とで測定する．**図8**には発光スペクトルの測定結果を示すが，従来の遠視野の場合と異なり，不均一ひろがりが除去でき，幅の狭い数本のスペクトルが分離されて観測されている[26]．特に矢印を施したスペクトル成分は内挿図と比較すると量子ドットからの発光と推定されている．

なお，関連する実験として温度2KにおいてGaAs/

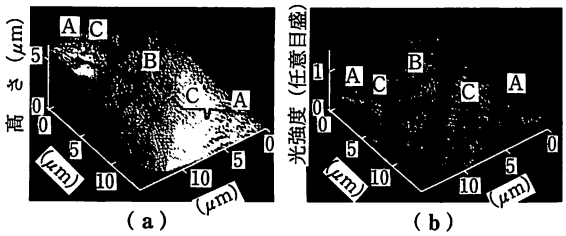

図9 段差加工を施したGaAs面発光素子（日本放送協会斉藤信雄博士の提供）の測定結果．A，B，Cはおのおのp形，n形，および遷移領域の範囲を表す．(a)原子間力顕微鏡像．図(b)の測定に用いたプローブにより同時測定した結果．(b)He-Neレーザー光をIモードにより試料表面に照射し，発生したフォトルミネッセンス強度をプローブを通して測定した結果．矢印の位置は遷移領域中での局所的な発光強度の大きい箇所を示す．

AlGaAsの厚さ2.3nmの単一量子井戸の励起子スペクトルが測定されている[27]．この実験ではポテンシャルエネルギーの異なる発光サイトからの鋭い発光スペクトルが分離測定されている．また，励起子がそのトラップサイトに捕獲されるまでの拡散距離，量子井戸の厚さの揺らぎの大きさ，などが推定された．最近ではプローブをとおして短パルス光により励起し，時間分解分光が行われている．おもにポンプ・プローブ法が用いられており，キャリア緩和の位置依存性に対して詳細な議論が行われている[28]．

（b） 面発光素子

PSTMは試料表面の情報を評価するのに適した装置であるので，特に面発光形の素子の評価に有効である．その一例として段差加工を施したGaAs基板上にSiをドープしたGaAs層をMBE成長させることにより形成された横方向pn接合のフォトルミネッセンス分光が行われている[29]．

Iモードのプローブ末端部からレーザー光を入射し，先端部のエバネッセント場で試料を励起して発光させる．その微弱な発光スペクトルを測定するが，エバネッセント場の発生効率を上げるために3章(D)に記したプローブが使われている．pn接合の各位置におけるスペクトルの中心波長，線幅，強度の分布などが測定されている．

この場合，キャリアの拡散長により測定の分解能が制限されるので，この制限を打破するために発光をプローブを通して検出する方法，すなわちCモードと組み合わせた方法が取られている．その測定結果の例を**図9**に示す．同図(**a**)はプローブ位置制御に用いたせん断応力をもとに計測した表面形状であり，原子間力顕微鏡像に他ならない．(**b**)は発光強度の分布である．p形とn形（図中の領域A，B）では発光強度が高く，遷移領域（図中の領域C）では低いことがわかる．後者に対する主要因は生成されたキャリアが空乏層における内部電場のためにドリフトして発光に寄与しないためと考えられる．

さらに，下接合のところどころに発光強度の高い部分（図中の矢印）が見られることから，局所的な結晶成長状態の変化およびそれに伴う内部電場の乱れが検出されていると考えられる．要因の特定はまだなされていないが，いずれにせよ微小な構造が光学応答を通して観測できており，PSTMの特長が顕著に現れた結果と解釈できる．

4.4 その他の試料の計測

（a） 色素分子の蛍光測定

励起領域に数個の色素分子しか存在しないような極めて低密度の試料を準備することができるので，単一色素分子からの蛍光測定が可能となる．直径約100nmと大きな開口つきプローブからIモードにて励起光を照射して単一分子からの蛍光を検出し，その蛍光の偏光特性より色素分子の向きも推定されている[30]．さらに数10秒という時間スケールで単一色素分子の退色過程，可逆的な蛍光強度変化を測定している．一方数nsの時間スケールで蛍光寿命の測定を行い，特に微小開口周囲の金属膜の影響による消光現象が観測されている[18]．

単一分子分光技術は生体試料に対する色素による標識化など幅広い応用が期待される．なぜなら色素分子の蛍光スペクトル形状，蛍光寿命，量子効率などが分子の置かれた環境に応じて敏感に変化するからである．ただし，単一分子からの蛍光測定では検出感度が最も大きな問題である．たとえば3章(D)に記したように高い感度が得られるように設計されたプローブを用いることが望ましい．

上記の単一分子分光の実験では，プローブの役割は一つ一つの分子を分離して測定することにある．したがって，低濃度に分散させた試料を準備すれば，高い空間分解能は要求されない．したがって，PSTMを使わなくとも測定可能な場合がある．現に，平面基板上にしみ出すエバネッセント場で励起して退色を抑えれば，溶液中でさえも単一分子からの蛍光測定などが可能である[31]．

（b） 固体の光学スペクトル

固体の分光の例として，応力下でのルビーの蛍光スペクトル[32]，ダイヤモンドのラマンスペクトル[33]などが報告されている．また，Fe: $LiNbO_3$の四波混合特性をプローブにより検出した例もある[34]．ただしこれらは分解能が低く，特に四波混合では遠視野の概念を使って論じており，今後に課題を残している．しかし，非線形光学現象を使うことによりナノメータ寸法の光機能を発現させるためのヒントになり得る．

さらには，金属膜上の表面プラズモン波動の検出[35]，さらには表面プラズモンを利用してPSTMの分解能を向上させる試み[36]などが報告されている．今後表面プラズモンセンサの微小化などへの応用が期待されている．

5. 微小加工と原子操作

5.1 微小光素子の加工など

エバネッセント場の持つ光エネルギーを利用すれば物質表面の加工が可能である．これまでにIモードのプローブ先端からしみ出すエバネッセント場により光メモリー材料に記録する試みが報告されている．従来の光記録とは異なり，回折限界を越えた記録が可能になる．光磁気記録材料であるCo/Ptにアルゴンレーザーを用いて，熱モードで記録し，ピットの直径約100nm，記録密度45Gb/inch^{2}を得ている[37]．記録装置寸法を小型化するために同じ記録を半導体レーザーを光源として行う試みも報告されている[38]．なお，2章の(2)に示したようにプローブと試料の寸法に関して共鳴効果が存在するので，光記録材料の粒径に等しい寸法の先端をもつプローブを用いることが最も効率がよいが，従来の試みではプローブ先端の大きさより材料の粒径の方が小さく，したがって記録ピットの大きさは材料の粒径によって決まっている．

なお，上記の熱モード光記録では再生の際にもIモードのPSTMを用いてエバネッセント場の偏光状態の変化を測定するが，プローブからしみ出すエバネッセント場の偏光状態自身がプローブ形状，構造に大きく依存するので，再生装置の再現性が問題である．これを解決するために光子モードでの記録が試みられている[39]．

これはジアゾベンゼン誘導体のフォトクロミック材料のラングミュア・ブロジェット（LB）膜を記録材料とし，波長350nmの紫外光のエバネッセント場を局所的に照射して，トランス形異性体からシス形異性体へと変化させることにより記録を行う．再生にはトランス形とシス形の異性体の吸光度が上記波長の光に対し互いに異なることを利用し，PSTMにより記録材料の光透過率の局所変化を測定することにより行う．この場合も上記の熱モード記録と同様の寸法の記録ピットが実現している．

なお，寸法に関する共鳴効果を利用するために基板上に単層で凋密に二次元配列された微粒子の上にLB膜を作製する方法が考案されている．直径40nm程度の微小ポリスチレン球をガラス基板上に二次元配列する技術[40]が開発されている．

実用化にむけて次の課題が残されている．(1)必要とする寸法を持つ記録ピットを得るために光伝達効率のよい形状をもつプローブを製作すること．(2)新しい光記録材料を開発すること．たとえば，より小さい粒径をもつ材料が必要である．フォトクロミック材料に関してはより高い光応答感度をもつものが開発されている[41]．(3)再生の際のプローブの高速走査機構を開発すること．

光メモリーのみでなく，微小な光機能素子への期待も高まっている．たとえば4.3(a)節の半導体量子ドットや4.4(b)節のFe: $LiNbO_3$などの微粒子の非線形光学現象を利用した光スイッチング，光増幅などの光機能が実現すれば，本稿冒頭に述べたような光素子の寸法の微小化が可能となる．

エバネッセント場を使って加工の極限形態としての単原子の操作の実現が期待されている．特にナノメータ領域に局在させたエバネッセント場の双極子力を用いると真空中の気相原子の運動を制御することができるであろう．従来は伝搬光を利用したレーザー冷却法や捕獲法[42]により光の回折限界による位置精度の範囲内で原子の熱運動が三次元的に制御されていた．このような原子操作の最近の傾向は，(1)ボーズ・アインシュタイン凝縮実現[43]のために原子の熱運動エネルギーをできるだけ減少させ，かつ密度を上げること，(2)原子の密度を下げ，一個または数個の原子を操作すること[44]，(3)制御の空間的次元を下げること，などである．

特に(2)，(3)については局在したエバネッセント場により回折限界を越えてナノメータ領域に至るまでの制御性を得ることが可能である．非伝搬光であるエバネッセント場では物質表面に対し法線方向の波数成分は虚数であり，平行方向の成分の値は伝搬光にくらべずっと大きい．つまり，物質表面と平行方向の場の運動量成分が大きく，この大きな場の運動量は原子のような微小粒子に対しては大きな力学的作用を及ぼす．これに対し，自由空間を伝搬する電磁場により同等の力学的作用を得るにはX線のようにエネルギーも同様に大きい光が必要となり，原子や原子核を励起するなどの複雑な現象をもたらしてしまう．

(3)で重要なのは一次元的または0次元的操作である．まず，一次元的な操作として，原子の共鳴周波数に対し高周波側に離調した光を円筒コア中空ファイバーのコア中に導波させ，そのとき内壁にしみ出した円筒状のエバネッセント場により中空ファイバーに飛び込む原子を内壁から反発させ，出口まで誘導する方法[45]が提案されている．図10の内挿図は内径7 μm，円筒コア幅4 μmを持つ中空ファイバーにレーザー光を入射した場合の最低次の導波モード（LP_{01}）の断面形状である．一方，同図にはこのモードのエバネッセント場の双極子力により，Rb原子（共鳴波長780nm）を閉じ込めるためのポテンシャルの断面形状，および内壁への引力としてのキャビティポテンシャルの計算値を示す．

この図によると内壁付近にできるポテンシャル障壁の厚みは約100nm，その高さを熱運動の等価温度で表すと数mKである（導波モードパワー1mWのとき）．横方向速度成分が約40cm/s以下のRb原子ビームを用いればトンネ

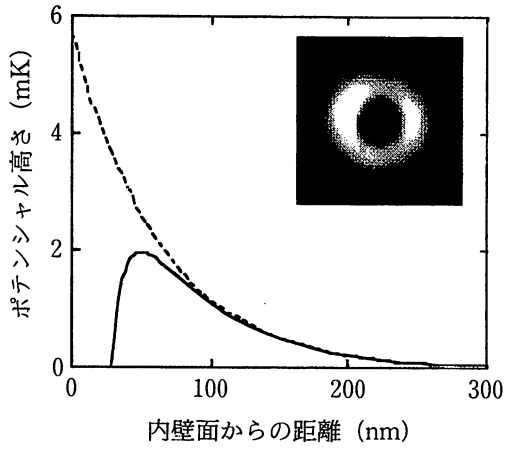

図10　円筒コアをもつ中空ファイバー内壁のエバネッセント場を使って中空部にRb原子を閉じ込めるためのポテンシャルの断面形状の計算値（実線）．縦軸の値はRb原子の熱運動の等価温度．破線はエバネッセント場の双極子力による寄与分．内挿図は対応するファイバーの導波モードの断面形状の観測結果．

ル効果によりこの障壁を突き抜ける確率はほぼ無視できる．毎秒100個程度の透過原子数が見込まれるが，これは光イオン化によるイオン数計数，または蛍光測定により検出可能である．原子ビームの代わりにレーザー冷却された原子を中空ファイバーに導入してもよい．

このような原子の誘導路が実現すると共振器内量子電気力学現象[46]，ベリー位相[47]，Aharonov-Casher効果[48]，など物理学の基礎的現象を調べるための有力な道具になるばかりでなく，結晶成長，同位体分離，など新しい物質創造などへの応用にも役立つと考えられる．

0次元的な操作としてPSTMプローブ先端にしみ出すエバネッセント場の中に一個または少数個の原子を捕獲する可能性も提案されている[49]．これは本章冒頭に示したようにプローブ表面と平行方向のエバネッセント場の波数が非常に大きいことを利用して，熱運動している原子の飛行方向を急速に反転させるとともに，強く局在した場からの双極子力で捕獲しようというものであり，その後は2章最後に記したようにエバネッセント場を介した近距離電磁相互作用により減速原子とプローブとが結合した状態になると考えられる．これは原子が捕獲されたことに相当するが，捕獲のためのポテンシャル深さを表す熱運動等価温度は数100 μKである．これはレーザー冷却された原子に対しては十分大きな値である．なお，同様の操作として平面基板の小さな窪に発生したエバネッセント場を利用する方法も提案されている[50]．

本方法の利点は原子の共鳴周波数に合致した光周波数をもつ光源を用意すれば多種類の原子を操作できることである．多くは波長200～400nmの光であり，Siなどの応用上重要な原子に対して適用できるが，赤外光を使えば分子に対しても適用可能と考えられる．

局在したエバネッセント場を用いれば原子，分子だけでなく光波長以下の寸法をもつ微粒子の捕獲，操作なども可能である．特に水中での生体微粒子捕獲，操作は従来は伝搬光を集光して行っていた[51~53]．このとき光のエネルギー伝搬方向と波数の方向とは通常は平行であるが，エバネッセント場の場合は直交するので，捕獲のみでなく，回転，並進など操作の自由度が増える．これにより生体微粒子の操作の多様性が増大すると考えられる．

5. 関連する理論

PSTMではプローブと試料の間の複雑な散乱過程を問題とするので，これを従来の光学理論で解こうとすると数値計算にたよることになる．これまでに，多重極子による多重散乱に関する積分方程式であるLippman-Schwingerの方程式を，自己無撞着の方法により数値計算する方法が提案されている[54]．これは厳密解を与えるが試料の形状により計算技巧と長い計算時間を要する．元来，表面物理，表面ラマン分光などの研究者が計算アルゴリズムを研究するために，その適用例として提案しているので，物理像が不明である．数値計算よりは現象をモデル化して解析的に記述し，三次元的な粒子に対してエバネッセント場がどのような特性を示すかを知る必要がある．

また，たとえばこの計算結果[55]は4.2(a)節で示した鞭毛像の特性（特に入射光の波数ベクトルの方向と，明瞭に見える鞭毛の方向との関係）を説明できないなど，実験結果との整合性が不十分である．なお，同様の方法にしたがい既存の計算機プログラムを用いて，走査するプローブの位置ごとにエバネッセント場を数値計算した例もある[56]．ただし，この場合，自己無撞着性の保証に関して明示していない．

STMにおいてBardeenのトンネル電流[57]のような見通しのよい概念を複雑な散乱過程から抽出することが重要であるように，PSTMでのおもな問題はプローブと試料との間の電磁相互作用を見通しよく求めることであるので，場の強度分布を計算することが，どれ程の情報を実験の解析にもたらすかは疑問である．

以上のように既存の理論は実験との比較において不都合が多いので，数値計算ではなく，物理的なモデルを設定し，それを解析的に表す試みがある．すなわちプローブ，試料表面に寸法依存の「しみ出しの厚み」を持つエバネッセント場を考え，その重なり積分から光検出器へ達する散乱光強度を求める方法である．これは上記のSTMにおけるBardeenのトンネル電流を求める方法と同等であり，エバネッセント場の多重散乱を非伝搬の仮想光子のトンネ

ル現象として捉えている[58]．この意味で本稿で扱う顕微鏡をPSTMと称するのは妥当である．この方法の最重要な点は試料形状と信号強度との間の関係を表す装置関数（伝達関数とも呼んでいる）が導出でき，測定された画像の解釈に役立つ結果が得られること，したがって空間分解能などとの概念と直接結びつくことである．また，2章の性質(2)に記した寸法に関する共鳴効果は仮想光子のトンネル現象における光子の運動量保存を表している．問題は寸法依存の「しみ出しの厚み」をもつエバネッセント場をどのような関数で記述するかである．このモデルでは湯川形関数を使っている．近接場光学の理論として今後必要とされるのは，このように実験結果と直接比較可能なモデルに基づくものである．

7. むすび

本稿ではエバネッセント場を利用したPSTMの原理，性能の現状について概説した．特にエバネッセント場を介したプローブと試料との間の近距離電磁相互作用に着目し，PSTMは微小試料の加工，さらには原子の操作に使用可能であることを示した．

今後の展望として解決可能ないくつかの課題を次に挙げる．(1)1nmより高い分解能を持つPSTMの実現．(2)PSTMによる光学スペクトルのデータの蓄積と利用．(3)信号変換用機能性プローブの開発と微小センサーへの応用．(4)溶液中や極低温中などの特殊環境下でのPSTMの動作．(5)ナノ加工，光機能素子の開発，原子の操作性の向上．(6)実験結果と直接比較でき，かつ物理的な直感に訴える新しい理論モデルの開発．

エバネッセント場を扱う近接場光学とその関連技術は近年の発展が著しい．また，応用物理学のみでなく広い分野への波及効果を有する．その発展はナノ加工技術に立脚しており，光の科学技術や産業の新しい展開が期待できるであろう．

本内容に関し山梨大学・堀裕和博士，ソウル国立大学・W. Jhe博士，(株)フジクラ・宮本末広博士，(財)神奈川科学技術アカデミー「フォトン制御」プロジェクト研究員諸氏から有益な助言を頂き，感謝します．

文献

1) E. Yablonovitch: Phys. Rev. Lett. **58**, 2059 (1987).
2) S. Haroche and D. Kleppner: Phys. Today, p. 24 (January, 1989).
3) D. W. Pohl: *Near Field Optics*. ed. by D. W. Pohl and D. Courjon, p. 1 (Kluwer, Dordrecht, 1993).
4) M. Ohtsu; J. Lightwave Technol. **13**, 1200 (1995).
5) E. H. Synge: Phil. Mag. **6**, 356 (1928).
6) W. Jhe: *Proc. Conf. Lasers and Electro-Optics/Pacific Rim, Makuhari, 1995*, p. 145 (IEEE, Piscataway, 1995).
7) K. Liberman, S. Harush, A. Lewis and R. Kopelman: Science **247**, 59 (1990).
8) T. Pangaribuan, K. Yamada, S. Jiang, H. Ohsawa and M. Ohtsu: Jpn. J. Appl. Phys. **31**, L1302 (1992).
9) T. Pangaribuan, S. Jiang and M. Ohtsu: Scanning **16**, 362 (1994).
10) R. Uma Maheswari, S. Mononobe and M. Ohtsu: J. Lightwave Technol. **13** (1996)印刷中.
11) S. Mononobe, M. Naya, R. Uma Maheswari, T. Saiki and M. Ohtsu: *Phoc. Int. Conf. Near Field Optics and Related Technol., Brno, 1995*, p. 105 (European Opt. Soc., Brno, 1995).
12) T. Saiki, S. Mononobe and M. Ohtsu: *Proc. Quantum Electronics and Laser Science, Baltimore, 1995*, p. 84 (Opt. Soc. Am., Washington, 1995).
13) T. Matsumoto and M. Ohtsu: *Proc. Int. Conf. Near Field Optics and Related Technol., Brno, 1995*, p. 107 (European Opt. Soc., Brno., 1995).
14) H. -U. Danzebrink and U. C. Fisher: *Near Field Optics*, ed. by D. W. Pohl and D. Courjon, p. 303 (Kluwer, Dordrecht, 1993).
15) W. Tan, Z. -Y. Shi and R. Kopelman: Anal. Chem. **64**, 2985 (1992).
16) 栗原一嘉，大津元一：第56回応用物理学会学術講演会，26pZK8 (1995).
17) M. Saiki, S. Mononobe and M. Ohtsu: *Proc. Int. Conf. Near Field Optics and Related Technol., Brno, 1995*, p. 127 (European Opt. Soc., Brno, 1995).
18) X. S. Xie and R. C. Dunn: Science **265**, 361 (1994).
19) E. Betzig, R. J. Chichester, F. Lann and D. L. Taylor: Bioimaging **1**, 129 (1993).
20) T. Hirano, S. Yamaguchi, K. Oosawa and S. Aizawa: J. Biotechnol. **176**, 5439 (1994).
21) M. Naya, S. Mononobe, R. Uma Maheswari, T. Saiki and M. Ohtsu: *Proc. Conf. on Scanning Probe Microscope III, San Jose, 1995*, p. 83, (SPIE, Washington, 1995).
22) E. Betzig, P. L. Finn and J. S. Weiner: Appl. Phys. Lett. **60**, 2484 (1992).
23) R. Uma Maheswari, H. Tatsumi, Y. Katayama and M. Ohtsu: Opt. Commun. **120**, 325 (1995).
24) H. Muramatsu, N. Chiba, K. Homma, K. Nakajima, T. Ataka, S. Ohta, A. Kusumi and M. Fujihira: Appl. Phys. Lett. **66**, 3245 (1995).
25) Y. Toda and M. Ohtsu: IEEE Photonics Technol. Lett. **7**, 84 (1995).
26) Y. Toda, M. Kourogi, Y. Nagamine, Y. Arakawa and M. Ohtsu: *Proc. Conf. Lasers and Electro-Optics/Pacific Rim, Makuhari, 1995*, p. 165 (IEEE, Piscataway, 1995).

27) H. F. Hess, E. Betzig, T. D. Harris, L. N. Pfeiffer and K. W. West: Science **264**, 1740 (1994).
28) S. Smith, B. G. Orr, R. Kopelman and T. Norris: *Proc. Quantum Electron. and Laser Science, Baltimore, 1995*, p. 85 (Opt. Soc. Am., Washington, 1995).
29) T. Saiki, S. Mononobe, M. Ohtsu, N. Saito and J. Kusano: Appl. Phys. Lett. **67**, 2191 (1995).
30) E. Betzig and R. J. Chichester: Science **262**, 1422 (1993).
31) T. Funatsu, Y. Harada, M. Tokunage, K. Saito and T. Yanagida: Nature **374**, 555 (1995).
32) P. J. Moyer, C. L. Jahncke, M. A. Paesler, R. C. Reddick and J. Warmack: Phys. Lett. **A 145**, 343 (1990).
33) D. P. Tsai, A. Othonos, M. Woskvits and D. Uttamachandani: Appl. Phys. Lett. **64**, 1768 (1994).
34) S. I. Bozhevolnyi, O. Keller and I. I. Smolyaninov: Opt. Lett. **19**, 1601 (1994).
35) P. Dawson, F. de Fornel and J. -P. Gouronnet: Phys. Rev. Lett. **72**, 2927 (1994).
36) M. Specht, J. D. Pedarning, W. M. Heckl and T. W. Hänsch: Phys. Rev. Lett. **68**, 476 (1992).
37) E. Betzig, J. Trautman, R. Wolfe, E. W. Gyorgy, P. L. Finn, M. H. Krder and C. -H. Chang: Appl. Phys. Lett. **61**, 142 (1992).
38) 保坂純男：近接場光学研究グループ第二回研究討論会予稿集, p. 28, 平成6年11月.
39) S. Jiang, J. Ichihashi, H. Monobe, M. Fujihira and M. Ohtsu: Opt. Commun. **106**, 173 (1994).
40) R. Micheletto, H. Fukuda and M. Ohtsu: Langmuir **11**, 3333 (1995).
41) 入江正浩：高分子 **43**, 544 (1994).
42) E. L. Raab, M. G. Prentiss, A. E. Cable, S. Chu and D. E. Pritchard: Phys. Rev. Lett. **59**, 2631 (1987).
43) M. H. Anderson, J. R. Ensher, M. R. Matthews, C. E. Wieman and E. A. Cornell: Science **269**, 198 (1995).
44) Z. Hu and H. J. Kimble: Opt. Lett. **19**, 1888 (1994).
45) H. Ito, K. Sakaki, T. Nakata, W. Jhe and M. Ohtsu: Opt. Commun. **115**, 57 (1995).
46) C. I. Sukenik, M. G. Boshier, D. Cho, V. Sandoghdar and E. A. Hinds: Phys. Rev. Lett. **70**, 560 (1994).
47) H. P. Breuer, K. Dietz and M. Holthaus: Phys. Rev. A **47**, 725 (1993).
48) Y. Aharonov and A. Casher: Phys. Rev. Lett. **53**, 319 (1984).
49) H. Hori, S. Jiang, M. Ohtsu and H. Ohsawa: *Proc. Int. Quantum Electron. Conf., Vienna, 1992*, p. 48 (Inst. Nachrichtentechnik der TU Wien, Vienna, 1992).
50) J. P. Dowling and J. Gea-Banacloche: *Proc. Int. Quantum Electron. Conf., Anaheim, 1995*, p. 185 (Opt. Soc. Am., Washington, 1994).
51) 佐藤俊一，稲場文男：光学 **21**, 77 (1992).
52) A. Ashkin, J. M. Dziedzic, J. E. Bjorkholm and S. Chu: Opt. Lett. **11**, 288 (1986).
53) S. Kawata, Y. Inouye and T. Sugiura: Jpn. J. Appl. Phys. **33**, L1725 (1994).
54) B. Labani, C. Girard, D. Courjon and D. Van Lebeke: J. Opt. Soc. Am. **B 7**, 936 (1990).
55) O. J. J. Martin, C. Girard and A. Dereux: Phys. Rev. Lett. **74**, 526 (1995).
56) L. Novotny, D. W. Phol and P. Regli: Ultramicroscopy **57**, 180 (1995).
57) J. Bardeen: Phys. Rev. Lett. **6**, 57 (1961).
58) H. Hori: *Near Field Optics*, ed. by D. W. Pohl and D. Courjon, p. 105 (Kluwer, Dordrecht, 1993).

(1995年9月20日 受理)

EDUCATIONAL COURSE

新しい近接場光学技術

教養のページ

大津元一

大津元一：正員 東京工業大学大学院総合理工学研究科

New Technology of Near-field Optics. By Motoichi OHTSU, Member (Interdisciplinary Graduate School of Science and Engineering, Tokyo Institute of Technology, Yokohama-shi, 226 Japan).

光通信や光情報処理の高速化，大容量化のためには光素子の小型化が必須である．しかし，従来は空間（導波路中も含む）を伝搬する光を使っているため光の回折現象（光ができるだけ広がろうとする現象）が光素子の寸法を制限していた．すなわち，この光を閉じ込めるために必要な光素子の寸法はおおむね光波長以下であった．一方，顕微鏡等の計測装置でも，その分解能は光の回折現象により制限され，光波長以下の寸法をもつ物体の像は観察できなかった．

以上のように光の回折現象が光素子，光応用システムの性能を制限していたが，これは絶対的ではない．すなわち従来は光を電磁場としてとらえ，利用していたのでこの制限が課せられていたが，形態の異なる光を使えばこの制限を受けない．例えば波長以下の寸法の空間において制御された電磁相互作用を媒介する場として光をとらえ，かつこれを利用することができる．そのような光はエバネッセント場とよばれる．これは物質表面にごく近い領域（光波長以下の距離で，近接場領域とよばれる）に存在する光のうちの非伝搬成分である．

エバネッセント場を利用した高分解能の顕微鏡の原理は半世紀以上前に提案されたが[1]，実験結果は1980年代に入って報告されるようになった．この顕微鏡は走査形近接場光学顕微鏡（SNOM），フォトン走査トンネル顕微鏡（PSTM）などとよばれている[2]．

なお，エバネッセント場は物質表面近傍に存在し，その強度分布は物質の構造に強く依存するので，その分布を利用して物質を極微加工したり，極微光素子を製作し，更にそれを駆動することに使える．このような技術分野を近接場光学技術とよぶが，近年この分野の進展が急である．

波長以下の寸法をもつ微粒子表面のエバネッセント場の強度分布の広がりはその微粒子の寸法程度であり波長にはよらない．これを検出するには図1（a）に示すように先鋭化した光ファイバをプローブとして用い，これを近づけて場を散乱させる．プローブを微粒子表面で走査しながらプローブの位置の関数として散乱光強度をプロットすると，微粒子表面の形状などの像を得ることができる．これがPSTMの原理であり，分解能はプローブ先端の寸法，形状などにより決まる．

プローブが必須素子であるが，最近になって化学エッチングにより光ファイバを先鋭化する技術が発展し，図1（b）に示すように先端曲率半径は数nmまで先鋭化されている．言い換えると，近接場光学技術はプローブを作るナノ加工技術に立脚しており，原理的提案以後，実験が半世紀間進展しなかった理由はこの加工技術の欠落にあった．作成されたプローブを用いて，PSTMにより多種の微小物体の像が観測され，数nm（光波長の約1/100）に達する分解能が得られている．電子のトンネル効果や原子間力を使った走査プローブ顕微鏡と対比すると，多種の試料を空気中，水中または極低温中で形状観測できること，更に分光特性が測定可能など，優れた特徴をもっている．

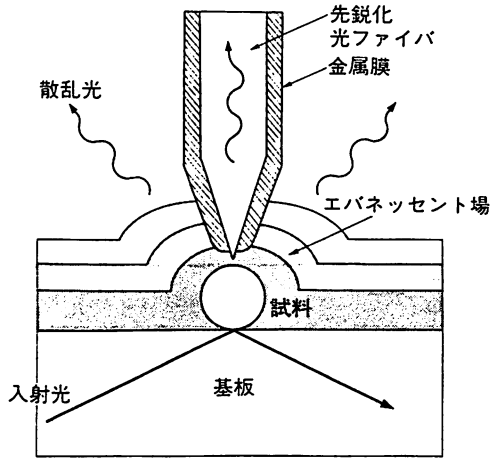

（a） PSTM の原理

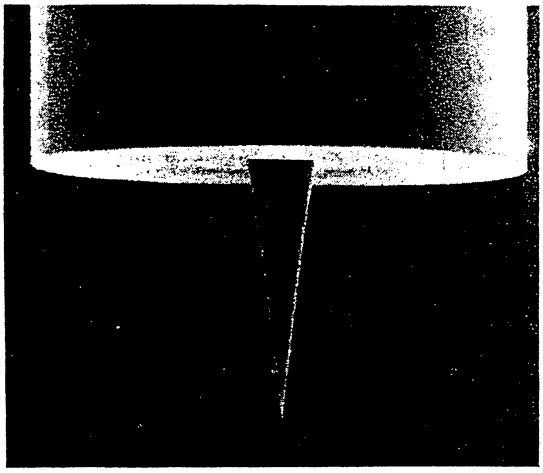

（b） 先鋭化された光ファイバの先端形状
（電子顕微鏡で観察．図の横幅は 24 μm に相当．）

図1 PSTM の構成の説明

図2には液体ヘリウム温度で観測した半導体量子ドット（一辺の寸法約 200 nm）1個からの微弱な発光スペクトルを示す．従来の顕微鏡では多数個の量子ドットからの発光スペクトルを同時に測定するので，図のように幅の狭い数本のスペクトルを分離測定することは不可能であった．このように空間座標軸上かつ周波数座標軸上において高分解能が得られるので今後の微小光素子の評価に有利である．また，生物試料の評価も行われており，バイオエレクトロニクスへの波及効果も大きい．

一方，エバネッセント場を用いた極微光加工も進展している．この場合はプローブ先端からしみ出したエバネッセント場の光エネルギーを用いる．これにより極微光記録などが可能となる．既存の光記録材料を用いて従来の光記録密度の数十倍の値が既に得られている．今後，材料開発により性能は更に向上するので，次の世代の超高密度光記録の期待がかかっている．

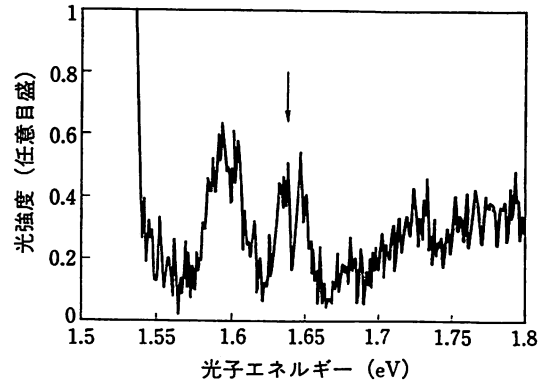

図2 液体ヘリウム温度で観測した半導体量子ドット1個からの発光スペクトル （矢印で示したピーク．試料は東大生産研荒川泰彦教授から提供された．測定は東工大戸田泰則氏による）

このほか，近接場での非線形光学特性を利用した光スイッチング，光増幅などの現象も引き出すことが可能で，これを利用すれば光波長に比べ極めて小さい寸法の光素子が可能となる．また，物質加工の極限的形態として，エバネッセント場による原子操作も提案されており，光により単原子の操作およびそれを使った単原子結晶成長などの可能性もでてくる．

以上のように近接場光学技術は多様な分野への展開が可能であるので，そのための新材料の開発も含め，今後の発展が期待される．

文　献

（1） E.H. Synge, "A suggested method for extending microscopic resolution into ultra-microscopic resolution," Phil. Mag., 6. pp.356-363, 1928.

（2） M. Ohtsu, "Progress of High-Resolution Photon Scanning Tunneling Microscopy Due to a Nanometric Fiber Probe," J. Lightwave Technol., 13, pp.1200-1221, 1995.

おおつ　もといち
大津　元一（正員）

昭48東工大・工・電子卒．昭53同大学院博士課程了．工博．同大助手，助教授を経て平3同教授．平5より神奈川科学技術アカデミー「フォトン制御」プロジェクト・リーダ兼任．量子操作工学などの研究に従事．電波科学国際連合KOGA-Medal，日本IBM科学賞，応用物理学会賞など受賞．

私の発言

東京工業大学　総合理工学研究科
大津　元一

☆光の周波数制御とフォトンSTM

1973年にこの大学の電子工学科を卒業したのですが，卒業研究の先生を決める際，当時伸びてきていた半導体産業とは違うものをやりたいと考えたのです。つまり半導体の次は何かということで，マイクロ波に比べると光の方が周波数が高いから光をやるべきじゃないかと思ったのです。

そういう目で卒業研究の先生方のリストを見ていましたら，計量研究所から来られたばかりの田幸敏治先生がレーザーをやっていることを知り，それで先生のところに配属させていただいたのです。それが光とのとっかかりです。

そして卒業研究は田幸先生の指導の下に，レーザーの周波数の自動制御をやりました。そして大学院を出て助手で置いていただいたのですが，大越先生などが提唱されていたコヒーレント光通信が有望視されており，その場合半導体レーザーの周波数制御が重要になると思い，それに関わることを少しずつやらせていただいて，その研究が最近まで続いているわけです。

しかしそのテーマはどちらかというと田幸先生にヒントを与えていただいて始めたものですので，もう少し乳離れしなければいけないなと思いまして，10年ほど前からフォトンSTMというものを始めました。それはファイバーの先をとがらせて，それを使って非常に倍率の高い顕微鏡を作るという研究です。その研究を光の周波数制御とは独立に並行してやってまいりました。

これは光のメモリーとか，非常に小さい光のデバイスの加工に使えたり，バイオとか化学にも応用できそうだということで，割と発展が見えてきているのです。2年半前から，大学での教育研究のほかに，この研究を推進するということで，神奈川県の財団法人である神奈川科学技術アカデミーが取り上げてくれまして，5年プロジェクトで「フォトン制御」という名で走り出しました。研究員は10人ほどでやっております。

このフォトンSTMというのは，ファイバーの先端を非常に細く，数10Åぐらいにとがらせたものをプローブとして使うのです。つまり先端に原子が100個ぐらいしか並んでいない程度までとがらせます。そこから光がわずかに浸み出しますと，非常に小さな懐中電燈のようなものになります。その非常に小さい光で物体の表面を照らすと像が見えます。それで非常に小さい寸法の像が見えるということになります。

またそれは像を見るだけではなくて，光を当てれば，場合によってはその表面が光のエネルギーで穴が開いたりします。そうしますとそれが光メモリーにもなります。そのほか光のデバイスの加工にも使えます。さらに原子1個1個をつかんだり，離したりということも可能だといわれていま

◀ニーズとかシーズとかのほかに、ウォンツ精神でやると、常識からは突拍子もない独自のアイデアが生まれます▶

す。理論的にはそういうことが可能だとわれわれのところで主張しているのです。

普通のSTMは電流が流れなければ見えません。ですから資料の表面に電流が流れる伝導体でなければ見ることはできません。しかしフォトンSTMは，絶縁体でも不透明体でも可能です。DNAでも測定可能なわけです。そしてそれが水の中でも空気中でもよく，ですから非常にバラエティーに富んだ計測が可能です。

さらに，STMでは形状しか見えませんが，これは使う光の色——つまり波長を変えると，その物質の構造を表わすような情報まで見えます。例えば，青い光に対する反射率と赤い光に対する反射率が違いますから，その差をうまく検出すると構造も分かるのです。そういう特徴もあります。

☆第2段階の夢

この原理の基本的な提案は1928年で，アインシュタインもそういうことを考えたという話もあります。ただ実験が行われるようになったのは1980年の中頃です。うちを含めて世界の4研究グループから，ほぼ同時に出はじめました。

どうして60年もギャップがあったかといいますと，その当時には使えるファイバーがなく，プローブができなかったのです。光通信とか光センサーの分野では日本のメーカーが先導していますが，そういう分野でファイバーの加工技術とか周辺技術が成熟してきたので，それで80年代になってようやくファイバープローブができるようになってきたのです。

それを裏返せば，そういうプローブをきちんと作ることが，この研究の初期の段階では，もっとも重要な課題だと思っています。ただこの研究は，半導体の微細加工のようなクリーンルームとか大きな装置は必要がなくて，割りとコロンブスの卵のようなところがあって，ファイバーを特別な溶液の中に漬けて，1時間ぐらい待っているだけでいいのです。プロジェクトに入る前の，学生と一緒に行った実験でも，とがるという可能性は示しました。

そういうように，半導体が平面でサブミクロン，ファイバープローブは立体で1nmとか10Åとかで，ものすごく小さいのですが，半導体製造のような大仰な装置ではなく，溶液に漬けて待っているということでできるわけです。

多分これは，日本のファイバーの性能が優れていて，そのファイバーの素材が均質だからうまくいっているのだろうと思います。硝子の専門家の先生にお聞きしても，これほど小さい硝子になると，硝子の構造がよく分からないので，なぜとがるか分からないといいます。そういうことを明らかにする専門分野はまだできておりません。しかし均質性が非常に優れたファイバーなので，この

ようにとがっても決しておかしくないでしょうねということです。そういう意味では理論よりも技術の方が先導しています。

理論物理は紙と鉛筆だけでできますが，実験となると，ものすごく先端的な科学はものすごく先端的な技術がないとできないようなところがあって，これなんかまさにその最たるものだと思います。そしてフォトンSTMでは，日本が先導しているファイバー技術を使ってできるということで，これはわれわれとしては嬉しいですね。外国ではなかなかこうはできません。

そのように，光ファイバーの先端を，いかに細く，再現性良く作るかという技術を開発するための研究を今やっているわけです。私は光との関わりを持った頃から，何とか新しい光の形態を作り出して，その光を何か物質にあてて新しい物質の加工とか，新しい物質そのものを作ることができないかと，ずっと考えていました。

そういう意味では，私の最初の研究である光周波数を制御することは，光の波をいかに綺麗な滑らかな波として作るかということで，それは新しい形態の光です。そしてその次のいかに光を小さい体積に集中させるかということも，新しい形態の光を作る1つだと思います。

それは綺麗な波を作っていないとできないということもありますし，体積の小さいところにパワーを集中させることができるということで，新しい利用の可能性が出てきました。ですから新しい形態の光を作るという，私の，いってみれば夢の第2段階にきているのだと思います。

☆教科書から飛び出た光の粒

その第2段階の新しい形態の光——われわれがイメージするのはゴルフボールのようなフォトンです。しかし普通のフォトンというのは，実は光の粒ではないのです。ある空間にゼリーのように満ち満ちており，本当の意味での光の粒というのは，ファイバーの先端に光をしみ出させるように，非常に小さいところにパワーが集中しているような光を形成しないと，ゴルフボールのようなイメージのフォトンという形態にはなりません。真の意味での光の粒を作りたいというのがわれわれの目的です。

粒が作れれば，その粒の持っているエネルギーで，材料の表面にものすごく小さい孔を開けたりすることができます。そうしますと，X線とか電子線とかを使う加工機ではなく，光を使う加工機ができます。つまり超高密度のメモリーとして使えますし，バイオテクノロジーの分野で，従来光では見えなかった小さな生体を，例えば水の中にいるようなものを観察するとか，量子力学の基本的な問題を研究するとか，それから真空中に浮いている原子をつかまえて，冷えた結晶基板の上に落として原子1個1個のレベルで結晶を作るとか，そういうことにも応用可能です。それから半導体の小さなデバイス——半導体レーザーとか量子井戸などを評価したり，新しい半導体光デバイスを作ったりすることにも使える可能性があります。

そのように光の万能な性能を引き出すために，

やはり光を粒のような形にしたいのです。

これは非常に広い範囲にわたってインパクトがあり，いろんな学会の方が興味を持ってくださっています。唯一の例外は数学と土木と建築，それに天文ぐらいで，生物，物理，化学，有機材料，もちろん応用物理，電気，電子の分野の方がたはずい分興味を持ってくださっています。

光協会さんでも，この4月からわれわれの方でお手伝いさせていただいて，応用に関わる調査をするための懇談会を発足させていただきました。発足時点で50社ぐらいが会員になっていて，いろいろな分野の方がたが興味を持ってくださっています。

そして，光の粒にしますと，普通の光の教科書には書いてなかった，常識ではとらえられていなかったような光の特性が，ずい分出てきました。ですから教科書に書いていないから，うちの実験は間違っているとか，そういうことは一切いえません。最初の頃は，そんなことは起こるはずはないとか，そんな形態の光はあるはずがないということを，ずい分言われたこともありました。

細くしたファイバーの先端から出る光の粒はどのくらいの大きさかといいますと，教科書に書いてあるような常識から考えると，光の波長程度だろうというのです。ですから1μm，そんな程度ですね。ところが実際にはファイバーの先端の直径とか半径ぐらいの大きさなのです。小さい径には小さく集中していますし，大きいものには大きく集中しているのです。これは光の波長とは全然関係がありません。どんな色の光を当てても先端の径によって決まるのです。先端が鋭ければ鋭いほど小さい粒が出てきます。

最近になって外国のある先生が，そんなことが起こるんでしたら，もう1回計算をやり直してみましょうということで，光学の教科書の最初に書いてある基本的な式を使って計算してみたのです。そしたら，まさにその通りになって，光の波長には全然無関係なのです。ほんの3か月ぐらい前の話ですが……。

そのように，だんだんと理論的バックグラウンドも完備しはじめてきました。

☆欧米先導型でない技術

ということで，新しいタイプの研究課題としてそして学問としてもかなり立ち上がってきました。私自身もエンジニアの端くれですから，これが国内外を通じて大きな産業に発展していただけるといいなと思っています。そのためには，例えば超高密度のメモリーを作っても，その上に保護膜を塗らなければいけないとか，プローブを動かすための信頼性の高い高速機械を作らなければならないとか，エンジニアリング的な周辺技術を固めなければいけません。そのためには多くの方がたのご協力が必要となります。

こういう分野に会社が参入する場合，まずマーケットとして成長するかどうかを予測するわけですけど，成長すると判断してもらえるかどうかというのは，これからの課題だと思っております。

こんなことをいうのは僭越ですが，従来の産業技術というのは割りと欧米主導型だったと思います。ですからこういうものが大きなマーケットになるかどうかを産業界の方が予測するには，欧米の産業界が先導してやっているか否かを判断基準

とするのですけど，このファイバープローブはそういう基準が使えません。

というのは，日本以外のファイバーでは，きちんとしたプローブはできません。外国で作るファイバーは，加工法が違っていて，実際先ほどお話ししたような方法で先のとがったプローブを作ろうとすると，へこんでしまったりするのです。

ヨーロッパあたりからこの分野が発展しはじめましたが，実験のデータの質としては，欧米のものはまだ十分高くはありません。ですから欧米のお手本があまりないのです。

ということは，日本のメーカーが産業レベルでものになると判断して一生懸命開発に努力すれば，ものになると思います。駄目だと判断したらものにはならないと思います。そういう意味では，自分の判断基準で決めなければならない時期にきていますが，そういうのはあまり日本は得意ではないかもしれません。ですから勇気を持ってやっていただかないとまずいのじゃないかというのが，私からの産業界への，僭越なメッセージです。

しかし光通信とか光メモリーのように日本が先導して成熟した光産業があります。そして，去年，今年あたり国際会議に出ていますと，この分野の研究がある程度飽和してきて，次にくるものは何だろうかというようなことを模索しているような雰囲気です。

その意味では光の新しい時代に入るかもしれないのです。従来の光通信や光メモリーなどに使っている光とはまったく違う光を使っていますからね。波長ではなくサイズによるとか，物質の表面にからみついているとかで，学問的な理論も含めてかなり新しいタイプの光技術で，第3段目の光技術ということになるような気がします。そういう意味で，なかなか面白そうな時期にきていると思っています。

非常に有り難かったことは，神奈川科学技術アカデミーがそのための研究費と，設備と，スペースと，それから人をつけてくれたことです。ですからワッと花開いているという感じです。

☆これからの光の課題

私の研究テーマのことばかりお話ししましたけれど，いまの光技術の最大の弱点は，光を光のままで貯えておくことができないことです。光のエネルギーをフルに貯えたり，利用したりすることができないので，光の時代とはいっても光の利用は弱電の分野——情報・通信分野に限られます。太陽電池の場合には，光を電圧の形で貯えますけど，光を光のままである入れ物の中に閉じ込めておくことはほとんどできません。そういうように光のエネルギーの蓄積ができ，フルに使えるようにすると光の飛躍的な発展があるといえます。

そして新しい物質を開発していかなければいけません。その物質を開発すれば，新しい形の光がそこから出てきます。新しい形の光が出てくれば，その光を使ってまた新しい形態の物質を作ることができて，フルに光を利用することができるようになりますから，物質と光というのはあくまでも車の両輪で開発されるべきだと思います。

例えば，サブミクロン加工ということで，デバイスを小さく加工する技術はすごく進んでいます。しかし，光デバイスとして使うためには，その中に光を閉じ込める必要があります。閉じ込め

1978年3月，東京工業大学大学院総合理工学研究科にて博士課程修了。1982年，同大学の理工学国際交流センターの助教授となり，91年に総合理工学研究科の教授となる。この間，86年～87年に，米国 AT＆T ベル研究所の研究員に従事する。

また，82年，応用物理学会賞（奨励賞），90年，The Third Optoelectronics Conference・Best Paper Award を受賞のほか，応用物理学会賞（会誌賞），91年には光産業技術振興協会・桜井健二郎氏記念賞など多くの賞を受賞。

るためには，従来のデバイスの寸法は光の波長より大きくなければいけなかったのです。ですからせっかく小さく作る技術を持っていても，大きなものとして使わざるを得ないのです。

ですから光のデバイスは電子のデバイスに比べると巨大なのです。それはどういうことかといいますと，電子デバイス用の加工技術を従来の光に適用しているからです。光に対して何の工夫もありません。ということは，光をうまく使うために物質をもう少し工夫しなければいけないことと，新しい物質ができれば，もう少し違う形態の光が出てきて，何も光の波長に合わせた体積の大きいものの中に閉じ込める必要はないのです。

例えば，その例がわれわれのファイバープローブです。新しい形のものが作れれば，光の波長よりずい分小さいところにパワーの集中している光が作れるわけです。これを使って何か加工をすれば，光の波長に比べてずい分小さいところで動作する光のスイッチとかアンプとか，そんなものができるはずです。そうしますと，加工精度を上げた分だけ小さい光デバイスができてくることになります。

ですから電子の技術から脱却した，新しい光の技術を確立することが必要です。

☆ウォンツ精神

技術とか科学というのは，大体25年周期で変わりますので，いま主流でないこともおじけづかずにやる勇気が必要です。それからニーズとかシーズという言葉がありますけど，このほかに先人もいわれたようにウォンツという言葉も重要だと思います。すなわち，必要だからやる，将来の研究の種になるかもしれないからやるということのほかに，自分自身はこうあって欲しいと思うからやるという考え方でやると，突拍子もない独自のアイデアが生まれます。

それは大体みんなから否定されますけど，すぐにあきらめないで，執念をもってやる勇気を失わないことだと思います。

新しいこととか，常識的ではないことをいうと，よく教科書を読んでいて，できる人ほど否定してきます。そしてそれが間違っていることを証明してみせようと意気込む人さえもいます。しかし，それに惑わされないで，自分自身が間違っていないと思っていれば，そのうち間違っていないことが分かってくるはずです。

みんなからいろいろいわれると自信がゆらぎますけど，それでもあきらめないで，石の上にも何年ということわざのように，しばらく食いついてみることが必要です。

そうはいっても，私もチャレンジャーとして，やらなければいけないことがいろいろとあります。私の手がけているフォトン STM も，人間の人生でいうと，まだ幼稚園に入ったか入らないかぐらいの技術です。それを何とか高校卒業ぐらいまでの年令に立ち上げるのが，大学の人間の役目だと思っています。

その後は，例えば大学生に月謝を払ったり，社会人に結婚式の式場を世話するのは，産業界の役目かなと思います。

（文責M. M.）

特集 ミクロの世界の掟……近接場光学

光の回折限界を超えるには

大津 元一（おおつ もといち）
（東京工業大学大学院 総合理工学研究科
(財)神奈川科学技術アカデミー）

光では見えないものを光で見たい

空間を伝搬する光には回折という性質がある．すなわち，光をその波長より小さい領域に閉じ込めようとすると，かえって広がろうとする性質である．光を扱う装置やデバイスの性能は，すべてこの性質により制限されている．たとえば光学顕微鏡の分解能(倍率)の限界は光の波長程度であり，これは回折限界とよばれている．

しかし，この限界は絶対的なものではなく，違う形態の光を使うことによって打破できる．たとえば空間を伝搬しない光を使えばよい．物質表面に存在する表面波はまさにそのような光であり，光学の教科書によるとこの光はエバネッセント波とよばれている．最近，この光を使った光学顕微鏡――フォトン走査トンネル顕微鏡(PSTM)などという――が開発されている．この顕微鏡は，従来，不可能であったナノメートル寸法の試料を空気中，水中で観察したり，さらには試料の加工にも使えることがわかり，これを扱う分野の進展が急である．このような分野を近接場光学という[1]．

フォトン走査トンネル顕微鏡とは？

空気に接しているガラスなどの平面に全反射角で光を入射すると，伝搬光はすべてガラス表面で反射される．このとき，その表面にはエバネッセント波とよばれる表面波の光が光波長程度の厚さにしみだしている．ここまでは光学の教科書に記されている事実である．PSTM ではこの表面波を利用するが，平面表面ではなく，光波長より小さい寸法の微粒子を扱う．その表面波のしみだし厚みは，上記の平面の場合とは異なり，微粒子寸法程度である．ただし，これは光学の教科書には記されておらず，最近わかった事実である．このように物質の寸法依存の領域内に強度の集中した表面波を使うため，顕微鏡としての分解能は非常に高くなる．

ただしこの表面波は，微粒子から遠ざかる方向には伝搬しないので，このままでは検出できない．これを検出するには図1(a)のようにもう一つの微粒子(プローブとよばれる)を表面波中に置き，表面波を散乱させてその光強度を測定する．プローブを走査しながらプローブの位置の関数として測定された光強度を図示すれば，これは表面波の空間分布，すなわち試料の微粒子の形状，構造を表すことになり，顕微鏡としての像が得られる．この場合の分解能は，プローブによってどれだけ小さい領域の表面波が散乱されるかによって決まる．したがって小さなプローブを使うことができれば，従来の光学顕微鏡の回折限界は打破できる．

なお，プローブにより散乱された光は，さらに試料の微粒子にも散乱されるので多重散乱となる．いい換えると，この多重散乱により二つの微粒子が光を交換

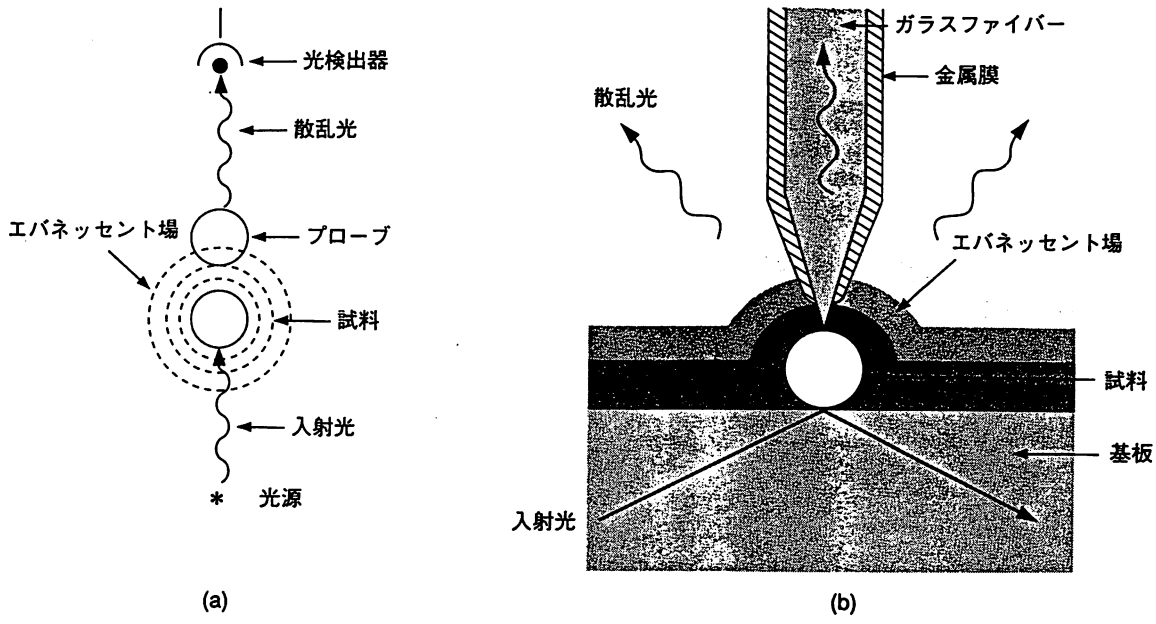

● 図1　(a) PSTM の原理的構造，(b) PSTM の実際的構造 ●

しながら結合した状態になっている．すなわち，この場合の表面波は微粒子を結合する場としての光であるので，以下これを「エバネッセント場」とよぶ．また，このエバネッセント場の交換は光子のトンネル効果に対応するので，この顕微鏡を上記のように PSTM とよぶ．実際には図1(a)のように微粒子をプローブとして使うのではなく，図1(b)のように先鋭化したガラスファイバーの根元に金属膜を蒸着したものを使う．

上記のように試料とプローブはエバネッセント場を介して結合しているので，従来の光学顕微鏡とは異なり，PSTM は接触型の顕微鏡といえる．このことは，PSTM は測定器である顕微鏡としてよりも，むしろ試料に対する光加工器に適しているといえる．

見えなかったものが見えた！

PSTM の必須素子は，図1に示すようなガラスファイバーを用いたプローブである．PSTM の基本的提案は1928年であるが[2]，実験が1980年代中頃まで行われなかった理由は，このプローブの作成技術が未成熟だったことにある．最近では熱したガラスファイバーを引っ張って先鋭化するなどの方法が開発されているが，10 nm 以内の先端曲率半径を再現性よく得ることは不可能である．

これに対しわれわれは，フッ酸系溶液による化学エッチングにより先鋭化する方法を考案した．ファイバー中心部のコアと外周部のクラッドが溶解する速度の違いにより先鋭化する．先端曲率直径は3 nm 以下であり，製作の歩留まりは90%以上である．詳しい先鋭化の素過程は不明であるが，筆者の研究グループの学生，研究員の試行錯誤により加工法が著しく進展した．このようにナノメートル寸法の加工については，まだそれを説明するための理論は存在しない．たとえ理論がなくとも実験を開始する勇気が成功の原因であった．次の段階として，先鋭化ファイバーに金属膜を蒸着し，その後，先端部分の金属膜を除去する．その際のナノメートル領域フォトリソグラフィーも，学生の勇気と努力で開発することができた．

このプローブを用いて，非常に高い分解能での測定が可能になった．とくに顕微鏡としての応用が期待されている生物試料観測では，電子を用いた従来のトンネル顕微鏡とは異なり，空気中や水中での観測が実現している．最大の特長は，半透明試料の内部構造が観

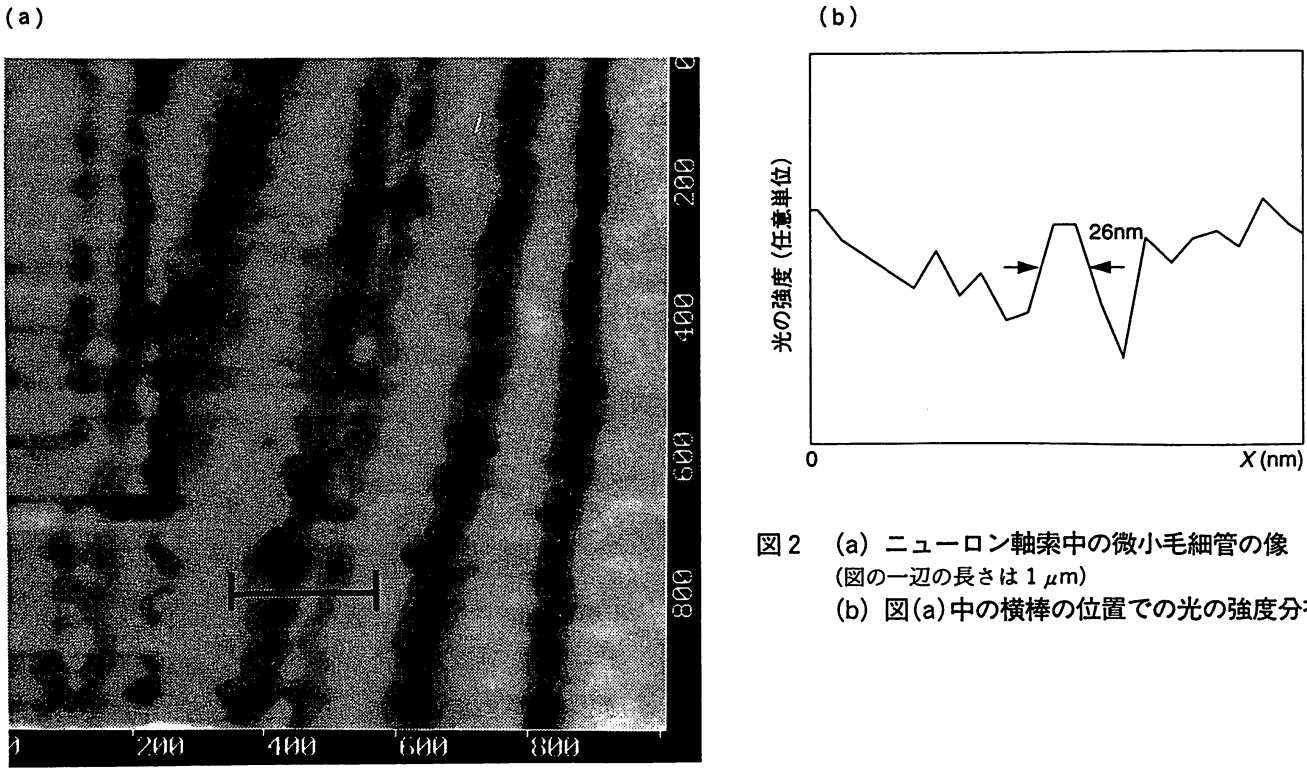

図2　(a) ニューロン軸索中の微小毛細管の像
(図の一辺の長さは 1 μm)
(b) 図(a)中の横棒の位置での光の強度分布

察できることである．図2(a)はその一例であり，ネズミの脳の神経細胞の軸索中にある微小毛細管の束が，軸索表面を通して外側から見えた結果を示す．電子顕微鏡観察の場合には軸索から取りだしてレプリカをとり，高真空中で観測しなければならない．毛細管の直径は25 nmであることがわかっているが，この図2(b)によるとその直径は26 nmであり，PSTMが電子顕微鏡と比べても遜色ない高い分解能をもっていることが示された．

さらに，ほかのプローブ顕微鏡と異なる点は光学スペクトルが測定できることであり，その例として液体ヘリウム温度にて，半導体量子ドット一つずつからの発光スペクトルも観測できるようになった(p. 7参照)．

なお，前にも述べたようにPSTMは測定器としてよりも加工器としての使用が有望である．その例として，プローブからしみだすエバネッセント場のエネルギーによりフォトクロミック薄膜表面の構造を変え，これによりフォトンモードでの消去可能光メモリーが実現し[3]，従来の光メモリーの約20倍の記録密度を達成している．

このほかにエバネッセント場を使った光スイッチ，光増幅器など，光波長より小さい領域で動作する光デバイスの提案などもなされている．さらに，物質加工の極限形態として原子の操作なども提案されており，今後は光を用いて原子レベルでの結晶成長などの実現が待望されている．

新しい物質の創造へ向けて

近接場光学は，従来使われていなかった新しい形態の光としてのエバネッセント場を利用することにより，単に測定器としてのPSTMを生みだしたのみでなく，加工器を実現して新しい物質の創造へと向かっている．プローブと試料との相互作用を媒介する力としてのエバネッセント場は，物質と両立させて考える必要があり，したがって新しい光と新しい物質とは車の両輪のように進化していくと期待される．

参考文献

1) M. Ohtsu, *J. Lightwave Technol.*, **13**, 1200 (1995). 2) E. H. Synge, *Phil. Mag.*, **6**, 356 (1928). 3) S. Jiang et al., *Opt. Commun.*, **106**, 173 (1994).

解説

フォトン走査トンネル顕微鏡によるナノメータ画像計測と加工・操作

大津　元一*

Nanometric Imaging, Fabrication, and Manipulation by a Photon Scanning Tunneling Microscope

by Motoichi OHTSU

キーワード　顕微鏡，エバネッセント光，フォトン，ファイバ，光記録

1. まえがき

従来より一般に論議されたり利用されている光は，その波長に比べてずっと大きな自由空間を伝搬している。この光を用いた光学顕微鏡の分解能は回折効果により決定される。すなわち，試料により散乱された光をレンズで集め，結像させようとすると光がわずかに広がり，像がぼけてしまう。そのぼけの大きさは光の波長程度であるので，光学顕微鏡では光の波長以下の寸法の試料は観察できない。同様にレーザの光を集光して加工に使おうとすると，その加工精度も回折効果により制限される。

しかし物質表面にしみ出たエバネッセント光*)を用いると回折限界を超える分解能を持つ光学顕微鏡が可能となる。これはフォトン走査トンネル顕微鏡（フォトンSTM）と呼ばれる。エバネッセント光は物質表面に近接した領域にある場であることからフォトンSTMおよび関連する光学現象に関する研究分野は近接場光学（Near Field Optics）と呼ばれる。フォトンSTMの原理と提案は60年前にさかのぼるが[1]，その実験は1980年代に入ってから開始された[2]。しかしここ数年その研究開発が急激に活発化している。その理由は近接場光学の基礎となる科学技術，さらに応用可能分野が極めて広い分野，特に将来の科学技術に関わる分野と密接に関わっているからである。

フォトンSTMとは先端の鋭いプローブで試料表面のエバネッセント光パワーの分布を測定する光学顕微鏡である。その詳細については過去にいくつか紹介させていただいているので[3),4)]，本稿ではその後の国内外の研究の進展の様子，さらに微細加工技術の一つである超高密度光記録，および極限技術である原子操作の試みについてご紹介する。

2. 顕微鏡の原理と構成

図1にフォトンSTMの基本的構成を示す。物体に光を照射するとその表面で光は反射，透過し，伝搬していく。そのとき同時に物体表面にはエバネッセント光が発生している。エバネッセント光は光照射により物体中に生じた分極の間の局所的相互作用を光として表現したものに他ならないので，上記の反射光，透過光と異なり，遠方へ伝搬せず，分極近傍に局在している。

先端の鋭いプローブを試料表面付近で走査しながらこのエバネッセント光を散乱して伝搬光に変換し，そのパワーを検出してプローブの位置の関数として図示すれば試料表面の三次元的像が表示できる。このとき像の分解能はプローブ先端の鋭さによって決まるので，通常の光学顕微鏡とは異なり光の回折限界を超えることができる。

* 東京工業大学総合理工学研究科（横浜市緑区長津田4259）
Interdisciplinary Graduate School of Science and Engineering, Tokyo Institute of Technology
神奈川科学技術アカデミー・大津「フォトン制御」プロジェクト（川崎市高津区坂戸3-2-1　KSP東棟408）
Ohtsu "Photon Control" Project, Kanagawa Academy of Science and Technology

*）英語名はEvanescent light。光を物質表面に照射したとき，表面にしみ出る表面波のこと。そのしみ出し長は照射する光の波長程度の大きさであり，その光パワーは表面からの距離の増加とともに急激に減少する。この光は表面に沿って伝搬する。より詳しい論議は光学に関する標準的教科書，たとえば大津元一，現代光科学Ⅰ（1994年，朝倉書店）第2．5節，などを参照のこと。

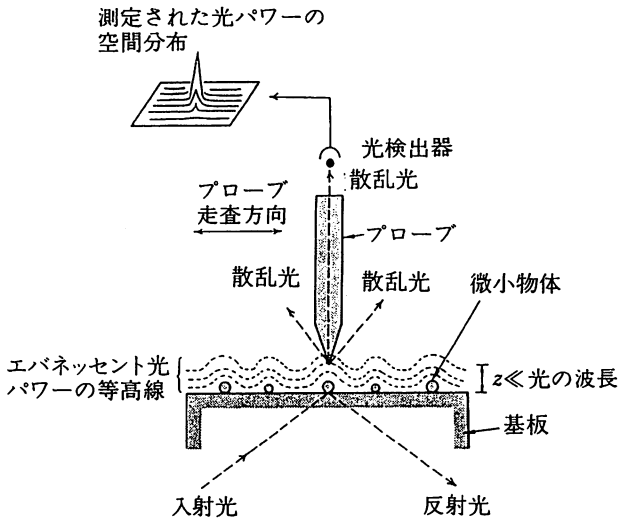

図1　フォトンSTMの基本的構成

フォトンSTM装置の中の基本となる素子はプローブである。従来，ガラス製のマイクロピペットを加熱して引き延ばしたもの[5]，光ファイバを加熱して引き延ばしたもの[6]，さらには微小球を用いるもの[7]，などがプローブとして用いられてきた。プローブにとって重要な性能は先端曲率半径が小さいこと（できれば10 nm以下），散乱した光の集光効率が高いこと，などである。しかし，従来のプローブではこれらの性能が必ずしも十分発揮されていなかった。そこで我々はこれらの性能の実現を目指し，かつ高い再現性で製作することを目指して，光伝送用のファイバを緩衝フッ酸溶液で選択化学エッチングした[8]。NH_4Fの体積比を調節することによりコア部のみを先鋭化すること，さらには二段階エッチングによりクラッド部を細径化すること[9]，四段階エッチングによりクラッド部の角のないペンシル形にすること[10),11]，などが可能となった。先端形状の電子顕微鏡写真を**図2**に示すが，10 nm以内の先端曲率半径が実現している。また，先鋭角の最小値は15度になる。

先鋭化したプローブの根元に金属膜をコーティングし，先端部分の金属膜をヨウ化カリウム溶液により除去してファイバ先端部を露出させ，開口を形成することができる。先端部の電子顕微鏡写真を**図3**に示すが，開口径30 nmが実現している[11]。

図1のように光を試料裏面から全反射角で入射させ，発生したエバネッセント光をプローブでピックアップする方法の他に，プローブ先端にエバネッセント光をしみ出させ，これを試料により散乱して測定する方法などがあるが，フォトンSTMの装置で重要なのはプローブの位置制御である。そのた

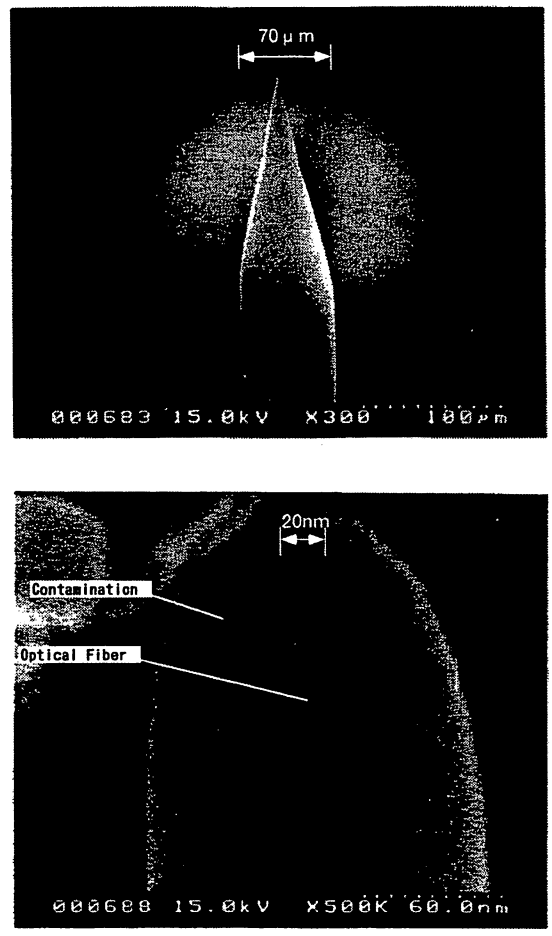

図2　ペンシル形プローブの電子顕微鏡写真（上）とその先端部拡大図（下）[10),11]。下図の最外部は電子顕微鏡による観測時に付着した汚れ，内部が金属膜の蒸着された先鋭化光ファイバ

めにプローブと試料との間のせん断応力をモニターする方法が考案されている[12]。この他に上記の二段階エッチングによりクラッド部が細径化されたプローブをわずかに傾けて試料に近づけ，試料との間の原子間力によるたわみをモニターしてプローブ位置を制御する方法もある[13]。これらの方法を使うとプローブと試料との間隔を制御することができるのみでなく，フォトンSTM像と同時に原子間力顕微鏡（AFM）像が測定できる利点を有する。

検出される光パワーは数pW～数nWなので低雑音の測定環境を準備する必要がある。フォトンSTM独自の雑音源は光検出の際のショット雑音である。我々の測定例では，フーリエ周波数10 Hz以上ではショット雑音が支配的であり，対応する縦方向分解能は3 pm／$\sqrt{\text{Hz}}$であった。10 Hz以下では音響振動の影響により雑音レベルが大きく，フーリエ周波数1 Hzで

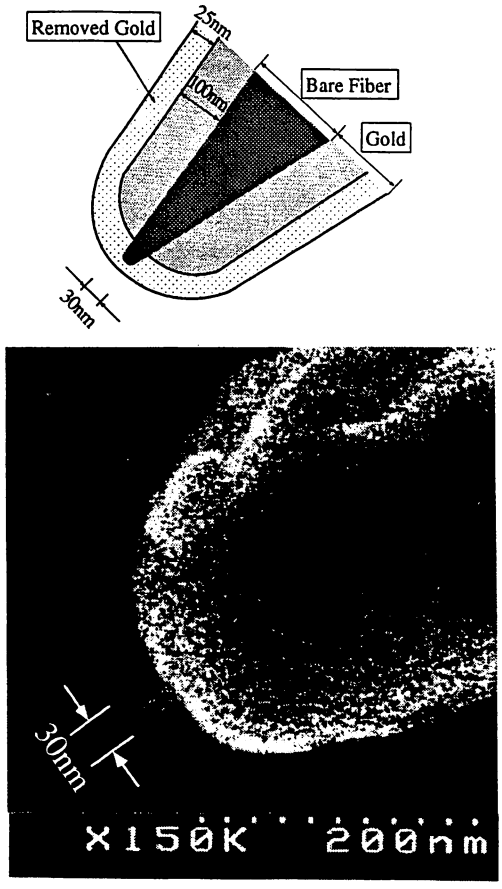

図3 金属膜を除去しファイバ先端部が露出したプローブの断面説明図（上）とその電子顕微鏡写真（下）[11]

は対応する縦分解能は0.1 nmであった。

上記の光パワー直接検出方式の他に共振形プローブを用いたヘテロダイン検出法も提案されているが[14]，その場合には微小開口を持つQ値の高い微小共振器を作成することが課題である。

一辺1 μ m以下の視野で像を観測するために，試料を基板に固定する際には注意が必要である。すなわち，試料固定時に散乱光発生源を作らないこと，などである。生体試料の基板への固定にはAFM像観察用試料に対する手法が使われている。フォトンSTMの特徴の一つは大気中での観察が可能なことであるが，そのときは試料とプローブとの間の水分子の存在，誘電体試料表面の帯電荷などに注意する必要がある。

3．ナノメータ計測

フォトンSTMの分解能を評価するために各種の微粒子（たとえば誘電体のラテックス球[15]，バクテリオファージT4[16]など）が観測されている。さらに**図4**に示すのは直径25 nmのサルモネラ菌の鞭毛の測定例である。これらの一連の測定結果

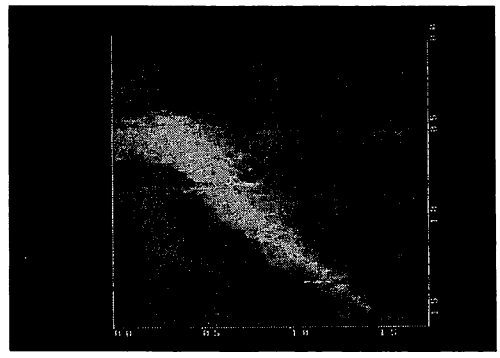

図4 サルモネラ菌の直径25 nmの鞭毛の観測像（写真中の棒状の明部）

より分解能は数nm以内に達していると評価されている。今後，システム性能の向上によりさらに高分解能化が進むであろう。

一方，フォトンSTMは光エレクトロニクス用微小デバイスの評価にも使われている。**図5**はプロトン交換$LiTaO_3$導波路の導波モード形状の測定結果であるが，これより波長以下の寸法を持つ散乱源の同定，ビーム伝搬法による計算結果との比較などが行われ，光導波路の新しい非破壊・高分解能評価法が提示されている[17,18]。一方，半導体の量子細線の形状測定なども試みられている[19]。

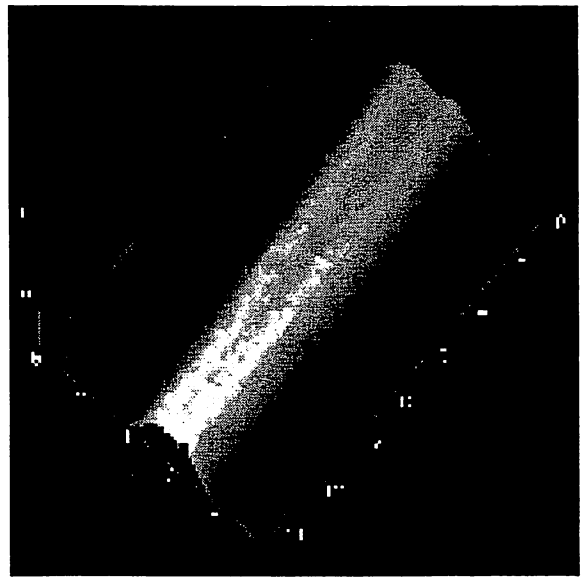

図5 プロトン交換$LiTaO_3$製のY分岐光導波路の導波モードの観測像[17,18]。画像の寸法は8 μ m × 15 μ m

他の走査プローブ顕微鏡と異なり，フォトンSTMでは入射光により励起された試料からの蛍光を局所的に測定すること

が可能である。ただしこの場合，光子計数法などの微弱光検出技術を組み合わせる必要がある。一例として，**図6**に色素がドープされた微小ラテックス球からの蛍光像を示す[20]。

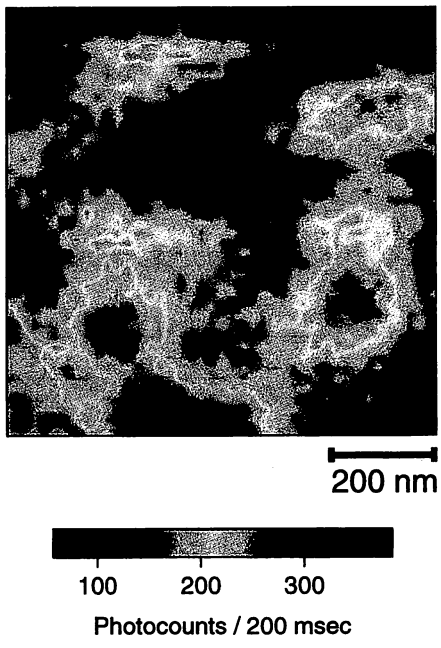

図6　色素ドープされた直径100 nmの複数個のラテックス球からの蛍光測定結果[20]。図下部の色表示は測定時間200 ms間に測定されたフォトン数を表す

さらにフォトンSTMの特徴として入射光の波長を掃引することにより試料の局所的光学スペクトルが観測可能である。これにより試料形状のみでなく，試料構造，特に生体試料の場合には局所的な化学種の同定が可能となる。今までに応力下のルビーの蛍光スペクトル[21]，ダイアモンドのラマンスペクトル[22]，さらには単一色素分子からの蛍光スペクトル[23]が測定されており，またプローブが近づいたときの蛍光クエンチングが検出されている[24]。これは量子電気力学に関連する現象として興味深い。また，上記の半導体量子細線の蛍光スペクトルが低温にて測定されている[19]。これらの分光実験では空間的分解能は100 nm程度であり，まだ予備実験の段階といえる。最近は分解能は低いが，低温技術，超短光パルスによる励起[25]，などの技術を組み合わせる分光法の開発が盛んになっている。

4．ナノメータ加工機・操作機としての使用

ナノメータ加工の一例として，プローブからエバネッセント光をしみ出させ，その光パワーを用いて光メモリ材料に記録する試みが報告されている。記録寸法はプローブ先端寸法によって決まるので，従来の光記録とは異なり，回折限界を超えた記録が可能になる。光磁気メモリ材料のCo／Ptにアルゴンレーザを用いて熱モードで記録し，記録寸法約100 nm，記録密度45 Gb／inch^{2}を得ている[26]。これは従来の光メモリの記録密度の約20倍の値に相当する。読み出しもフォトンSTMを用いている。記録装置寸法を小型化するために同じ記録を半導体レーザにより行う試みも報告されている[27]。なおこの方法では光の偏光を利用しているが，光波長以下の微小開口からのエバネッセント光の偏光状態は入射光の偏光を保存しないので今後の高密度化には不利である。この点を解決するためにフォトンモードによる記録が試みられている[28]。**図7**にフォトンモードによる記録，再生の原理を示す。すなわち：

[記録] フォトンSTM用プローブ先端にエバネッセント光をしみ出させ，プローブとメモリ用媒体との距離を光波長以下(すなわち近接場の領域)に保ったまま掃引する。このときエバネッセント光のエネルギーにより媒体表面の構造を変化させる。

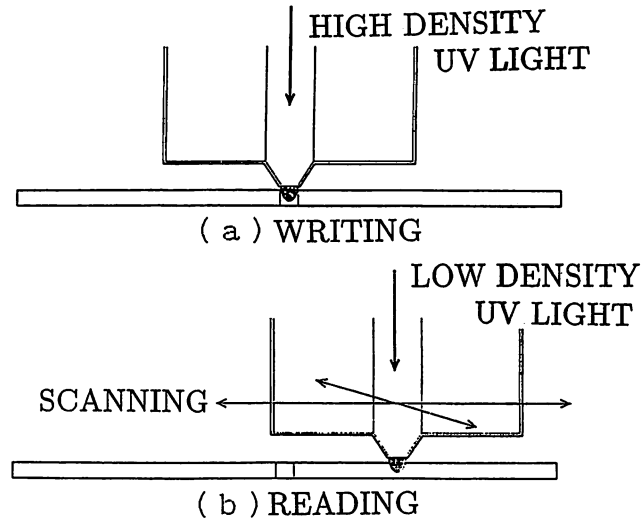

図7　フォトンモードの光記録(a)，再生(b)の装置の基本構成

[再生] 上記の記録過程での構造変化を顕微鏡としてのフォトンSTMで測定する。

フォトクロミック材料であるジアゾベンゼン誘導体のLB膜(60層)が記録媒体として使われている[28]。**図8**に示すように波長350 nmの紫外光により記録媒体をトランス形異性体からシス形異性体へと変化させることにより記録を行う。上記の紫外光は出力パワー60 mWのアルゴンレーザから得た。なお，実際の記録の際のエバネッセント光パワーは約30 nWであった。

再生にも同じ光源を用いたが，出力パワーを0.6 mWまで減

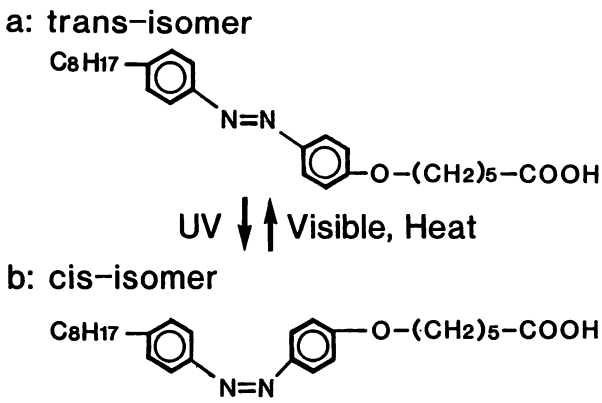

図8　記憶媒体の分子構造

少させている。波長350 nmにおける吸光度はトランス形異性体では0.31，シス形異性体では0.16であること，すなわちその差が0.15と大きく異なることを利用し，再生には同じ装置をフォトンSTMとして用い，記録媒体の透過率の面内での局所変化を測定することにより行った。このときエバネッセント光パワーを0.3 nWに減少させて記録媒体の透過率を測定した。**図9**には再生結果の例を示す。円形スポットがシス形異性体に構造変化している箇所であり，記録されたピットに相当する。

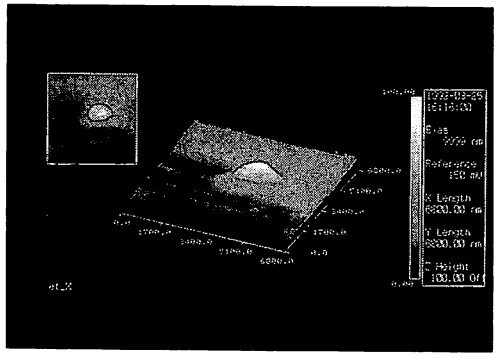

図9　光記録されたピットの再生像(写真中の円形の明部)
直径は約100 nm，図の一辺は700 nmに相当

なお，この図では円形スポットの直径は約100 nmであり，記録時の光波長以下の値になっている。これらの直径の値は周囲温度揺らぎによる記録中のプローブ位置の横方向揺らぎにも依存することがわかった。今後，プローブ位置揺らぎを抑圧する制御を施すことにより，より小さい直径が期待される。

ここで示した近接場光学による光記録・再生方式はまだ研究開発の初期段階であり，さらに進展させるには下記の基本的な問題を解決する必要がある。

(1) 最適記録媒体の探索
(2) プローブへの入力可能レーザ光パワーの上限とプローブ熱破壊限界の推定
(3) 再生の際の光検出雑音の評価と記録密度上限，再生速度上限の推定

しかし記録できるピット径は最終的にはプローブ先端曲率半径により制限される値まで小さくすることが期待され，数nmとなり得る。この意味で本方法は超高密度の光記録実現のための有望な方法といえる。

また，ここで示したフォトンモードの光記録は見方を変えれば局所的な光化学反応の実験と考えることができる。したがって熱モードによる方法も合わせ考えると光記録のみならず，将来はその他のナノメータ加工，すなわちレーザトリミング，レーザアニーリングなどへの発展も期待できる。従来のレーザ光を利用した微細加工の代表例はレーザマスクリペアであり，最小加工線幅0.7 μm，修正位置精度0.1 μm程度がすでに実現しており，64 MbのDRAM用のマスク修正などに用いられているが，これ以上の高分解能化は従来法ではかなり困難と考えられている。本節でご紹介した方法はこの問題を打破する新技術となり得る。特に256 MbのDRAM以降のフォトマスク修正が可能となれば，将来のULSI製造プロセスでも大きなインパクトが期待できる。

ところで極限的な微細加工の方向を示す研究として，最近では三次元構造を持つエバネッセント光を用いた原子操作が活発になっている。たとえば，直径数μmの微小リング共振器から共振器外周にしみ出すエバネッセント光による原子の周回[29]，さらに中空ファイバ中にしみ出したエバネッセント光による原子導波路[30]，さらには凸状先端を持つファイバからのエバネッセント光中による原子の捕獲[31]などの提案がなされている。我々もすでにプローブ先端にしみ出すエバネッセント光により真空中に浮遊する原子を一つずつ捕獲する方法を提案している[32),33)]。

以上の原子操作は捕獲された原子を冷却結晶基板の上に一つずつ固定して単原子レベルの結晶成長や光メモリの作製を行うなどの応用が期待される。

5．おわりに

フォトンSTMは単に光の波長以下の寸法の物体像やその構造を観察する測定器としてのみでなく，新しい微小物質を作り出す加工機，操作機としての機能を持っている。この特徴こそが微小半導体デバイス，光メモリ，さらにはバイオテクノロジー，マイクロマシンなどの広い分野で最近注目を集めている理由である。また，その動作原理の基礎も奥深く，従

来の光学ではカバーしきれない内容も含まれる。すなわちフォトンSTMを扱う「近接場光学」,「ナノ・フォトニクス」の基礎と応用は極めて多岐にわたる。

最近はフォトンSTM装置の市販品も現れ，ユーザ数も増えている。研究人口も増加し，既に過去三回の国際会議が開催されている[34),35)]。第三回目は来秋イスラエルのエルサレム市で開催されることが決まっている。また，日本でも研究が活発化し，学会レベルでも近接場研究グループが発足している。今後は新しい光学，フォトニクスの分野として発展することを期待したい。

謝辞

サルモネラ菌の鞭毛試料をご提供頂いた，帝京大学理工学部・相沢慎一先生，また試料固定法に関して教示頂いたNTT境界領域研究所・梅村茂博士に感謝します。実験結果の写真をご提供頂いた神奈川科学技術アカデミー，物部秀二氏（**図2，3**），納谷昌之氏（**図4**），斎木敏治氏（**図6**）に感謝します。

参考文献

1）E. H. Synge：A Suggested Method for Extending Micorscopic Resolution into Ultra-microscopic Resolution, Phil. Mag., 6, pp.356-362,（1928）

2）E. Betzig and J. K. Trautman：Near-Field Optics：Microscpy, Spectroscopy, and Surface Modification, Science, 257, pp.189-195,（1992）

3）大津元一，堀　裕和：光による原子レベルの計測と制御，計測と制御，31, pp.943-948.（1992）

4）大津元一：フォトン走査トンネル顕微鏡：光の回折限界を越えて，48, pp.25-28,（1993）

5）E. Betzig, M. Issacson, H. Barshatzky, A. Lewis and K. Lin：Near-field scanning optical microscopy（NSOM）, SPIE, 897, pp.91-99,（1988）

6）U. Durig, D. Pohl and F. Rohner：Near-field optical scanning microscopy with tunnel-distance regulation, IBM J. Res. Dev., 30, pp.478-483,（1986）

7）片岡俊彦，高田和政，遠藤勝義，井上晴行，森　勇蔵，稲垣耕司：走査型近接場工学顕微鏡（SNOM）の開発Ⅳ，第41回応用物理学関係連合講演会，1994年（平成6年）春季，講演番号28aC4

8）T. Pangaribuan, K. Yamada, S. Jiang, H. Ohsawa and M. Othsu：Reproducible Fabrication Technique of Nanometric Tip Diameter Fiber Probe for Photon Scanning Tunneling Microscope, Jpn. j. Appl. Phys., 31. pp. L1302-L1304,（1992）

9）T. Pangaribuan, S. Jiang and M. Ohtsu：Two-step etching method for fabrication of fibre probe for photon scanning tunneling microscope, Electron. Lett., 29, pp. 1978-1979,（1993）

10）物部秀二，R. ウママヘスワリ，斎木敏治，納谷昌之，大津元一：フォトン走査トンネル顕微鏡用ペンシル形ファイバプローブの作成，第41回応用物理学関係連合講演会，1994年（平成6年）春季，講演番号28pDl

11）物部秀二，納谷昌之，R. ウママヘスワリ，斎木敏治，大津元一：フォトン走査トンネル顕微鏡用ペンシル形ファイバプローブと微小開口の作製法"，第13回光波センシング技術研究会，1994年6月，講演番号LST13-13

12）E. Betzig, P. L. Finn and J. S. Weiner：Combined shear force and near-field scanning optical microscopy, Appl. Phys.Lett., 60, pp.2484-2486,（1992）

13）今井一宏，興梠元伸，蒋　曙東，大津元一：AFM同時動作可能なフォトン走査トンネル顕微鏡，第41回応用物理学関係連合講演会，1994年（平成6年）春季，講演番号28pD4

14）S. Jiang, K. Nakagawa and M. Ohtsu：Reflection-Resonance-Type Photon Scanning Tunneling Microscope, Jpn. J. Appl. Phys., 33, pp. L55-58,（1994）

15）S. Jiang. N. Tomita, H. Ohsawa and M. ohtsu：A Photon Scanning Tunneling Microscope Using an AlGaAs Laser, Jpn. J. Appl. Phys., 30, pp.2107-2111（1991）

16）S. Jiang, H. Ohsawa, K. Yamada, T. Pangaribuan, M. Ohtsu, k. Imai and A. Ikai：Nanometric Scale Biosample Observation Using a Photon Scanning Tunneling Microscope, Jpn. J. Appl. phys., 31, pp.2282-2287,（1992）

17）戸田泰則，大津元一：フォトン走査トンネル顕微鏡による$LiTaO_3$導波路の導波モード観測，第41回応用物理学関係連合講演会，1994年（平成6年）春季，講演番号30pG12

18）戸田泰則，大津元一：フォトン走査トンネル顕微鏡による光導波路の高分解能力評価"，第13回光波センシング技術研究会，1994年6月，講演番号LST13-15

19）R. D. Grober, T. D. Harris. J. K. Trautman, E. Betzig, W. Wegscheider, L. pfeiffer and K.West：Optical spectroscopy of GaAs/AlGaAs quantum wire structure using near-field scanning optical microscopy, Appl. Phys. Lett., 64, pp.1421-1423,（1994）

20）斎木敏治，納谷昌之，R. ウママヘスワリ，物部秀二，大津元一：先鋭化光ファイバ・プローブの分光への応用"，日本物理学会第49回年会，1994年3月，講演番号29aD2

21）P. J. Moyer, C. L. Jahncke, M. A. Paesler, R. C. Reddic and R.

J. Warmack：Spectroscopy in the Evanescent Field with an Analytical Photon Scanning Tunneling Microscopy, Phys. Lett. A, 145, pp.343-347, (1990)

22) D. P. Tasi, A. Othonos, M. Moskvits and D. Uttamachandani：Raman spectroscopy using a fiber optic probe with subwavelength aperture, Appl. Phys. Lett., 64, pp.1768-1770, (1994)

23) W. P. Anbrose, P. M. Goodwin, J. C. Martin and R. A. Keller：Single Molecule Detection and Photochemistry on a Surface Using Near-Field Optical Excitation, Phys. Rev, Lett., 72, pp.160-163, (1994)

24) R. C. Dunn, G. R. Holton and X. S. Xie：Fluorescence spectroscopy on a single molecule basis with a near-field spectrometer, Tech. Digest of Int. Quantum Electron. Conf. 94, May 1994, Anaheim, pp.2-3

25) S. Smith, B. G. Orr, R. Kopelman and T. Norris：Femtosecond near field scanning optical microscope, Tech. Digest of Conference on Lasers and Electro-Optics, May 1994, Anaheim, pp.147-148

26) E. Betzig, J. k. Trautman, R. Wolfe, E, M. Gyorgy, P. L. Finn, M. H. Kryder and C.-H. Chang：Near-field magneto-optics and high density data storage, Appl. Phys. Lett., 61, pp.142-144, (1992)

27) 新谷俊通，中村公夫，丸山洋治，保坂純男，井村　亮：半導体レーザを用いたSNOMの試作，第41回応用物理学会関係連合講演会，1994年（平成6年）春季，講演番号31aMC7

28) S. Jiang, J. Ichihashi, H. Monobe, M. Fujihira and M. Ohtsu：Highly localized photochemical processes in LB films of photochromatic material by using a photon scanning tunneling microscope, Opt. Commun., 106, pp.173-177, (1994)

29) H. Mabuchi and H. J. Kimble：Atom galleries for whispering atoms：binding atoms in stable orbits around an optical resonator, Opt . Lett., 19, pp.749-751, (1994)

30) M. A. 01' Shanii, Yu. B. Ovchinnikov and V. S. Letokhov：Laser guiding of atoms in a hollow optical fiber, Opt. Commun., 98, pp.77-79, (1993)

31) J. P. Dowling and J. Gea-Balacloche：Atomic quantum dot, Tech. Digest of Int. Quantum Electron. Conf. 94, May 1994, Anaheim, pp.185-186

32) 大津元一：フォトンSTM（V）—単原子レベル結晶成長"，第51回応用物理学会学術講演会，1990年（平成2年）秋季，講演番号27aL79

33) H. Hori, S. Jiang, M. Ohtsu and H. Ohsawa：A Nanometer -Resolution Photon Scanning Tunneling Microscope and Proposal of Single Atom Manipulation, Tech. Digest of the 18th Int. Quantum Electron. Conf., June 1992, Vienna, pp.48-49

34) 大津元一，堀　裕和：近視野光学ワークショップ報告"，応用物理，62, p.292, (1993)

35) 大津元一：第2回近接場光学国際会議報告，応用物理，63, p.77, (1994)

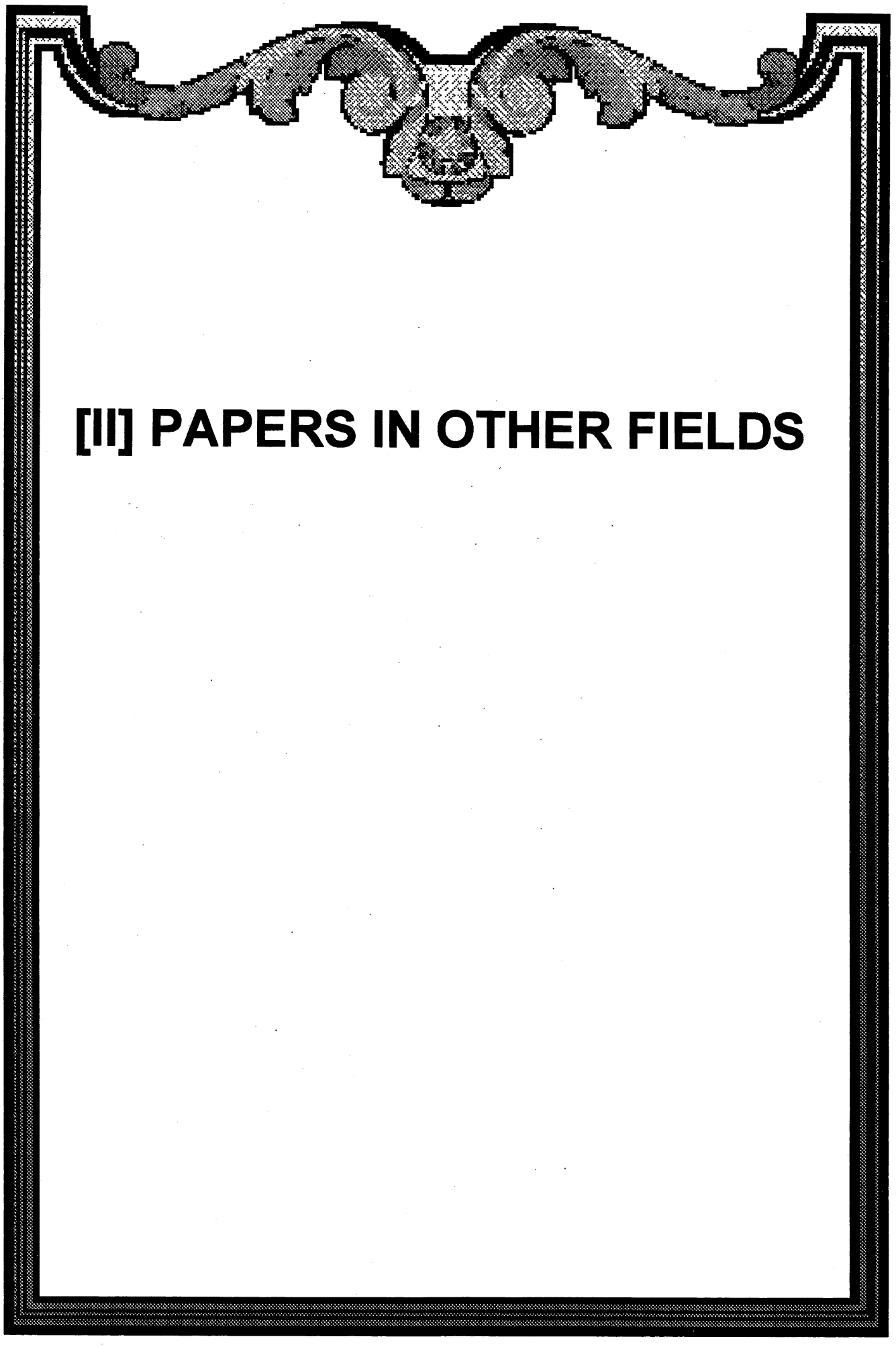

[II] PAPERS IN OTHER FIELDS

Highly sensitive and wideband optical detection in patterned $YBa_2Cu_3O_{7-\delta}$ thin films

Ken'ichi Tanaka,[a] Yoshiro Arikawa, Matsuo Sekine, and Motoichi Ohtsu[b]
Department of Applied Electronics, Tokyo Institute of Technology, 4259 Nagatsuta, Midori-ku, Yokohama 226, Japan

Yuichi Harada
NTT Basic Research Laboratories, Morinosato-Wakamiya, Atsugi 243-01, Japan

Martin Danerud[b]
Department of Physics, Chalmers University of Technology, S-412 96 Göteborg, Sweden

(Received 2 January 1996; accepted for publication 15 March 1996)

We have measured the optical responses up to 18 GHz in patterned $YBa_2Cu_3O_{7-\delta}$ thin films at various wavelengths by optical heterodyne mixing. The responsivity of the detectors is higher than 50 V/W below 1 Hz at various wavelengths and the responsivity is 20 mV/W at 780 nm and 150 mV/W at 1.55 μm wavelengths in the regime of the modulation frequency from 3 GHz to 18 GHz.
 [S0003-6951(96)00522-0]

Since the discovery of high-T_C superconductors (HTSCs), several experiments have shown great possibilities for a device operated at 77 K. One of these devices is an optical detector using a HTSC thin film.[1] When the resistance of a superconducting film rapidly drops to zero at the superconducting transition, the temperature rise by laser irradiation produces a large increase of resistance in this regime. This is called a bolometric detection.[2] As long as the light can be regarded as a thermal source, the sensitivity of the detector should be independent of its wavelength.

On the other hand, the nonequilibrium responses have also been observed in $YBa_2Cu_3O_{7-\delta}$ (YBCO) thin films.[3] When a YBCO thin film is irradiated by the laser, photons can produce excited quasiparticles with the energy well above the superconducting energy gap Δ. Then, the distribution of quasiparticles can be changed far from the equilibrium Fermi-Dirac function. In fact, some experiments[4,5] suggested that the nonequilibrium photoresponse can be attributed to the rearrangement of the quasiparticle distribution in the vicinity of the superconducting transition. The optical response thus includes not only a bolometric component but also a nonequilibrium one.

Many researchers used the pulsed light with the picosecond full width at half maximum or the continuous wave (cw) light modulated at very high frequency in order to distinguish each component. The frequency spectrum gives us the insight into the relaxation process of excited quasiparticles such as the lifetime. Recently, ultrafast optical responses, 1.5 ps pulse response[4] and 18 GHz modulation frequency,[5] have been reported. Furthermore, a responsivity of 10^4 V/W in the 1–8 μm wavelength region has also been reported in granular $BaPb_{1-x}Bi_xO_3$ thin films, although the detection mechanism is based on the Josephson effect.[6]

In this work, we investigated the optical responses of patterned YBCO thin films at various optical wavelengths. The responsivity of these patterned YBCO thin films was estimated at the wavelength of 780 nm, 830 nm, 1.33 μm, and 1.55 μm. We succeeded in detecting the responses up to 18 GHz at 780 nm and 1.55 μm wavelengths by the optical heterodyne mixing. We explain the mechanism for the fast response in terms of an electron heating model including the wavelength dependence.

We used 50-nm-thick YBCO thin films prepared by laser deposition onto $LaAlO_3$ substrates. The samples were fabricated by standard photolithography and Ar^+ ion milling. The active detection area in the YBCO thin film consisted of ten parallel striplines, whose width and length were 1 and 20 μm. Thus, the whole detector area was 10×20 μm^2. A detailed description of the fabrication process is given elsewhere.[7] The patterned YBCO sample was mounted on a cold finger in the cryostat, which can be cooled down to 4.2 K by a liquid-He flow. In order to get a good thermal contact between the sample and the stage, silver paste was used. Measurement leads from the sample were bonded to a 50 Ω coplanar line on the finger. The opposite side of the coplanar line was connected to an impedance-matched coaxial cable and the signals at room temperature were obtained through this cable. A special polyimide film was used as a coplanar line to reduce the thermal conduction.

The optical responses were measured using two methods: direct amplitude-modulation and optical heterodyne mixing. Below the frequency of 1 GHz, we used an AlGaAs laser diode (LD) with 830 nm wavelength. The frequency can be modulated up to 1 GHz by superimposing ac current onto a dc bias current. The peak to peak value of the radiation power is fixed at 3 mW. 1.33 μm and 1.55 μm wavelength distributed feedback LDs coupled to an optical fiber were also used. The peak to peak value of the radiation power for each laser was fixed at 2 mW. To measure the optical responses above 1 GHz, we adopted an optical heterodyne mixing method as shown in Fig. 1.[8] The optical heterodyne mixing system needs almost identical lasers. Figure 1(a) shows the light source part. The wavelength of the laser was controlled by fine and coarse tuning of both the bias current and the temperature. For stable operation, each of almost identical 1.55 μm LDs was packed into a module together with a thermocooler device, a thermistor, and an optical isolator giving more than 60 dB isolation.[9] The op-

[a]Electronic mail: ketanaka@ae.titech.ac.jp
[b]Also at Kanagawa Academy of Science and Technology (KAST), KSP East Room, 3-2-1 Sakado, Takatsu-ku, Kawasaki 213, Japan.

 0003-6951/96/68(22)/3174/3/$10.00

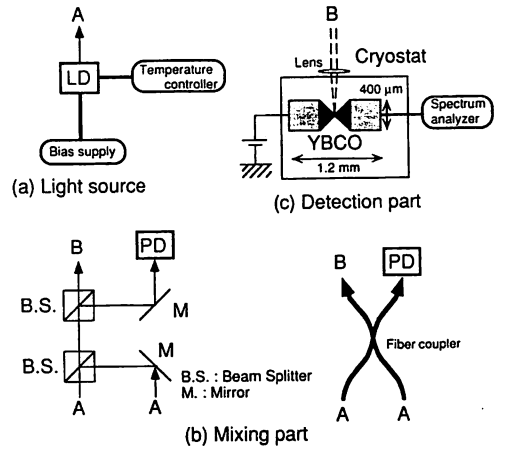

FIG. 1. Diagram of an experimental mixing setup. (a) Laser control system, (b) mixing system where light at 1.55 μm wavelength is mixed using a 3 dB fiber coupler and light at 780 nm wavelength is mixed via an open beam path, (c) detection system where the mixed beam is focused on the detector part in the patterned YBCO film.

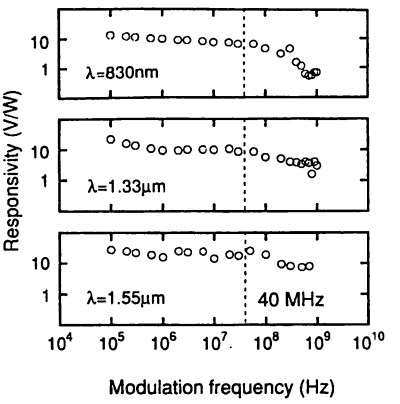

FIG. 2. Frequency dependence of optical responses at 77 K using direct amplitude modulation of an induction current. Three lasers with the wavelengths 830 nm, 1.33 μm, and 1.55 μm were used. The vertical broken line at 40 MHz shows the calculated cutoff frequency of the bolometric response.

tical source using a 780 nm LDs is composed of an optical grating feedback system[10] in order to choose an arbitrary wavelength of the LDs. Figure 1(b) shows the mixing methods with a 3 dB fiber coupler for the 1.55 μm LDs and with an open beam path for the 780 nm LDs. The intermediate frequencies of the mixed light can be easily varied from 100 MHz to 18 GHz by adjusting the injection current of each LD. The peak to peak value of the radiation power was fixed at 3 mW for the 780 nm laser and at 0.3 mW for the 1.55 μm laser in the present experiments.

The laser beams with a diameter of about 50 μm were directly irradiated to the detection area of the patterned YBCO thin film through the quartz window as shown in Fig. 1(c). The bias current ($\simeq$ 20 mA) of the detector, which is 1.1 times larger than the critical current, was carefully adjusted to give a maximum response. We found that the optical response has the maximum peak value in the resistive state when the bias current just exceeds the critical current. The output signals from the detector were measured by a spectrum analyzer after pre-amplifying the signals.

The frequency dependence of the optical responsivity in the patterned YBCO thin film at various wavelengths is shown in Fig. 2. The direct amplitude-modulation method was used to irradiate a sample at $T=77$ K. We can see the two different slopes of the responsivity around 40 MHz. Table I summarizes the responsivities for three wavelengths at the modulation frequencies below 1 Hz and at 200 MHz. The responsivities at 830 nm, 1.33 μm, and 1.55 μm were deduced to be 50, 60, and 50 V/W below 1 Hz in Table I.

Over 1 GHz modulation frequency, we had to use the optical heterodyne mixing. The modulation frequency dependence of the responsivity above 1 GHz is shown in Fig. 3. We could observe the optical responses up to 18 GHz at two different wavelengths, 780 nm and 1.55 μm. The modulation frequency 18 GHz is the maximum value using the present experimental setup, which is limited by the bandwidth of the amplifier and the signal loss in the cables. It should be noted that there is a plateau from 3 GHz to 18 GHz at both wavelengths. The responsivity of the detector in the plateau region is about 150 mV/W at 1.55 μm, and approximately 20 mV/W at 780 nm.

The curves in Fig. 3 represent the theoretical calculations using the two temperature model,[11] where two different temperatures for the quasiparticles and the phonons are assumed to describe the quasiparticle and phonon nonequilibrium distribution. In this model, two fitting parameters, the electron-phonon scattering time and the phonon escape time are assumed. The frequency dependence for the optical responses at 1.55 μm wavelength can be fit with this model as shown in Fig. 3(b), but the frequency dependence at 780 nm deviated from curve *A* in Fig. 3(a) around the flat region.

We first discuss the optical responsivity of the patterned YBCO thin films. Commercial Si-avalanche photodiodes (Si-APDs)[12] have relatively narrow bandwidth from 400 nm to 1.0 μm and show a maximum responsivity of 25 V/W for 800 nm wavelength. Ge-APDs[13] have a bandwidth from 800 nm to 1.7 μm and a responsivity of 40 V/W at 1.5 μm wavelength. On the contrary, our patterned YBCO thin films have relatively higher responsivity at low modulation frequency as shown in Table I, although the APDs outperform the YBCO detectors at the modulation frequencies over 100 MHz. We believe that the performance of YBCO detectors can be improved by optimizing the device configuration and the signal lines. The optical responsivity between 830 nm and 1.55 μm seems to be at the same level and we estimated that $D^* = 5 \times 10^8$ cm $W^{-1}Hz^{1/2}$. This implies that YBCO optical detectors work in a rather wider bandwidth compared to the commercial optical ones. Moreover, these values of the responsivity are much higher than other reported values for YBCO thin films[13] or $La_{2-x}Sr_xCuO_4$ (LSCO).[14] Tanabe *et al.* suggested that the responsivity is inversely propor-

TABLE I. Optical responsivity at various wavelengths. A direct amplitude-modulation method was used to change the frequency.

Wavelength	830 nm		1.33 μm		1.55 μm	
Modulation frequency	<1 Hz	200 MHz	<1 Hz	200 MHz	<1 Hz	200 MHz
Responsivity (V/W)	>50	7	>60	10	>50	9

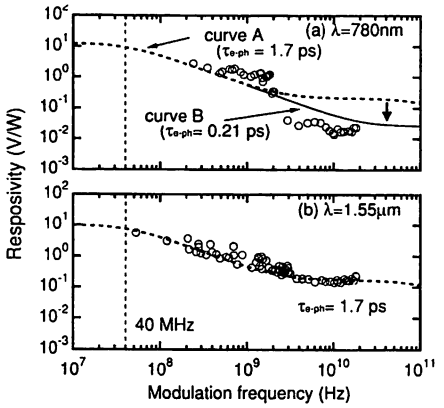

FIG. 3. Intermediate frequency dependencies of optical responses at 77 K by an optical heterodyne mixing method. We measured the signals at two different wavelengths, (a) λ = 780 nm and (b) λ = 1.55 μm. The broken and solid curves in (a) and (b) are obtained by the two temperature model. Curve *A* in (b) is a fitting to the region near 1 GHz (τ_{e-ph} = 1.7 ps). Curve *B* in (a) shows the theoretical line when τ_{e-ph} = 0.21 ps.

tional to the pair density of states, $N(0)\Delta$, where N(0) is the density of states at the Fermi level.[14] Although $N(0)\Delta$ of YBCO is larger than that of LSCO, our YBCO detectors have a higher responsivity than those made of LSCO. This is because a high sensitivity can be obtained by an improvement of the crystal quality in YBCO thin films, the configuration of the detection area[7] and their substrates.[15]

In the low frequency region in Fig. 3 as well as around 1 GHz in Fig. 2, the same slope of the frequency dependence is observed. This is due to the bolometric response. To estimate the cutoff frequency of the bolometric response, we calculated the phonon escape time constant τ_{es}. The thermal time constant can be determined by the phonon escape time $\tau_{es}=R_{bd}C_p d$,[11] where R_{bd} is the thermal boundary resistance, C_p is the phonon specific heat, and d is the film thickness. We can thus estimate the cutoff frequency $f_C=40$ MHz, where $R_{bd}=0.83\times10^{-3}$ K cm^2/W,[16] $C_p=0.9$ J/cm^3 K,[16] and $d=50$ nm. The cutoff frequency is shown as the vertical broken line in Figs. 2 and 3. This agrees with the bending point of the slope. Even at the modulation frequency well above 100 MHz as shown in Fig. 3, we can see the plateau region, where the optical responsivity is independent of the modulation frequency. (We will comment later.) We thus propose the existence of a nonequilibrium response in addition to the simple bolometric response.

To explain the fast response above 1 GHz, we have used the electron heating model.[17] In this model, the change of the resistance in the thin film is assigned to the nonequilibrium quasiparticle distribution. When a photon with high energy well above the energy gap Δ is impinged on a superconducting thin film, quasiparticles with high energy are excited. As quasiparticles with high energy well above Δ relax toward the edge to the energy gap Δ, they create a cascade scattering with quasiparticles at low energy. Considering the modulated frequency in the plateau region, electron-phonon scattering may contribute to the response in this plateau. Curve *A* in Fig. 3 was based on the two temperature model, where τ_{e-ph} = 1.7 ps for 1.55 μm wavelength is used.[7] The value of τ_{e-ph}^{-1} depends on the photon energy $\hbar\omega$, as $(\hbar\omega/\Delta)^3$.[18] Therefore, we should use τ_{e-ph} = 0.21 ps for 780 nm laser, which is shown as the curve *B*. It fits to the data better. This suggests that the nonequilibrium response of YBCO thin film detectors has frequency dependence, which is caused by the energy dependence of the electron-phonon scattering time. Instead of the different electron-phonon scattering time τ_{e-ph}, we may use two different temperatures between electrons, T_e, and phonons, T_{ph}, in the electron heating model. The relaxation time (τ_{e-ph}), when a quasiparticle is in the higher energy state, is so short that the difference between T_e and T_{ph} seems to be effectively smaller for the frequencies in this plateau. The electron heating model can well explain the experiments by taking into account for the frequency dependence of the electron-phonon scattering time. Although we need more detailed experimental results to confirm the electron heating model, this model explains the optical response in the resistive state reasonably well. Our results also agree with those obtained by Semenov *et al.*[19]

In summary, we have measured the optical responses at various wavelengths in patterned YBCO thin films and estimated an optical responsivity which is better than those of commercial detectors. We used a direct modulation method at low frequency and an optical heterodyne mixing method at high frequency in order to change of the irradiation frequency. An optical response up to 18 GHz was achieved and we have explained this fast optical response in terms of the electron heating model. A HTSC optical detector can be expected to be a high speed and relatively broad band detector.

The authors would deeply like to thank Y. Higashino at Teratec Co., E. Kawate, and M. Okaji at NRLM and M. Kourogi at TIT for their constant encouragement and critical comments on this work.

[1] Q. Hu and P. L. Richards, Appl. Phys. Lett. **55**, 2444 (1989).
[2] P. L. Richards, J. Appl. Phys. **76**, 1 (1994).
[3] H. S. Kwok, J. P. Zheng, Q. Y. Ying, and R. Rao, Appl. Phys. Lett. **54**, 2473 (1989); A. Ghis, J. C. Villegier, S. Pfister, M. Nail, and Ph. Gibert, Appl. Phys. Lett. **63**, 551 (1993).
[4] F. A. Hegmann, D. Jacobs-Perkins, C. C. Wang, S. H. Moffat, R. A. Hughes, J. S. Preston, M. Currie, P. M. Hauchet, T. Y. Hsiang, and R. Sobolewski, Appl. Phys. Lett. **67**, 285 (1995).
[5] M. Lindgren, M. A. Zorin, V. Trifonov, M. Danerud, D. Winkler, B. S. Karasik, G. N. Gol'tsman, and E. M. Gershenzon, Appl. Phys. Lett. **64**, 3398 (1994).
[6] Y. Enomoto and T. Murakami, J. Appl. Phys. **59**, 3807 (1986).
[7] M. Danerud, D. Winkler, M. Lindgren, M. Zorin, V. Trifonov, B. S. Karasik, G. N. Gol'tsman, and E. M. Gershenzon, J. Appl. Phys. **76**, 1902 (1994).
[8] H. Tsuchida, T. Tako, and M. Ohtsu, Jpn. J. Appl. Phys. **22**, L19 (1983).
[9] H. Tsushima, S. Sasaki, K. Kuboki, S. Kitajima, and M. Okai, J. Lightwave Technol. **10**, 947 (1992).
[10] M. Ohtsu, K. Nakagawa, K. Kourogi, and W. Wang, J. Appl. Phys. **73**, 1 (1993).
[11] A. D. Semenov, R. S. Nebosis, Yu. P. Gousev, M. A. Heusinger, and K. F. Renk, Phys. Rev. B **52**, 581 (1995).
[12] Hamamatsu Photonics Co., Si-APD (S2381) and Ge-APD (B2384-1).
[13] K. Tanabe, Y. Enomoto, and Y. Yamaji, Appl. Phys. Lett. **57**, 2719 (1990).
[14] K. Tanabe, Y. Enomoto, M. Suzuki, T. Iwata, and A. Yamaji, Jpn. J. Appl. Phys. **29**, L466 (1990).
[15] A. Piqu, K. S. Harshavardhan, J. Moses, M. Mathur, T. Venkatesan, J. C. Brasunas, and B. Lakew, Appl. Phys. Lett. **67**, 1920 (1995).
[16] C. D. Marshall, A. Tokmakoff, I. M. Fishman, C. B. Eom, J. M. Phillips, and M. D. Fayer, J. Appl. Phys. **73**, 850 (1993).
[17] E. M. Gershenzon, G. N. Gol'tsman, A. D. Semenov, and A. V. Sergeev, Solid State Commun. **76**, 493 (1990).
[18] S. B. Kaplan, C. C. Chi, D. N. Langenberg, J. J. Chang, S. Jafarey, and D. J. Scalapino, Phys. Rev. B **14**, 4854 (1976).
[19] A. D. Semenov, I. G. Goghidze, G. N. Gol'tsman, A. V. Sergeev, and E. M. Gershenzon, Appl. Phys. Lett. **63**, 681 (1993).

3.17-THz Frequency-Difference Measurement Between Lasers Using Two Optical Frequency Combs

M. Kourogi, B. Widiyatmoko, and M. Ohtsu, *Senior Member, IEEE*

Abstract— **In order to increase the signal-to-noise ratio in the measurement of frequency-difference between two lasers by using an optical frequency comb generator (OFC-G), two laser beams were combined into the OFC-G. Then many sidebands that contribute to the beat signal generation were generated. We observed spectrum of the beat signal with a signal-to-noise ratio of 30 dB when the frequency-difference between two lasers was 3.17 THz.**

I. Introduction

In order to measure several THz frequency-difference between two lasers, an optical frequency comb generator (OFC-G) have been proposed [1]–[7]. We have demonstrated an OFC generation with a span of 7.6 THz [7] by employing a Fabry–Perot (FP) electrooptic (EO) modulator [8] as an OFC-G, and measured 1-THz frequency-differences between molecular lines around 1.5 μm wavelength [6]. In this letter, we propose and demonstrate a new technique to increase the signal-to-noise ratio (SNR) of the beat signal in the frequency-difference measurement using OFC-G's.

An OFC-G consists of an EO modulator installed in a FP cavity, so that the modulation efficiency is increased by multiple passes of light through the modulator which a sinusoidal voltage signal with a constant frequency f_m is fed into. In [1], we have demonstrated the conventional method of frequency-difference measurement between Laser1 and Laser2 (whose frequencies are ν_1 and ν_2, respectively) by using an OFC-G for Laser1. Even if $|\nu_2 - \nu_1|$ is higher than the response frequency of photo-diodes, it can be determined by $f_b + Kf_m$, where f_b is the beat frequency between Laser2 and Kth sideband of Laser1 whose frequency is close to ν_2, K is the number of the sidebands existing between the two laser frequencies. The measurable frequency-difference depends on SNR of the beat signal. In the conventional method, SNR depends on the power of the one sideband which contributes to beat generation. Fig. 1(a) shows the method we propose in this letter. Two laser beams from Laser1 and Laser2 are injected into two OFC-G's which are driven by the same frequency with a phase-difference of ϕ_μ, and the beat signal between two beams from OFC-G's are observed. In this case, a lot of pairs of kth sideband of Laser1 and the $k - K$th sideband of Laser2, whose frequency-difference is f_b, can contribute to beat generation, then SNR can be increase.

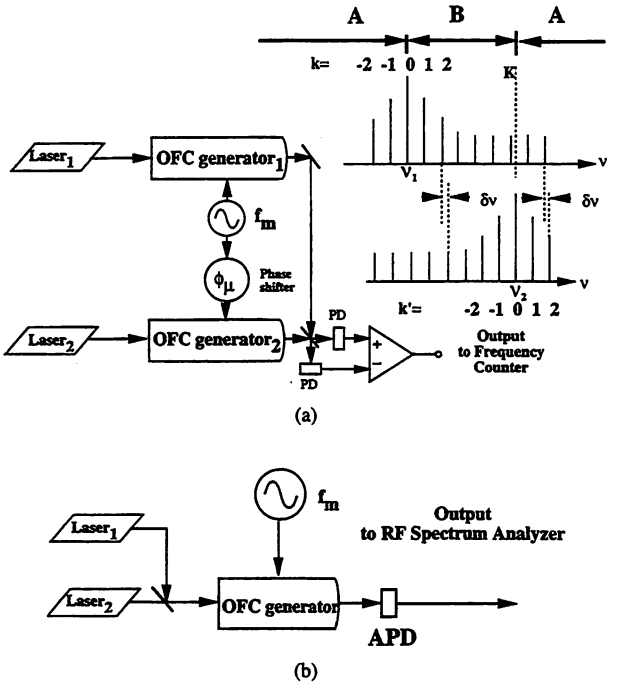

Fig. 1. Schematic illustration of frequency-difference measurement. (a) Proposed method for frequency-difference measurement. (b) Experimental setup. PD's: photo-diodes. Laser1, Laser2: Grating feedbacked semiconductor lasers. APD: avalanche photodiode.

For the conventional method, when the crystal dispersion is small, SNR in the shot noise limit is expressed as [1],

$$\mathrm{SNR}_K = \frac{\eta_{\mathrm{PD}}\eta_{\mathrm{FP}}\left(\frac{\pi}{2\beta F}\right)^2 P_1 \exp\left(-\frac{|K|\pi}{\beta F}\right)}{h\nu B}, \quad (1)$$

where η_{FP}, F, η_{PD}, β, P_1 and B are the efficiency of the FP cavity, the finesse, the quantum efficiency of the

Manuscript received July 24, 1995; revised November 22, 1995.

M. Kourogi is with the Interdisciplinary Graduate School of Science and Engineering, Tokyo Institute of Technology, 4259 Nagatsuta, Midori-ku, Yokohama, Kanagawa 226, Japan. He is also with the Kanagawa Academy of Science and Technology, KSP East Building, Room 408, 3-2-1 Sakado, Takatsu-ku, Kawasaki, Kanagawa 213, Japan.

B. Widiyatmoko is with the Interdisciplinary Graduate School of Science and Engineering, Tokyo Institute of Technology, 4259 Nagatsuta, Midori-ku, Yokohama, Kanagawa 226, Japan. He is also with the Research and Development Center of Applied Physics, Indonesia Institute of Sciences, Komplek PUSPIPTEK Serpong, Tangerang 15310, Jakarta, Indonesia.

M. Ohtsu is with the Interdisciplinary Graduate School of Science and Engineering, Tokyo Institute of Technology, 4259 Nagatsuta, Midori-ku, Yokohama, Kanagawa 226, Japan. He is also with the Kanagawa Academy of Science and Technology, KSP East Building, Room 408, 3-2-1 Sakado, Takatsu-ku, Kawasaki, Kanagawa 213, Japan.

Publisher Item Identifier S 1041-1135(96)02595-5.

photodiode, the modulation index, the power of the Laser1, and the bandwidth of the beat signal detection, respectively. To consider the proposed system, we must take into consideration the phase of the each beat generated between the kth sideband of Laser1 and the $k-K$th sideband of Laser2 for all k. In order to get high efficient total beat generation, the phase of the each beat signal must be the constant for a lot of k values. There are two cases to satisfy this condition.

1) $\phi_\mu = 0$, and K is even.
2) $\phi_\mu = \pi$.

When the phase of 0th sideband of Laser1 is defined to be zero, the phase of the kth sideband of Laser1 ($\phi_{1,k}$) is π for the odd number of k when $k \leq 0$, and zero for otherwise. For the case of A), the phase of the k'th sideband of Laser2 ($\phi_{2,k'}$) is π for the odd number of k' when $k' \leq 0$, and zero for otherwise, then the phase of the each beat signal between kth sideband of Laser1 and $k-K$th sideband of Laser2, i.e., $\phi_{2,k-K} - \phi_{1,k}$, are zero for $k \leq 0$, $K \leq k$ and the even number of k when $0 < k < K$, and $\phi_{2,k-K} - \phi_{1,k}$ is $-\pi$ for the odd number of k when $0 < k < K$. It means that only the beat between kth sideband of Laser1 and $k-K$th sideband of Laser2 in the range of $k \leq 0$ and that of $K \leq k$ ["A" range shown in Fig. 1(a)] can contribute to the beat generation because the beat signal generated by sidebands in the range of $0 < k < K$ disappears by the interference between the beat generated by the sidebands of the even numbers of k and those of the odd numbers of k. SNR in the shot noise limit in the case A) is described as

$$\mathrm{SNR}_K = \frac{\eta_{\mathrm{PD}}\eta_{\mathrm{FP}}\dfrac{P_1P_2}{P_1+P_2}\left(\dfrac{\pi}{2\beta F}\right)^3 \exp\left(-\dfrac{K\pi}{\beta F}\right)K^2}{h\nu B}, \tag{2}$$

where P_2 is the power of the Laser2. For the case of B), the phase of the k'th sideband of Laser2 ($\phi_{2,k'}$) is π for the odd number of k' when $0 \leq k'$, and zero for otherwise, then $\phi_{2,k-K} - \phi_{1,k}$ are zero for $0 \leq k \leq K$. Only the beat between kth sideband of Laser1 and $k-K$th sideband of Laser2 in the range of $0 \leq k \leq K$ ["B" range shown in Fig. 1(a)] can contribute to the beat generation. SNR in the shot noise limit in the case B) is described as,

$$\mathrm{SNR}_K = \frac{\eta_{\mathrm{PD}}\eta_{\mathrm{FP}}\dfrac{P_1P_2}{P_1+P_2}\dfrac{\pi}{2\beta F}\exp\left(-\dfrac{K\pi}{\beta F}\right)}{h\nu B}. \tag{3}$$

Fig. 2(a) shows numerical results of SNR in the shot noise limit. In this calculation, we used experimental parameters, such as the wavelength of both lasers are ~780 nm, the both of P_1 and P_2 is 4 mW, F, η_{FP}, β, f_m, B, and η_{PD} are 300, 0.15, 0.36 πrad, 6.3 GHz, 100 kHz, and 0.7, respectively. Lines A and B show the results of present method expressed by (2) and (3), respectively. Line C shows the result of the conventional method expressed by (1). As shown in this figure, SNR for $\phi_\mu = \pi$ is larger than that of the conventional method by ~40 dB around the frequency-difference of 8 ~ 9 THz. This value corresponds to 6 THz increase of measurable frequency-difference. Even in the case of $\phi_\mu = 0$, SNR is increased by

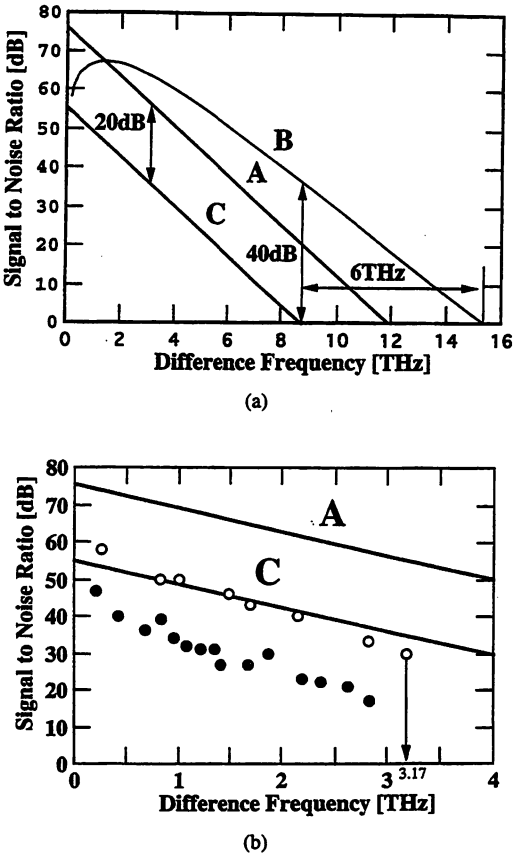

Fig. 2. Signal-to-noise ratio. (a) The numerical results. (b) The experimental results. Closed circles: Experimental result of conventional method. Open circles: Experimental results of proposed method: A and B shows the results of the proposed method. A: $\phi_\mu = 0$. B: $\phi_\mu = \pi$. C: Numerical result of the conventional method.

20 dB. The reason why the case of $\phi_\mu = \pi$ is better than that of $\phi_\mu = 0$ is that the sidebands which contribute to the beat generation are existed between the frequencies of the two lasers, and the total sideband power in this range is larger than that of the otherwise.

For the experiment, we made a simplified setup as shown in Fig. 1(b). We also made a setup for the conventional method by using the same OFC-G for the comparison. Two grating feedbacked semiconductor laser beams were incident into one monolithic OFC-G [7], and then output beam was detected by an avalanche photodiode and monitored by an RF spectrum analyzer. In comparison with the setup in Fig. 1(a), this setup lacks flexibility, however this needs only one OFC-G. Since both laser share the OFC-G, this experimental setup corresponds to the case of line A shown in Fig. 2(a). Since the FP cavity of OFC-G cannot be tunable independently for the two lasers, f_b which can be observed is limited to be lower frequency range because the phase of the sidebands also depend on the frequency-difference between the laser frequency and the resonant frequency of the FP cavity. From the measurement, it was known that SNR is decreased when f_b is higher than 20 MHz.

Fig. 3(a) and (b) show the spectral profiles of the envelope measured when two lasers with different wavelengths were simultaneously injected into the OFC-G and when one laser

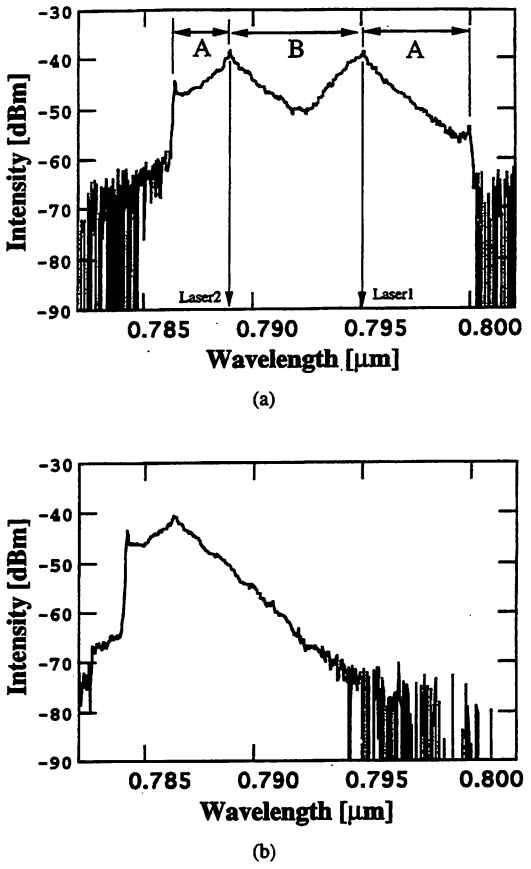

Fig. 3. Spectral profiles of the envelopes. (a) When two diode lasers were simultaneously injected. (b) When one diode laser was injected. The resolution was 0.1 nm for both figures.

was injected, respectively. We can find the stepwise discontinuities on the both edges of envelope spectra of OFC due to material dispersion of the EO crystal. Since the sidebands in the region indicated by A in Fig. 3(a) contribute to the beat generation, f_m was set to be between the frequencies by which each spectrum of OFC from two lasers show symmetrical shape in order to get wide range of A. (f_m was not exactly set to be the center frequency, therefore the spectrum is not perfectly symmetric.) Therefore, in Fig. 3(b), we can find that the envelope from the one of the lasers is not symmetric.

Fig. 2(b) shows SNR of the beat signals as a function of $|\nu_2 - \nu_1|$. Closed and open circles are measured by conventional method and present method, respectively. As shown in this figure, SNR of the present method was larger than that of conventional method by 10 dB. The maximum value of $\nu_2 - \nu_1$ was 3.17 THz when the wavelength of the used lasers were 788.171 nm and 783.132 nm. To our knowledge, this value is the largest frequency-difference of two lasers for which a beat signal was observed. However, SNR is still lower than the shot noise limit level shown by line A by 20 dB because the shot-noise limited detection was not realized in this experiment due to very low total power of the OFC and large excess noise of the avalanche photodiode, and large spectral linewidth lasers (~1 MHz) were used. The excess noise factor of the avalanche photodiode was about 10 dB, and the spectral linewidth of the beat signal was about 1 MHz ($= 10 \times B$), therefore, SNR is lower than that of the shot noise limit level by 20 dB. The detected power in the present method is estimated to be only $(\eta_{FP}\pi/2\beta F) \times (P_1 + P_2) = 4\ \mu W$. When we tried the conventional method in which one of the lasers was used for comb generation and the other one was used for local lasers, the shot-noise limited detection could be realized by use of normal photodiodes because the detected power in the conventional method was as large as the power of the local laser. In order to increase SNR to reach shot noise limit of the present method, high-efficient OFC-G is required. A FP EO modulator with three mirrors [9] can increase the conversion efficiency. If the efficiency of our OFC-G is increased by 100 times, shot noise limited detection will be realized, and then SNR will be increased by ~40 dB. Furthermore, if proposed method shown Fig. 1(a) for $\phi_\mu = \pi$ is realized by employing the FP EO modulator using three mirrors, SNR can be increased by ~60 dB which corresponds to increase of ~10 THz measurable frequency-difference.

In summary, in order to expand measurable frequency-difference between two lasers, we proposed a new technique for beat generation by using two OFC-G's. For the demonstration of this proposal, two laser beams were combined into the optical frequency comb generator and then many sidebands which contribute to the beat signal generation were generated. We observed spectrum of the beat signal with a signal-to-noise ratio of 30 dB when the frequency-difference between two lasers was 3.17 THz.

ACKNOWLEDGMENT

The authors would like to thank Prof. Kobayashi and Dr. Morimoto of Osaka University for helpful comments on an electrooptic modulator.

REFERENCES

[1] M. Kourogi, K. Nakagawa, and M. Ohtsu, "Wide-span optical frequency comb generator for accurate optical frequency difference measurement," *IEEE J. Quantum Electron.*, vol. 29, no. 10, pp. 2693–2701, 1993.
[2] M. Kourogi, T. Enami, and M. Ohtsu, "A monolithic optical frequency comb generator," *IEEE Photon. Technol. Lett.*, vol. 6, no. 2, pp. 214–217, 1994.
[3] K. Nakagawa, M. Kourogi, and M. Ohtsu, "Proposal of a frequency-synthesis chain between the microwave and optical frequencies of the ca intercombination line at 657 nm using diode lasers," *Appl. Phys. B*, vol. 57, pp. 425–430, 1993.
[4] L. R. Brothers, D. Lee, and N. C. Wong, "Terahertz optical frequency comb generation and phase locking of an optical parametric oscillator at 665 Ghz," *Opt. Lett.*, vol. 19, no. 4, pp. 245–247, 1994.
[5] H. Keang-Po and J. M. Kahn, "Optical frequency comb generator using phase modulation in amplified circulating loop," *IEEE Photon. Technol. Lett.*, vol. 5, no. 6, pp. 721–725, 1993.
[6] K. Nakagawa, M. de Labachelerie, Y. Awaji, M. Kourogi, T. Enami, and M. Ohtsu, "Highly precise 1 T-Hz optical frequency difference measurement of 1.5-μm molecular absorption lines," *Opt. Lett.*, vol. 20, pp. 410–412, 1995.
[7] M. Kourogi, W. Bambang, Y. Takeuchi, and M. Ohtsu, "Limit of optical frequency comb generation due to material dispersion," *IEEE J. Quantum Electron.*, vol. 31, pp. 2120–2126, 1995.
[8] T. Kobayashi, T. Sueta, Y. Cho, and Y. Matsuo, "High-repetition-rate optical pulse generator using a Fabry–Perot electro-optic modulator," *Appl. Phys. Lett.*, vol. 21, no. 8, pp. 341–343, 1972.
[9] A. Morimoto, A. Shibagaki, and T. Kobayashi, "Efficient ultrashort pulse generation using a modified Fabry–Perot modulator," in *Proc. CLEO'93*, 1993, paper no. CThS84.

Observation of Temporal Behavior of an Atomic Wave Packet Localized in an Optical Potential

M. Kozuma,[1] K. Nakagawa,[2] W. Jhe,[3] and M. Ohtsu[1,4]

[1]*Interdisciplinary Graduate School of Science and Engineering, Tokyo Institute of Technology, 4259, Nagatsuta-cho, Midori-ku, Yokohama 226, Japan*

[2]*Tokyo Institute of Polytechnics, 1583, Iiyama-cho, Atugi 243-02, Japan*

[3]*Department of Physics, Seoul National University, Seoul 151-742, Korea*

[4]*Kanagawa Academy of Science and Technology, KSP East 408, 3-2-1 Sakado, Takatsu-ku, Kawasaki 213, Japan*

(Received 8 November 1995)

We have investigated the dynamic temporal behavior of atomic motion in a periodic optical potential by detecting a recoil-induced resonance signal. In the slowly moving optical potential, damped oscillations are observed in the transient signal and the oscillation frequency is found to be independent of the moving speed of the potential. By using a Monte Carlo wave-function method, the signal can be attributed to the oscillatory motion of atomic wave packet localized in the potential, where the oscillation frequency corresponds to the energy separation between vibrational levels.

PACS numbers: 32.80.Lg, 32.80.Pj

There has been much interest in the quantized motion of cold atoms inside a periodic optical potential. The discrete vibrational energy spectrum therein has been spectroscopically observed by using a stimulated Raman technique [1] and a heterodyne technique [2,3]. However, in spite of the natural expectation, the dynamic behavior of the atomic motion localized in the optical potential, which can be understood as a result of quantum interference between the stationary discrete vibrational eigenstates, has not been observed yet. Observation of such a dynamics can provide one the information on an atomic coherence time.

Recently, atomic motion traversing a periodic optical potential was observed [4] by detecting the transient response of the recoil-induced resonance signal [5,6] when two probes were introduced into cold atoms. In that work, localized atoms were first produced in a stationary periodic optical potential produced by the interference between two probe beams having the same frequencies. With the frequency difference shifted to some large value, the atoms were then made to acquire an initial kinetic energy, in the frame of the moving optical potential, much larger than the potential depth itself. Therefore, they could transverse many such potentials, which was manifested as a decaying signal oscillating at the frequency difference of the probes.

In this Letter, we describe the first observation of the temporal oscillation of an atomic wave packet localized in a periodic optical potential. When a potential is made to move very slowly by a small frequency difference, initially localized atoms will follow the moving potential and oscillate around the potential minimum. By detecting the transient response of the recoil-induced resonance, one can observe the temporal behavior of localized atomic motion.

In our experiment, a cold 4 μK cloud of ^{87}Rb atoms was produced [4] by a magneto-optical trap [7] and polarization-gradient cooling [8,9] in a rubidium-vapor cell. The $5S_{1/2}$, $F = 2$–$5P_{3/2}$, $F = 3$ cyclic transition of the ^{87}Rb D_2 line was used as a cooling cycle. After the preparation of the cold sample, two probe beams with wave vectors $\vec{k}_1, \vec{k}_2$ ($\vec{q} \equiv \vec{k}_2 - \vec{k}_1$) and angular frequencies ω_1, ω_2 ($\delta \equiv \omega_2 - \omega_1$) detuned from the atomic resonance by Δ, having parallel linear polarizations, are intersected inside the sample at an angle θ (Fig. 1). Because of the small frequency difference δ, an optical potential with a periodicity of $\cos(qr_q - \delta t)$, i.e., a potential moving with speed $v_0 = \delta/q$ along $\vec{q}$, was generated in the beam crossing area. Here $q = |\vec{q}|$, and r_q is the projection of the position vector on $\vec{q}$. The small fre-

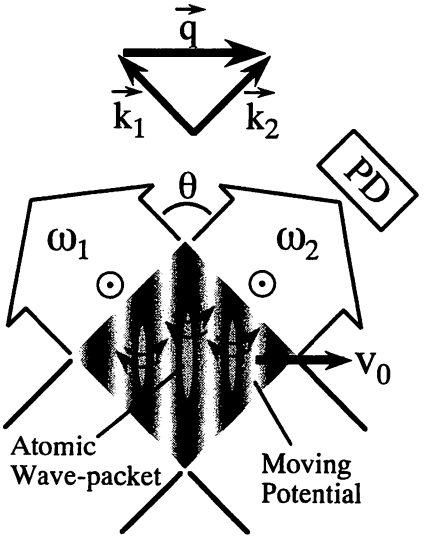

FIG. 1. An experimental scheme to observe the oscillation of an atomic wave packet localized in an optical potential. The optical standing wave moving with speed v_0 of δ/q is generated by two probe beams with wave vectors $\vec{k}_1$ and $\vec{k}_2$ and with angular frequencies ω_1, ω_2, which cross in the cold atomic vapor at an angle θ. Here $\delta = \omega_2 - \omega_1$, $\vec{q} = \vec{k}_2 - \vec{k}_1$, and $q = |\vec{q}|$. The intensity change of the transmitted probe beam is monitored by the photodetector (PD).

 0031-9007/96/76(14)/2428(4)$10.00

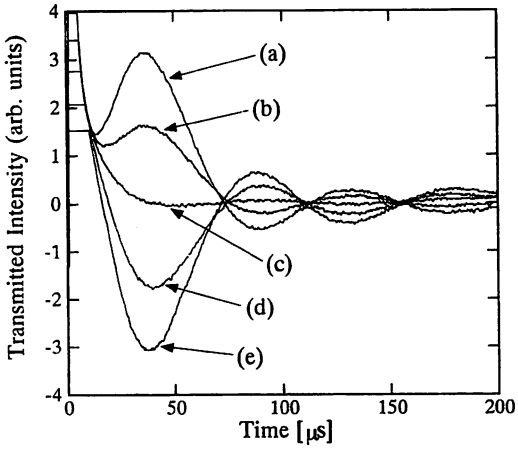

FIG. 2. Experimental results of the dependence of the transmitted intensity of the probe beam on frequency differences. Frequency differences $\delta/2\pi$ were (a) -8 kHz, (b) -4 kHz, (c) 0 kHz, (d) 4 kHz, and (e) 8 kHz, respectively.

quency difference between two probe beams was made by using acousto-optic modulators (AOM) [4]. We observed the transmitted intensity change of the probe beam as a signal by a photodetector.

In Fig. 2 we present typical transmitted probe signals. Here the intensity of the probe beams was 4 mW/cm^2, cross angle θ was 14.4°, and detuning was fixed at $\Delta/2\pi = -60$ MHz with respect to the $F = 2$–$F = 3$ transition. The frequency difference $\delta/2\pi$ was set smaller than 8 kHz. Under these experimental conditions, the atomic kinetic energy in the frame of the moving optical potential $(m\delta/q)^2/2m \leq (4\hbar k)^2/2m$ was much smaller than the optical potential depth $(19\hbar k)^2/2m$. From this value, we can find that the signal oscillating frequency was independent of the value of $\delta/2\pi$ and the signal amplitude became larger as $\delta/2\pi$ increased from 0 kHz. Moreover, when the sign of $\delta/2\pi$ was reversed, the signal shape was also reversed.

We now describe the physical mechanism responsible for the signals observed here. As depicted in Ref. [4], the intensity change of the transmitted probe beam arises from the recoil-induced resonance [5,6] and can be represented by the imaginary part of the polarization P induced by two probe beams which is approximately given by

$$\mathrm{Im}\{P\} \cong -\frac{2\mu\Omega}{\Delta}\int dr_q \sin(qr_q - \delta t)\psi^*(r_q,t)\psi(r_q,t). \quad (1)$$

Here Ω, μ, and $\psi(r_q,t)$ are the Rabi frequency, the transition dipole moment, and the atomic wave function for center of mass motion. From Eq. (1), we can easily understand that the intensity change of the transmitted probe beam originates from a component of the atomic density distribution modulated by $\sin(qr_q - \delta t)$. Because the optical potential has a periodicity of $\cos(qr_q - \delta t)$, the time evolution of the atomic density distribution asymmetrical to the optical potential leads to a change in the transmitted probe intensity.

Next, we rewrite Eq. (1) with the vibrational eigenstates in the moving optical potential. We substituted the atomic wave function represented as a superposition of vibrational eigenstates, i.e., $\psi(r_q',t) = \sum_n c_n\phi_n(r_q')e^{-iE_nt/\hbar}$, into Eq. (1), where ϕ_n, c_n, and E_n are the eigenfunction, the probability amplitude, and the energy of the nth vibrational state, respectively, also $r_q' = r_q - \delta t/q$. By this substitution, Eq. (1) is rewritten as

$$\mathrm{Im}\{P\} \cong -\frac{2\mu\Omega}{\Delta}\sum_n \int dr_q' \sin(qr_q')c_n^*c_{n+1}\phi_n^*(r_q') \times \phi_{n+1}(r_q')e^{-i(E_{n+1}-E_n)t/\hbar}. \quad (2)$$

From Eq. (2), we also observe that the quantum interference between even and odd numbered vibrational states leads to an intensity change of the probe beam. This is quite reasonable because such an interference makes the atomic density distribution asymmetrical with respect to the optical potential.

In our experiment, the initial atomic kinetic energy $(m\delta/q)^2/2m$ was much smaller than the potential depth. Therefore it is proper to interpret the damped oscillation in Fig. 2 as arising from the oscillation of an atomic wave packet localized in the potential due to the dynamic interference between the even and odd numbered vibrational states, as shown in Eq. (2).

In order to understand the dependence of the signals on the frequency difference shown in Fig. 2, we have simulated the time evolution of the atomic wave function inside a moving periodic optical potential and the corresponding recoil-induced resonance signal by using the Monte Carlo wave-function method [10]. In order to simulate the temporal behavior of an atomic wave packet, we have solved the master equation which consists of the relaxation operator and Hamiltonian given by Eqs. (67) and (77) of Ref. [10]. Evaluating Eq. (1), we have also obtained the transmitted intensity change of the probe beam. In this calculation, we treat atoms (here ^{87}Rb) as two-level atoms, and assume the initial atomic momentum distribution to be a δ function; i.e., the initial atomic density distribution is constant in all space. The cross angle, detuning, and Rabi frequency of each probe beam are assumed to be $\theta = 180°$, $\Delta = -\Gamma/2$, and $\Omega = \Gamma/2$, respectively, which give an optical potential depth of $(16\hbar k)^2/2m$. We set the moving speed of the optical potential v_0 such that $mv_0^2/2$ is much smaller than the potential depth. Note that since atoms oscillate in a one-dimensional optical potential, their characteristic behaviors can be observed for an arbitrary value of θ without any loss of generality. Therefore, for convenience, we have assumed a large value for θ, which decreases much of the computing time (as the angle increases, the reciprocal lattice vector of the optical potential increases, and thus the number of expansion coefficients of the atomic wave-function momentum space decreases, which then reduces the computing time).

Figures 3 and 4 present the numerical results of the time evolution of the atomic density distribution in the

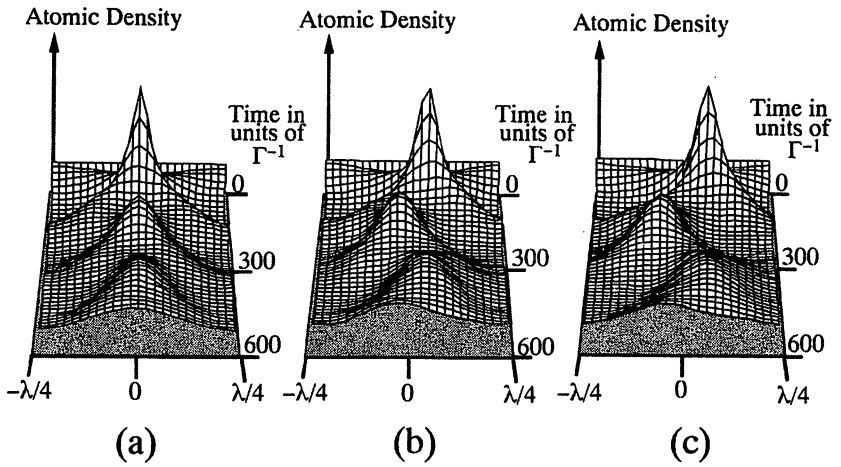

FIG. 3. The time evolution of the atomic density distribution in a periodic optical potential calculated by the Monte Carlo wave-function method. The detuning Δ and Rabi frequency Ω of each probe beam were $\Omega = -\Delta = \Gamma/2$, where the depth of the optical potential becomes $(16\hbar k)^2/2m$. The speeds of the optical potential v_0 were (a) 0, (b) $3\hbar k/m$, and (c) $5\hbar k/m$, respectively. The region of one period of an optical potential is considered, and the potential minimum is located at the origin on the spatial axis.

moving optical potential and the corresponding transmitted intensity change of the probe beam, respectively. Because the optical potential is spatially periodic, we show only the time evolution of the atomic density distribution inside one period of the optical potential in Fig. 3. The zero point on the spatial axis corresponds to the moving optical potential minimum.

In the case of a stationary optical potential, the spatially symmetrical vibrational states, i.e., even numbered (mainly 0th and 2nd) vibrational states, are excited because the initial atomic momentum is zero. Because of quantum interference between these even numbered vibrational states, the atomic density distribution oscillates symmetrically with respect to a potential with a frequency of $(E_2 - E_0)/\hbar$ (Bohr frequency) [Fig. 3(a)]. Because of the spatial symmetry of an atomic oscillation, the intensity of the probe beam does not change

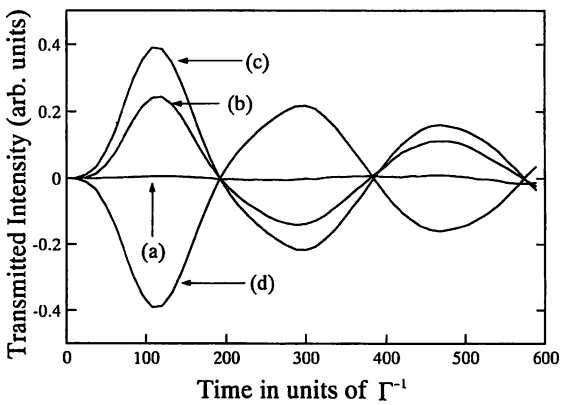

FIG. 4. The dependence of the transmitted intensity change on the moving speed of the optical potential v_0 calculated by the Monte Carlo wave-function method. The speeds of the potential v_0 were (a) 0, (b) $3\hbar k/m$, (c) $5\hbar k/m$, and (d) $-5\hbar k/m$, respectively. The detuning and Rabi frequency were the same as the values in Fig. 3.

[Fig. 4(a)]. Now, the reason why the signal amplitude became a minimum at $\delta/2\pi = 0$ kHz in Fig. 2 is clear; because at $\delta/2\pi = 0$ kHz, the optical potential is stationary.

In the case of a moving optical potential, spatially asymmetrical vibrational levels, i.e., odd numbered vibrational levels (mainly 1st), are also excited because the initial atomic momentum in the frame of the moving optical potential is nonzero. Because of quantum interference between even and odd numbered vibrational states, the atomic density distribution now oscillates asymmetrically with respect to the potential with a Bohr frequency of $(E_1 - E_0)/\hbar$ [Fig. 3(b)]. This additional atomic oscillation manifests itself as the damped oscillating signal [Fig. 4(b)]. As the moving speed of the optical potential increases, the population of odd numbered vibrational levels increases, and thus the amplitude of atomic oscillation, i.e., signal oscillation, increases [Figs. 3(c) and 4(c)]. When the moving direction of the potential is reversed, the time evolution of the atomic density distribution is also reversed spatially (we do not show this result in Fig. 3), and consequently the sign of the corresponding signal is reversed [Fig. 4(d)]. Here the reasons why the signal amplitude becomes larger as $\delta/2\pi$ is far from 0 kHz and why the signal shape is reversed when the sign of $\delta/2\pi$ is reversed in Fig. 2 are now clarified, because the moving speed of the optical potential is proportional to $\delta/2\pi$.

Moreover, in Fig. 4, the oscillation frequency of the signal is independent of the moving speed of the optical potential, which indicates that the oscillation frequency is determined only by the Bohr frequency between vibrational states. If the atoms traverse the optical potential, on the other hand, the signal oscillation frequency is determined by the time of flight for atoms traversing one period of the optical potential and thus strongly depends on the value of v_0 [4]. Therefore the fact that the oscillation frequency in Fig. 2 is independent of $\delta/2\pi$ is strong

evidence that we have observed localized atomic motion. Note that the Bohr frequencies can also be obtained by classical analysis, which implies that the oscillatory motion can be approximately understood as the classical harmonic oscillation.

As the simulation results show, the spatial localization of the atomic density distribution is gradually lost as time goes on [Figs. 3(a), 3(b), and 3(c)]. This is due to the fact that the quantum interference between atomic momentum states results in the spatial localization of the atomic density distribution. In other words, the atomic localization is gradually lost as spontaneous emission destroys the coherence between these momentum states. Such a dissipation of spatial localization of the atomic density distribution also manifests itself as the signal decay [Figs. 4(b), 4(c), and 4(d)]. Moreover, the signal decay time of $590\Gamma^{-1}$ representing the atomic coherence time is much longer than the inverse of the optical pumping rate Γ^{-1} at the antinodes of the optical standing wave. This can be explained by the fact that the energy separation between vibrational states is much larger than the recoil energy as a result of the strong confinement of the atomic wave function [11]. Similar effects appear in Fig. 2, where the signal decay time (40 μs) is much longer than the inverse of the optical pumping rate at the antinode of the optical standing wave (1 μs).

Note that the spatial localization of an atomic wave packet can also be lost due to the dephasing effect between different vibrational states. Moreover, the atomic wave packet is repeatedly squeezed and stretched during the asymmetrical oscillatory motion [Figs. 3(b) and 3(c)]. This indicates that the atomic wave function which is not in a coherent state is equivalent to a classical harmonic oscillator. Therefore, quantum mechanical treatments may be needed for fully understanding these effects.

Finally, we have checked that the signals observed here originate from the localized atomic motion by using another method. We compared the signal oscillation frequency and the theoretically calculated Bohr frequency $\Delta\omega_{vib} = (E_1 - E_0)/\hbar$ under various depths of the optical potential, i.e., various detunings of probe beams. The intensity and the cross angle of the probe beams were set equal to the values in Fig. 2. The frequency difference $\delta/2\pi$ was fixed at 4 kHz. In Fig. 5, dots represent the experimental data and the solid curve represents the theoretically calculated Bohr frequency $\Delta\omega_{vib}$. We also show a comparison between experimental oscillating frequencies and the theoretically calculated Bohr frequencies in the inset of Fig. 5. The slope of the fitted line is 0.9, which is smaller than unity. This slight systematic deviation can be attributed to the imperfect contrast of the interference between the probe beams whose wave fronts are not, in practice, perfectly plane. The slightly distorted wave fronts reduce the effective optical potential depth so that the experimental values become slightly smaller than the ideal theoretical values.

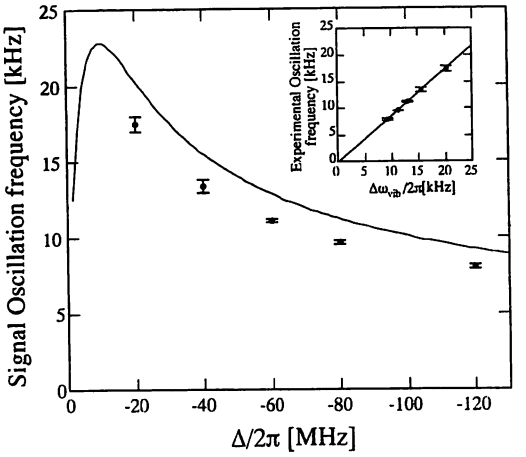

FIG. 5. The dependence of the signal oscillating frequency on probe detuning $\Delta/2\pi$. The intensity and cross angle of the probe beams were equal to the values in Fig. 2. The frequency difference $\delta/2\pi$ was fixed at 4 kHz. Dots represent the experimental results, and the solid curve represents the theoretical Bohr frequencies $\Delta\omega_{vib}/2\pi$ between 0th and 1st vibrational states. Inset shows the comparison between experimental oscillating frequencies and theoretical Bohr frequencies. The slope of the fitted line was 0.9.

In summary, we have demonstrated the novel *in situ* method to observe the oscillating motion of an atomic wave packet localized in a periodic optical potential. Our method will be a powerful tool for investigating the fundamental dynamics of cold atoms localized in an optical potential.

The authors wish to thank Dr. A. Hemmerrich (University of Munich) and Dr. W. D. Phillips (NIST) for their valuable comments and discussions.

[1] P. Verkerk, B. Lounis, C. Salomon, C. Cohen-Tannoudji, J.-Y. Courtois, and G. Grynberg, Phys. Rev. Lett. **68**, 3861 (1992).

[2] C. I. Westbrook, R. N. Watts, C. E. Tanner, S. L. Rolston, W. D. Phillips, P. D. Lett, and P. L. Gould, Phys. Rev. Lett. **65**, 33 (1990).

[3] P. S. Jessen, C. Gerz, P. D. Lett, W. D. Phillips, S. L. Rolston, R. J. C. Spreeuw, and C. I. Westbrook, Phys. Rev. Lett. **69**, 49 (1992).

[4] M. Kozuma, Y. Imai, K. Nakagawa, and M. Ohtsu, Phys. Rev. A. **52**, R3421 (1995).

[5] D. R. Meacher, D. Boiron, H. Metcalf, C. Solomon, and G. Grynberg, Phys. Rev. A **50**, R1992 (1994).

[6] J. Guo, Phys. Rev. A **49**, 3934 (1994).

[7] E. L. Raab, M. Prentiss, Alex Cable, Steven Chu, and D. E. Pritchard, Phys. Rev. Lett. **59**, 2631 (1987).

[8] C. Salomon, J. Dalibard, W. D. Phillips, A. Clairon, and S. Guellati, Europhys. Lett. **12**, 683 (1990).

[9] C. Monroe, W. Swann, H. Robinson, and C. Wieman, Phys. Rev. Lett. **65**, 1571 (1990).

[10] K. Mølmer, Y. Castin, and J. Daribard, J. Opt. Soc. Am. B **10**, 524 (1993).

[11] J. Courtois and G. Grynberg, Phys. Rev. A **46**, 7060 (1992).

Proposal of a Multiplex Optical Frequency Comb Generation System

T. Saitoh, E. Durand, M. Kourogi, and M. Ohtsu, *Senior Member, IEEE*

***Abstract*—A multiplex optical frequency comb generation system was proposed by using a waveguide type optical frequency comb generator. It was estimated that the maximum span of the multiplex optical frequency comb was 240 nm (=29 THz) which was limited by the index dispersion of the $LiNbO_3$ waveguide. Experimental results of the span as wide as 100 nm (=12 THz) were obtained by using five lasers around 1.5 μm wavelength.**

FUTURE systems of heterodyne optical communication and coherent optical sensing could require an optical frequency synthesizer, i.e., a stable and accurate coherent light source with the capabilities of frequency setting and tuning for over several THz. One of the preliminary works for realizing such a synthesizer is used a heterodyned pair of a master laser and slave laser [1], [2]. However, in such preliminary system, the maximum tunable frequency range was limited to only about 10 GHz by the bandwidth of the heterodyne receiver. In order to overcome this difficulty, an optical frequency comb (OFC) generator was developed as a local oscillator [3]–[7]. This device can generate many modulation sidebands with the span as wide as several THz. The generated modulation sidebands have the same frequency stability and accuracy as that of the master laser. By utilizing the OFC generator, one can realize optical frequency synthesizer whose frequency is tunable in the range as wide as several THz. Recently, we have fabricated a compact waveguide type optical frequency comb (WG-OFC) generator by coating high reflection films on the facets of a Ti:$LiNbO_3$ waveguide [7], and realized the span as wide as 2.7 THz of the generated OFC.

In this letter, for further expansion of the span of the OFC, we propose a multiplex optical frequency comb generation system at 1.5 μm wavelength region consisting of one OFC generator and several diode lasers, as schematically explained by Fig. 1(a). In this figure, MLD is a master laser whose frequency could be stabilized to an absorption line of for example, C_2H_2, HCN, NH_4, and so on. Frequencies of the MLD and LDi (i = 1 to n), ν_M and ν_i are almost equally spaced on the frequency axis. By introducing all the laser beams into the OFC generator, the output from the OFC generator has $n+1$ OFC's. As in Fig. 1(b), if carrier frequency differences between adjacent OFCs are $\Delta\nu$, the total span of the multiplex OFC has $(n+1)\,\Delta\nu$, by which the total span of OFC can be increased to over 10 THz in a straightforward manner by increasing the number of lasers. The heterodyne signals between adjacent two OFC's [8] are detected by a photo detector (PD). For example, the heterodyne signal between MLD and LD1 of frequency f_{M-1}, is passed through a band pass filter (BPF1) due to pick up from heterodyne signals and phase-compared with a reference oscillator (RO1) by a phase comparator (PC1) so as to provide an error signal used to control the frequency of LD1. By this frequency offset locking, these two OFC's are linked between each other. By further frequency offset locking between all the adjacent OFC's, i.e., LD1-LD2, LD2-LD3, $\cdots$, and LDn – 1-LDn, all modulation sidebands in the multiplex OFC are frequency-linked to improve their frequency accuracies. It is advisable to use narrow linewidth lasers such as external cavity semiconductor lasers for high sensitivity heterodyne detection. For example, one carries out frequency offset locking under the condition of $\Delta\nu$ = 1 THz, n = 9, one can generate the multiplex OFC with the span as wide as 10THz, where f_{M-1} = 50 MHz, f_{1-2} = 100 MHz, f_{2-3} = 150 MHz, $\cdots$, and f_{8-9} = 450 MHz as in Fig. 1(c). In this system, the square root of Allan variance of frequency fluctuation of the LDn is described by $\sigma_n = (\sigma_M^2 + n\sigma_{\mathrm{OF}}^2)^{1/2}$, where σ_M^2 and σ_{OF}^2 are the Allan variance of frequency fluctuation of the master laser and frequency difference fluctuation between the adjacent OFC's at frequency offset locking, respectively. However, the frequency stability of the master laser which is stabilized to an absorption line is about $\sigma_M = 10^{-10}$ at τ = 1s and the stability of frequency difference of the frequency offset locking is about $\sigma_{\mathrm{OF}} = 10^{-12}$ at τ = 1 s. So one can approximated as $\sigma_n = \sigma_M$.

In the case of generating the multiplex OFC with the span as wide as 10 THz, one cannot neglect the effect of the index dispersion of the OFC generator. To study this effect, we have estimated the maximum span of the multiplex OFC expected for the WG-OFC generator. The WG-OFC generator was composed of a phase modulator that is installed in an optical resonator. An optical waveguide (the product of Anritsu Corporation) was used as a phase modulator at 1.5 μm wavelength. It was fabricated by diffusing Ti into a 38 mm long $LiNbO_3$. An optical resonator was formed by

Manuscript received May 15, 1995; revised July 10, 1995.

T. Saitoh is with the Kanagawa Academy of Science and Technology, KSP East Building, Room 408, 3-2-1 Sakado, Takatsu-ku, Kawasaki, Kanagawa 213, Japan. He is also with the Anritsu Corporation, 1800 Onna, Atsugi, Kanagawa 243, Japan.

E. Durand is with The Kanagawa Academy of Science and Technology, KSP East Building, Room 408, 3-2-1 Sakado, Takatsu-ku, Kawasaki, Kanagawa 213, Japan.

M. Kourogi and M. Ohtsu are with the Kanagawa Academy of Science and Technology, KSP East Building, Room 408, 3-2-1 Sakado, Takatsu-ku, Kawasaki, Kanagawa 213, Japan. They are also with The Interdisciplinary Graduate School of Science and Engineering, Tokyo Institute of Technology, 4259 Nagatuta, Midori-ku, Yokohama, Kanagawa 226, Japan.

Publisher Item Identifier S 1041-1135(96)00504-6.

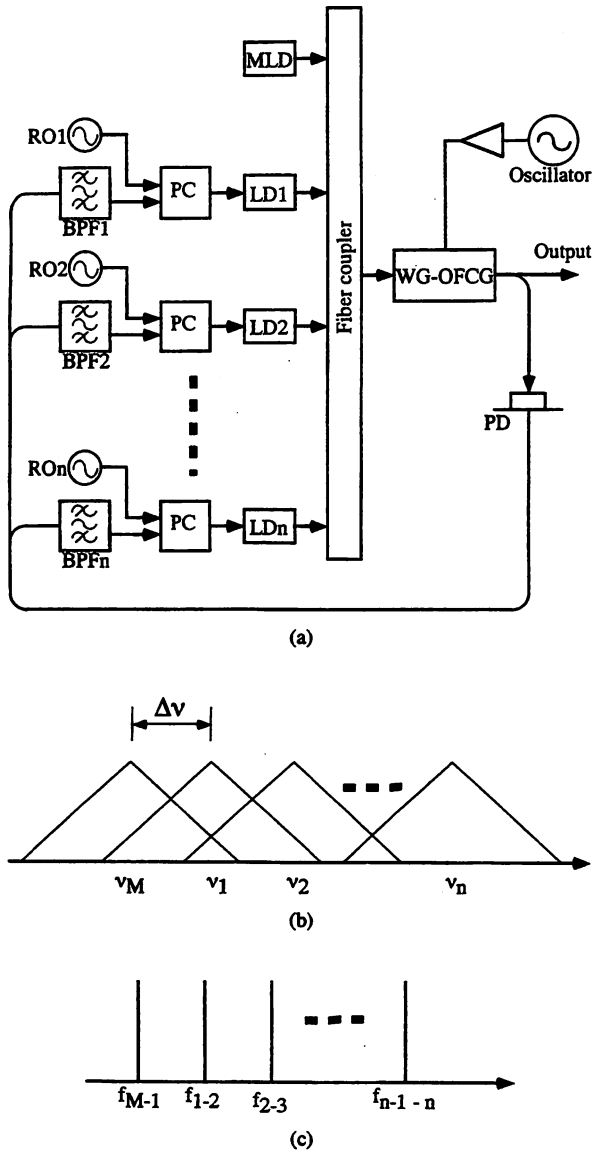

Fig. 1. (a) Schematic explanation of a multiplex OFC generation system. MLD is a master laser stabilized to an absorption line of a gas. LDi, BPFi, ROi, and PCi (i = 1 to n) are slave lasers, bandpass filters, reference oscillators and phase comparators, respectively. (b) Schematic explanation of a multiplex OFC. (c) Schematic explanation of heterodyne signals output from PD.

coating high reflection films on the two end facets of the waveguide. By carefully selecting a low loss waveguide and by dielectric mirror coating with the reflectivity higher than 97% in the range of 1.4–1.7 μm, the measured value of the finesse was as high as 30, which is, to our knowledge, the highest record documented so for [7], [9]. In the range of 1.4–1.7 μm, the wavelength dependence on the finesse could not be detected. The free spectral range (FSR) of the resonator was measured to be 1.87 GHz. The phase modulation index and the microwave power were 2π and 1 W, respectively. Since the optimum phase modulation frequency $f_{m-\mathrm{opt}}$ for maximizing the span of OFC, is integral multiples of the FSR of the optical resonator, $f_{m-\mathrm{opt}}$ was fixed to 7 times the FSR of the optical resonator, which was 13.089 GHz.

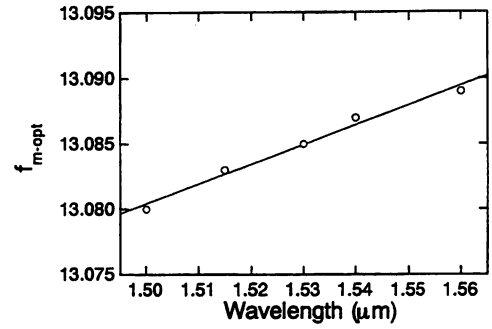

Fig. 2. Dependence of the optimum phase modulation frequency $f_{m-\mathrm{opt}}$ on the incident laser wavelength. A solid line is the numerical result from (3).

Because the FSR of the optical resonator depends on the incident laser wavelength due to the index dispersion of the waveguide, the optimum phase modulation frequency depends also on the incident laser wavelength. By using the Taylor expansion up to the second order, the index of the waveguide is described by

$$n(\lambda) = n(\lambda_0) + \left.\frac{\partial n}{\partial \lambda}\right|_{\lambda_0} (\lambda - \lambda_0) + \frac{1}{2}\left.\frac{\partial^2 n}{\partial \lambda^2}\right|_{\lambda_0} (\lambda - \lambda_0)^2, \quad (1)$$

where λ and λ_0 are the incident laser wavelength and the reference wavelength around which $n(\lambda)$ is Taylor-expanded, respectively. The FSR of the optical resonator is described by

$$\mathrm{FSR}(\lambda) = \frac{c}{2 \cdot l \cdot n_g(\lambda_0)} \left\{ 1 + \left.\frac{\partial^2 n}{\partial \lambda^2}\right|_{\lambda_0} \frac{\lambda_0(\lambda - \lambda_0)}{n_g(\lambda_0)} \right\}$$

$$n_g(\lambda_0) \equiv n(\lambda_0) - \left.\frac{\partial n}{\partial \lambda}\right|_{\lambda_0} \lambda_0, \quad (2)$$

where n_g, c and 1 are the group index of refraction, the light velocity and the length of the optical resonator, respectively. From this equation, one obtains

$$\frac{\partial f_{m-\mathrm{opt}}}{\partial \lambda} = \frac{7c\lambda_0}{2 \cdot l \cdot n_g^2(\lambda_0)} \left.\frac{\partial^2 n}{\partial \lambda^2}\right|_{\lambda_0} = 0.15 \ [\mathrm{MHz/nm}] \quad (3)$$

because $f_{m-\mathrm{opt}} = 7$ FSR.

To find the value of $f_{m-\mathrm{opt}}$, we measured the span of OFC, i.e., the width of the envelope of the OFC spectrum displayed by an optical spectrum analyzer. Fig. 2 shows the measured dependency of the $f_{m-\mathrm{opt}}$ on the incident laser wavelength. It was found that the value of $f_{m-\mathrm{opt}}$ fell within the range of 13.080–13.090 GHz for the wavelength range of 1.50–1.56 μm and its variation coefficient corresponding to (3) was 0.17 MHz/nm. The difference between (3) and experimental value is considered to be originated from the effect of waveguide dispersion of $LiNbO_3$.

We have measured the dependency of the frequency span ΔW of the OFC on the phase modulation frequency detuning Δf from its optimum value (i.e., $f_m - f_{m-\mathrm{opt}}$) by varying f_m from 7 FSR to 7.5 FSR (i.e., $0 \leqq \Delta f \leqq 0.5$ FSR) at the wavelength of 1.525 μm. Fig. 3 shows the measured value of ΔW, which is displayed after normalizing to the value of the span ΔW_0 at $\Delta f = 0$. This figure shows that the value of ΔW decreases monotonically for $\Delta f \geqq 0.01$ FSR (=20

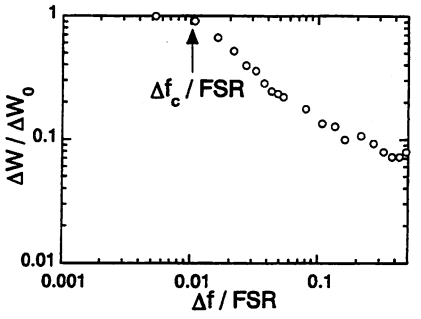

Fig. 3. Dependence of normalized span of the OFC ($\Delta W/\Delta W_0$) on the phase modulation frequency detuning $\Delta f = f_m - f_{m-\mathrm{opt}}$, where ΔW_0 is a span of the OFC when the phase modulation frequency is optimized and ΔW is a span of the OFC for the detuned phase modulation frequency. Δf_c is defined to be the cut-of frequency detuning.

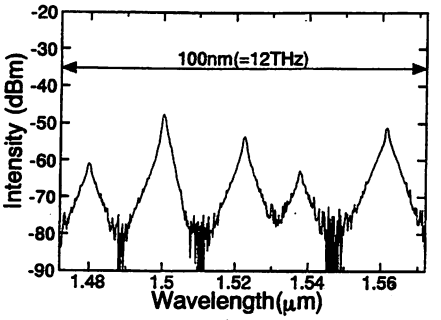

Fig. 4. Envelope of the multiplex OFC measured by an optical spectrum analyzer with the resolution bandwidth of 0.2 nm (=25 GHz).

MHz), which is represented by using a cut-off detuning Δf_c in this figure.

By dividing $2\Delta f_c$ (=40 MHz) by the measured value of variation coefficient (=0.17 MHz/nm), the maximum span of the multiplex OFC was estimated to be 240 nm (=29 THz). Here the dependence of reflectivities of the two end facets on laser wavelength was neglected.

For confirming a generation of the multiplex OFC, we have assembled the multiplex OFC generation system which consisted of a WG-OFC generator and five diode lasers. Wavelengths of five lasers were 1.48, 1.50, 1.52, 1.54, and 1.56 μm. Incident powers on the WG-OFC generator from these lasers were −25, −20, −25, −35, and −15 dBm, respectively.

Fig. 4 shows the envelope of the multiplex OFC. Each OFC has a span of about 20 nm and an envelope slope of 21 dB/THz. The total span of the five families of OFC's is about 100 nm (=12 THz). This value corresponds to about 40% of the maximum span of the multiplex OFC, which was estimated from index dispersion of the waveguide. If other lasers with shorter or longer wavelengths are available, total span can be increased up to the theoretically estimated value of 29 THz without any technical difficulties. Now each OFC is not linked, but it can be expected that all OFC's are linked by frequency offset locking in the future.

In summary, a multiplex optical frequency comb generation system was proposed. By using a waveguide type optical frequency comb generator, it was estimated that the maximum span of the multiplex optical frequency comb was 240 nm (=29 THz), which is limited by the index dispersion of the waveguide. It was confirmed that the multiplex optical frequency comb had a span as wide as 100 nm (=12 THz) by using five lasers.

REFERENCES

[1] K. Kuboki, and M. Ohtsu, "A synthesized method to improve coherence in semiconductor lasers by electrical feedback," *IEEE J. Quantum Electron.*, vol. 25, no. 10, pp. 2084–2090, 1989.

[2] O. Ishida and H. Toba, "Lightwave synthesizer with lock-in-detected frequency references," *J. Lightwave Technol.*, vol. 9, no. 10, pp. 1344–1352, 1991.

[3] R. E. Drullinger, K. M. Evenson, D. A. Jennings, F. R. Petersen, J. C. Bergquist, and L. Burkins, "2.5-THz frequency difference measurement in the visible using metal insulator-metal diodes," *Appl. Phys. Lett.*, vol. 42, pp. 137–138, 1983.

[4] M. Kourogi, K. Nakagawa, and M. Ohtsu, "Wide-span optical frequency comb generator for accurate optical frequency difference measurement," *IEEE J. Quantum Electron.*, vol. 29, no. 10, pp. 2693–2701, 1993.

[5] L. R. Brothers, D. Lee, and N. C. Wong, "Terahertz optical frequency comb generation and phase locking an optical parametric oscillator at 665 GHz," in *Opt. Lett.*, vol. 19, no. 4, pp. 245–247, Feb. 1994.

[6] M. Kourogi, T. Enami, and M. Ohtsu, "A monolithic optical frequency comb generator," *IEEE Photon. Technol. Lett.*, vol. 6, no. 2, pp. 214–217, 1994.

[7] T. Saitoh, M. Kourogi, and M. Ohtsu, "Waveguide type optical frequency comb generator," *IEEE Photon. Technol. Lett.*, vol. 7, no. 2, pp. 197–199, 1995.

[8] T. Saitoh, E. Durand, M. Kourogi, and M. Ohtsu, "Waveguide type optical frequency comb generator," in *Proc. SPIE*, vol. 2378, 1995, p. 212.

[9] T. Suzuki, J. M. Marx, V. P. Swenson, and O. Eknoyan, "Optical waveguide Fabry–Perot modulators in $LiNbO_3$," *Appl. Opt.*, vol. 33, no. 6, pp. 1044–1046, 1994.

0.4-THz Frequency Offset Locking Between Two Optical Frequency Combs

E. Durand, T. Saitoh, M. Kourogi, and M. Ohtsu

Abstract—**A frequency offset locked loop between two different optical frequency combs spaced from 0.4 THz is reported. In a new experiment, a frequency offset locked loop between one comb and one laser diode as a way to link two combs together is realized. A spacing as wide as 0.6 THz is achieved between the linked combs.**

I. Introduction

INDUSTRIAL applications such as coherent optical communication systems and precise measurement of physical constants require highly accurate laser frequency measurement as an indispensable technique [1]. In order to measure absolute frequency to establish frequency standard or to fabricate a stable and accurate coherent lightsource tunable over several THz, i.e., an optical frequency synthesizer, measurement of frequency difference among lasers which are spaced from a span as wide as several THz is required. However, it is not straightforward to measure such a large frequency difference because of the lack of reliable ultra-high speed optical heterodyne receiver. To overcome these difficulties, an optical frequency difference measurement system using an optical frequency comb (OFC) generator has been proposed [2]–[4]. An OFC generator consists of a phase modulator within a Fabry–Pérot cavity. Due to the multiple roundtrips in the modulator it generates a precisely spaced comb of frequencies. Recently, a compact waveguide-type optical frequency comb (WG-OFC) generator that was fabricated by coating high reflection films on the facets of a Ti:$LiNbO_3$ waveguide [5] was reported.

In this letter, we report frequency offset locking experiments between OFC's. Such a technique could be very important to expand further the comb's width and obtained a multiplex OFC of reference frequencies as proposed in [6]. A frequency offset locked loop between two combs spaced from 0.4 THz is reported. As far as we know the frequency offset locked loop between two combs is the first one reported so far. Then, a frequency offset locked loop between one OFC and one laser diode is reported. Once locked, the original experimental setup used here allows simultaneously to link two combs together with a spacing as wide as 0.6 THz.

The power P_k of the kth sideband and the amplitude of the electric field E_k can be expressed, neglecting the waveguide index dispersion

$$P_k = \eta_{FP}\left(\frac{\pi}{2mF}\right)^2 \exp\left(-\frac{|k|\pi}{mF}\right) P_i \tag{1}$$

$$E_k = \sqrt{2P_k}\exp\{2\pi j(v + kf_m)t\}u(k)$$

$$u(k) = \begin{cases} 1 & : k \geq 0 \\ (-1)^k & : k < 0 \end{cases} \tag{2}$$

where P_i is the power of the incident laser beam, F is the finesse of the Fabry–Pérot cavity, m is the modulation index, η_{FP} is the efficiency of the Fabry–Pérot cavity, f_m is the modulation frequency and ν is the carrier frequency of the comb. In a frequency offset locked loop experiment between two OFC's whose frequencies are ν_1 and ν_2, the heterodyne signal results from the superposition of many sidebands pairs. A pair is composed of one sideband of each comb. When an OFC is generated there is a π radians phaseshift between the adjacent sidebands generated under the carrier frequency. If the incident powers of the two laser diode are equal and the two combs are generated with the same OFC generator (i.e., the two combs are identical), the heterodyne signal can be expressed by

$$\sum_{k=-\infty}^{\infty} E_k E_{k-N} = 2\eta_{FP}\left(\frac{\pi}{2mF}\right)\exp\left(-\frac{N\pi}{2mF}\right) \cdot P_i \cos(2\pi f_B t). \tag{3}$$

The carrier frequencies ν_1 and ν_2, integer N and the heterodyne signal frequency f_B are related by

$$\nu_2 = \nu_1 + Nf_m + f_B. \tag{4}$$

The signal to noise ratio of the heterodyne signal can then be expressed

$$\frac{S}{N} = \frac{\eta_{PD}\eta_{FP}}{2h\nu B}\left(\frac{\pi}{2mF}\right)\exp\left(-\frac{N\pi}{mF}\right) P_i \tag{5}$$

where h is the Planck's constant, $\nu = (\nu_1 + \nu_2)/2$, η_{PD} is the efficiency of the photodiode, B is the detection bandwidth.

Fig. 1(a) shows the experimental setup of the frequency offset locked loop between two different combs. The laser light from two external cavity fiber-coupled laser diodes (LD1

Manuscript received June 12, 1995; revised July 24, 1995.

E. Durand is with the Kanagawa Academy of Science and Technology, KSP East Building, Room 408, 3-2-1 Sakado, Takatsu-ku, Kawasaki, Kanagawa 213, Japan.

T. Saitoh is with the Kanagawa Academy of Science and Technology, KSP East Building, Room 408, 3-2-1 Sakado, Takatsu-ku, Kawasaki, Kanagawa 213, Japan and the Anritsu Corporation, 1800 Onna, Atsugi, Kanagawa 243, Japan.

M. Kourogi and M. Ohtsu are with the Kanagawa Academy of Science and Technology, KSP East Building, Room 408, 3-2-1 Sakado, Takatsu-ku, Kawasaki, Kanagawa 213, Japan and the Interdisciplinary Graduate School of Science and Engineering, Tokyo Institute of Technology, 4259 Nagatsuta, Midori-ku, Yokohama, Kanagawa 226, Japan.

Publisher Item Identifier S 0018-9197(96)00522-8.

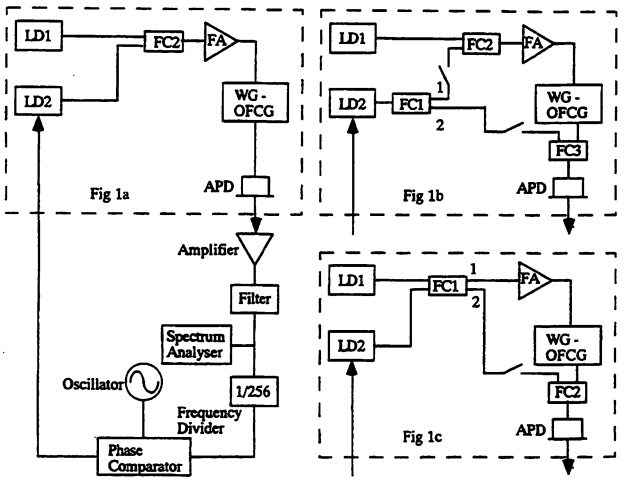

Fig. 1. Experimental setup of frequency offset locked loops. (a) The loop between two combs. (b) The loop between one comb and one laser diode as a way to link two OFC's. (c) Another scheme to link two OFC's by a frequency offset locked loop between one comb and one laser diode. LD: External cavity laser diode. FC: Fiber coupler. FA: Fiber amplifier. WG-OFCG: Waveguide type optical frequency comb generator. APD: Avalanche photodiode.

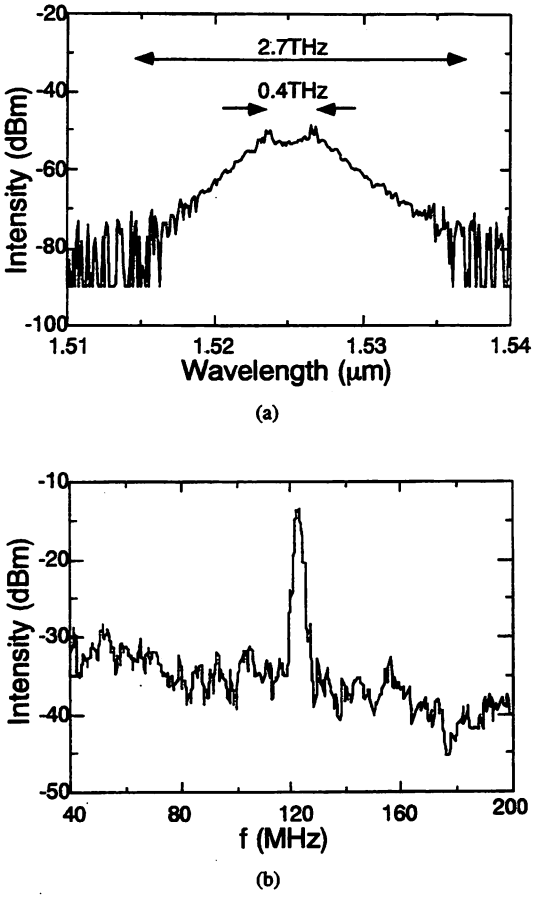

Fig. 2. 0.4 THz frequency offset locking between two optical frequency combs. (a) Envelope of the two frequency combs observed with an optical spectrum analyzer. (b) Heterodyne signal between the two optical frequency combs.

and LD2 emitting about 0.5 mW at 1.5 μm with a linewidth narrower than 1 MHz) are amplified through a fiber amplifier ($P_{\text{amplified}}$ = 10 mW) and then coupled into the WG-OFC generator [5], [6]. The measured free spectral range (FSR) and finesse of the optical resonator of the WG-OFC generator are 1.86 GHz and 30, respectively. The modulation frequency of 13.089 GHz is 7 times the FSR of the cavity. A microwave power of only 1 W is enough to obtain a 2π modulation index. The heterodyne signal between the two combs is detected, amplified, filtered, and down converted. This down converted heterodyne signal is compared to a reference oscillator. This provides an error signal used to control the current of LD1.

Fig. 2(a) shows the envelope of the two combs under the frequency offset locked loop condition. The carrier frequencies ν_1 and ν_2 measured by an optical wavemeter were 196.9854 and 196.5795 THz, respectively. So the frequency spacing between the two combs and N of (4) were 0.406 THz and 31, respectively. On this figure, due to the resolution of the optical spectrum analyzer of 0.2 nm it is impossible to observe the many sidebands that are generated in these combs. The total span covered by the two linked combs is about 2.7 THz. The heterodyne signal between the combs, observed with a spectrum analyzer is shown on Fig. 2(b). It occurs at about 120 MHz. The signal to noise ratio of the heterodyne signal is higher than 20 dB. Taking the experimental value of the parameters involved in (3) into account, i.e., N = 31, $\eta_{FP} = 10^{-2}$, P_i = 10 mW, B = 200 MHz, η_{PD} = 0.5, the calculated signal to noise ratio S/N is 37 dB. This value agrees reasonably with the measured value, because the discrepancy can be attributed to amplifier noise in the feedback loop.

To evaluate the frequency tracking capability of the frequency-locked loop, the square root of Allan variances $\sigma(\tau)$ of the heterodyne signal, unlocked and frequency locked, have been measured. The measurement results are shown on Fig. 3. The minimum value of $\sigma(\tau)$ under frequency offset locked loop condition (closed circles) is 4.8×10^{-12} at τ = 7 s. This value is five orders of magnitude lower that the corresponding free running value (crossings).

The WG-OFC generator used is not temperature controlled but, because the modulation index is as large as 2π, the modulation sidebands are efficiently generated, even without precise length and temperature control [5]. But even if the comb width remains stable, the temperature changes induce modifications of the comb's shape during the time. Consequently, the amplitude E_k of the modulation sideband k is modified and so is the comb's shape. When two combs are beating together the waveguide index dispersion has to be taken into account and produces further instabilities of the heterodyne signal. For these reasons, it was experimentally much easier and stable to frequency-lock one OFC with one laser diode than two OFC's. So, using an offset locked loop between one OFC and a laser diode, we have implemented an experiment to link two combs together. The experimental setup is shown on Fig. 1(b). In this experiment the heterodyne signal between LD2 and the comb generated by LD1 is observed. The detection and electronic loop are the same as in the former experiment. When the loop is closed, by connecting the output1 of the fiber coupler FC1 to the input of FC2 a second comb is generated. Only 25% of LD2 is used to generate this comb and its width is narrower than the other

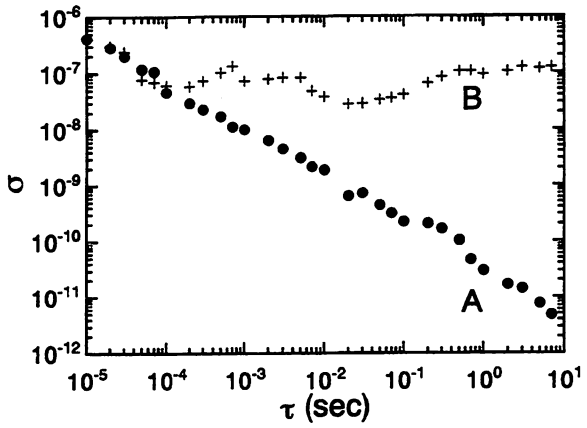

Fig. 3. Square root of Allan variances of the heterodyne signal under unlocked (curve B) and frequency-locked (curve A) conditions.

one generated by LD1. Due to the frequency offset locked loop between LD2 and the comb generated by LD1, the two combs are linked together. In this way, a link between two combs spaced from a frequency difference as wide as 0.6 THz was observed. Fig. 4(a) shows the envelope of the combs and the spectrum of LD2 under frequency offset locked loop condition. Curve A is observed when the two outputs of the fiber coupler FC1 are connected. It is impossible, on this curve, to see the comb generated by LD2 which is hidden by LD2. Curve B is observed when the output 2 is disconnected.

There are other ways to perform the same experiment, i.e., a frequency offset locked loop between one comb and one laser diode as a way to lock two combs together. On Fig. 1(c) another experimental setup is shown. In this case, a frequency offset locked loop was realized with a comb to diode frequency difference of 0.6 THz. Fig. 4(b) shows the envelope of the two combs and the spectrum of the two laser diodes under frequency offset locking condition. Curve A is observed on the spectrum analyzer when the two outputs of the fiber coupler FC1 are connected. Curve B is observed while disconnecting the output2 of FC1. The two combs linked together had in this case comparable widths giving a global width of about 2.9 THz. Although the square root of the Allan variance of the heterodyne signal was not measured in the exact experimental conditions of Fig. 1(b) and (c), a value of 4.8×10^{-13} was measured at $\tau = 7$ s under frequency offset locking between one OFC and one laser diode. At this point the detected signal is not shot noise limited, due to extra noise in the electronic feedback loop, spontaneous emission noise of the fiber amplifier.

In summary, a frequency offset locked loop between two combs spaced from 0.4 THz was reported. In the case of the frequency offset locked loop between one comb and one laser diode as a way to link two OFC's together, a frequency spacing as wide as 0.6 THz was measured under frequency offset locking condition.

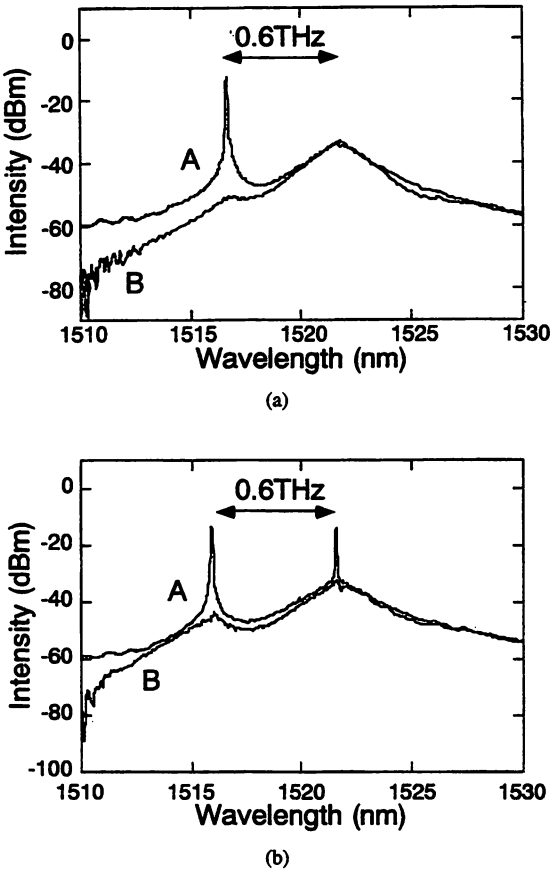

Fig. 4. Frequency offset locked loop between one comb and one laser diode as a way to link two combs together. (a) The envelope of the combs and the spectrum of LD2 observed with an optical spectrum analyzer under frequency offset locking condition. Curve A is observed when the two outputs of the fiber coupler FC1 are connected [Fig. 1(b)]. Curve B is observed when the output 2 of FC1 is disconnected. (b) The envelope of the combs and spectrum of LD1 and LD2 observed with an optical spectrum analyzer under frequency offset locking condition (new scheme). Curve A is observed when the two outputs of the fiber couplers FC1 are connected [Fig. 1(c)]. Curve B is observed when the output 2 of FC1 is disconnected.

REFERENCES

[1] R. E. Drullinger, K. M. Evenson, D. A. Jennings, F. R. Petersen, J. C. Bergquist, and L. Burkins, "2.5-THz frequency difference measurement in the visible using a metal insulator-metal diodes," *App. Phys. Lett.*, vol. 42, pp. 137–138, 1983.

[2] M. Kourogi, K. Nakagawa, and M. Ohtsu, "Wide-span optical frequency comb generator for accurate optical frequency difference measurement," *IEEE J. Quantum Electron.*, vol. 19, no. 10, pp. 2693–2701, 1993.

[3] L. R. Brothers, D. Lee, and N. C. Wong, "Terahertz optical frequency comb generation and phase locking an optical parametric oscillator at 665 GHz," *Optics Lett.*, vol. 19, no. 4, pp. 245–247, Feb. 1994.

[4] M. Kourogi, T. Enami, and M. Ohtsu, "A monolithic optical frequency comb generator," *IEEE Photon. Technol. Lett.*, vol. 6, no. 2, pp. 214–217, 1994.

[5] T. Saitoh, M. Kourogi, and M. Ohtsu, "Waveguide type optical frequency comb generator," *IEEE Photon. Technol. Lett.*, vol. 7, no. 2, pp. 197–199, 1995.

[6] T. Saitoh, E. Durand, M. Kourogi, and M. Ohtsu, "Waveguide type optical frequency comb generator," in *Proc. SPIE*, vol. 2378, Series P, Feb. 95, San Jose, CA.

Limit of Optical-Frequency Comb Generation Due to Material Dispersion

M. Kourogi, B. Widiyatomoko, Y. Takeuchi, and M. Ohtsu, *Senior Member, IEEE*

***Abstract*—The limit of optical frequency comb (OFC) generation (i.e., the limit of frequency difference measurement) due to the material dispersion in the EO crystal is experimentally studied. By using a modified monolithic OFC generator, we observed the OFC spectrum, and confirmed that the envelope of the OFC around 780 nm extended to a span as wide as 16 nm (or 7.6 THz) reaching the limit of the OFC generation. We also proposed a method of stabilizing the Fabry–Perot cavity for the monolithic OFC generator.**

I. Introduction

THE measurement of the difference between two laser frequencies that are spaced as wide as several THz is an essential and important technique for laser frequency synthesis. To measure the difference frequency between two lasers, the beat signal between them has to be measured. However, it has been difficult to measure such a large difference because of the lack of a reliable ultra high-speed optical heterodyne receiver. To measure the difference between two laser frequencies exceeding the bandwidth of optical heterodyne receiver, it is attractive to use a Fabry–Perot (FP) electro-optic (EO) modulator [1] as an optical frequency comb (OFC) generator, which consists of an EO phase modulator installed in a FP cavity [2]–[4]. In this paper, we use a word "OFC generator" instead of an "FP EO modulator". The OFC generator generates high-efficiency sideband in that the light passes multiply through the modulator, and as a result, OFC contains a large number of optical sidebands and can be applied for frequency difference measurement as frequency marker, even if the difference frequency is out of the detector bandwidth. Recently, similar configurations for measuring difference frequency and/or synthesizing laser frequency by using such an OFC generator have been studied (e.g., a similar experiment using an OFC generator and an optical parametric oscillator has been reported [5]). Further, OFC generators using an optical amplifier inside a FP cavity with EO phase modulator [6] have been proposed.

Manuscript received May 15, 1995; revised July 24, 1995.

M. Kourogi and M. Ohtsu are with the Interdisciplinary Graduate School of Science and Engineering, Tokyo Institute of Technology, 4259 Nagatuta, Midori-ku, Yokohama, Kanagawa, 226 Japan, and the Kanagawa Academy of Science and Technology, KSP East Building, Room 408, 3-2-1 Sakado, Takatsu-ku, Kawasaki, Kanagawa, 213 Japan.

B. Widiyatomoko and Y. Takeuchi are with the Interdisciplinary Graduate School of Science and Engineering, Tokyo Institute of Technology, 4259 Nagatuta, Midori-ku, Yokohama, Kanagawa 226, Japan.

IEEE Log Number 9414686.

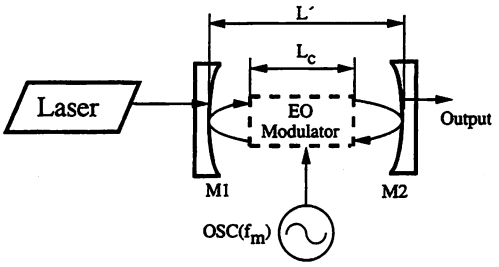

Fig. 1. Schematic illustration of an optical-frequency comb generator. EO modulator: electro-optic phase modulator; $M1$, $M2$: mirrors for a Fabry–Perot cavity; OSC: microwave oscillator.

The limit of the frequency difference measurement using an OFC generator depends on the power of the sidebands. In the ideal condition, where material dispersion does not exist, the k-th sideband power P_k of the OFC is given by $\eta_{FP}(\frac{\pi}{2\beta F})^2 \exp(-\frac{|k|\pi}{\beta F})P_i$, where β, η_{FP}, F, and P_i are the index of phase modulation, the efficiency of the FP cavity, the finesse of the FP cavity, and the input laser power, respectively. To increase the higher order sideband power, it is required to increase β, η_{FP}, F, and P_i. Although the method of [7] is to increase η_{FP} in actual condition, there is a limit on the span of the OFC generation due to material dispersion in the EO crystal, even if those parameters get large values. Therefore, the limit due to the dispersion is an important issue of OFC generation. However, even though the limit due to material dispersion in the EO crystal has been pointed out, theoretically, since 1984 [8], and the effect of material dispersion in FM laser is observed [9], the limit had not been observed experimentally. In this paper, we report an experimental study on the limit of the OFC generation due to the material dispersion, and we propose methods of stabilizing the resonant frequency of a FP cavity used in an OFC generator.

II. Theory

Previous analysis of the OFC generator, including material dispersion, has been given in [2], however, we need a modified analysis to make a more precise estimation. Fig. 1 shows a schematic illustration of an OFC generator. The OFC generator consists of an EO phase modulator installed in an FP cavity so that the efficiency of the modulation is increased by multiple passes of light through the EO phase modulator. An OFC is generated when a sinusoidal voltage signal with a constant frequency f_m is fed into the EO phase modulator.

The evolution of the light amplitude with time inside the FP cavity used in the OFC generator is described by

$$E_c(t, z+2L') = \sqrt{T}E_i + R\exp\left\{-j2\beta' - 2v_0\frac{\partial}{\partial t} + j\frac{1}{M}\frac{\partial^2}{\partial t^2}\right\} \times \exp\{-j2\beta\sin(2\pi f_m t)\}E_c(t, z) \quad (1)$$

where R and T are the reflectivity and transmittivity of the mirrors. The electric field of the light inside the FP cavity and the incident laser beam are described as $E_c\exp(j2\pi\nu_0 t)$ and $E_i\exp(j2\pi\nu_0 t)$, respectively, where the E_i and E_c are, respectively, the complex amplitudes of the electric field inside the FP cavity and the incident laser beam, and ν_0 is the laser frequency. β' is $\frac{\pi(\nu_0-\nu_R)}{\mathrm{FSR}}$, where ν_R and FSR are one of the resonant frequencies which stands near ν_0, and the free spectral range at the optical frequency of ν_0 of the FP cavity in the absence of modulation, respectively. v_0 is defined as $\frac{\Delta f_m}{2FSRf_m}$, where Δf_m is defined as $f_m - N \times \mathrm{FSR}$, where N is an integer to satisfy that the value of $|\Delta f_m|$ is smallest. M is defined as $\frac{2\pi c}{D\lambda_0^2 L_c}$, where $D \equiv \frac{\lambda_0}{c}\frac{\partial^2 n_e}{\partial\lambda^2}_{\lambda=\lambda_0}$ is the material dispersion of the crystal used for the EO phase modulator, in which $\lambda \equiv \frac{c}{\nu}$ is wavelength of light and $\lambda_0 \equiv \frac{c}{\nu_0}$ is the wavelength of incident laser, c is the speed of light in vacuum, ν is frequency of light, and L_c is the length of the crystal used for the EO phase modulator. β is the amplitude of phase modulation. The variable z is a total distance of space through which intracavity light is propagated. The variable t is a retarded time and is defined such that for any distance z along the optical axis inside the cavity, zero phase of the modulation is at the time $t = 0$. Since L' is the length of the FP cavity, when the $E_c(t, z)$ expresses the complex amplitude of the electric field inside the FP cavity in any place at any time, the $E_c(t, z+2L')$ expresses that in the same place, in the time which is delayed for a round-trip time ($\equiv \frac{1}{\mathrm{FSR}}$) of light inside the FP cavity. This equation is driven by performing reverse Fourier transformation of (1b) in [2] and using $\frac{D\lambda_0}{2}$ ($\equiv \frac{\partial n_e}{\partial\nu}_{\nu=\nu_0} + \frac{\nu_0}{2}\frac{\partial^2 n_e}{\partial\nu^2}_{\nu=\nu_0}$) instead of $\frac{\partial n_e}{\partial\nu}$ which is used in [2], where n_e is the refractive index.

In the approximation of the short cavity, (1) becomes a conventional differential equation such as

$$2L'\frac{\partial}{\partial z}E_c(t, z) = \left\{-\frac{\pi}{F} - j2\beta' - 2v_0\frac{\partial}{\partial t} + j\frac{1}{M}\frac{\partial^2}{\partial t^2} - j2\beta\sin(2\pi f_m t)\right\} \times E_c(t, z) + \sqrt{\frac{\pi}{F}}E_i \quad (2)$$

The amplitude of the output light field $E_0(t)\exp(j2\pi\nu_0 t)$ in steady state is described by

$$E_0(t) = \lim_{z\to\infty}\sqrt{\frac{\eta_{\mathrm{FP}}\pi}{F}}E_c(t, z). \quad (3)$$

Equation (2) can be numerically analyzed by the beam propagation method [10], [11], which has been used for the analysis of light propagation in waveguide such as an optical coupler, an optical switch, an nonlinear optical fiber, etc.

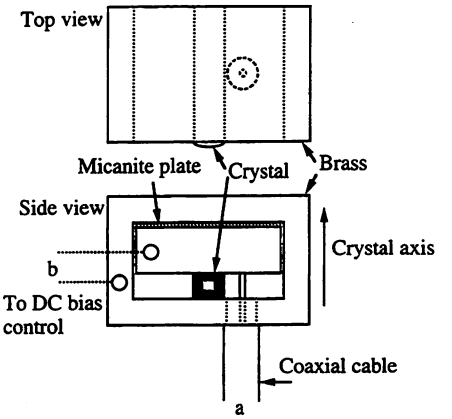

Fig. 2. Structure of a modified monolithic optical frequency comb generator.

From the consideration of an analogy with Schrödinger equation of (2), as given by Appendix A, the OFC can exist in the frequency span of $\pm\frac{\sqrt{2(-\beta'+\beta)M}}{2\pi}$ from the carrier frequency. The frequency span Δf of the OFC is derived as

$$\Delta f = \frac{\sqrt{2(-\beta'+\beta)M}}{\pi}. \quad (4)$$

When the $-\beta'+\beta$ is set to be 2β, which is maximum in the limit of (6), Δf can be equivalent to the dispersion limit of the frequency difference measurement $f_{d-\mathrm{limit}}(\equiv 2\frac{\sqrt{\beta M}}{\pi})$. The way to derive the formula of $f_{d-\mathrm{limit}}$ is shown in Appendix A. Even if $f_{d-\mathrm{limit}}$ is too large to observe it, Δf can be observed because the maximum absolute value of the frequency distance from the carrier frequency is less than half of the $f_{d-\mathrm{limit}}$. If $-\beta'+\beta$ is set to be much less than 2β, it is possible to estimate $f_{d-\mathrm{limit}}$ from the value of Δf, which is much smaller than $f_{d-\mathrm{limit}}$.

III. Experiment

An extended-cavity semiconductor laser at 780 nm was used for the experiment. The laser-power incident on the OFC generator was about 4 mW. A monolithic OFC generator [3] was used. It consists of an EO crystal ($LiNbO_3$, 1.25 × 1 × 21 mm^3) with high-reflection coatings (99.5% at the wavelength of 830 nm) on both ends, i.e., the EO crystal becomes a monolithic optical FP cavity so that the OFC generator can be made to have lower optical round-trip loss than previous OFC generator, which was composed of separated parts, such as an anti-reflection coated EO phase modulator and high-reflection coated mirrors. For obtaining a high finesse of the optical resonance, two ends of the crystal were polished to be flat and convex (with a curvature radius of 50 mm), respectively. The EO crystal was installed in the microwave waveguide resonator, which was made of brass to increase the microwave electric-field intensity in the EO crystal for highly efficient EO modulation. The free spectral-range FSR and the modulation frequency f_m were 3.15 GHz and 6.3 GHz (= 2 FSR), respectively. The maximum of the single-pass modulation index β was measured to be 0.36π radian when the microwave power was about 10 W. The values of η_{FP} and

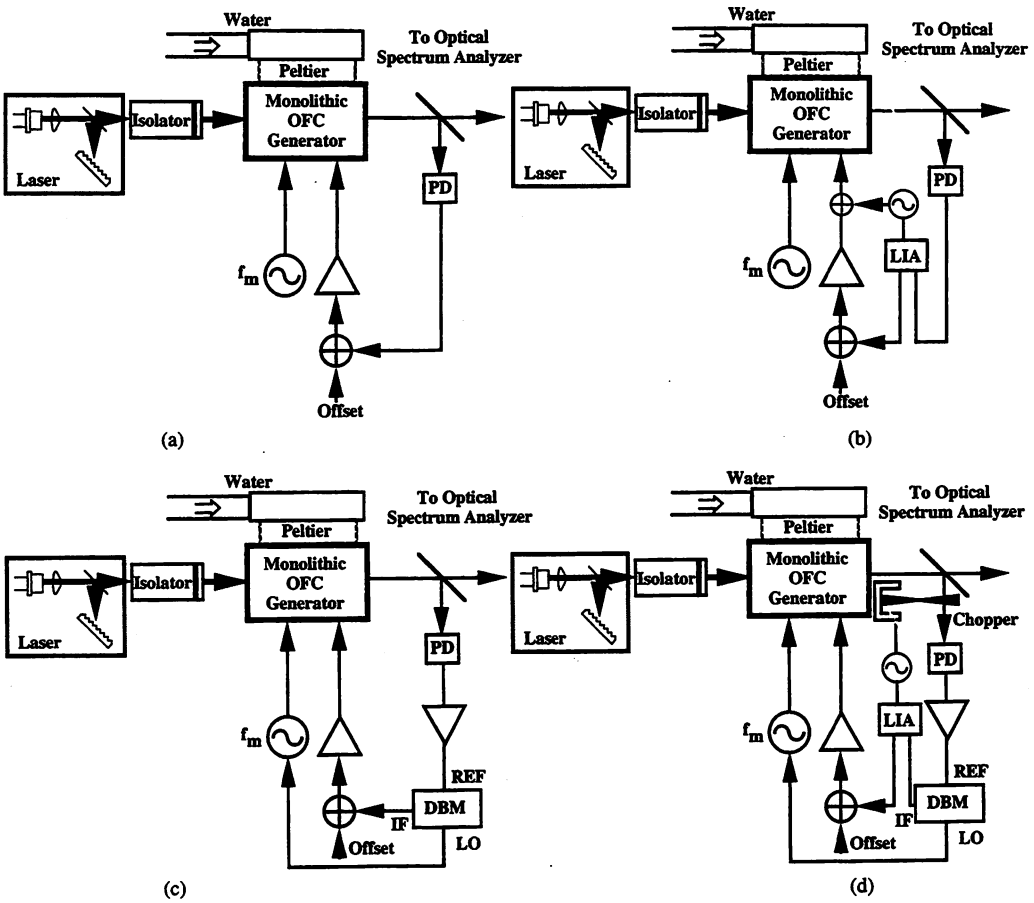

Fig. 3. Schematic illustration of the experimental setups. PD: photo-diode; DBM: double balanced mixer; LIA: lock in amplifier. (a), (b), (c), and (d) are the experimental setups for the different methods to get the error signal.

finesse F were ~20% and ~300, respectively. A portion of the output was monitored by an optical spectrum analyzer.

The resonant frequency of the OFC cavity must be set to be close to the laser frequency, i.e., the value of β' must be set to be a constant value between $-\beta$ and β, as shown Appendix A. For this purpose, two problems should be solved. One of the problems is how to change the value of β', and the other is how to know the value of β'. In order to change β' without changing the laser frequency, the monolithic OFC generator was modified for supplying dc bias on the EO crystal as shown in Fig. 2. To supply dc bias on the crystal, a micanite plate is inserted between the metal block on the crystal and the outside of the microwave resonant cavity for electrical isolation between both electrodes on the crystal. By supplying the dc bias to the crystal, the value of β' can be changed precisely with a coefficient of ~0.02 rad/V. To obtain the error signal in proportion to the value of β', we tried to use four methods and compared each other. The method in Fig. 3(a) is the simplest one whose error signal in the output of the photo-diode is shown in Fig. 4(a) as a function of the β' for the particular case of $\beta = 0.21\pi$ rad. In this method, the bandwidth of the photo-diode is so low that the average power of the output of the OFC generator was used as an error signal directly. By changing the offset in the error signal and changing the sign of the feedback, we can change the lock point of β' between $\pm\beta$. This method is stable enough for the experiments, however, it cannot be used for locking β' to 0. The method of Fig. 3(b) is the modified version of Fig. 3(a) for locking β' to 0, and its error signal is shown in Fig. 4(b). By modulating the cavity of the OFC generator at low frequency < 1 MHz and detecting the signal amplitude in the output of the OFC generator by using a locking amplifier, the error signal of Fig. 4(b) was obtained. Since the error signal shown in Fig. 4(b) is the differential signal of Fig. 4(a), this method can be used for locking β' to be 0. However, as shown in Appendix B, this method dithers the phase and intensity of the higher order sidebands in the OFC. Fig. 4(c) shows the error signal in the IF port of double-balanced mixer. However, there were problems in the detection of the error signal for the feedback. The problems were the offset much larger than the distance between the peak-to-peak of the error signal and its drift, which corresponds to ~0.1 rad/min in the detection β'. The offset and drift are due to the microwave soaking into the photo-diode through the air. In order to solve this problem, it is effective to use a chopper in front of the photo-diode and a lock-in amplifier, as shown in Fig. 3(d). In this case, the large offset was removed and the drift was decrease to < 0.001 rad/min. Fig. 4(d) shows the error signal in the output of the lock-in amplifier.

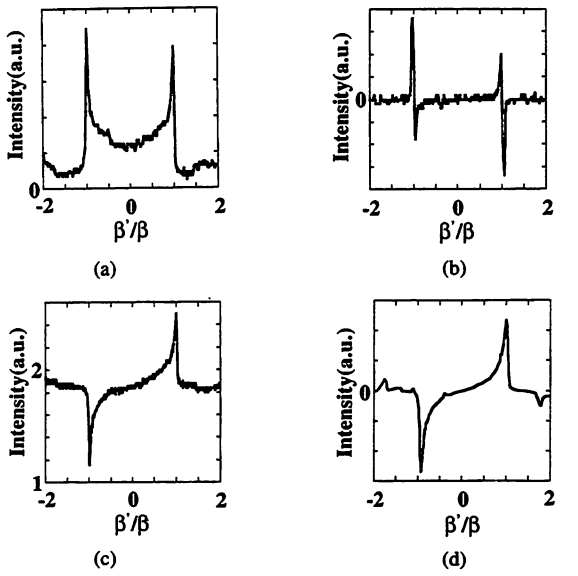

Fig. 4. Demodulated error signal as a function of β'/β, where β was 0.21π rad. (a), (b), (c), and (d) show the error signals given in the setup shown by Fig. 2(a), (b), (c), and (d), respectively.

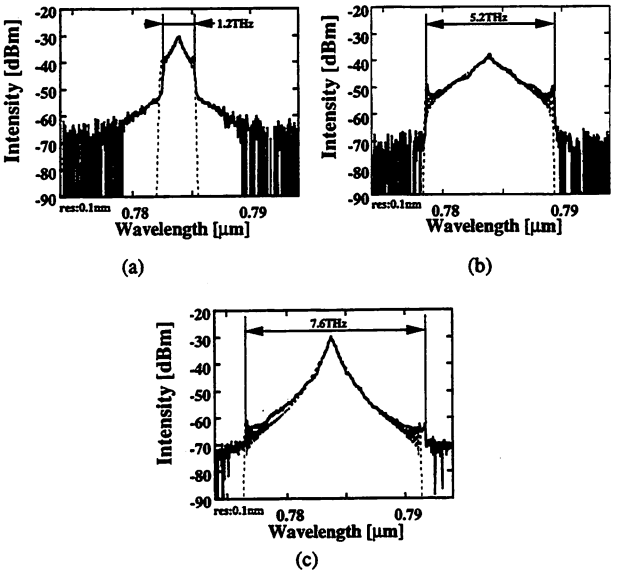

Fig. 6. Envelope spectra of the frequency comb. Solid lines, experimental results. Broken lines, calculated results using (2), $\beta = 0.36\pi$. (a) $\beta'/\beta = 0.95$; (b) $\beta'/\beta = 0$; and (c) $\beta'/\beta = -0.95$.

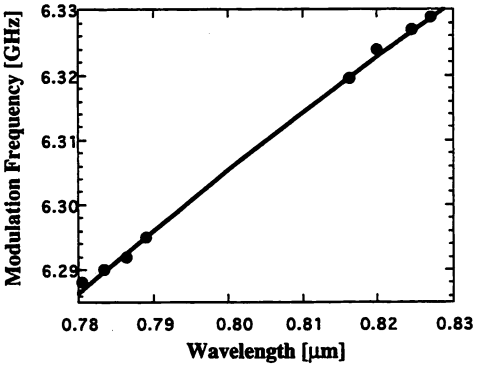

Fig. 5. Modulation frequencies which make the spectrum of the OFC to be symmetric. Dots are experimental results. The solid line is the calculated result. In this calculation, crystal temperature, and crystal length L_c were assumed to be 25 °C and 20.995 mm, respectively.

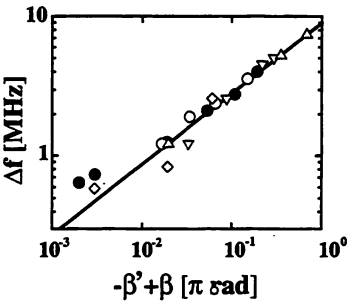

Fig. 7. Experimental results of the span Δf of the optical-frequency comb as a function of $-\beta' + \beta$. ◇, ○, •, ▽, and △ are experimental results for $\beta = 0.1\pi$, $\beta = 0.15\pi$, $\beta = 0.18\pi$, $\beta = 0.21\pi$, and $\beta = 0.36\pi$, respectively. The solid line is calculated result for $D = 1.2 \times 10^{-3}$ s/m^2.

The modulation frequency was accurately set to make the spectrum of the OFC to be symmetric for setting v_0 to be ~0. Fig. 5 shows the measured modulation frequencies which make the spectrum of the OFC symmetric. To measure them for wide-wavelength range, an extended-cavity semiconductor laser at 830 nm was also used. In this figure, the solid line is the calculated result from a Sellmeier's equation given in [12], and we can see experimental results are in good agreement with the calculated result. Fig. 6(a), (b), and (c) shows the examples of the observed OFC spectrum for the particular case of $\beta = 0.36\pi$ rad. Since the resolution (0.1 nm ≅ 50 GHz) was larger than $f_m = 6.3$ GHz, the envelope of the OFC's were observed. In these figures, we can find the stepwise discontinues on the both edges of envelope spectra of the OFC's. In these figures, the calculated results are also shown as dotted lines, and we can see experimental results are in good agreement with the calculated results. The observed Δf, which is defined as the frequency distance between both edges of envelope spectra of OFC's, is plotted as a function of $-\beta' + \beta$ in Fig. 7. The solid line is the calculated result of (4). The value of the D is 1.2×10^{-3} s/m^2, which is achieved from a Sellmeier's equation of $LiNbO_3$, given in [12]. We can see the experimental results are in good agreement with the calculated result. Our theoretical estimate is, therefore, applicable to the experiment, and we achieved the OFC spectrum extended to the limit of EO modulation due to the material dispersion in the crystal for the first time. The value of Δf, which is seen in Fig. 6(c), was 7.6 THz for the case of $\beta = 0.36\ \pi$ and $-\beta' + \beta = 1.95 \times \beta$. This value is almost equal to $f_{d-\text{limit}}$ for the case of $\beta = 0.36\ \pi$. The number of the sidebands in this envelope is estimated to be as large as 1200. To our knowledge, this value is the widest span of an OFC generated by EO modulation.

IV. Summary

The limit of the span of the OFC generation due to the material dispersion of the EO crystal is experimentally studied. By using a modified monolithic OFC generator, we observed the OFC spectrum in detail, and confirmed that the envelope of the OFC extended to a span as wide as 16 nm (or 7.6

THz), which corresponds to the dispersion limit. We can see experimental results are in good agreement with the calculated result. We also proposed methods of detecting the error signal for the FP cavity stabilization of the OFC generator.

APPENDIX A

We estimate the limit of OFC generation and frequency difference measurement by considering an analogy with Schrödinger equation. Equation (2) is simplified by setting $\frac{\partial}{\partial z} = 0$ and $F = \infty$. In this case, (2) becomes

$$\frac{Mv_0^2}{2}E_c(t) = -\frac{\left(\frac{\partial}{\partial t} + jMv_0\right)^2}{2M}E_c(t) + \{\beta \sin(2\pi f_m t) + \beta'\}E_c(t). \quad (5)$$

By replacing t by spatial coordinate, (5) is equivalent to a Schrödinger equation in which Planck's constant h is equivalent to unity. This equation represents the motion of a particle in the potential of $\beta \sin(2\pi f_m t) + \beta'$, whose mass, momentum, and total energy are M, $-j\frac{\partial}{\partial t} + Mv_0$ and $\frac{Mv_0^2}{2}$, respectively. Since $-j\frac{\partial}{\partial t}$ is equivalent to $2\pi k f_m$, which is the difference of angular frequency between the k-th sideband and the laser, it is considered that v_0 represents the initial velocity and the initial potential energy is 0. For E_c not being 0, β' must be

$$-\beta < \beta' < \beta. \quad (6)$$

When the velocity of the particle becomes v, the potential energy U of the particle can be solved by the energy conservation law as

$$U = \frac{Mv_0^2}{2} - \frac{Mv^2}{2}. \quad (7)$$

The dispersion limit of the frequency difference measurement $f_{d-\text{limit}}$ can be achieved by calculating the maximum value of $|\frac{1}{2\pi}\frac{\partial}{\partial t}|$ which corresponds to $\frac{1}{2\pi}|Mv - Mv_0|$. To realize the maximum value, the v_0 is set to be $\pm 2\sqrt{\frac{\beta}{M}}$ and the initial potential β' is set to be $-\beta$. In this case, the particle goes to the top of the potential, then comes to the initial point at which the velocity v becomes $\mp 2\sqrt{\frac{\beta}{M}}$. $f_{d-\text{limit}}$ is then achieved as

$$f_{d-\text{limit}} = \frac{2\sqrt{\beta M}}{\pi} = \frac{2\sqrt{\beta M}}{\pi}. \quad (8)$$

It should be pointed out that (8) is equivalent to the theoretical limit of a phase modulation in a dispersive long EO material [8], and that it corresponds to (5b) in [2].

The condition to get dispersion limit of the frequency difference measurement (which is mentioned above) can be realized easily, however, now it is not easy to observe the sideband at a frequency separation of $f_{d-\text{limit}}$ from the carrier frequency by using a conventional optical-spectrum analyzer because the sideband power at a such large frequency separation from the carrier frequency is very low. To overcome this difficulty, v_0 was set to be 0 in our experiment. In the case of $v_0 = 0$, the velocity of the particle which drops to the bottom of the potential $\beta' - \beta$ is

$$v = \pm\sqrt{\frac{2(-\beta' + \beta)}{M}}. \quad (9)$$

This results corresponds that the OFC can exist in the frequency span of $\pm\frac{\sqrt{2(-\beta'+\beta)M}}{2\pi}$ from the carrier frequency, and the maximum span reaches to $f_{d-\text{limit}}$ when $-\beta' + \beta \to 2\beta$.

APPENDIX B

Acoustic, electrical, and/or temperature fluctuations or additional modulation induced in an OFC generator disturbs the FP cavity resonant frequency of the OFC generators, and the intracavity light is modulated. To design a system for frequency difference measurement or frequency synthesis using an OFC generator, estimation of the permissible level of the fluctuations in the EO crystal is an essential. Here, we show the result of an theoretical and experimental study on the phase modulation coefficient of each sideband of an OFC induced by the modulation of the OFC generator FP cavity resonant frequency.

By setting $\frac{\partial}{\partial z} = \frac{\partial}{\partial t} = 0$ in (2), the amplitude $E_0(t)$ of the output light is derived as

$$E_0(t) = \sqrt{\eta_{\text{FP}}}\frac{E_i}{1 + \frac{j2\beta' F}{\pi} + \frac{j2\beta F \sin(2\pi f_m t)}{\pi}}. \quad (10)$$

To simplify (10), we consider the case $|2\pi f_m t| \ll 1$ and $\frac{2\beta' F}{\pi} \ll 1$. Then, this equation is approximated as

$$E_0(t) \cong \sqrt{\eta_{\text{FP}}}\frac{E_i \exp(j2\pi\nu_0 t)}{1 + j4F\beta f_m(t - \Delta t)} \quad (11)$$

where Δt is equal to $-\frac{\beta'}{2\pi f_m \beta}$. From the Fourier transform of (11), the phase delay ϕ_k in the electric field of the k-th sideband is given by

$$\phi_k = 2\pi k f_m \Delta t = -\frac{k}{\beta}\beta'. \quad (12)$$

From this result, it is seen that when β' accounts for the fluctuation of FP resonant frequency, and light passing through the modulator suffers additional modulation. The modulation coefficient of the additional modulation in β' is in direct proportion to the order of the sideband, and is in inverse proportion to the modulation index β. Since β' expresses the single pass modulation index of the light which passes through the EO crystal, the additional modulation of the k-th sideband is $\frac{k}{\beta}$ times larger than that of the single-pass modulation through the EO crystal. These results are understood by considering that the k-th sideband was generated by the light passing through the FP cavity $\frac{k}{\beta}$ times. The purpose of our experiments is the to confirm (12).

The experimental setup is shown in Fig. 8. The lasers were extended-cavity semiconductor lasers tunable between 1.51 and 1.58 μm with a very effective mode-hop suppression [13], and their short-term spectral linewidths were narrower than

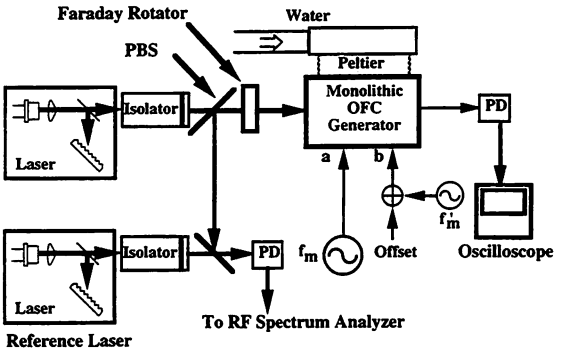

Fig. 8. Schematic illustration of the experimental setups. PD's: photo-diodes.

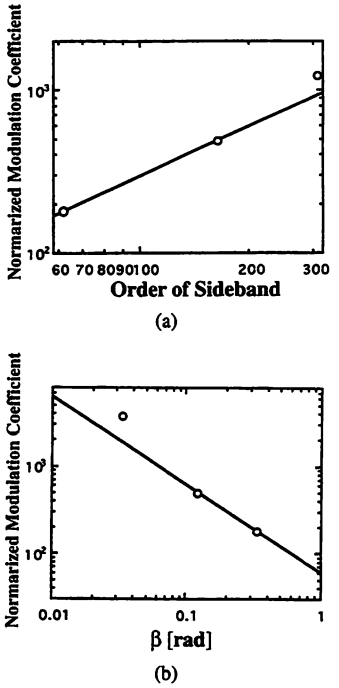

Fig. 9. Experimental results of normalized modulation coefficient. The solid lines are calculated results. (a) Normalized modulation coefficient is plotted as a function of the order of sideband, where β was 0.11π rad. (b) Normalized modulation coefficient is plotted as a function of β, where k was 61.

100 kHz. For the OFC generator, a modified monolithic OFC generator was used. It consists of an EO crystal ($LiNbO_3$, 1.25 × 1 × 22.6 mm^3) with high reflection coatings (99.6% at the wavelength of 1540 nm) on the both ends. The FSR and the modulation frequency f_m were 3.03 GHz and 6.06 GHz (= 2 FSR), respectively. The finesse was 410. By supplying a dc offset to the crystal, the value of β' can be controlled with a coefficient of 0.004π rad/V.

Under modulation of the OFC generator cavity at low frequency f'_m = 100 kHz simultaneously with a high-frequency modulation at f_m, the OFC cavity was set to make the intensity modulation signal seen on the oscilloscope to be small, i.e., the dc level of β' was set to be ~0. The beat signal between the reflection light of the OFC generator and the tunable reference laser was observed with an RF spectrum analyzer. In Fig. 9(a), the modulation coefficient which is normalized to the single pass modulation coefficient 0.004π rad/V is shown as a function of the order of sideband. In Fig. 9(b), normalized modulation index is also shown as a function of the modulation index. Calculated results are also shown in these figures. It can been seen that the experimental results are in good agreement with the calculated results, and it is confirmed that the modulation coefficient of the additional modulation is in direct proportion to the order of sideband and in inverse proportion to the modulation index β. Therefore, (11) can be used to estimate the permissible level of the β' for phase fluctuations of the sideband.

For example, if the permissible level of the fluctuation of β' for the phase fluctuations of the sideband is less than 1π rad, the fluctuations of β' must be lower than 10^{-3} rad in the case of k = 1000 and $\beta = 0.1\pi$ rad. This value corresponds to 1 MHz of resonant frequency fluctuation of the FP cavity for the OFC generator. To obtain this permissible level without any feedback technique, the fluctuation of bias voltage and temperature must be < 0.1 V and < 0.0003 degree, respectively.

ACKNOWLEDGMENT

The authors would like to thank Prof. T. Kobayashi and Dr. A. Morimoto of Osaka University for helpful comments on an electro-optic modulator. They would also like to thank Dr. K. Nakagawa and Dr. M. de Labachelerie for helpful discussions.

REFERENCES

[1] T. Kobayashi, T. Sueta, Y. Cho, and Y. Matsuo, "High-repetition-rate optical pulse generator using a Fabry–Perot electro-optic modulator," *Appl. Phys. Lett.*, vol. 21, no. 8, pp. 341–343, 1972.

[2] M. Kourogi, K. Nakagawa, and M. Ohtsu, "Wide-span optical frequency comb generator for accurate optical frequency difference measurement," *IEEE J. Quantum Electron.*, vol. 29, no. 10, pp. 2693–2701, 1993.

[3] M. Kourogi, T. Enami, and M. Ohtsu, "A monolithic optical frequency comb generator," *IEEE Photon. Technol. Lett.*, vol. 6, no. 2, pp. 214–217, 1994.

[4] K. Nakagawa, M. de Labachelerie, Y. Awaji, M. Kourogi, T. Enami, and M. Ohtsu, "Highly precise 1-THz optical frequency difference measurement of 1.5 μm molecular absorption lines," *Opt. Lett.*, vol. 20, no. 4, pp. 410–412, 1995.

[5] L. R. Brothers, D. Lee, and N. C. Wong, "Terahertz optical frequency comb generation and phase locking of an optical parametric oscillator at 665 gHz," *Opt. Lett.*, vol. 19, no. 4, pp. 245–247, 1994.

[6] H. Keang-Po and J. M. Kahn, "Optical frequency comb generator using phase modulation in amplified circulating loop," *IEEE Photon. Technol. Lett.*, vol. 5, no. 6, pp. 721–725, 1993.

[7] A. Morimoto, A. Shibagaki, and T. Kobayashi, "Efficient ultrashort pulse generation using a modified Fabry-Perot modulator," in *Proc. CLEO*, Baltimore, MD, May 1993, paper CThS84.

[8] T. Kobayashi and T. Sueta, "High-speed electro-optic devices and materials," in *Proc. CLEO*, June 1984, paper WG1.

[9] A. Morimoto, T. Okimoto, A. Soga, and T. Kobayashi, "FM laser operation of a Ti:Sapphire laser," *Trans. IEICE J.*, vol. E78-C, no. 1, pp. 88–90, 1995.

[10] T. B. Koch, J. B. Davies, and D. Wickramasinghe, "Finite element/finite difference propagation algorithm for integrated optical device," *Electron. Lett.*, vol. 25, no. 8, pp. 514–516, 1989.

[11] J. A. Fleck, J. R. Morris, and M. D. Feit, "Time-dependent propagation of high energy laser beams through the atmosphere," *Appl. Phys.*, vol. 10, no. 1, pp. 129–160, 1976.

[12] R. C. Eckardt, C. D. Nabors, W. J. Kozlovsky, and R. L. Byer, "Optical parametric oscillator frequency tuning and control," *J. Opt. Soc. Amer. B*, vol. 8, no. 4, pp. 646–667, 1991.

[13] M. de Labachelerie, C. Latrasse, K. Diomandé, P. Kemssu, and P. Cerez, "A 1.5 μm absolutely stabilized extended-cavity semiconductor laser," *IEEE Trans. Instrum. Meas.*, vol. 40, no. 2, pp. 185–190, 1991.

M. Kourogi was born in Shiga, Japan, in 1966. He received the B.S. degree from Shizuoka University, Shizuoka, Japan, in 1988, and the M.S. and Ph.D. degrees from the Tokyo Institute of Technology, Tokyo, Japan, in 1990 and 1993, respectively.

Since 1993, he has been with Tokyo Institute of Technology as a research associate. His current research interests are frequency synthesis of semiconductor lasers.

Dr. Kourogi is a member of the Japan Society of Applied Physics.

B. Widiyatomoko was born in Boyolali, Indonesia in 1962. He graduated from Gadjahmada University, Yogyakrta, Indonesia, in 1987, and received the M.S. degree in applied electronics from the Tokyo Institute of Technology, Tokyo, Japan, in 1994.

Y. Takeuchi was born in Saitama, Japan, in 1972. He received the B.S. degree in electronics engineering from the Tokyo Institute of Technology, Tokyo, Japan, in 1994 and is currently a graduate student at the Tokyo Institute of Technology.

M. Ohtsu (M'88–SM'90) was born in Kanagawa, Japan. He received the B.E., M.E., and Dr.E. degrees in electronic engineering from the Tokyo Institute of Technology, Tokyo, Japan, in 1973, 1975, and 1978, respectively.

In 1978, he was appointed a research associate; and in 1982, he became an associate professor at the Tokyo Institute of Technology. From 1986 to 1987, while on leave from the Tokyo Institute of Technology, he joined AT&T Bell Laboratories, Crawford Hill Laboratories, Holmdel, NJ. In 1991, he became a professor at the the Tokyo Institute of Technology. Since April 1993, he has been concurrently the leader of the "Photon Control" Project of Kanagawa Academy of Science and Technology, Kanagawa, Japan. His main fields of interest are photon scanning tunneling microscopy, its application to nanoscale photonics and quantum optics, and laser frequency control.

Dr. Ohtsu has written over 130 papers, and has received a number of patents. He is the author and coauthor of thirteen books, including two in English, entitled *Highly Coherent Semiconductor Lasers* (Boston, MA: Artech House, 1992) and *Coherent Quantum Optics and Technology* (Dordrecht: Kluwer, 1993). He has been a tutorial lecturer on the SPIE and OSA. He has been awarded eight prizes from academic institutions, including the Issac Koga Gold Medal of URSI in 1984, Japan IBM Science Award in 1988, and two awards of the Japan Society of Applied Physics in 1982 and 1990, respectively. He is a member of OSA, Japan Society of Applied Physics, IEICE of Japan, and IEE of Japan.

PHYSICAL REVIEW A VOLUME 52, NUMBER 5 NOVEMBER 1995

Observation of a transient response of recoil-induced resonance: A method for the measurement of atomic motion in an optical standing wave

M. Kozuma,[1,*] Y. Imai,[1,*] K. Nakagawa,[1,*] and M. Ohtsu,[1,2,*,†]

[1]*Interdisciplinary Graduate School of Science and Engineering, Tokyo Institute of Technology, 4259 Nagatsuta-cho, Midori-ku, Yokohama 226, Japan*

[2]*Kanagawa Academy of Science and Technology, KSP East 408, 3-2-1 Sakado, Takatsu-ku, Kawasaki 213, Japan*

(Received 2 May 1995)

We demonstrate a method to directly observe the dynamics of motion of cold atoms in an optical standing wave using a recoil-induced resonance. By detecting a transient response of this resonance, we observed the interaction between an atomic population grating and a periodic optical potential. Using this method, we investigated the lifetime of the atomic grating under various conditions in the optical potential. As a result, we obtained the appropriate conditions for the long lifetime and observed the narrowest linewidth in the recoil-induced resonance corresponding to the atomic temperature of 4.4±0.3 μK for ^{87}Rb atoms.

PACS number(s): 32.80.Pj

Recent developments of laser cooling and manipulation techniques of atoms have made it possible to investigate the wave nature of atoms in such fields as atomic interferometers [1]. Under the typical condition for the cold atoms in an optical standing-wave potential, where the atomic de Broglie wavelength is comparable to the optical wavelength, we have to consider atoms as atomic waves rather than particles. The interaction between the cold atoms and such a periodic optical potential is essential for the cooling processes of stimulated [2,3] or polarization gradient [4–7] cooling and the quantized motions of atoms in an optical crystal [8–14]. Most of the related experiments have mainly showed the stationary properties of atoms, such as final velocity distribution of cooled atoms and the quantized energy structure of atoms in the optical potential. Besides the stationary properties, the dynamic properties of atomic motion are also important and are inevitable in understanding the cooling process involving the damping force to the atoms in the optical potential [15]. In recent experiments [16–20], the velocity distribution of cold atoms was precisely measured using a recoil-induced resonance. In this paper, we propose a method to measure the dynamic property of atomic motion in a periodic optical potential using the recoil-induced resonance. Detecting the transient response of the recoil-induced resonance, we can observe the damping oscillation that reflects the interaction between the atomic grating and the periodic optical potential. By using this method, we can obtain the lifetime of the atomic grating or the coherence time of atomic momentum states in the periodic optical potential.

In the following part of this paper, we will first show the theoretical interpretation of the transient response of the recoil-induced resonance. Next, we will present the experimental results obtained by this method and will show the experimental approach to study the dynamics of cold atoms. From these experimental results, we obtained the conditions for the long lifetime of the atomic grating. Finally, as an application of the present study of atomic dynamics, we will show the results of the velocity distribution measurement of cold ^{87}Rb atoms using the recoil-induced resonance under these conditions.

We consider the situation where the two probe beams with wave vectors $\vec{k}_1$ and $\vec{k}_2$ cross in a cold atomic vapor at an angle θ. Their angular frequencies ω_1, ω_2 are detuned from the atomic resonant frequency by Δ, and their frequency difference $\delta=\omega_2-\omega_1$ is much smaller than Δ. Two beams have parallel and linear polarization in the direction perpendicular to the probe beam plane. Initially, frequency difference δ is fixed to zero and then rapidly switched to a nonzero value. The transient response of the recoil-induced resonance can be measured by detecting the transmitted intensity of one of the probe beams. The intensity change of the probe beam is given by the imaginary part of the polarization P induced by two probe beams, and is approximately expressed as

$$\mathrm{Im}\{P\}\cong-\frac{2\mu\chi}{\Delta}\int dr_q \sin(qr_q-\delta t)\psi^*(r_q,t)\psi(r_q,t). \tag{1}$$

Here, χ, μ, $\psi(r_q,t)$, and r_q are the Rabi frequency, the transition dipole moment, the atomic wave function of the motion of the center of mass, and the projection of radius vector on $\vec{q}$, where $\vec{q}=\vec{k}_2-\vec{k}_1$ and $q=|\vec{q}|$. It is a modified equation that describes the signal of the recoil-induced resonance in terms of the coherence between the momentum states [20]. From Eq. (1), one can easily observe that the signal is contributed only from the component of atomic density modulated by $\sin(qr_q-\delta t)$. The motion of the atomic center of mass is governed by the Hamiltonian that includes the potential with the periodicity of $\cos(qr_q-\delta t)$. Therefore, initially, atomic population grating modulated by $\cos(qr_q-\delta t)$ is generated with δ fixed to zero. After rapidly switching δ to a nonzero value, periodic interaction between the atomic grating and the optical standing wave moving with the speed of δ/q is induced. As it can be understood by Eq. (1), this periodic interaction manifests itself as an oscillation of the probe signal with frequency δ. The time evolu-

*FAX: +81-45-921-1204.
†FAX: +81-44-819-2072.

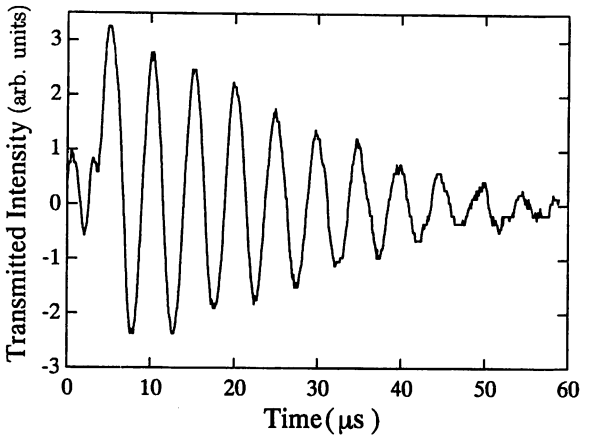

FIG. 1. Transient signal of recoil-induced resonance. At 0 μs, the frequency difference was switched to a nonzero value.

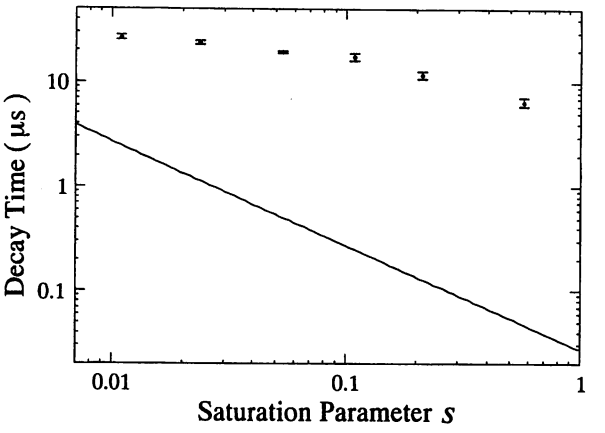

FIG. 2. Dependence of the signal decay time on the saturation parameter. Dots represent the measured decay times. The solid line represents the inverse of the optical pumping rate.

tion of the atomic grating by this interaction can also be observed by this method. The atomic grating will dissipate if the periodic interaction gives rise to heating. However, in the case of cooling, the atomic grating tends to follow the moving optical standing wave, where the term "cooling" means the atomic motion is damped in the frame of moving optical potential. In both cases the time evolution of the atomic grating appears as a decay of oscillating signal.

In our experiment, a cold cloud of ^{87}Rb atoms was produced by a magneto-optical trap (MOT) in a rubidium-vapor cell [21]. The $5S_{1/2}F=2-5P_{3/2}F=3$ cyclic transition of the ^{87}Rb D_2 line was used as a cooling cycle. To produce a greater cooling effect, we used polarization-gradient cooling (PGC) [6,7]. First, the magnetic field was turned off quickly. After 5 ms, the detuning of the cooling light was increased, and 5 ms later, its intensity was reduced to $\frac{1}{5}$ of the original intensity. Finally, after 2 ms, the cooling and repumping lights were shut off. In MOT and PGC, $\sigma^+-\sigma^-$ laser configuration was utilized. The final temperature of the cold atoms was measured by the time-of-flight method [6,22,23] to be 4 ± 1 μK, where the error was mainly due to uncertainty in the determination of the initial size of the molasses.

For this cold sample, we measured the transient response of recoil-induced resonance. Two probe beams intersect inside the sample of prepared cold atoms. Initially, the frequency different δ was kept at zero, and after 20~40 μs, it was rapidly switched to more than 100 kHz. The light interaction time was assured to be sufficiently long to prepare coherence between the momentum states. In this experiment, two probe beams were generated from the same extended-cavity diode laser, and were frequency shifted by individual acousto-optic modulators (AOM). One of these acousto-optic modulators was driven by an rf synthesizer in order to control the frequency difference between the two probe beams. The intensities of the two beams were controlled by another AOM. A typical transient signal is shown in Fig. 1. Here the intensities of probe beams were 12 and 13 mW/cm^2. The beams's crossing angle θ was 14.0°. The probe beams's detuning was fixed to $\Delta/2\pi=+200$ MHz with respect to the $F=2$-$F=3$ transition. The frequency difference of the probe beams was switched from $\delta/2\pi=0$ to 200 kHz in order to observe the signal of damping oscillation.

We first measured the dependency of the decay time of the transient signal on the saturation parameter of probe fields. Figure 2 shows the result, where the solid line represents the inverse of optical pumping rate Γ' $(=s\Gamma)$, where s and Γ are the saturation parameter and a natural width of the atomic excited state, respectively. The intensity, frequency difference, and cross angle of the probe beams were equal to the values in Fig. 1. In order to change the saturation parameter, we changed the detuning $\Delta/2\pi$ from $+15$ to $+110$ MHz. From Fig. 2, one can observe that the decay time increases with decreasing saturation parameter. The induced atomic grating dissipates due to the optical pumping, where the rate is proportional to the saturation parameter. The decay time is expected to become longer as the saturation parameter becomes smaller. A comparison of the solid line and the closed circle in Fig. 2 reflects that the observed decay time is much longer than that expected from the saturation parameter. This result is consistent with the previous result obtained from the width of the recoil-induced resonance [16]. Such a long decay time of the atomic grating or the momentum space coherence can be explained by the energy separation, which is much larger than the recoil energy and the optical pumping rate [5,9].

We also compared the decay time in cases of both blue $(\Delta>0)$ and red $(\Delta<0)$ detuning of probe beams, where $|\Delta|/2\pi=20$ MHz for both cases. Measured transient response signals are shown in Fig. 3. The intensities of probe beams were 5.1 and 5.6 mW/cm^2 and the crossing angle θ was 14.4°. The frequency difference $\Delta/2\pi$ was switched from 0 to 140 kHz. In Fig. 3 the decay times in the cases of blue and red detuning were 14 ± 1 and 10 ± 1 μs, respectively. This implies that the decay time for the blue detuning was longer than that for the red detuning. This difference can be easily understood by considering the effect of stimulated cooling, which occurs only for the blue detuning of probe beams. In the case of red detuning, only the heating effect takes place to dissipate the atomic grating. However, in the case of blue detuning, a stimulated cooling effect is also expected under some conditions. If this effect is valid, the atomic grating tends to follow the moving standing-wave potential with the velocity of δ/q. As a result, the mean time of atoms staying at the potential minimum, where the field intensity is also minimum for the blue detuning, is longer

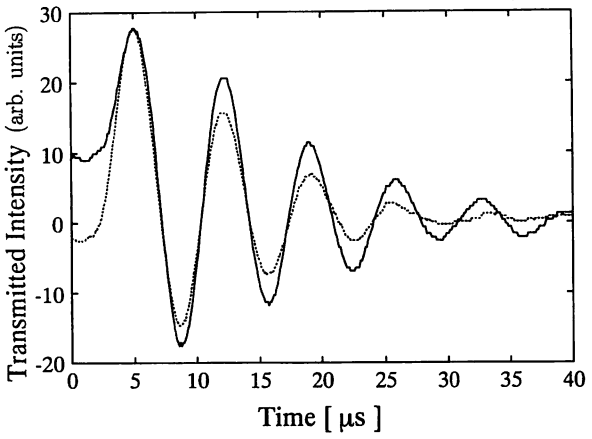

FIG. 3. Signals of transient response for blue and red detunings. The solid and broken curves are the signals for blue detuning $\Delta/2\pi = +20$ MHz and for red detuning $\Delta/2\pi = -20$ MHz, respectively.

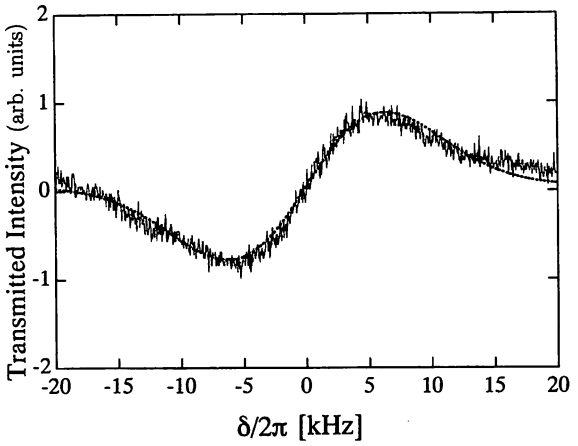

FIG. 4. Signal of the recoil-induced resonance (stimulated optical Compton scattering) for a very cold cloud of ^{87}Rb atoms. The solid curve represents the obtained signal averaged over 16 times of measurements. The broken curve is the theoretical fitting curve.

than the time of staying at the potential maximum. This time difference causes a smaller optical pumping rate for the blue detuning than that for the red detuning. It leads to the difference in the decay time of the transient response. The decay-time difference between blue- and red-detuning cases becomes smaller as the absolute value of detuning becomes larger, because the stimulated cooling effect also becomes smaller.

These two types of time evolution of the atomic grating can be distinguished more clearly by switching the frequency difference δ back to zero again, after observing the first transient response. If the atomic grating moves due to cooling, periodic interaction between the moving atomic grating and the stationary optical standing wave will be generated by this additional switching and the second transient response will be observed. This cannot be observed in the case of heating.

The decay-time measurement provides us with the conditions to achieve the narrow homogeneous width in the temperature measurement using the recoil-induced resonance. The evolution time of the atomic grating corresponds to the coherence time between atomic momentum states, which is related to the homogeneous width of the recoil-induced resonance [16–20]. Therefore, it can be understood that for a narrower homogeneous width, the saturation parameter should be smaller and blue detuning is preferable. Based on this consideration we measured the temperature of cold ^{87}Rb atoms. Figure 4 shows the experimental results. The intensity of the probe beams were 12 and 13 mW/cm^2, and the crossing angle θ was 14.0°. The detuning of the probe beams was fixed to $\Delta/2\pi = +730$ MHz. Under this condition, saturation parameter s becomes 2.5×10^{-4}, which corresponds to the optical pumping rate of 1.5 kHz. The temperature corresponding to the inhomogeneous width 1.5 kHz is lower than 0.1 μK. We fitted the signal shape by the derivative of Gaussian profile and estimated the temperature to be as low as 4.4 ± 0.3 μK. The measurement error was mainly due to the sweep rate of relative frequency $d(\delta/2\pi)/dt = 44$ kHz/ms. This temperature is in good agreement with that measured by the time-of-flight method (4 ± 1 μK).

In summary, we demonstrated the method to directly observe the dynamics of cold atoms. It was confirmed experimentally that this method observes the periodic interaction between the atomic grating and the moving optical standing wave and time evolution of the atomic grating due to this interaction. This method can be a tool for the investigation of the fundamental process in the atomic cooling or in the interaction between atoms and field.

The authors wish to thank Dr. C. Salomon (ENS) and Dr. W. Jhe (Seoul National University) for their valuable comments and discussions.

[1] M. Kasevich and S. Chu, Phys. Rev. Lett. **67**, 181 (1991).
[2] J. Daribard and C. Cohen-Tannoudji, J. Opt. Soc. Am. B **2**, 1707 (1985).
[3] A. Aspect, J. Daribard, A. Heidmann, C. Salomon, and C. Cohen-Tannoudji, Phys. Rev. Lett. **57**, 1688 (1986).
[4] J. Dalibard and C. Cohen-Tannoudji, J. Opt. Soc. Am. B **6**, 2023 (1989).
[5] Y. Castin and J. Daribard, Europhys. Lett. **14**, 761 (1991).
[6] C. Salomon, J. Dalibard, W. D. Phillips, A. Clairon, and S. Guellati, Europhys. Lett. **12**, 683 (1990).
[7] C. Monroe, W. Swann, H. Robinson, and C. Wieman, Phys. Rev. Lett. **65**, 1571 (1990).
[8] P. Verkerk, B. Lounis, C. Salomon, C. Cohen-Tannoudji, J.-Y. Courtois, and G. Grynberg, Phys. Rev. Lett. **68**, 3861 (1992).
[9] J.-Y. Courtois and G. Grynberg, Phys. Rev. A **46**, 7060 (1992).
[10] A. Hemmerich and T. W. Hänsch, Phys. Rev. A **70**, 410 (1993).
[11] A. Hemmerich, C. Zimmermann, and T. W. Hänsch, Europhys. Lett. **22**, 89 (1993).
[12] G. Grynberg, B. Lounis, P. Verkaer, J.-Y. Courtois, and C. Salomon, Phys. Rev. Lett. **70**, 2249 (1993).

[13] A. Hemmerich, C. Zimmermann, and T. W. Hänsch, Phys. Rev. Lett. **72**, 625 (1994).

[14] A. Kastberg, W. D.Phillips, S. L. Rolston, and R. J. C. Spreeuw, Phys. Rev. Lett. **74**, 1542 (1995).

[15] M. Doery, M. Widmer, J. Bellanca, E. Vredenbregt, T. Bergeman, and H. Metcalf, Phys. Rev. Lett. **72**, 2546 (1994).

[16] D. R. Meacher, D. Boiron, H. Metcalf, C. Salomon, and G. Grynberg, Phys. Rev. A **50**, R1992 (1994).

[17] J-Y. Courtois, G. Grynberg, B. Lounis, and P. Verkerk, Phys. Rev. Lett. **72**, 3017 (1994).

[18] J. Guo, P. Berman, B. Dubetsky, and G. Grynberg, Phys. Rev. A **46**, 1426 (1992).

[19] J Guo and P. Berman, Phys. Rev. A **47**, 4128 (1993).

[20] J. Guo, Phys. Rev. A **49**, 3934 (1994).

[21] E. L. Raab, M Prentiss, Alex Cable, Steven Chu, and D. E. Pritchard, Phys. Rev. Lett. **59**, 2631 (1987).

[22] P Lett, R. Watts, C. Westbook, W. Phillips, P. Gouid, and H. Metcalf, Phys. Rev. Lett. **61**, 169 (1988).

[23] D. S. Weiss, E. Riis, Y. Shevy, P J. Ungar, and S. Chu, J. Opt. Soc. Am. B **6**, 2072 (1989).

Optical frequency measurement of the $H^{12}C^{14}N$ Lamb-dip-stabilized 1.5-μm diode laser

Y. Awaji, K. Nakagawa,* M. de Labachelerie,† and M. Ohtsu‡

Interdisciplinary Graduate School of Science and Engineering, Tokyo Institute of Technology, 4259, Nagatsuta-cho, Midori-ku, Yokohama 226, Japan

H. Sasada

Department of Physics, Faculty of Science and Technology, Keio University, 3-14-1 Hiyoshi, Kohoku-ku, Yokohama 223, Japan

Received May 18, 1995

We have measured the frequency of the $P(27)$ line of $H^{12}C^{14}N$ at 1556 nm, using the 778-nm two-photon transition of Rb as a frequency reference. The measured frequency was 192,622,446.9 ± 0.1 MHz. We believe that this experiment is the first absolute frequency measurement of a laser stabilized to a saturation dip at 1.5 μm and also the most accurate measurement of a 1.5-μm optical frequency. © 1995 Optical Society of America

Frequency standards in the optical region are required for various applications such as high-resolution spectroscopy, optical communications, and metrology. Such a frequency standard with high accuracy is especially useful in the 1.5-μm region as a reference for frequency-division multiplexing optical fiber communication systems. Although a visible I_2-stabilized He–Ne laser (λ = 0.633 μm) and a mid-IR CH_4-stabilized He–Ne laser (λ = 3.39 μm) are popular, highly accurate frequency standards, there were no frequency standards in the 1.5-μm region with an accuracy as high as 10^{-9}. Since we carried out saturation spectroscopy of weak overtone bands of molecules in the 1.5-μm region, using an external buildup cavity,[1] it has become possible to establish new accurate optical frequency standards in this region.

However, absolute frequency measurements for these molecular lines are still necessary. Such frequency measurements using a frequency chain from the mid-IR standards were reported for the 1.52-μm He–Ne laser frequency[2]; however, the accuracy was only $\sim 1.3 \times 10^{-7}$, and many intermediate IR lasers were required. We have proposed a method for frequency measurements at 1.5 μm, using two He–Ne lasers as references.[3] However, because the frequencies of the Rb two-photon transition at 778 nm were recently determined from same two He–Ne lasers with an accuracy of 10^{-11},[4] Rb may be used as a new reference to measure 1.5-μm frequencies directly by frequency doubling.

In this Letter we demonstrate what is to our knowledge the first absolute frequency measurement of the $P(27)$ line in $H^{12}C^{14}N$ (HCN) at 1556 nm, with this Rb two-photon transition at 778 nm as a reference. Figure 1 shows the experimental setup. A grating-feedback-type external-cavity semiconductor laser module was used as a tunable oscillator from 1.51 to 1.58 μm. Its output optical power is higher than 5 mW in the entire tuning range at a typical 100-mA injection current. Part of its output beam was injected into a Fabry–Perot cavity-type glass cell filled with HCN gas. The finesse of the cavity was ~200. The laser frequency was locked to the cavity resonance frequency by the Pound–Drever method. Then the length of the Fabry–Perot cavity was modulated by a piezoelectric transducer actuator, which allowed the laser frequency to stabilize to the peak of the saturated-absorption signal by detecting the Fabry–Perot transmitted power with a lock-in amplifier.[5] The assignment of the absorption signal was determined with a wavemeter. Figure 2(a) shows the Fabry–Perot transmitted power corresponding to the saturated absorption dip of the $P(27)$ line in HCN; its FWHM linewidth was 2.2 MHz. The stability of the locked laser frequency was better than 10^{-11}, with a 140-mW intracavity power and a beam waist diameter of 1 mm. The reproducibility of the stabilized frequency was of the order of 20 kHz (10^{-10}).

The probe laser at 778 nm was obtained with a high-power (30 mW typically) semiconductor laser at 785 nm (Hitachi HL7852G) without antireflection coating. The diode was mounted upon a grating-feedback-type external-cavity laser and kept at 10 °C to yield oscillation at 778 nm. The laser power was ~ 20 mW for a 100-mA injection current, and its output beam was split by an acousto-optic modulator (AOM, Fig. 1) whose diffracted light of the first order was injected into a glass cell containing natural Rb and reflected back to the incident direction by a 100%-reflectivity mirror. The Rb cell temperature was kept at 90 °C, and the fluorescence was observed with a photomultiplier. A typical fluorescence spectrum of the ^{87}Rb $5S_{1/2} \rightarrow 5D_{3/2}$ transition is shown in Fig. 2(b). There are three hyperfine components, which correspond to the transitions between $F_g = 1$ and $F_e = 1, 2, 3$. The fluorescence linewidth was ~1.6 MHz, with an incident power (at the input of the Rb cell) of 10 mW and a beam diameter of ~1 mm. We locked the 778-nm laser frequency to the absorption peak of the ($F_g = 1 \rightarrow F_e = 3$) line by modulating the injection current of the laser at 20 kHz and detecting the intensity of the modulated fluorescence with a lock-in amplifier. The absolute frequency of this Rb line has been measured to be 385,243,555,144.5(5.0) kHz.[4]

0146-9592/95/192024-03$6.00/0

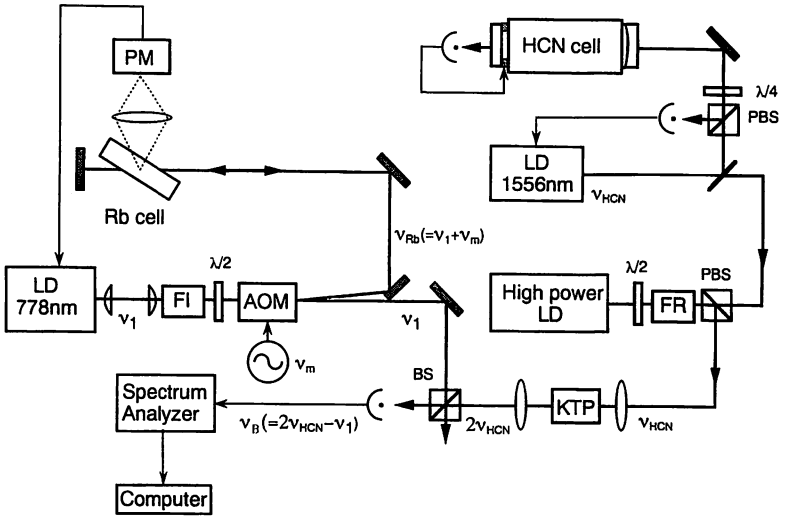

Fig. 1. Experimental setup for frequency measurement of the $P(27)$ line in HCN: LD's, laser diodes; FI, Faraday isolator; BS, beam splitter; PBS's, polarizing beam splitters; FR, Faraday rotator; PM, photomultiplier.

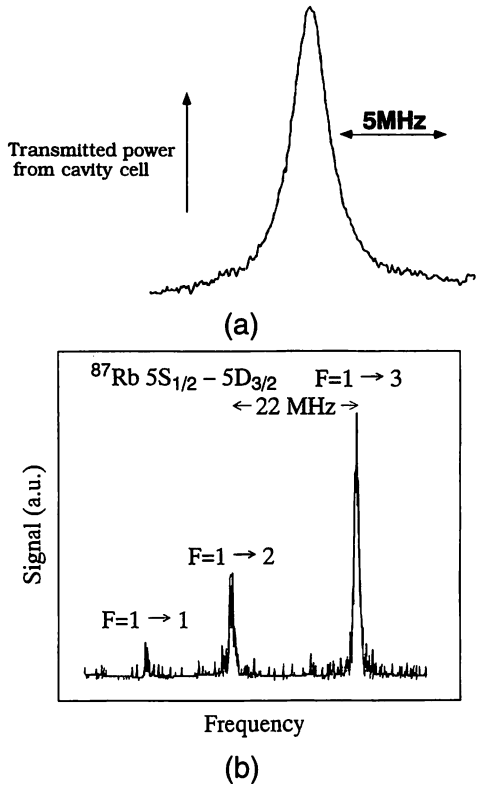

Fig. 2. (a) Saturated-absorption spectral shape of the $P(27)$ line of HCN at 1565 nm. (b) Fluorescence spectral shape of the ^{87}Rb $5S_{1/2}-5D_{3/2}$ $F_g = 1 \rightarrow F_e = 1-3$ transitions.

Inasmuch as the 1.5-μm laser output power was too low for efficient frequency doubling, the output of the stabilized 1.5-μm laser was used to injection lock a high-power 1.5-μm semiconductor laser to produce single-mode output power of as much as 30 mW. For the highest-frequency stability of the injection-locked laser the optimum power of the master laser was ~0.3 mW. The output of the injection-locked laser was then focused into a 10-mm-long KTP crystal (Fig. 1) to generate several nanowatts of its second-harmonic frequency at $\lambda = 778$ nm. This second-harmonic beam was mixed with the AOM zeroth-order beam of the 778-nm laser locked to the Rb transition, and we observed the beat signal with a 2-GHz-bandwidth photodiode and a spectrum analyzer. The typical signal-to-noise ratio of the beat was ~10 dB. The beat signal obtained when both lasers are locked is shown in Fig. 3. The sidebands next to the center signal at 6 MHz come from the modulation of the Pound–Drever method for the 1.5-μm laser. Because both lasers are slightly frequency modulated for locking to the reference lines, the beat position is also modulated, resulting in a rectangular line shape when it is averaged over a long time. The optical frequency ν_{HCN} of the HCN $P(27)$ saturated absorption is then given by

$$\begin{aligned}\nu_{HCN} &= (\nu_1 + \nu_B)/2 \\ &= (\nu_{Rb} - \nu_m + \nu_B)/2 \\ &= 192,622,446.9 \pm 0.1 \text{ MHz}, \end{aligned} \quad (1)$$

where the beat center frequency is $\nu_B = 1418.7$ MHz, ν_{Rb} is the frequency of the two-photon transition, and ν_m is the 80.0-MHz frequency shift introduced at the AOM first order of diffraction.

The width of the beat spectrum was ~4 MHz, with a dip at the center frequency; therefore direct

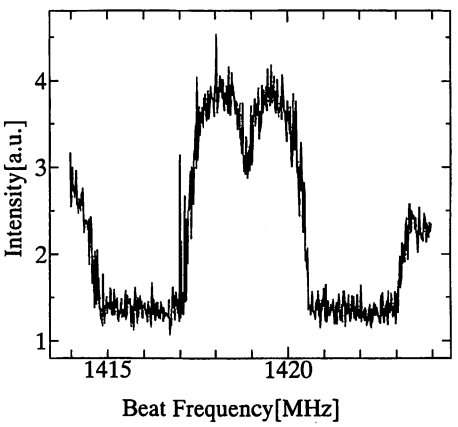

Fig. 3. Spectral shape of the beat signal between the Rb-stabilized 778-nm laser and the second harmonic of the HCN-stabilized 1.5-μm laser.

observation of the beat signal permits a determination of its center frequency with an ≈ 0.2-MHz precision. To improve the beat measurement precision we recorded the beat signal with a computer with 500-point resolution and integrated the beat spectrum to compute its center of gravity. From a comparison of several files in various conditions, we estimated that the resulting beat measurement error was less than ± 0.05 MHz($\delta\nu_B$). On the other hand, in a previous study we found that the frequency offsets of the stabilized lasers from the top of the absorption lines were lower than ± 50 kHz for the 1.5-μm laser ($\delta\nu_{1.5}$) and ± 50 kHz for the 778-nm laser ($\delta\nu_{\mathrm{Rb}}$). Then the accuracy is

$$\delta\nu_{\mathrm{HCN}} = (\delta\nu_{\mathrm{Rb}} + \delta\nu_B)/2 + \delta\nu_{1.5}\,. \qquad (2)$$

Thus we believe that the accuracy of our frequency measurement is certainly better than the ± 0.1 MHz cited in Eq. (1). The absorption frequency was measured in two cases of HCN pressure ($p = 30$ and $p = 55$ mTorr). Between the two cases, we slightly changed all adjustments for locking the 1.5 μm laser, such that we unlocked the laser and removed the cell to be refilled with HCN. When both lasers were locked again, any differences between the measured frequencies were found to be within our measurement error of ~ 0.1 MHz. This comparison allowed us to verify that the reproducibility of the frequency beat is actually better than 0.1 MHz.

To our knowledge, the measurement of the 1.52-μm He–Ne laser frequency[2] was the most precise absolute frequency measurement in the 1.5-μm region and was obtained with a 25-MHz accuracy. Therefore our measurement gives an absolute frequency reference at 1.5 μm with the precision improved by more than 2 orders of magnitude. Moreover, we could roughly predict the absolute frequency of this $P(27)$ line by using the most accurate molecular constants of the HCN $2\nu_1$ band, which were obtained from wavelength measurements with CO lines as frequency references,[6] and by a more precise fit obtained after the measurement of the HCN $P(16)$ line by a heterodyne method.[7] As our result is shifted only by 15 MHz from the value computed with these constants, both measurement are fairly consistent.

The present absolute frequency measurement is useful for absolute frequency calibrations at 1.5 μm: By measuring the difference frequency between this HCN $P(27)$ line and an unknown frequency, using an optical frequency comb generator,[8] an absolute measurement of the unknown frequency is possible. This method was used to measure the relative frequencies between rovibrational lines of C_2H_2 (Ref. 9) and will be used again to compare these frequencies with our absolute reference. Such measurements will allow us to establish soon an atlas of the absolute frequencies of the C_2H_2 lines in this 1.5-μm wavelength region within an accuracy of a few hundred kilohertz. These new accurate references can be used, for instance, to calibrate high-resolution wavemeters precisely or to synthesize with high accuracy, with the help of an optical comb generator, almost any 1.5-μm optical frequency. Such calibrations could be especially valuable for frequency-division multiplexing optical fiber communications.

In summary, we have measured the frequency of a 1.5-μm semiconductor laser stabilized to the saturated-absorption dip of the HCN $P(27)$ line with 10^{-9} (± 0.1-MHz) accuracy, using the Rb two-photon transition at 778 nm as a frequency reference. This first result improved the precision of 1.5-μm frequency references by 2 orders of magnitude. Although this is the most accurate frequency measurement in the 1.5-μm region, improvements are still possible, such as in the laser frequency locking method and in beat frequency measurements. It is worth improving the absolute frequency measurement further for metrologic applications. These frequency references should also be linked directly to He–Ne laser-based references and should become key elements of the network of frequency standards in the optical domain.

*Present address, Tokyo Institute of Polytechnics, 1583, Iiyama, Atsugi 243-02, Japan.

†Permanent address, Laboratoire de l'Horloge Atomique/Centre National de la Recherche Scientifique, Université de Paris-Sud, Bat. 221, 91405 Orsay, France.

‡Also with the Kanagawa Academy of Science and Technology, Ohtsu Photon Control Project, KSP East Room 408, 3-2-1, Sakato, Takatsu-ku, Kawasaki 213, Japan.

References

1. M. de Labachelerie, K. Nakagawa, and M. Ohtsu, Opt. Lett. **19,** 840 (1994).
2. D. A. Jennings, F. R. Petersen, and K. M. Evenson, Opt. Lett. **4,** 129 (1979).
3. Y. Awaji, M. Kourogi, K. Nakagawa, T. Enami, and M. Ohtsu, in *Quantum Electronics and Laser Science*, Vol. 12 of 1993 OSA Technical Digest Series (Optical Society of America, Washington, D.C., 1993), paper QThE7.
4. F. Nez, F. Biraben, R. Felder, and Y. Millerioux, Opt. Commun. **102,** 432 (1993).
5. M. de Labachelerie, K. Nakagawa, Y. Awaji, and M. Ohtsu, Opt. Lett. **20,** 572 (1995).
6. H. Sasada and K. Yamada, Appl. Opt. **29,** 3535 (1990).
7. H. Sasada, S. Takeuchi, M. Iritani, and K. Nakatani, J. Opt. Soc. Am. B **8,** 713 (1991).
8. M. Kourogi, K. Nakagawa, and M. Ohtsu, IEEE J. Quantum Electron. **29,** 2693 (1993).
9. K. Nakagawa, M. de Labachelerie, Y. Awaji, M. Kourogi, T. Enami, and M. Ohtsu, Opt. Lett. **20,** 410 (1995).

AD.3

AD : Lasers, stabilisation and applications

High efficient electro-optic modulation of Semiconductor lasers

M. KOUROGI[1,2], T.SAITO[2,3] and M. OHTSU[1,2]

1)Interdisciplinary Graduate School of Science and Engineering, Tokyo Institute of Technology, 4259 Nagatsuta, Midori-ku, Yokohama, Kanagawa 226 Japan.
Phone: +81-45-924-5455, Fax+81-45-921-1204
2)Kanagawa Academy of Science & Technology, KSP East Building, Room 408, 3-2-1 Sakado, Takatsu-ku, Kawasaki, Kanagawa 213 Japan.
3)Anritsu Corporation, 1800 Onna, Atsugi, Kanagawa, 234 Japan.

High efficient electro optic modulation of semiconductor lasers makes it possible to control optical signals in the picosecond range and tera hertz frequency range for optical communication, optical sensing, and optical frequency standards. This paper reviews resent progress of the field of reserch and development about optical frequency synthesis using electro optic modulation of semiconductor lasers.

The electro optic modulation with the very high modulation index produces wide optical sidebands spreading over several terahertz region. The amplitudes, frequencies and phases of sideband-components are decided by those of the modulation signal and those of the modulated laser. When the frequency and phases of the sideband-components are compared with those of the other lasers, the relative frequency and phase between the modulated laser and the other lasers can be measured in great precision.

Toward realizing 10THz class optical frequency synthesis, we have developed a monolithic optical frequency comb (OFC) generators which is one kind of developed Fabry-Perot electro-optic modulator[1]. and the sidebands generation spreading over 6~8THz range around 0.8μm wavelength[2] and 1.5μm wavelength region[3] have been realized. One tera hertz class optical phase locking. optical frequency measurement of several ten molecular lines have been realized by applying it for semiconductor lasers. It will also be applied for optical frequency chain.

Toward realizing 100THz class optical frequency synthesis, we have tried new techniques. By using dual-cavity technique, the conversion efficiency of the OFC generation was increased by 18dB. This technique will make it possible to employ optical nonlinear pulse compression technique to expand the region in which the sidebands are generated.

References

1. T. Kobayashi. et.al.,*Appl. Phys. Lett.*, vol.21, pp.341-343, 1972.
2. M. Kourogi. et.al., *IEEE J. Quantum Electron.*, vol.31, pp.2120-2126. 1995.
3. M. Kourogi. et.al., *IEEE Photon. Technol. Lett.*, vol.6, pp.214-217, 1994.

特　集　マルチメディア時代に期待される波長多重通信

光周波数の基準と計測

東京工業大学
大津　元一

1．まえがき

波長多重光通信のチャンネル間のクロストーク，誤切り替えなどを防ぐためには，各チャンネルの光波長が安定であり，その値が正確に計測可能である必要がある。多重度が大きくなり，隣り合うチャンネルの波長間隔が小さくなると，より精度の高い計測が必要となり，波長ではなく周波数を扱うことになる。周波数は光源から発するフォトンのエネルギーによって決まるのに対し，波長は測定環境（空気の屈折率の値など）にも依存するからである。

本稿では通信用の波長1.5μm帯の半導体レーザの周波数を安定化し，その値を高精度計測する方法について概説する。具体的には次の項目からなる。

(1)安定な周波数ν_rを供給する周波数基準を見い出す。

(2)上記の基準となる周波数ν_rに半導体レーザ周波数ν_lが一致するように自動制御を施す。この結果，$\nu_l=\nu_r$となる。

(3)既知の周波数ν_sを有する安定なレーザと，上記のレーザとの間の差周波数ν_d（$=\nu_l-\nu_s$）を測定する。この結果をもとに半導体レーザ周波数ν_lの値を$\nu_d+\nu_s$により求める。これは周波数基準値ν_rを求めていることに他ならない。

以下の各節ではこれらの項目に従って記述する。

2．周波数基準

周波数基準としては温度変動，機械振動などの外乱の影響を受けないものが必要である。そのようなものとして気体原子，分子の共鳴スペクトルの中心周波数が挙げられる。固体や液体の場合にはスペクトル線幅が広く，またその形が複雑なので，スペクトル中心周波数を見い出すのが困難である。それに対し気体原子，分子のスペクトル幅は数kHz～1GHzであり，その形が比較的単純なので，中心周波数を見い出しやすい。これらの気体にレーザ光を入射させ，レーザ周波数を掃引することによりこの気体の吸収スペクトル，または蛍光スペクトルを測定する。レーザ周波数がスペクトル中心周波数からずれると，そのずれの大きさによって吸収量，蛍光強度が変わるので，この変化量よりレーザ周波数とスペクトル中心周波数との差を知ることができる。

このような周波数基準となりうる原子として波長1.5μm帯にはクリプトン（Kr）の放電気体などがある。分子の例を**表1**に示す。これらの分子はその振動，回転運動の特性に起因し，実際には**表1**の波長付近に多数のスペクトル線を有する。従って，波長のばらつきの多い半導体レーザの周波数基準としてこれらのスペクトル線のいずれか一つが使用し得る。この表のなかで，シアン（HCN），アセチレン（C_2H_2）などがよく用いられる。ただし，シアンは猛毒気体なので使用にあたり十分な注

表1　波長1.5μm帯での周波数基準となりうる分子

分子名		スペクトル波長（μm）
（2原子分子）	CO	1.57
	HI	1.55
（3原子分子）	CO_2	1.58
	D_2O	1.53，1.55
	HCN	1.53−1.54
	H_2O	1.5
	HDO	1.56，1.55
（4原子分子）	C_2H_2	1.52−1.53
	NH_3	1.51
（5原子分子）	SiH_4	1.54

意が必要である。これらの吸収スペクトルの線幅は従来は1GHz程度あったが，最近では高パワーの光を入射させ，非線形光学効果の一種である飽和吸収を誘起することにより，そのスペクトル幅は数MHzまで小さくできるようになったので，周波数基準としての精度が向上した。

3．レーザ周波数の安定化

使用する半導体レーザの周波数ν_lが前節の基準周波数ν_rに一致するように自動制御を施し，半導体レーザ周波数を安定化する必要がある。半導体レーザの温度や注入電流を変化させると，レーザ共振器の屈折率および長さが変化して，レーザ周波数が変化する。その変化率はおよそ−10GHz/℃，−1GHz/mAである。特に注入電流変化によるレーザ周波数変化の応答周波数は半導体レーザ特有の緩和振動周波数によって決まり，それは数GHzである。すなわち，レーザ周波数変化の応答速度は1ns以下であるので，広帯域・高速の自動制御が可能になる。

注入電流によりレーザ周波数を変化させながら，レーザ光を前節の気体分子に照射し，吸収スペクトル量を測定する。スペクトル強度の値からレーザ周波数とスペクトル中心周波数（基準周波数）の差がわかるので，その差が0になるように注入電流を自動制御する。

1μs以内の応答速度の高速自動制御によりレーザ周波数の短期ゆらぎが抑圧でき，レーザ発振スペクトルが狭窄化される。極限的な値として非制御時の数100kHzの発振スペクトル幅の値をこの制御により数Hzまで狭窄化することも可能である。応答速度1μs以上の低速自動制御によりレーザ周波数の長期ゆらぎ（温度変動にともなうドリフトなど）が抑圧される。

高速自動制御の結果，周波数計測を行う意義のある高スペクトル純度の半導体レーザ光源が実現し，一方，低速自動制御の結果，長時間にわたる周波数計測に耐えうる低ドリフト光源が実現する。両者の自動制御が不可欠である。これらの自動制御装置の設計は通常の電子回路における雑音抑圧のための自動制御装置の設計と同等である。

4．差周波数の測定

通常の光検出器の応答帯域は数1GHz以下であるので，これより高い周波数をもつ電磁波の計測は不可能である。従って光の周波数は測定できないことになるが，金属−絶縁体−金属の点接触ダイオードを用いた特殊な方法で1970年代にHe-Neレーザなどの気体レーザの周波数が10^{-10}程度の誤差で測定されている。従って，前節までで準備した半導体レーザの周波数を測定する方法は，1．節(3)で示したように，このような既知周波数ν_sをもつレーザと半導体レーザとの差周波数ν_dを光検出器で測定することである。

しかし上記の気体レーザの波長は可視〜近赤外であり，必ずしも半導体レーザの波長と近接していない。従って，差周波数ν_dは極めて大きな値となり，通常の光検出器では測定できない。そこで，半導体レーザの周波数ν_lを変換し，既知周波数に近い周波数を発生させる方法が必要である。そのような方法として，酸化物非線形光学結晶に1台の半導体レーザ光を入射し，第二高調波（周波数$2\nu_l$）を発生する方法，さらには波長の異なる2台の半導体レーザ光（周波数ν_{l1}，ν_{l2}）を同時入射させて両者の和または差周波数（$\nu_{l1}+\nu_{l2}$または$\nu_{l1}-\nu_{l2}$）を発生する方法がある。半導体レーザは波長1.5μm帯以外にも多くの波長帯で発振する素子が多数あるので，これらを援用すると図1に示すように波長0.33μmから

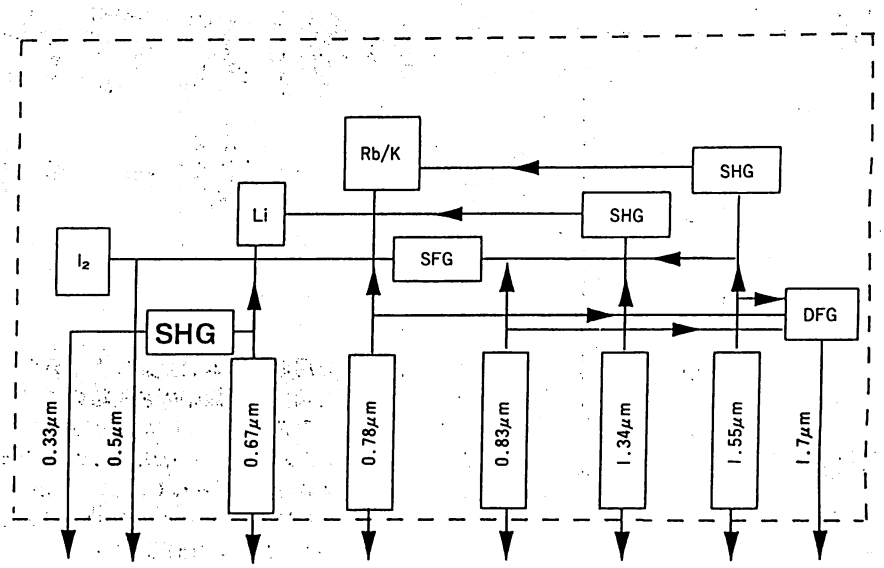

図1　非線形光学効果を利用した周波数変換の概念図。SHG：第二高調波発生，SFG：和周波数発生，DFG：差周波数発生。Rb，K，Li，I_2などの原子，分子はその共鳴スペクトルを周波数基準に使う。□内の数値（単位：μm）は現存する各種半導体レーザの発振波長帯を表す。□外の数値（単位：μm）は周波数変換の結果発生した光の波長を表す。

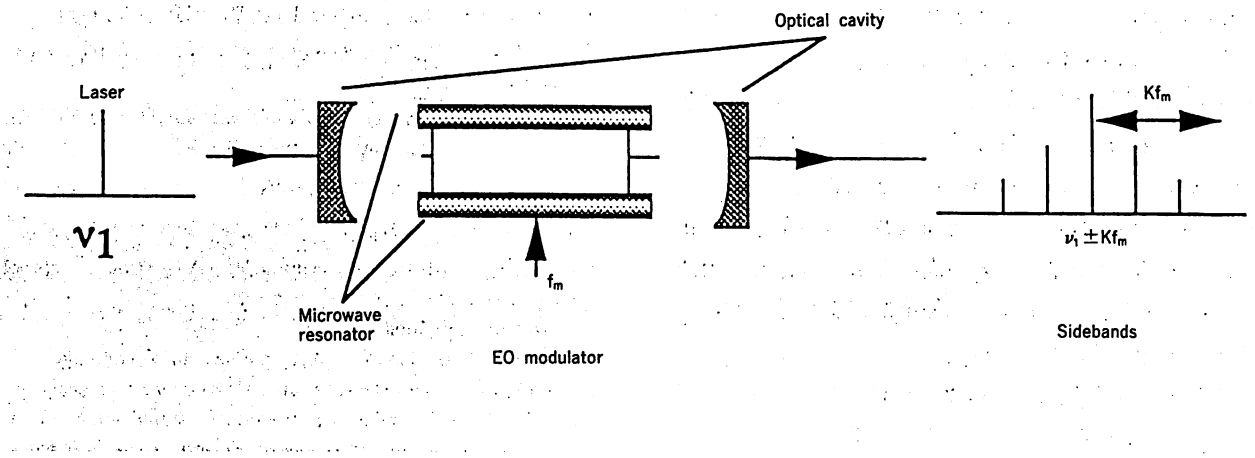

図2　光周波数コム発生器の構造

1.7μmにわたって多数の波長の光を発生することができ，上記のような既知周波数のレーザとの差周波数を測定するのに都合がよい。

ただし上記の非線形光学効果を用いた周波数変換では細かい周波数範囲での変換が不可能である。そこで，これを可能にするために電気光学結晶を用いた高効率の光位相変調器が考案されている。このための装置の一つが図2に示す光周波数コム発生器である。発生した変調側波帯が周波数変換された光に相当するが，この側波帯のスペクトルの分布が同図に示すように櫛（Comb）のように見えることからこの名前がつけられた。リチウムナイオベート（$LiNbO_3$）の電気光学結晶をファブリ・ペロー共振器の中に設置し，変調用のマイクロ波周波数をファブリ・ペロー共振器の自由スペクトル域の整数倍にする。これによりファブリ・ペロー共振器内を往復する光が互いに同じ位相で変調され，高効率の位相変調が実

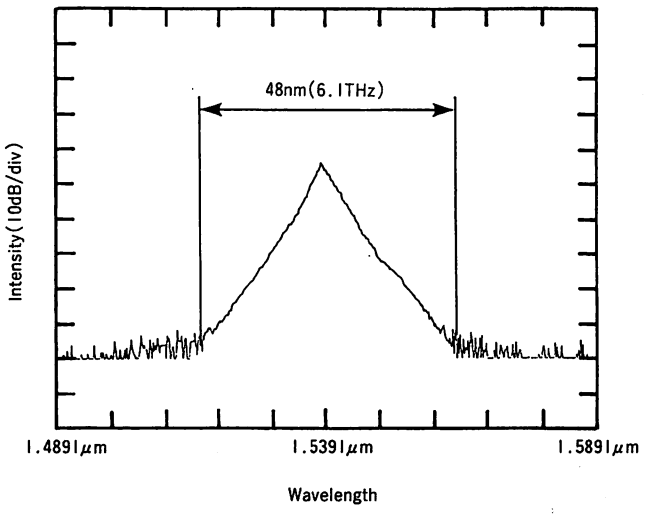

図3　光周波数コム発生器により発生した位相変調側波帯の包絡線のスペクトル測定結果。これは低分解能（0.2nm）の測定装置を用いた結果なので，個々の側波帯は分離されていない。しかし，この6.1THzの幅内には1,040本の変調側波帯が5.9GHzの等間隔で並んでいる。

現する。図3は周波数5.9GHz，パワー10Wのマイクロ波により変調した時に発生した変調側波帯の包絡線のスペクトルの測定結果である。周波数6.1THzにわたって側波帯が発生していることがわかる。その間隔は5.9GHzなので，1,040本の側波帯が得られている。

側波帯の発生範囲は電気光学結晶の屈折率の波長分散によって制限されると推定され，その上限値は約7THzと見積もられている。従って，上記の非線形光学効果を用いた周波数変換と，光周波数コム発生器とを組み合わせれば，側波帯の内の少なくとも1つは既知周波数と極めて近くなり，通常の光検出器により差周波数が測定可能となる。

このような方法を使い，最近ではHCNやC_2H_2の吸収スペクトル中心周波数に安定化された半導体レーザ周波数を誤差10^{-9}程度で測定することが可能になってきている。

5．まとめ

自動制御された半導体レーザの周波数安定度は波長多重光通信システムへの使用に耐えるほど高くなってきている。一方，周波数の計測も1970年代の実験室内で特殊レーザ，特殊検出器を用いていた時代から実用的技術へと急速に発展している。今後は真に実用的な可搬システムの実現が望まれる。

参考文献

1）大津元一，コヒーレント光量子工学，朝倉書店 1990年
2）M. Ohtsu, *Highly Coherent Semiconductor Lasers,* Artech House, Boston, 1992
3）M. Ohtsu, *Frequency Control of Semiconductor Lasers,* Wiley Interscience, New York, 1996

Optical reference frequencies and their measurements

by Motoichi Ohtsu
Graduate School, Tokyo Institute of Technology

Search of highly accurate optical frequency references, principle and practice of frequency stabilization of a semiconductor laser are reviewed. Further, recent progress of highly accurate measurement of stabilized frequency is presented.

〈著　者〉　オオツ モトイチ（東京工業大学・大学院総合理工学研究科）
〈連絡先〉　045－924－5455